HARVARD UNIVERSITY

THE GRADUATE SCHOOL OF ARTS AND SCIENCES

THESIS ACCEPTANCE CERTIFICATE

(To be placed in Original Copy)

The undersigned, appointed by the

Division

Department of Physics

Committee

have examined a thesis entitled

"Electronic Quantum Interference in Ballistic Semiconductor Nanostructures"

presented by Jordan Asher Katine

candidate for the degree of Doctor of Philosophy and hereby certify that it is worthy of acceptance.

Signature .....

Typed name Robert M. Westervelt, Chair

Signature .....

Typed name Michael Tinkham

Signature .....

Typed name Efthimios Kaxiras

Date August 22, 1996

Electronic Quantum Interference in Ballistic Semiconductor Nanostructures

A thesis presented

by

Jordan Asher Katine

to

The Department of Physics

in partial fulfillment of the requirements

for the degree of

Doctor of Philosophy

in the subject of

Physics

Harvard University

Cambridge, Massachusetts

August, 1996

Abstract

This thesis examines phase coherent ballistic electron transport in the two-dimensional electron gas formed in a remotely doped GaAs/$Al_xGa_{1-x}As$ heterostructure. As a precursor to these measurements, the weak localization effect in an array of narrow channels is used to measure the electronic phase coherence time at temperatures between 4.2 K and 100 mK. The measured values agree well with those predicted by theories based on electron-electron interactions above 200 mK; below this temperature there is an apparent saturation in the amplitude of the localization correction.

Next we report on the observation of coherent backscattering in very open ballistic devices consisting of a quantum point contact and two reflector gates. Unlike quantum billiards in which this effect has previously been measured, our devices are designed to yield many backscattered trajectories enclosing very similar areas. An array of devices is used to average away magnetoconductance fluctuations, which would otherwise prevent a quantitative analysis of the coherent backscattering effect in our system.

We also report on measurements in which quantum interference of forward-scattered trajectories is studied. These devices consist of two closely-spaced point contacts and a reflector gate. Electrons may travel between the point contacts directly or by scattering off the reflector. Quantum interference between these two paths is evident when a perpendicular magnetic field is applied. In addition, interference oscillations are also observed by changing the bias voltage applied to the reflector gate, allowing our devices to function as electron interferometers.

Strong, periodic conductance oscillations are observed at low temperatures in electron interferometers very similar to a Fabry-Perot cavity. The devices consist of a quantum point contact in the tunneling regime and a single reflector gate designed to focus reflected electrons back to the point contact. By changing the spacing between the reflector

and point contact, we observe the conductance resonances due to constructive and destructive interference of multiply-scattered electron waves within the cavity.

Table of Contents

Acknowledgements

The second floor of Gordon McKay is a great place to work, and this thesis would not have been possible without the assistance I received from many of my colleagues there. First I must thank my advisor Bob Westervelt. Bob allows his students the freedom to work on their own ideas, while at the same time providing guidance during the inevitable rough times. I would also like to thank the other members of my committee, Professors Tinkham and Kaxiras, for their interest in my work. In addition, my research has benefited greatly from discussions with Professor Heller and his student Stella Chan.

Much of my actual laboratory training came from elder students in the Westervelt group, and I want to thank Charlie Marcus, Alex Rimberg, John Baskey, Doug Mar, Fred Waugh, Junmin Hu, and Scott Yang for their willingness to be pestered by a clueless new student. I owe a special debt to Michael Berry with whom I worked during my first two years in the lab. Aram Adourian and I joined and graduated from the group together, and I was fortunate to have his assistance throughout my graduate career, especially in installing our friend the Kelvinox. Mark Eriksson worked with me on several of the experiments in this thesis, and invariably provided valuable insights into our results. More importantly, though, he always got me the ball when I was open. The younger students in the group: Catherine Crouch, Rex Beck, Carol Livermore, and Mark Topinka, have all helped me along the way, and I wish them the best of luck in their future work here.

The Westervelts' neighbors down the hall have always been accommodating when it came to sharing equipment. Though all of Tinkham students and post-docs have been helpful, I want to particularly acknowledge Chuck Black and Dan Ralph. Dan in many ways became a *de facto* Westervelt post-doc, and I will feel fortunate if I can give his students at Cornell even a small fraction of the assistance he has provided to the students in the Westervelt group. I was lucky to have a friend like Chuck in graduate school. Chuck

was always willing to help me both in and outside of lab, and his support was particularly important in helping me survive the endless series of problem sets that was our first year at Harvard. I also want to thank Dave Carter and Steve Shepard for their excellent management of the McKay cleanroom. In particular Steve suggested the ammonium hydroxide cleaning that helped make wirebonding possible.

Graduate school is the culmination of many years of study, and I certainly would not have been at Harvard were it not for the teachers I had along the way. I especially want to recognize my high school physics instructor William Atherton and my Princeton thesis advisor Gordon Cates, who both encouraged my interest in the subject.

Finally, I need to thank my first and best teachers, my parents. They instilled in me the love of learning and curiosity that are so important in science. Their encouragement and support have made this work possible.

Chapter 1

Introduction

1.1 Perspective

Recent advances in semiconductor growth technology have made it possible to control the chemical composition of crystals down to thicknesses approaching an atomic monolayer. It is possible to fashion interfaces so that they contain a thin layer of highly mobile electrons. This layer is known as a two-dimensional electron gas (2DEG), because momentum perpendicular to the growth (z) direction has been quantized, constraining the electron motion to the xy-plane.

New lithographic techniques offer many ways to laterally constrain the motion of the electrons in the 2DEG. The length scales of these devices can be as small as 100 nm, allowing one- or even quasi-zero-dimensional systems to be studied. Furthermore, the mean free path in high-mobility 2DEGs can be several microns, which makes it easy to fabricate devices in which electron motion is ballistic rather than diffusive. In addition, the low electron sheet density in semiconductors leads to long Fermi wavelengths. The Fermi wavelength in 2DEG systems can be comparable to device dimensions, which facilitates the study of quantum transport.

This thesis describes several experiments that probe the transport properties of ballistic electrons. Ballistic motion is intriguing, because a designed potential, rather than random impurities, determines electron motion. This element of control, along with the short lengthscales and speed of ballistic semiconductor devices, makes them appealing candidates for eventual commercial applications, but an understanding of the fundamental properties of ballistic transport must be achieved before any such applications may be realized.

A number of techniques can be used to control the motion of ballistic electrons. Magnetic fields can be used to steer ballistic electron trajectories. Electrostatic gates can serve as both lenses and mirrors that focus electrons in much the same way as their optical counterparts do. In fact, the term "electron optics" is often used to describe such experiments, because of the similarity between the behavior of electron waves in 2DEGs and that of light.

In optics, interference effects are often utilized to perform precise measurements. In the same vein, quantum interference experiments in 2DEGs provide a means to sensitively probe the transport of ballistic electrons. Such experiments are possible in two-dimensional electron gas systems, because the elastic collisions with impurities and device boundaries that determine the electron's motion do not destroy the phase memory of the electron. At sufficiently low temperatures in these systems, it is possible for an electron to have a phase coherence length which is longer than its mean free path.

1.2 Contents

This section presents a brief overview of the contents of this thesis. The remainder of this chapter will be spent reviewing some of the fundamentals of the two-dimensional electron gas systems used in our experiments. Included in this review are descriptions of quantum point contacts and the Landauer-Büttiker formalism.

Chapter 2 is mainly concerned with the fabrication of the samples. It begins with a description of the GaAs/AlGaAs heterostructures that furnish the 2DEG systems for our experiments. Important fabrication procedures such as the formation of ohmic contacts, electron-beam lithography, metallization, and wirebonding are all discussed. The chapter also includes a brief description of some problems commonly encountered in the fabrication of 2DEG samples.

The focus of Chapter 3 is cryogenics and electronics. The chapter goes into great detail in describing both the ^{3}He cryostat and the Kelvinox 100 dilution refrigerator. As the Kelvinox is a new piece of a equipment that has yet to be decried in a Westervelt group dissertation, it is hoped that Chapter 3 and its associated appendices will serve as a useful reference to future users of the refrigerator. In describing the electronics used to measure our samples, particular attention is given to the low-noise voltage supplies that were built to bias our gated samples.

Chapter 4 is the first of four chapters that deal with the actual experiments. This chapter describes measurements of the electronic phase coherence time. The phase coherence time is determined by studying the weak localization effect in narrow channels. In addition to being an interesting result in its own right, this measurement is an important precursor to the quantum interference experiments discussed in later chapters.

Chapter 5 deals with experiments in which the coherent backscattering effect is used to study ballistic trajectories in very open microstructures. In many ways, it is a sequel to similar experiments in quantum dots; a reprint of these earlier results is included as an appendix. We find that the coherent backscattering effect is observable in very open devices, but that the presence of disorder in 2DEG systems destroys the periodic modulation of the effect that would otherwise be visible in our structures.

Chapter 6 studies similar open structures, but this time forward scattered rather than backscattered trajectories are examined. In an ideal system, Aharonov-Bohm type oscillations should be observable in ballistic devices without the need for a doubly-connected geometry. In the chapter, we describe quantum interference oscillations that are created when a perpendicular magnetic field is applied to such ballistic devices. We also find that the structures studied in these experiments function as electrostatically tunable electron interferometers.

In Chapter 7, the electrostatically tunable interferometer concept is expanded upon in a series of Fabry-Perot electron interferometers. These devices exhibit very large quantum

interference oscillations, and demonstrate that it is possible to use reflection from electrostatic gates to trap ballistic electrons in a resonance cavity. These interferometers are fairly robust devices, and could prove useful in future ballistic electron experiments.

Finally, Chapter 8 provides a summary of the experimental results presented in this thesis. In addition, future directions for this work are discussed.

1.3 2DEG Fundamentals

Scattering

In this section we review some of the fundamentals for electron transport in two-dimensional systems. Consider first the case of diffusive electron motion where the Drude model may be applied. In the presence of an electric field located in the plane of the 2DEG, electrons acquire an average drift velocity

$$\bar{v}_{drift} = -\mu_e \bar{E}, \text{ where the electron mobility, } \mu_e = \frac{e\tau}{m}, \qquad (1.1)$$

and τ is the elastic (or momentum) scattering time. Throughout this thesis, m will represent the effective electron mass in GaAs ($m = 0.067\ m_e$). Using the relationship, $-en_s\bar{v}_{drift} = \sigma\bar{E}$, the resistivity, ρ, may be expressed as:

$$\rho = \sigma^{-1} = \frac{m}{e^2 n_s \tau}, \qquad (1.2)$$

where n_s is the electron sheet density. Experimentally, the resistivity is easy to obtain by means of a van der Pauw measurement [Look, (1989)]. Since it is only electrons near the

Fermi energy that contribute to the conductivity, the Einstein relation may be used to express σ in terms of N_0, the density of states at the Fermi energy:

$$\sigma = e^2 N_0 D; \tag{1.3a}$$

the diffusion coefficient, D, is related to the Fermi velocity and the elastic scattering time,

$$D = \frac{1}{2} v_f^2 \tau. \tag{1.3b}$$

In transport measurements, we actually measure resistance, not resistivity. For a large, homogeneous sample, the two are related by the number of squares:

$$R = \frac{L}{W} \rho. \tag{1.4}$$

Note that this relation is only valid for lengthscales longer than the mean free path. For ballistic motion, resistance cannot be calculated from a local resistivity; instead the Landauer-Büttiker formalism described later in this chapter needs to be applied.

The elastic scattering time, τ, is a measure of time required before elastic collisions randomize the direction of electron motion. The elastic scattering time and the Fermi velocity determine the mean free path, $\ell = v_f \tau$. The momentum scattering rate is equal to:

$$\frac{1}{\tau} = \int dk' \, W_{k,k'} (1 - \cos\theta), \tag{1.5}$$

where $W_{k,k'}$ represents the transition probability from momentum state k to k'. The integral is weighted by (1-cosθ), since large-angle scattering events are more apt to randomize the direction of motion.

τ_s, the single particle scattering time (or lifetime), is also determined by elastic scattering. The single particle scattering time is a measure of how long an electron remains in any given momentum eigenstate in the presence of elastic scattering. Since all scattering events contribute equally to τ_s, we do not weight the integral by the angular size of the scattering event:

$$\frac{1}{\tau_s} = \int dk' W_{k,k'} . \qquad (1.6)$$

In remotely-doped GaAs/AlGaAs heterostructures such as those used in our experiments, the majority of elastic scattering is from ionized impurities spatially separated from the 2DEG. As a result of screening, elastic scattering is dominated by small-angle scattering, and $\tau >> \tau_s$ [Das Sarma and Stern, (1985)]. We have measured τ_s by observing the effect of collisional broadening of the Landau levels on the amplitude of Shubnikov-de Haas oscillations, and found $\tau_s \sim 0.5$ ps in material where $\tau \sim 15$ ps [Berry, (1994)]. From these measurements, the single particle scattering length, $\ell_s = v_f \tau_s$, was calculated to be 130 nm. Since this length is smaller than any device studied in this thesis, small-angle scattering likely plays a role in all of our devices, including those several times shorter than the mean free path.

The final important scattering time involved in our experiments is the phase coherence time, τ_ϕ. As discussed in detail in Chapter 4, the phase coherence time determines how long an electron may travel before losing its phase memory. This time, therefore, establishes the lengthscales over which quantum interference effects may be observed. Unlike the elastic scattering time which is essentially constant below 4.2 K in our devices, τ_ϕ grows dramatically at low temperature, and has been measured to be an order of magnitude larger than τ at 100 mK.

Band Structure

The Fermi surface of an unbounded 2DEG is circular. The energy of conduction electrons in a given 2D subband is

$$E(\bar{k}) = \frac{\hbar^2}{2m}\left(k_x^2 + k_y^2\right). \tag{1.7}$$

In two dimensions, the density of states is independent of energy,

$$N_0 = \frac{m}{\pi\hbar^2}. \tag{1.8}$$

The electron sheet density, therefore, is simply the product of the Fermi energy and N_0. Equating E_f to $\frac{\hbar^2 k_f^2}{2m}$, we find,

$$k_f^2 = 2\pi n_s; \tag{1.9}$$

the Fermi velocity is simply $\frac{\hbar k_f}{m}$. If the 2DEG is laterally confined to one dimension, each 2D subband will be split into a series of 1D subbands,

$$E_n(k_x) = E_n + \frac{\hbar^2 k_x^2}{2m}, \tag{1.10}$$

where E_n, the ground state energy of each 1D subband, depends on the nature of the confining potential.

Magnetic Field and Shubnikov-de Haas Oscillations

If a perpendicular magnetic field is applied to the 2DEG, a Lorentz force will bend electron trajectories with a cyclotron radius equal to

$$\ell_{cyc} = \frac{\hbar k_f}{eB}. \qquad (1.11).$$

A magnetic field also leads to the formation of quantized energy states known as Landau levels,

$$E_n = \left(n - \frac{1}{2}\right)\hbar\omega_c, \ \omega_c = \frac{eB}{m}. \qquad (1.12)$$

Ignoring disorder induced broadening of the Landau levels, the density of states in the presence of a perpendicular field is given by

$$N(E) = \frac{2eB}{h} \sum_{n=1}^{\infty} \delta(E - E_n). \qquad (1.13)$$

The longitudinal resistivity, ρ_{xx}, is proportional to the scattering rate, which in turn is proportional to the density of states at the Fermi level. Therefore, as the perpendicular field is swept, oscillations are observed in longitudinal resistance of the 2DEG, with maxima occurring whenever $E_f = E_n$. This is the origin of Shubnikov-de Haas oscillations which are periodic in inverse magnetic field,

$$\Delta\left(\frac{1}{B}\right) = \frac{2e}{hn_s}. \qquad (1.14)$$

Fig. 1.1 shows an example of such oscillations taken at temperature of 385 mK for the one-dimensional array of channels described in Chapter 4. Thermal broadening washes out oscillations at low field where $kT > \hbar\omega_c$. Even in the absence of thermal effects, disorder broadening of the Landau levels rounds the δ-function density of states described by Eq. (1.13). Experimentally, Shubnikov-de Haas oscillations provide a means for determining the electron sheet density (Eq. 1.14).

Landauer-Büttiker Formalism

In this thesis, much of the transport considered is in the ballistic regime. Unlike the diffusive regime where conductance can be described by a Drude model based on scattering from impurities, in the ballistic limit, it is no longer to possible to view conductance in terms of a local conductivity. In the absence of impurity scattering, conductance is dominated by narrow constrictions which allow only a finite current to flow in response to a potential difference. For this ballistic limit, a formalism has been developed in which conductance is treated as a scattering problem involving propagating modes at the Fermi energy [Landauer, (1957); Landauer, (1970); Büttiker, (1986)].

As an illustration of the Landauer-Büttiker formalism, consider the system shown in Fig. 1.2. Each of the reservoirs is connected to a central scattering region. As originally formulated by Büttiker, the scattering in this region was assumed to be elastic, but he subsequently showed that the formalism could be extended to include inelastic scattering as well [Büttiker, (1988a)]. Each reservoir is in thermal equilibrium at a chemical potential μ_i, and is connected to central region via leads (typically quantum point contacts) supporting N_i transverse modes.

Let $t_{ij,\alpha\beta}$ define the complex coefficient for scattering from mode β in lead j to mode α in lead i. T_{ij}, the total transmission probability from lead j to lead i is given by:

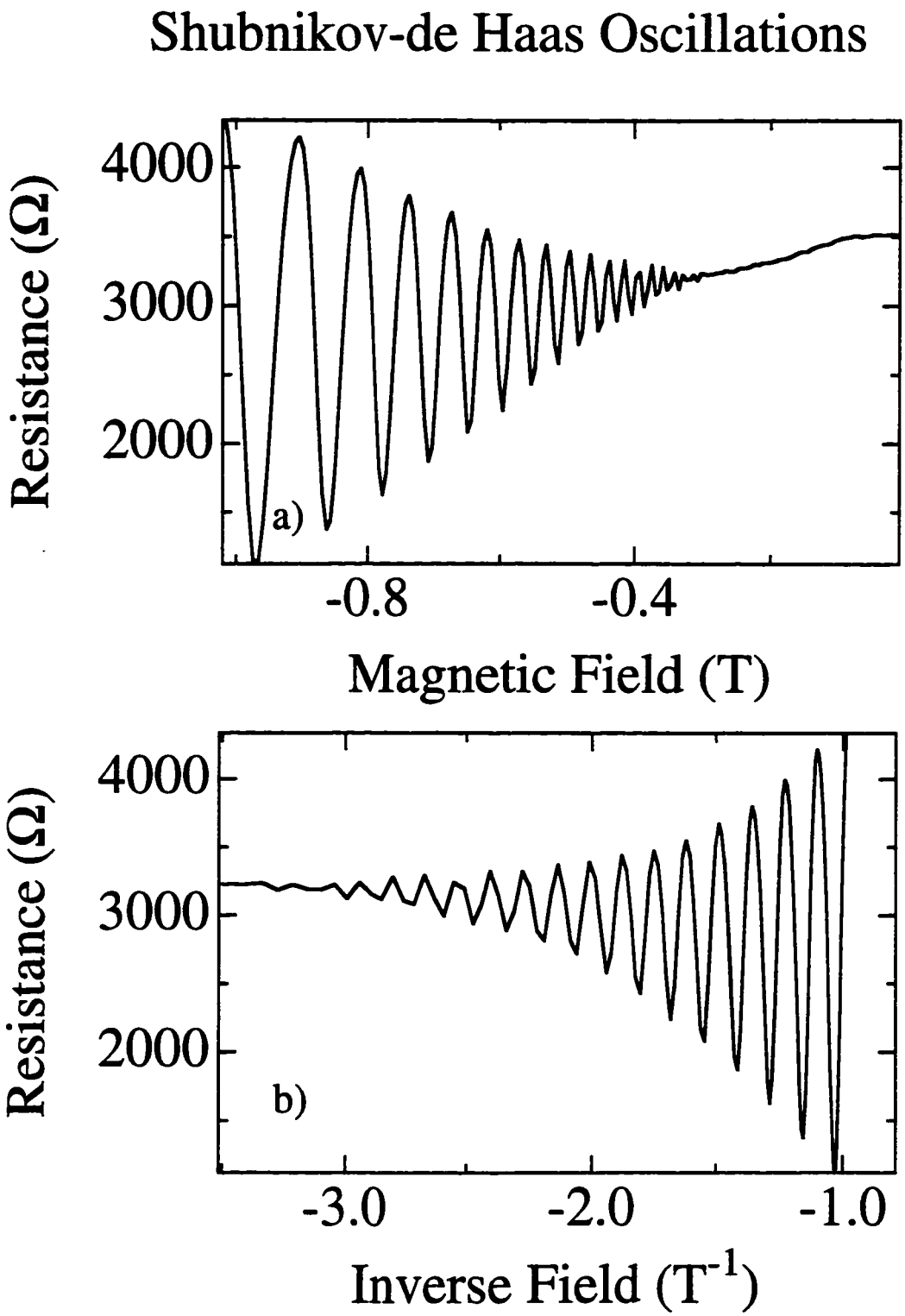

Fig. 1.1 a) 385 mK magnetoresistance trace from the array of channels described in Chapter 4. The oscillatory behavior of the longitudinal resistance is the result of the Shubnikov-de Haas oscillations described in the text. b) We replot this data vs. inverse field to show the periodicity of the effect. From the period, a sheet density 3.74×10^{15} m^{-2} was calculated.

$$T_{ij} = \sum_{\alpha=1}^{N_i} \sum_{\beta=1}^{N_j} \left| t_{ij,\alpha\beta} \right|^2 . \qquad (1.15)$$

Conservation of current implies:

$$N_i = \sum_j T_{ij}, \qquad (1.16)$$

where the sum is over all reservoirs. To take the possibility of backscattering into account, the j = i term is included in the sum.[1] T_{ij}/N_i represents the fraction of the total current injected through the i^{th} lead that is transmitted to reservoir j.

In response to a difference in chemical potential, a current $I_i = e\Delta\mu\rho_i v_i$ flows, where v_i is the group velocity of electrons in the i^{th} mode, and ρ_i is the density of states. The density of states for each mode is inversely proportional to its group velocity, $\rho_i = 1/hv_i$, which leads to an equipartition of current among all available modes:

$$I_i = \frac{2e}{h} N_i \Delta\mu. \qquad (1.17)$$

The current flowing into the i^{th} lead from the other reservoirs, $-I_i$, is equal to 2e/h times the sum of all T_{ij}, weighted by the difference in chemical potential between the i^{th} and j^{th} reservoirs,

$$\frac{h}{2e} I_i = -\sum_j T_{ij}\mu_j + \sum_j T_{ij}\mu_i. \qquad (1.18)$$

Invoking conservation of current (Eq. 1.16), the last term in the above equation may be replaced by $N_i\mu_i$:

---

[1] In some cases, $T_{ii} \equiv R_i$.

$$\frac{h}{2e} I_i = N_i \mu_i - \sum_j T_{ij} \mu_j . \qquad (1.19)$$

Eq. (1.19) is known as the Landauer-Büttiker formula. This formula will typically yield a system of linear equations that may be solved to determine the conduction properties of a sample. For example, if the current flows from contact 1 to contact 2, and the voltage difference is measured between contacts 3 and 4, the Landauer-Büttiker formula can be used to find the 4-probe resistance,

$$R_{12,34} = \frac{\mu_3 - \mu_4}{e I_{21}} . \qquad (1.20)$$

The Landauer-Büttiker formalism may be used to derive a number of important symmetry relations [Büttiker, (1988b)]. In particular, the work in this thesis is frequently concerned with the symmetry of device resistances in magnetic field. By using the unitarity ($t^\dagger = t^{-1}$) and time-reversal symmetry ($t^*(B) = t^{-1}(B)$) of the scattering matrix, it is possible to prove that $T_{ij}(B) = T_{ji}(-B)$. From this, it follows that

$$R_{12,34}(B) = R_{34,12}(-B); \qquad (1.21)$$

in other words, the 4-probe resistance is invariant when the current and voltage leads are swapped and the direction of the applied field is reversed. In most of our 4-probe resistance measurements, the current and voltage contacts are located next to one another in the same reservoir far from the leads. In this case, our measurement is effectively a 2-probe resistance which is symmetric in magnetic field:

$$R_{12,12}(B) = R_{12,12}(-B). \qquad (1.22)$$

Quantum Point Contacts

One of the most striking examples of ballistic conduction is the quantum point contact (QPC). The QPC is a single narrow constriction that separates two wide electron gas reservoirs. From Eq. (1.17) above, the ballistic conductance, $G \equiv eI/\Delta\mu$, of a QPC transmitting N transverse modes is equal to $(2e^2/h)N$. If the constriction is defined by means of electrostatic gate, it is possible to continuously narrow its width by increasing the negative bias applied to the gate. As the constriction narrows, the number of transverse modes, $N \approx \mathrm{Int}(2W/\lambda_f)$, decreases, which should result in a stepwise decrease in conductance.

The development of high-mobility 2DEG layers allowed this quantized conductance to be observed [van Wees, *et al.*, (1988); Wharam, *et al.*, (1988)]. An example of this quantization from one of our samples is illustrated in Fig. 1.3. The constriction shown in the figure inset has a lithographic width of 200 nm and is approximately 100 nm long. Eleven conductance steps are clearly visible in the figure. At voltages less than -1.35 V, the electron gas between the constriction is said to be "pinched off." Only a fraction of a mode is transmitted, forcing electrons to tunnel between the reservoirs. In this tunneling regime, the conductance of the constriction decreases exponentially with decreasing gate voltage.

The conductance steps are slightly rounded in this example (385 mK), due to thermal broadening of the Fermi surface. This rounding becomes more pronounced at higher temperatures, with the plateaus barely visible at 4.2 K. In addition to temperature, several factors can adversely affect the conductance quantization, the most obvious of which are deviations in the transmission probabilities of propagating and non-propagating modes from unity and zero respectively. By keeping the length of the constriction short, impurity backscattering in the contact is minimized, allowing transmission coefficients near unity to be achieved. Even for short point contacts, we occasionally see oscillatory structure on a conductance step, which is likely the result of interference created by backscattering in the

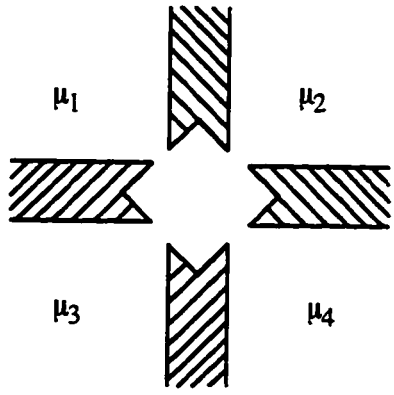

Fig. 1.2 An illustration of the generalized multiprobe system that may be treated using the Landauer-Büttiker formalism. Each reservoir is in thermal equilibrium at a chemical potential μ_i, and is connected to a central scattering region by a lead supporting N_i transverse modes.

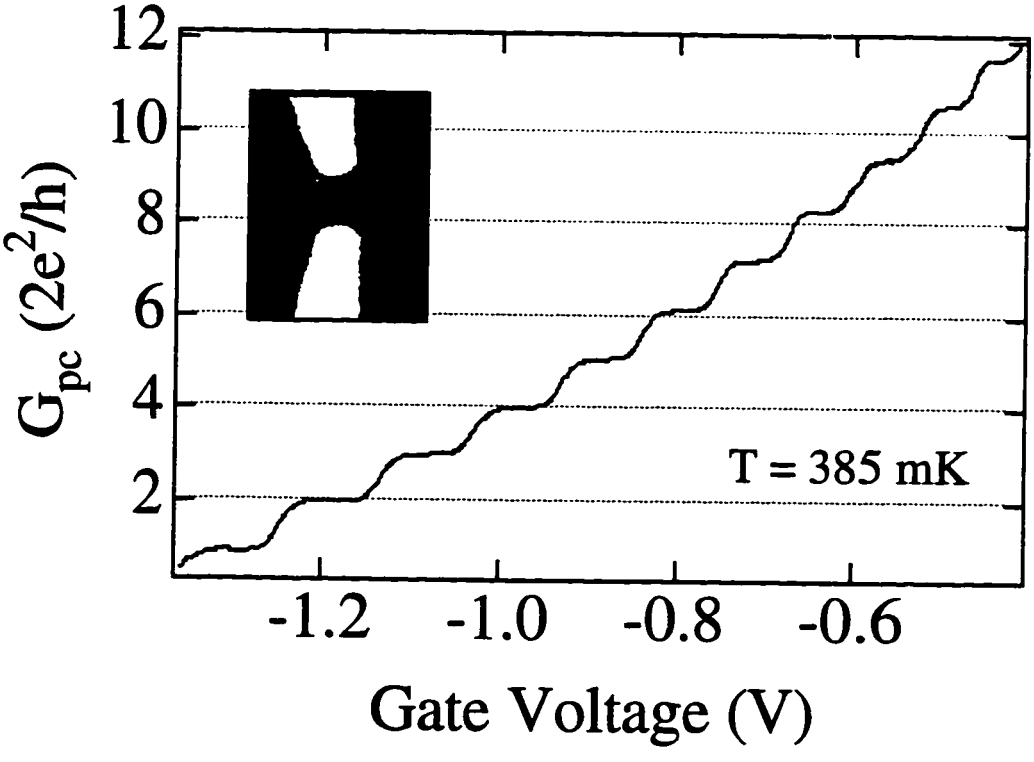

Fig. 1.3 Plot illustrating the quantized conductance steps found in a QPC. As the negative bias is increased, the number of transverse modes decreases. The inset shows an SEM photo of the QPC, with lithographic width 200 nm.

point contact [Timp, *et al.*, (1992)]. If the transition from the constriction to the wide 2DEG is abrupt, there can be considerable reflection of propagating modes at this interface; such reflection is minimized in our point contact design by adiabatically opening the constriction. The splitting in energy between consecutive modes decreases for larger N. This may allow easier propagation of evanescent modes (i.e., tunneling) at higher N, which would explain the higher than expected conductances observed at those plateaus. In practice, a small series resistance must be subtracted from our measurements in order for the conductance plateaus to lie on integer values of $2e^2/h$. Although a constant series resistance is subtracted (= 250 Ω for the example shown), the actual series resistance may be dependent on the gate voltage, which could also explain the deviation from integer conductance values visible above N = 5.

Almost all of the devices used in the experiments presented in this thesis utilize quantum point contacts. Quantum point contacts can serve as both sources and detectors of coherent electron waves, which makes them an essential building block for quantum interference measurements. In performing the experiments described in this thesis, well over one hundred QPCs were measured. It is clear from this large sample that the impurity potential in a QPC has a dramatic impact on its conduction properties. Lithographically identical point contacts fabricated only a few microns from one another typically have ~ 10% variation in the value of the pinch off voltage. In addition, the quality of the conductance steps can vary considerably in neighboring contacts.

Chapter 2

Sample Design and Fabrication

2.1 Introduction

In this chapter, we will describe sample design and fabrication considerations important to the experiments discussed in this thesis. The first section will describe the GaAs/AlGaAs heterostructure two-dimensional electron gas systems (2DEGs) used in our experiments. Special attention will be given to the formation of the electron gas layer, and to the design parameters that affect the quality of the 2DEG.

The next portion of the chapter will focus on the processing techniques necessary for the fabrication of the samples used in our electronic transport measurements. These include cleaving and cleaning the wafer, making ohmic contact to the 2DEG, electron-beam lithography, metallization, and wirebonding the sample. The optimal layout for samples with multiple devices will also be discussed.

The final section of the chapter deals with the problems that are commonly found in 2DEG experiments. These include problems that are caused by mistakes in the processing, such as creating shorts between the electron gas and the gates, as well as problems that arise because of inherent flaws in the electron gas itself.

2.2 Wafer Design and Growth

The experiments presented in this thesis all examine electron transport in two-dimensional electron gas systems. In this section, we will describe the physics of two-dimensional electron gas formation. We will then discuss how our GaAs/AlGaAs heterostructures are optimized to satisfy the needs of our experiments: e.g. high mobility

and near-surface electron gas depth. The GaAs/AlGaAs wafers used in our experiments were all grown via molecular beam epitaxy (MBE) at UCSB in the laboratory of Art Gossard by either Bob Westervelt or Ken Campman. The MBE growth itself will not be discussed here, but several previous theses have described the apparatus at UCSB [Hopkins, (1990); Baskey, (1994)], and several good overviews of MBE exist [e.g. Herman and Sitter, (1989)].

Many semiconductors can be grown epitaxially such that a two-dimensional electron gas layer is formed, but we use GaAs/AlGaAs in our experiments for several reasons. First, there is excellent lattice matching between GaAs (5.65 Å) and AlAs (5.66 Å), which allows strain-free interfaces to be formed. The absence of boundary scattering at the interface increases mobility. Mobility is also increased by the low effective mass ($m = 0.067\ m_e$) in GaAs. Unlike silicon, GaAs has a direct band gap, with a single conduction band minimum. When epitaxial growth is performed on a substrate with a [100] orientation, a simple circular Fermi surface is obtained. Furthermore, it is possible to customize the band structure by varying the Al mole fraction in the $Al_xGa_{1-x}As$. For $0 < x < 0.45$, the energy of the conduction band edge is directly proportional to x [Adachi, (1987)]. In our design, we use a mole fraction of $x = 0.3$ which results in a 260 mV conduction band offset.

Fig. 2.1a shows the growth profile of a typical sample. The substrate is commercially available [100] GaAs. On top of this there is a 25 period superlattice (20 Å $Al_{0.3}Ga_{0.7}As$, 20 Å GaAs) which is present to smooth the effect of defects present in the substrate [Petroff, *et al.*, (1984)]. A micron of GaAs further separates the active portion of our heterostructures from the substrate. As will be described shortly, if the doping is done correctly, the two-dimensional electron gas is formed at the interface between this GaAs and the $Al_{0.3}Ga_{0.7}As$ grown on top of it. The $Al_{0.3}Ga_{0.7}As$ is grown in two stages which are separated by the fractional monolayer of Si used to δ-dope the sample. A setback layer, whose thickness will be denoted by d', separates the Si donors from the 2DEG. This

Wafer Design

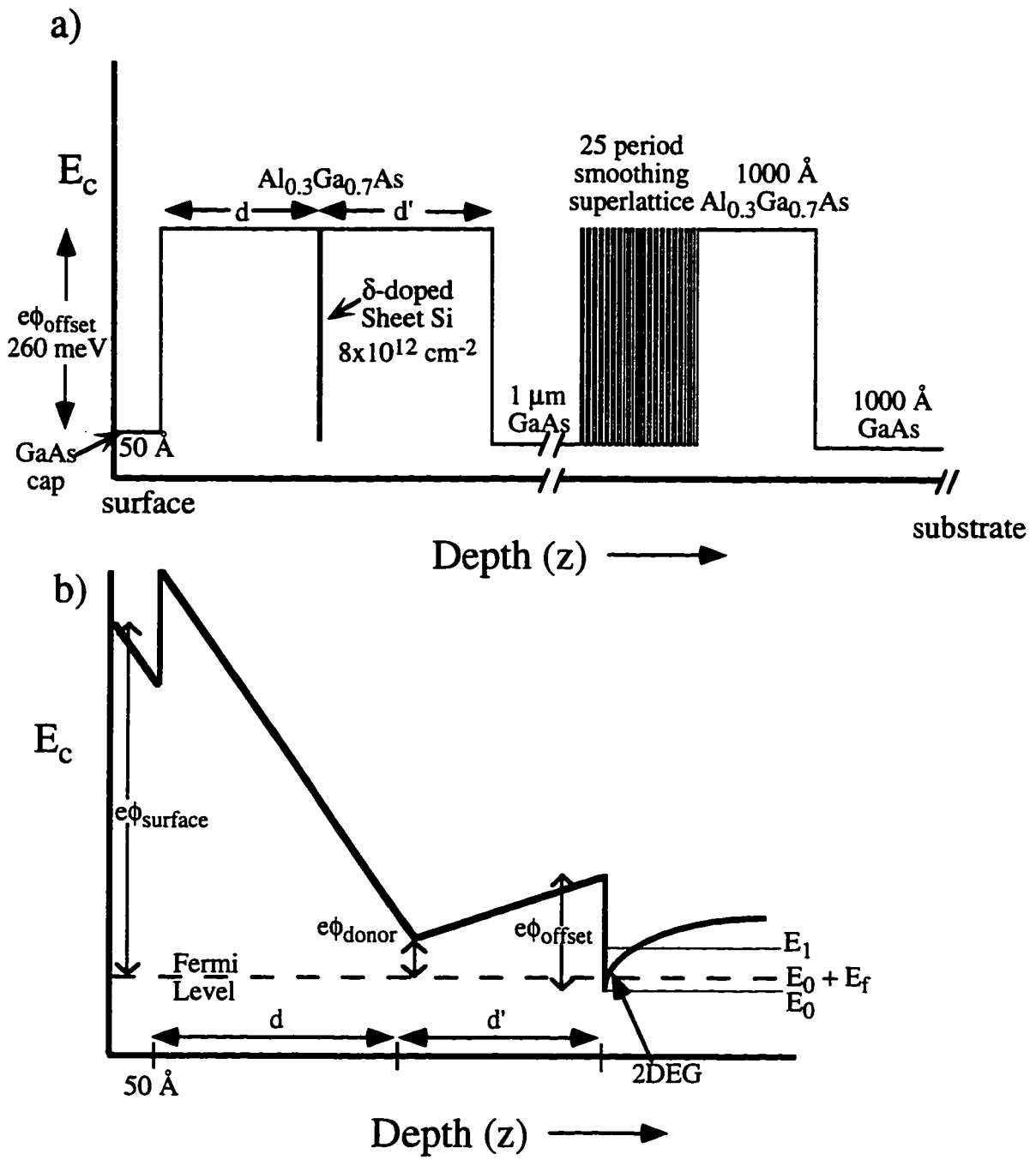

Fig. 2.1 a) Conduction band profile of typical wafer in the KC series. Note that the scale of the z-axis changes following the break at the 1 μm GaAs layer. b) Schematic of conduction band after equilibration of the ionized donors, illustrating formation of a triangular well by electrostatically induced band bending.

setback allows the electrostatic potential due to the ionized donors to be partially screened. Following the Si layer, a further amount of undoped $Al_{0.3}Ga_{0.7}As$ is grown. This layer, whose thickness will be denoted by d, is required to satisfy the surface states. Finally, a 50 Å GaAs cap layer is added to prevent the oxidation of the Al that would occur if the $Al_{0.3}Ga_{0.7}As$ were exposed at the surface.[1]

In Fig. 2.1b, we show the band structure after the electrons from the Si donors have reached their equilibrium configuration. The electric fields produced by the ionized donors and the surface states induce bending of the conduction band. At the GaAs/AlGaAs interface, the conduction band forms a roughly triangular potential well which constrains the 2DEG. Airy function solutions to the Schrödinger equation give a good approximation of the energy eigenvalues of the well [Harris, (1989)] :

$$E_i \equiv \left(\frac{\hbar^2}{2m^*}\right)^{1/3}\left(\frac{3\pi}{2}(i+\frac{3}{4})F\right)^{2/3}$$
$$\equiv 26\left[\left(i+\frac{3}{4}\right)n_s \Big/ 10^{11}cm^{-2}\right]^{2/3} meV, \qquad (2.1)$$

where n_s is the electron sheet density in the 2DEG, $\varepsilon = 12.9$ is the dielectric constant of GaAs, and $F = 4\pi n_s/\varepsilon$ is the electric field arising from the ionized donors. The actual "thickness" of the two dimensional electron gas can be approximated by the expectation value of the depth:

$$\langle z_i \rangle = \frac{2E_i}{3F}. \qquad (2.2)$$

In our samples, we typically have a sheet density $n_s \approx 4x10^{11}$ cm^{-2}, which corresponds to a Fermi energy, $E_f \approx 14$ meV. Comparing this value to Eq. (2.1), we see that only the

[1] An inversion layer does not form at the interface between the cap layer and the $Al_{0.3}Ga_{0.7}As$ because of the band bending associated with the surface states. See Fig. 2.1b.

lowest subband of the 2DEG is occupied in our samples, since the second subband will not begin to fill until E_f is equal to the energy gap between E_1 and E_0.[2] From Eq. (2.2) we estimate that the 2DEG extends approximately 65 Å beneath the interface.

The simple model illustrated in Fig. 2.1b can be used to estimate n_s. Equating potentials we have

$$E_f + e\phi_{donor} + Fd' - e\phi_{offset} = E_0, \tag{2.3}$$

where $\phi_{offset} \approx 260$ meV is the conduction band offset, and $\phi_{donor} \approx 80$ meV is the depth of the Si donor levels. This model can also be used to calculate the sheet density of the Si dopants necessary to satisfy the surface states:

$$\sigma = \frac{e(\phi_{surface} + \phi_{offset} - \phi_{donor})\varepsilon}{4\pi r\eta}, \tag{2.4}$$

where the doping efficiency, $\eta \approx 1/2$, refers to the fraction of thermally activated Si donors, $\phi_{surface} \approx 800$ meV, and r is the separation between the Si donors and the surface. Note that more electrons from the ionized donors migrate to the surface states than to the 2DEG if d and d' are comparable.

In designing our wafers, we want to achieve high electron mobility while keeping our electron gas close to the surface. High electron mobility yields the long mean free paths that are required if our experiments are to be in the fully ballistic regime. We desire a near-surface gas, because lateral confinement of the 2DEG is achieved by applying negative bias voltages to gates on the surface. The shape of the electrostatic confining potentials in the 2DEG undoubtedly differs from the shape of the surface gates, but by minimizing the surface/2DEG separation, we hope to minimize this distortion.

---

[2]This is verified experimentally by Shubnikov-de Haas measurements.

By remotely doping the samples, the electron gas is physically separated from the ionized impurities of the donor layer, which can greatly enhance the 2DEG mobility [Dingle, (1978)]. Intuitively, it may seem plausible to expect that if we were to increase the separation between the 2DEG and the donors, we would obtain a monotonic increase in the 2DEG mobility. While the scattering would be reduced, Eq. (2.3) shows that the equilibrium sheet density in the 2DEG decreases as this separation increases. From experience, we find the longest mean free paths are obtained with sheet densities around 3.7×10^{11} cm^{-2}, which constrains the setback to around 200 Å. We could overcome this constraint by illuminating the sample with an LED. Following illumination, the persistent photocurrent would increase the number of electrons in the well from its unilluminated equilibrium value [Klem, *et al.*, (1983)]. Similar illumination techniques have been used to produce the record 10^7 cm^2/Vs mobility material grown at Bell Labs [Pfeiffer, *et al.*, (1989)].

Ken Campman grew a series of wafers (KC4, KC5, KC6) in which he successively increased the setback. As shown in Table 2.1a, the sheet density and mobility of these wafers is poor when not illuminated. Following illumination, the mobility of these wafers increases; for example, the mobility of KC6 was measured to be 1.1×10^6 cm^2/Vs. The problem with these wafers, however, is that the configuration of the wafer following illumination is only metastable. Once the electron gas is depleted with an electrostatic gate, the sheet density only returns to its unilluminated equilibrium value when the negative bias is removed. This creates hysteretic behavior in gated samples fabricated on these wafers, which makes them unsuitable for the experiments described in this thesis.

Table 2.1 Wafer characteristics for two series in which a) d' and b) d are varied. KC4 was broken during shipment from UCSB. Mobility and sheet density values are from unilluminated measurements taken at 1.5 K. KC7 - KC9 were grown several months after KC1 - KC3.

	wafer	d (Å)	d' (Å)	μ (cm^2/Vs)	n_s (10^{11} cm^{-2})
a)	KC4	200	450	na	na
	KC5	200	350	350,000	1.9
	KC6	200	250	380,000	2.3
b)	KC1	100	220	250,000	2.6
	KC2	150	220	500,000	3.6
	KC3	200	220	700,000	3.7
	KC7	300	220	560,000	3.5
	KC8[3]	250	220	540,000	3.0
	KC9	200	220	510,000	3.6

If the setback is fixed, the only other parameter to vary is d, the separation between the donors and the GaAs cap layer. Increasing d will increase the mobility of the 2DEG. As described by Eq. (2.4), a longer distance between the donors and the surface requires a smaller electric field to achieve the same potential drop at the surface, resulting in fewer donors being ionized. Although increasing d increases mobility, it obviously also increases the depth of the electron gas. In order to determine the optimum tradeoff between mobility and depth, a series of six wafers was grown, varying d. The characteristics of these wafers are summarized in Table 2.1b. In analyzing these results it is important to realize that wafers KC1-KC3 were grown several months before wafers KC7-KC9; so that even though wafers KC3 and KC9 are nominally identical, the mobility of KC3 is higher. This is likely because the MBE chamber was cleaner during the first series.[4] From Table 2.1b,

[3]As will be discussed later in this chapter, KC8 behaves in an anomalous fashion, which may explain its low sheet density.

[4]Scattering from impurities in the crystal also limits mobility. The highest mobility electron gases are grown in machines dedicated for that purpose. Unfortunately, the machines at UCSB are more general purpose and contain beryllium and other elements which are known to degrade 2DEG mobility. In a cleaner machine, our wafer design would easily produce mobilities in excess of 10^6 cm^2/Vs.

we see that there is a striking increase in mobility as d is increased from 100 Å to 200 Å. The sheet density in KCl is especially low as almost all of the ionized electrons are required to satisfy surface states, resulting in depletion of the 2DEG. Once d is grown thicker than 200 Å, the mobility continues to increase, but at a far less dramatic rate. From this series of wafers, the optimum tradeoff between mobility and depth appears to occur at $d \approx 200$ Å.

2.3 Wafer Preprocessing

The heterostructures supplied to us by our collaborators at UCSB are 50 mm diameter circular wafers, with major and minor flats that allow us to locate the [110] crystallographic planes. Typically, we fabricate samples on small chips 3 x 5 mm^2, so the wafer must be cleaved into smaller pieces before it can be used. Cleaving the wafers is a delicate procedure and large amounts of very valuable heterostructure material can be lost if mistakes are made. The following procedure has been found to work well:

1) Place the wafer to be cleaved on a clean sheet of graph paper, with the [110] crystallographic axes aligned along the axes of the paper. This and the entire cleaving process should be performed under a non-inverting, binocular microscope. Only touch the wafer with teflon tweezers, and only touch the edge. Also, wear gloves at all times while handling the material.

2) Cover the back of a metal ruler with a strip of teflon tape in order to avoid scratching the GaAs surface. Align the ruler parallel to a [110] axis and place the ruler flush against the crystal. The ruler is there to serve as a guide for the diamond scribe, so be sure to compensate for the width of the tip of the diamond scribe when positioning the ruler.

3) With the diamond scribe positioned vertically, make a short scribe mark (~ 0.5 mm) along the crystal surface. In order to hold the pen vertically, it may be necessary to

move the microscope head out of the way. Do not apply excessive pressure when making the scribe, as this will generate GaAs dust that can scratch the surface. Also, do not make a long scribe mark, as any deviation in your ruler alignment could cause the wafer to cleave off-axis.

4) Remove the ruler and blow any dust generated off the wafer with high-purity N_2. Place the wafer on a folded piece of filter paper, with the scribe mark parallel to the edge of the paper. Most of the wafer should be on the filter paper with the portion to be cleaved left dangling over the edge.

5) Take two Q-tips and press gently on either side of the scribe mark. Assuming a good scribe mark was made, the wafer should cleave easily.

6) Because of the epilayer that is visible on the front of the wafer, it is easy to tell which side is up. But once a piece is separated from this epilayer, it is virtually impossible to distinguish which side is up, because UCSB is now using substrates with polished GaAs backs. Therefore, once a piece is cleaved, it is advisable to lightly scratch the back side for identification purposes. Needless to say, it is important to watch the cleave take place in case the chip flips during the cleaving procedure.

Once the chip has been cleaved, the next step is to clean it. Clean surfaces are absolutely necessary for putting good ohmic contacts on the sample. Cleaning should be performed just prior to applying the resist used in the contacting procedure (see next section). Whenever glass beakers are used during cleaning, the chips are placed in teflon boats to protect their surfaces from scratches. In the recipe that follows, all organic solvents are cleanroom semiconductor grade (Doe and Ingalls):

1) 15 minutes in boiling trichloroethylene (TCE)
2) 15 minutes of ultrasonic cleaning in acetone
3) > 5 minutes of ultrasonic cleaning in methanol

2.4 Ohmic Contacts

In order to perform electronic transport measurements in our two-dimensional electronic gas layers, it is necessary to place contacts on the surface that are electrically connected to the buried 2DEG. A good contact will behave very much like a resistor, hence the adjective ohmic is included in the name. As shown in Fig. 2.1b, the high density of surface states in GaAs produces a large potential barrier, $\phi_{surface}$, that makes contacting the 2DEG difficult. Fortunately, this is a problem of great interest to the semiconductor industry, and several techniques have been developed that allow good ohmic contacts to be produced [Look, (1989)]. Though effective, these processes are surprisingly poorly understood, and making good ohmic contacts is still very much a black art.

For our samples, the ohmic contacts must function at temperatures as low as 20 mK and at magnetic fields up to several Tesla. One of the simplest methods of producing suitable contacts is through annealing indium into the sample. Near the surface, InAs is formed and there is no barrier at the In/InAs interface. A conduction band discontinuity would exist at an abrupt InAs/GaAs interface. It is believed that such a barrier does not exist following annealing in these systems, because a graded $In_xGa_{1-x}As$ alloy is formed as the indium diffuses toward the 2DEG [Lakhani, (1984); Woodall, *et al.*, (1981)]. For several years, the Westervelt group made contact to the 2DEG by placing ≈ 1 mm^2 pieces of indium on the surface and then annealing the samples. The most successful recipes can be found in previous dissertations [Yang, (1995); Baskey, (1994)]. Despite our best efforts, this technique has some inherent difficulties:

1) The yield is low. At best, the contacts work only about 80% of the time, leading to the loss of valuable material. Bake time, surface cleanliness, careful indium preparation, and contact size all have to be considered carefully when making contacts.

2) Because of the low yield, the contacts on every sample need to be tested at liquid helium temperatures before further processing is done.

3) Even when successful, the contacts often have very large resistances, sometimes several thousand ohms. In addition to their high resistance, indium contacts are often slightly "diodic."[5]

4) For best results, large contacts (> 1 mm^2) are required. These large contacts take up over half the surface area of the sample, leaving very little room for gated devices. In addition, when using the wirebonder, it is very difficult to loop wires around these protruding mounds of indium.

5) Because the indium balls up when it melts, the exact shape and size of a contact cannot be controlled.

Although the process is somewhat more complicated, for the last several years the group has been phasing out indium contacts in favor of AuNiGe contacts. These contacts are the industry standard and typically give lower resistances than other techniques. As with indium, the precise mechanism through which AuNiGe contacts are formed is not known. It is known that the metallic elements intermix with the Ga and As during annealing and form several new compounds such as AuGa and NiAs [Shih, *et al.*, (1987)]. It has been postulated that spikes of highly doped Ge protrude into the 2DEG and that conduction occurs through these channels [Braslau, (1981); Taylor, *et al.*, (1994)].

We have found that the AuNiGe contacts offer many advantages over the indium. These include:

1) High Yield. Out of over 500 contacts I have measured, only one has failed. They are very insensitive to bake time and to the actual thicknesses of the deposited materials.

2) Because of their reliability, it is not necessary to test the contacts.

---

[5]Diodic refers to a situation where the reversing of bias current polarity in a 2-probe, current-biased dc measurement induces a change in the voltage measured. Such behavior indicates that a barrier still exists.

3) Typical resistances are on the order of 50 Ω, and contact resistances under 10 Ω are not unusual.

4) Since the wafer is patterned lithographically, AuNiGe contacts can be placed more precisely than indium contacts can be. In addition, the contacts can be made as small as 1 μm^2, allowing contacts to be positioned between gates and, in general, freeing up space on the chip for the actual devices.

5) The AuNiGe contacts are flat, which facilitates easy wirebonding to the gates. In addition, unlike the sticky indium which can ruin the wirebonder head, the AuNiGe contacts can be directly wirebonded.

6) The manual dexterity necessary for positioning indium contacts without scratching the GaAs surface is no longer required.

7) The AuNiGe contacts make our samples look far more attractive than the gray blobs of indium did.

Unlike the indium which is manually placed on the surface, some type of lithography must be done to define contact pads before thermally evaporating the AuNiGe alloy. Photolithography would seem to be the obvious choice for exposing large contact pads, but we do not use photolithography for a couple of reasons. First, the chips are so small that the photoresist forms thick ridges at the edge of the sample which take over 60 seconds to expose. Unfortunately these hard-to-expose regions are usually where we wish to place the contacts. More importantly, photolithography seems to leave a residue over the entire chip that is difficult to clean away in areas that were not exposed. When we have patterned contacts with photolithography, the Cr/Au gates deposited in these regions in subsequent evaporations had adhesion problems. Solutions to these problems need to be found before photolithography may be reliably used for patterning ohmic contacts. Our current e-beam lithography techniques, however, are very reliable, so there has been very

little motivation to solve the photolithography problems. In addition, electron-beam lithography is significantly more flexible than photolithography, allowing us to customize the contact configuration for any chip, whereas photolithography limits us to patterns that can be made from our available masks.[6]

The following list of steps describes the current procedure used to make AuNiGe contacts. It is a modification of a recipe used at M.I.T. that was given to us by former cleanroom head Dave Carter. Because of the high temperatures involved in annealing the contacts, this step must be done before any metallic surface gates are placed on the sample. Otherwise, at 400° C, the Cr/Au gates would begin to diffuse through the GaAs, leading to poor gate/gas isolation.

1) Clean the chip as outlined in the section 2.3.

2) Spin on a trilayer of PMMA electron beam resist.[7] The first two layers are 496 K, and the top layer is 950 K. All layers are spun at 4000 rpm for 60 sec and then baked on a hotplate at 180° C for 15 minutes. Further details on the electron beam resist and other aspects of e-beam lithography can be found in the next section of this chapter.

3) Mount chip(s) on a brass sample mount with carbon paint, making sure the paint does not cover the areas to be exposed.

---

[6]The biggest advantage of photolithography over e-beam is speed of exposure. With the right mask, photolithography allows us to expose many contacts simultaneously, while e-beam contact pads are written sequentially, with a 0.05 mm^2 pad requiring about 30 seconds to write. If chips are being processed in small batches, the speed of the e-beam system is adequate. Someday, however, the group may start working on a semi-industrial scale and wish to place contacts on entire wafers with a single large mask and only dice the wafer up following the ohmic contact processing. Photolithography would be required at that time.

[7]This trilayer is necessary to avoid unintentional formation of ohmic contacts. With every layer of PMMA, small cracks usually form. If a bilayer is used, cracks from adjacent layers may overlap, creating pinholes in the resist. When using a bilayer technique, we often had ohmic shorts between our surface gates and the 2DEG. Mark Eriksson postulated that these shorts were due to the formation of unwanted microcontacts that were deposited through the pinholes. When we adopted the trilayer technique, these shorts disappeared.

4) Rotate the stage to straighten the sample. Using low current (CL 15 at Mag. x1000 will not expose PMMA) measure the chip and write down the positions where contacts are to be drawn.

5) Transfer control to the Nanometer Pattern Generation System (NPGS) and draw the contact pads. Typically, the contact pads should extend to the edge of the sample to avoid potential Corbino effects at high magnetic fields. Since the PMMA tends to be quite thick at the sample edge, a dose of 1,200 $\mu C/cm^2$ is recommended. 1,000 is the maximum dose allowed by the Nabity software, so you must trick the program into allowing the higher dose by intentionally entering in a low value for the measured beam current. For the sake of speed, high currents (CL 3) can be used. For wirebonding purposes, pads should measure at least 100 μm in each dimension; with such large features, great care need not be taken to optimize the focus or stigmation. Typically, we simply focus on a corner of the chip, rather than using silver paint. With practice, 10 contact pads can be written on a chip in around 10 minutes.

6) Following lithography, develop the PMMA, and quench the developer in isopropanol.

7) To remove surface oxides and form the best possible contacts, the samples are dipped into a dilute solution of ammonium hydroxide (by volume, 5 parts distilled water: 1 part 30% ammonium hydroxide solution). The samples are dunked for 5 seconds and then blown dry with nitrogen. Since the ammonium hydroxide solution can actually dissolve PMMA, avoid agitating the sample during cleaning.

8) Inspect the chips under a microscope to confirm that the contacts are correctly placed.

9) Mount the chips on a thermal evaporator stage. If the contacts prevent a clip from being used, carbon paint can be used to attach the chips. To avoid potential germanium[8] contamination problems, do not use the stage dedicated for Cr/Au gates.

10) Load the samples into the general purpose thermal evaporator (see Section 2.6 for a description of the evaporator). It is most efficient to process many chips per evaporation. Use the copper arms labeled Au, Ni, Ge, and Gnd. Place Au on electrode #1, Ge on electrode #2, and Ni on electrode #3. Since very high currents

[8]A dopant for GaAs.

are required to thermally evaporate Ni, 20 mil thick tungsten boats (R.D. Mathis, Long Beach, CA, #S47-0.020W) must be used. Also, to prevent the Ni boat from breaking, make sure the Ni is cut into small pieces in the boat.

11) After pumping down for at least an hour, evaporate 50 Å Ni, 50 Å Au, 250 Å Ge, 400 Å Au, and 100 Å Ni. For wirebonding purposes, a final gold cap layer of at least 200 Å should also be evaporated. From unintentional experimentation, we have found that contact performance seems to be unaffected by variations in these thicknesses. Good contacts have also been achieved without the final 100 Å of Ni. The stage should be air-cooled during the evaporation. Following the evaporation, the germanium electrode should be cleaned, and the aluminum foil covering the baseplate changed.

12) Place the chips in acetone for at least an hour to dissolve the PMMA.

13) Perform liftoff. First spray the chip with acetone. This should remove almost all of the unwanted metal. Since a lot of metal and carbon paint have now contaminated the acetone, use a fresh beaker and clean the chip ultrasonically for about 30 seconds. Do not leave the chip in ultrasound too long, because eventually the contact pads themselves will be ripped from the sample surface. Dunk the chip in methanol for a few seconds and then blow dry with 99.999% N_2. Before annealing, inspect the chip under a microscope to insure that no unwanted metal remains on the surface.

14) Next anneal the contacts using the strip heater built by Alex Rimberg [Rimberg, (1992)]. When placing the chip on the strip heater, be careful to insure that the chip is lying flat; otherwise dimples in the strip heater can lead to non-uniform heating of the sample. The strip heater is surrounded by a flow of forming gas (80% He, 20% H_2) to prevent oxidation of the contact metal during the high-temperature annealing process. We maintain a flow rate of 3.0 mm as measured by the Air Products flow meter. Though essential when In contacts are annealed, we have never checked if the AuNiGe contacts benefit from a reducing atmosphere. To drive water vapor from the surface, the heater is kept at 110° C for at least a minute.[9] The variac is then turned

[9]The temperature is measured by a JK thermocouple attached to the bottom of the strip heater. All temperatures in the recipe refer to the K setting. Also note that a gradient related to the forming gas flow rate probably exists between the sample temperature and the strip heater temperature. All values quoted in this recipe refer to temperatures with the flow meter reading 3 mm.

up to ~12% which should raise the strip heater to ~260° C. Once the thermocouple reaches 240° C, begin timing. After 10 seconds, the variac is increased to ~16%. Once the heater temperature reaches 390° C, the timing starts again, and the sample is heated for 20 seconds. The variac is adjusted to keep the temperature somewhere between 390° C - 410° C during annealing. After 20 seconds, the variac is quickly turned to zero, and the sample is cooled below 40° C by the forming gas.

15) As mentioned earlier, the AuNiGe ohmic contacts are so reliable that they do not usually require a cryogenic test measurement. Before further processing is done, however, a visual inspection should always be performed. Following annealing, the once-smooth metal should be textured and resemble a surface of melted pizza cheese. If the sample was not lying flush on the strip heater, one corner may have contacts that appear smooth — an indication that uneven sample heating occurred. If this happens, simply repeat step 14, and see that this corner is heated properly this time. Unlike indium contacts, it seems impossible to bake the AuNiGe contacts too long.

16) If a cryogenic test of the contacts is desired, the sample should be mounted on a chip carrier (see Chapter 3). Since the sample will need to be removed from this carrier for further processing, a temporary means of adhesion (e.g. carbon paint) must be used. Once the paint is dry, wirebond the contact pads to the chip carrier leads, and perform 1μA current-biased, two-probe measurements in a helium storage dewar using the contact test probe built by Michael Berry [Berry, (1994)] and subsequently adapted for the new chip carrier/socket system.

17) Before further sample processing, the chips should be cleaned ultrasonically in TCE, acetone, and methanol.

2.5 Electron-beam Lithography

Electron-beam lithography is currently the easiest and most reliable technique available for patterning feature sizes as small as 30 nm on planar surfaces. The principle of electron beam lithography is easy to understand, and is illustrated in Fig. 2.2. In a scanning electron microscope (SEM) a cathode filament produces electrons which are

E-Beam Lithography

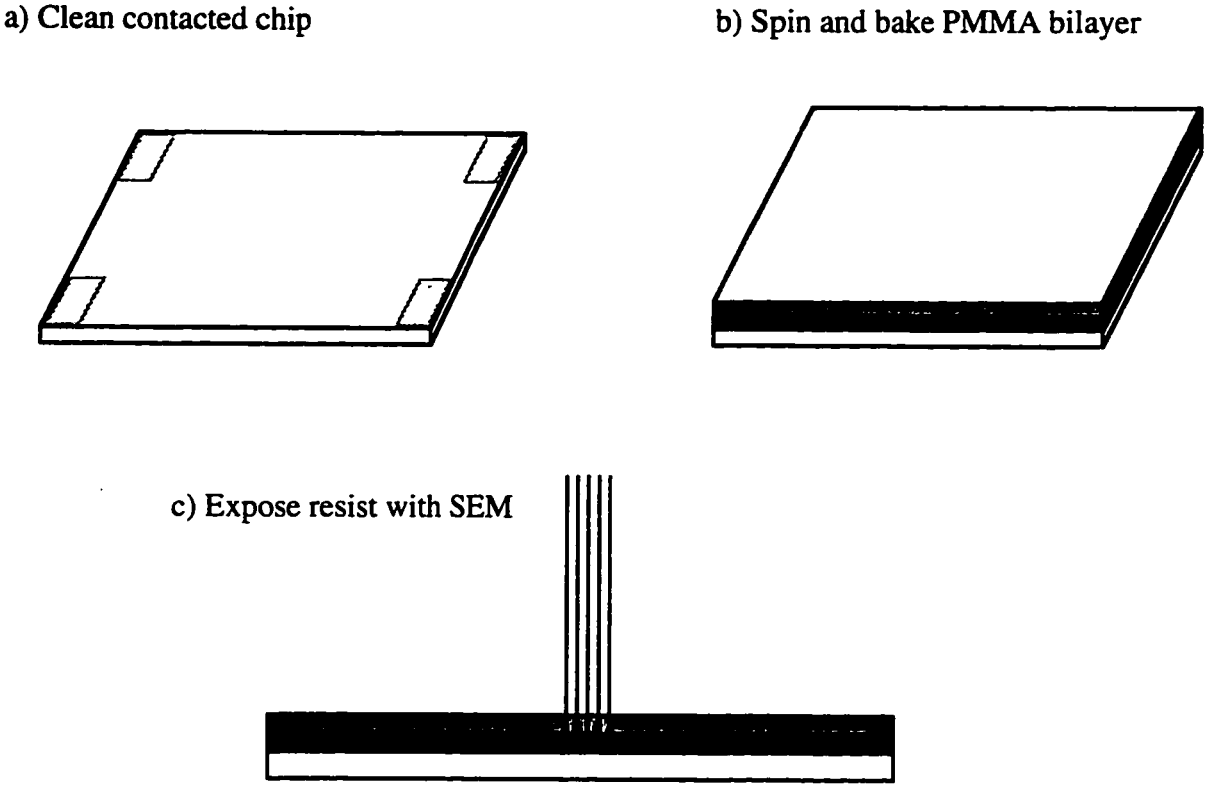

Fig. 2.2 Schematic representation of the electron beam lithography process. The undercut is produced by a combination of the electron backscattering from the GaAs (shown in [c]), and the lower molecular weight of the bottom layer of PMMA.

accelerated by a large voltage. Using magnetic lenses, these electrons are focused into a narrow beam which can be scanned over the surface of a sample by a set of precision magnetic deflection coils. In electron-beam lithography, a substrate is coated with a cross-linked polymer. A computer is used to control the deflection coils and "write" the desired pattern on the sample surface. When the polymer is exposed by a suitable dose of high-energy electrons, the cross-links are broken, rendering the polymer soluble in a chemical developer. During developing, the polymer is removed from the exposed regions, leaving the unexposed polymer as a positive resist mask for subsequent etching or metallization steps. In this section, we will discuss how e-beam lithography is used to prepare such a mask for the evaporation of the metal gates.

PMMA Bilayer

After the ohmic contacts have been annealed and the chip has been carefully cleaned (see previous section), we coat the sample surface with a bilayer of electron-beam resist: the cross-linked polymer polymethylmethacrylate (PMMA). The bilayer consists of a bottom layer of low molecular weight PMMA (496 K) and a heavier (950 K) top layer. The lower molecular weight layer is more easily exposed by the electron beam, resulting in the formation of an undercut following developing (see Fig. 2.2) [Mackie and Beaumont, (1985); Rooks, *et al.* (1987)]. This undercut aids during the liftoff step that follows metallization of the samples.

Below we outline the recipe for spinning the PMMA bilayer. All steps are performed in the hoods of the inner clean room (class 100) to minimize the chance of stray dust ruining the lithography. For further details, the dissertation of the recipe's inventor may be consulted [Yang, (1995)].

1) Place a single drop of 496 K PMMA/chlorobenzene (2% PMMA by weight) solution onto the chip and spin at 4,000 rpm for 1 minute.

2) Set the chip on a hotplate and bake at 180° C for 15 minutes. The hotplate bake is faster and more effective than earlier oven baking techniques.

3) Set the chip on the spinner and begin rotating at 500 rpm. Place a single drop of 950 K PMMA/chlorobenzene solution (2% PMMA by weight) onto the chip and increase the spin rate to 4,000 rpm. Spin for 1 minute. By spinning the chip before this second drop is applied, we hope to prevent the chlorobenzene in this second drop from dissolving the layer that was just baked on.

4) Bake at 180° C for 15 minutes.

With this recipe, preparing one chip takes about 35 minutes, while each additional chip adds only two minutes to the total required time. It is most efficient to prepare several chips in a single session, as chips may be exposed months after the PMMA is baked without ill effects.

Following the spin/bake procedure, the resulting chip should be covered in a uniform coating of PMMA[10]. Occasionally, colored streaks will be visible in the PMMA. These streaks are caused by several hundred Angstrom variations in the thickness of the resist. Such small thickness variations will not affect the ultimate resolution of our electron-beam lithography. Their presence, however, may reflect that the sample was not properly cleaned — a problem that could lead to poor gate adhesion later. It may be worthwhile to dissolve the resist in acetone, reclean the sample, and repeat the spin/bake.

Mounting the Sample

Although properly mounting the sample prior to exposure need only take a few minutes, this step must be done correctly if the best possible SEM resolution is to be

[10]Except around the sample edges where thickness variations are expected.

obtained. First apply a few small specks of Ag paint (Structure Probe Incorporated, West Chester, PA) to the PMMA surface. This paint will be used to focus and stigmate the electron beam. As a result, the areas containing Ag paint will probably be exposed, which means that the paint should be placed where such exposure will not lead to difficulties. After the Ag paint is applied, the sample is placed onto a brass SEM sample mount. A small amount of conductive carbon paint (SPI) is used to secure the sample and to connect the insulated sample surface to brass mount. Without such electrical connection, electron charging effects would occur.

It is absolutely crucial that the sample is perfectly flat during lithography. The electron beam focusing cone has a solid angle of between 1-4 mrad. In order to obtain 20 nm resolution, the sample must have less than ~10 μm variation in its surface height. If the sample is jostled while applying the carbon paint, it is easy to disturb it by more than this amount. Other potential sources of height variation include tilting of the microscope stage and improper loading of the brass sample mount into its holder[11]; fortunately, all of these problems are easily avoidable once one is aware of them.

Exposing the Sample

The electron-beam writing itself is performed on a JEOL 6400 SEM controlled by a Hewlett Packard Vectra 386/25 microcomputer running the Nanometer Pattern Generation System (NPGS) (J.C. Nabity Lithography Systems, Bozeman, MT). Detailed literature describing the system is available [Nabity, (1989); Nabity (1991)], so only the basics of the system will be described here. Using the drawing program DesignCad (American Small Business Machines, Inc., Pryor, OK), the desired pattern is created. In addition to standard CAD objects like circles, rectangles, etc., there is a filled polygon command

[11]This can occur if the screw is overtightened or if a previous user left a layer of carbon paint or tape in the holder.

which is especially useful in drawing arbitrary shapes. The drawing is divided into layers which may be written at different magnification and condenser lens (CL) settings; different colors in the drawing can be used to designate different doses. After the drawing is finished, it must be converted into a set of commands that will control the SEM. With the Make Run File (MRF) routine, the user enters the measured beam currents, the dose assignments, the point and line spacing, and the appropriate origin offsets for each layer. The resulting pattern generation (PG) file dissects the drawing into a series of discrete points, much like a Georges Seurat painting. The point spacing, measured beam current, and assigned dose determine the exposure time for each point. This exposure time is controlled by a TTL signal which operates the external beam blanking shutter on the SEM. The NPGS uses a pair of 16-bit digital/analog converters to precisely control the magnetic deflection coils which position the beam over the proper x,y-coordinates.

In designing the patterns, fine lithographic features should be written at high magnification (x5000) and low beam current (CL 16). For the sake of speed, large features such as bonding pads should be written with large point spacing and high bias currents (CL 3). Before discussing the actual exposure process, we list some of the idiosyncrasies of the NPGS.

1) If the computer and monitor are not plugged into the same outlet as the SEM, 60 Hz noise will ruin the lithography.

2) Long diagonal lines drawn in DesignCad will be misinterpreted[12] by the NPGS software; use filled polygons instead.

3) For unknown reasons, sometimes a filled polygon will cause the system to reproducibly crash in the middle of the drawing process. Redraw the polygon, reversing the fill direction, to fix this problem. Once these bugs are eliminated from a drawing, it will not crash again.

[12]The program breaks the long diagonal lines into shorter, discontinuous segments.

4) If the SEM magnification or CL changes between layers, there will be a somewhat reproducible shift in the position of the origin. In order to compensate for this, origin offsets may be included in the MRF. It is usually easier to make sure there is sufficient overlap between layers to prevent these shifts from causing a problem.

5) There is a very large origin shift when the SEM scan speed is changed from fast to slow. To avoid this problem, do all writing on the slow setting.

6) There is some hysteresis in the deflection coils. To prevent this from causing problems, adjacent features should be drawn consecutively. In each layer, objects are drawn in the order in which they were created in the DesignCad program.

The following is a brief description of the procedure used to expose a sample. A more complete description can be found in the theses written by the group's lithography pioneers [Yang, (1995); Berry, (1994)]. For detailed instructions on the operation of the microscope, the JEOL 6400 manual may be consulted.

1) Load sample in SEM, and position stage out of the beam path.

2) Turn on accelerating voltage (35 kV) and saturate the filament.

3) Hit lens clear. This degausses the magnetic lenses.

4) Iteratively adjust the shift and tilt to maximize beam current. This will likely need to be redone after the current has stabilized (~ 20 minutes).

5) Using a low current (e.g. CL 15) to prevent exposure of the PMMA, scan around the edges of the chip. Rotate the stage to align the chip with the xy-axes, and measure the chip's position.

6) Wobble, focus, and stigmate the electron beam using the Ag paint specks. For best results, this should be done with at least x30,000 magnification on several flecks.

7) Using the Faraday cup, measure the beam currents on the CL settings that will be used. Make sure the readings are stable. A small drift in the shift can significantly lower the measured current on low CL settings. Once the readings are stable, enter the measured currents in the MRF.

8) Refocus and stigmate once the beam current is stable.

9) Switch to slow speed and external beam blanking. Switch over control to Nabity system.

10) Position the sample for the drawing and execute the pattern generation file. Turn off the computer monitor while drawing. Turn down the brightness on the SEM monitors to protect them during drawing.

11) When the last pattern is finished drawing, shut down the SEM and remove the sample.

Following the exposure, the sample is developed. The developer is a 3:1 mixture of isopropyl alcohol (IPA) and 4-methyl 2-pentanone (MIBK) by volume, with a small amount (1.3%) of 2-butanone (MEK) added to improve the contrast. The sample should be immersed in developer for 60 seconds (this time is not crucial), quenched in IPA, and blown dry with high-purity N_2.

High-Resolution Lithography

The devices pictured in Fig. 2.3 show the limits in linewidth and line separations that we have been able to obtain using our electron-beam lithography system. The device in Fig. 2.3a (called a pacman for obvious reasons) has a central bar whose width is less than 50 nm. In this section, we discuss what limits the ultimate linewidths attainable via e-beam lithography, and the experimental procedures that must be followed to achieve these limits.

Lithography Examples

a)

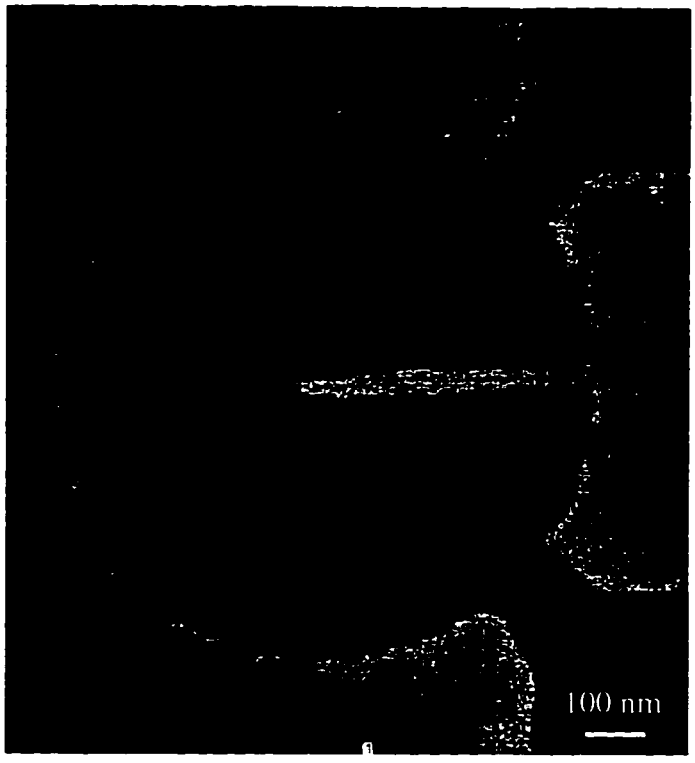

b)

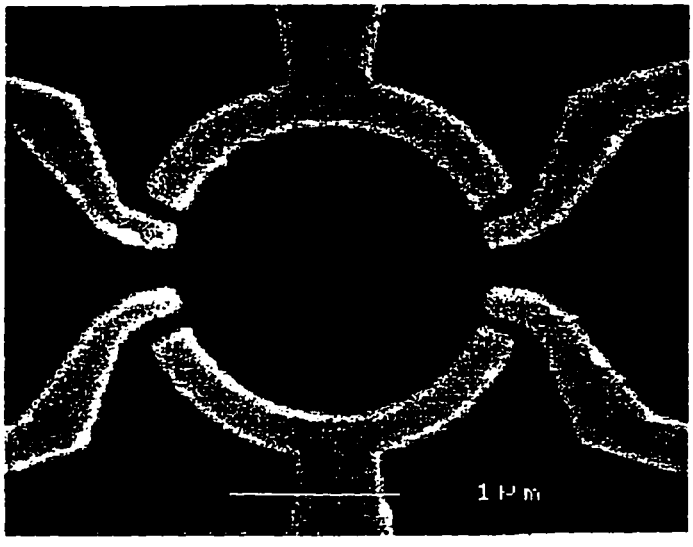

Fig. 2.3 a) SEM photo of "pacman" billiard. Central bar is < 50 nm wide. b) SEM photo of multiple-gate circle illustrating the close spacing that is possible between adjacent gates.

In photolithography, the wavelength of light determines the linewidths that may be achieved.[13] The 35 kV electrons used in our system have a wavelength of 0.06 Å, which is orders of magnitude smaller than our features. In the JEOL 6400 SEM, Coulomb repulsion within the electron beam broadens the spot size to ~2 nm, but this is still an order of magnitude smaller than our narrowest lines. It is scattering of the electron beam by nuclei that limits the resolution. As illustrated in Fig. 2.2c, some spreading of the e-beam occurs as electrons are forward scattered by the carbon nuclei in the PMMA. The electron scattering cross-section, however, is proportional to the square of the atomic number, so it is actually backscattering from the GaAs substrate that dominates this process [Parikh and Kyser, (1979); Wittels, (1980)]. These backscattered electrons can expose nearby resist, leading to proximity effects. In designing closely spaced gates such as those depicted in Fig. 2.3b, this proximity effect must be taken into account by supplying additional separation in the DesignCad drawing. If such precautions are not taken, closely-spaced features often bleed together.

When trying to draw very narrow lines like those in Fig. 2.3a, or closely-spaced features like those in Fig. 2.3b, the dose and proximity effects play a crucial role. In order to achieve the best results, test lithography is required. Obviously, high-quality heterostructure material should not be used for test purposes, but the test substrate should be GaAs as proximity effects are substrate dependent. During test exposures, we typically repeat the same drawing while systematically varying a parameter such as the dose, linewidth, or separation of the features. The test is then developed and inspected. One way to inspect the sample is to perform a metal evaporation and then image the sample with the SEM. This technique has the added advantage that it can detect potential liftoff problems inherent to a design. Alternatively, the PMMA mask itself may be inspected under the SEM, as good contrast exists between the GaAs surface and the PMMA. Such

[13]This is not exactly true. Using some tricks with non-linear resists, it is possible to achieve linewidths over a factor of two narrower than λ with photolithography.

imaging needs to be done quickly, because inspecting the features under high magnification will melt the PMMA. The PMMA may also be directly imaged with the lab's new Park Scientific atomic force microscope (AFM). This should be done in non-contact mode to prevent the tip form scratching the resist. Because of tip effects, the AFM does not usually provide imaging resolution as good as that attainable with the SEM.

Despite our best attempts to duplicate beam currents and conditions, it is not always possible to reproduce fine lithographic features on successive days (especially if the microscope has been abused in the interim). For best results, the test lithography and the writing of the real sample should be performed in a single marathon session. By turning off the detector, samples can be loaded and unloaded while the filament is left saturated. Doing so is the only way to really insure that the test lithography and the actual sample are being written under identical conditions.

2.6 Surface Gate Deposition

After the positive resist mask is patterned using e-beam lithography, a number of techniques can be used to define the devices in the heterostructure. Most of these techniques involve physically etching the top layers of the heterostructure until the 2DEG no longer exists in the etched region. These etching techniques have two significant limitations. First, the etch usually diffuses laterally as well as vertically, making it difficult to define very narrow features with precision. In addition, unlike gate-defined devices, it is not possible to adjust the dimensions of etched structures, or to "deactivate" these structures once they are etched.

Rather than etching, we use metal gates evaporated onto the sample surface to define our devices. These gates are electrically isolated from the electron gas. Application of a small negative bias voltage depletes the electron gas underneath the gate; a larger

negative bias laterally extends the depletion region allowing for electrostatic tuning of the dimensions of the device.

In choosing the metal for the surface gates, several criteria need to be considered. The metal should be deposited in a uniform film which adheres well to the GaAs surface and facilitates easy liftoff. The adhesion criteria is more stringent if wirebonding to the gates is planned. To avoid poor gate/gas electrical isolation, the metal should not diffuse into the GaAs at temperatures under 200° C. The metal should resist oxidation, and be visible under both optical and electron microscopes. Finally, to simplify our magnetotransport measurements, metals that exhibit physical properties such as superconductivity and ferromagnetism should be avoided.

No single metal satisfies all of the criteria considered above, but good results have been achieved by thermally evaporating a thin bottom layer of Cr, followed by a thicker top layer of Au. The purpose of the Cr is twofold. Cr adheres well to the GaAs surface, while the Au (which adheres poorly to GaAs) sticks to the Cr. The Cr also prevents the Au from diffusing into the GaAs. Although Cr is antiferromagnetic, this should not interfere with our experiments because below its Curie temperature (311 K) it has zero magnetization and very low magnetic susceptibility [Fisher, (1962)]. The other metal considered for the bottom layer, Ti, has excellent adhesion properties but requires electron-beam evaporation (which may damage the sample) and goes superconducting below 0.4 K (which could interfere with low-field measurements). The top Au layer prevents gate oxidation and the high atomic number of Au allows thin layers to be easily imaged by the SEM. In addition, the malleability of Au facilitates the formation of very strong wirebonds.

The Cr/Au evaporation is performed in a diffusion-pumped thermal evaporator equipped with a liquid nitrogen (LN_2) cold trap. Chamber pressure is monitored by a Varian ion gauge. There are electrodes for three independent sources, so multiple metals may be evaporated without breaking vacuum. The sample stage is positioned roughly 30 cm above the metal sources, and a manual shutter may be positioned over the stage to

prevent the deposition of metal. The stage may be air-cooled or cooled with chilled water or LN_2. For the ~ 600 Å total Cr/Au thicknesses usually deposited, air-cooling is sufficient; but if very thick (> 2000 Å) metal layers are to be evaporated, LN_2 may be required to prevent the sample from heating to the point where the PMMA may crack (190° C). There is a feed through for a thermocouple if the stage temperature needs to be measured. A 5 MHz piezoelectric crystal (Phelps Electronics Inc.) and Sloan Model 200 digital thickness monitor are used to measure the deposition. All thicknesses quoted in this section refer to the values read by this monitor, although profilometry and AFM measurements of our samples indicate that the actual metal films are roughly 30% thicker than the crystal readings.

After we began performing AuNiGe contact evaporations in the same evaporator used for the Cr/Au gates, the switching problems described in Section 2.8 began appearing very frequently in our samples. It just may be coincidence, but we feared that germanium contamination in the evaporator was being deposited along with the Cr/Au gates, and possibly diffusing into the GaAs crystal. As a precaution, we now have separate stages, electrodes, and Au boats dedicated to both types of evaporations. In addition, the germanium electrode and the bottom foil are cleaned following each AuNiGe contact evaporation. After these precautions were taken, the sample yield increased.

Below, we outline the current recipe for depositing metal gates on our samples.

1) Just before the sample is to be loaded into the evaporator, immerse it for 2 seconds in a dilute ammonium hydroxide solution (see Section 2.3) and blow dry with high-purity N_2. If this is not done, the gates will probably survive liftoff, but there is almost no chance that the metal will adhere during wirebonding. Although this immersion usually does not affect the PMMA mask in any way, on rare occasions the solution catastrophically dissolves the PMMA. To minimize the chance that this will occur, avoid agitating the chip in the solution.

Thermal Evaporation of Cr/Au Gates

a) Top view of electrode configuration

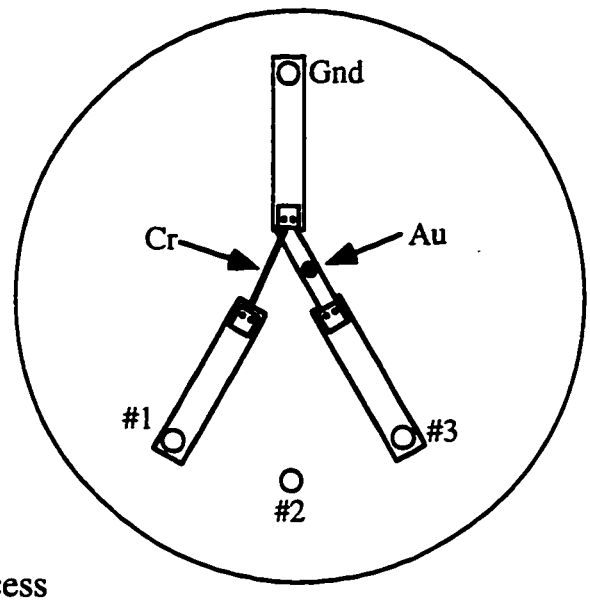

b) Liftoff process

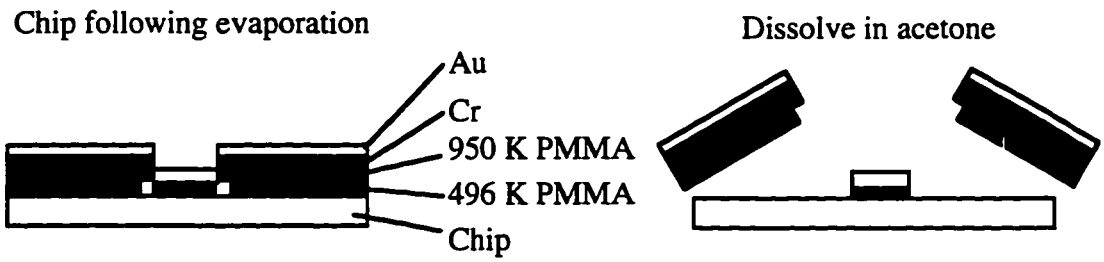

c) Shadow effects

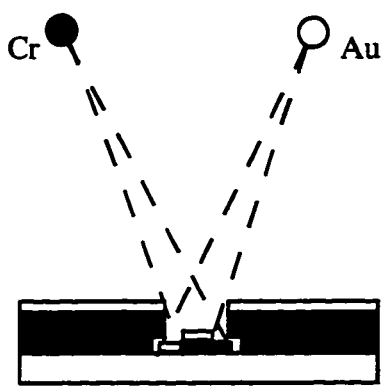

Fig. 2.4 a) Schematic view of the electrode placement in the thermal evaporator for Cr/Au gates. b) The sample following successful evaporation and liftoff. c) Cartoon showing shadow effects when the two metal sources are evaporated at different angles.

2) Mount the sample on the dedicated Cr/Au stage. When indium ohmic contacts are present, they provide a convenient spot to clip the sample to the stage. Carbon paint is used to mount the chips with AuNiGe contacts.

3) Fill the LN_2 cold trap. If the trap runs dry during the evaporation, oil will enter the chamber and contaminate the sample surface.

4) Load the sample stage and place the copper electrode arms in the configuration illustrated in Fig. 2.4a. A thin Cr rod is attached to #1 and alumina covered molybdenum boat (R.D. Mathis) holding the 99.999% Au is attached to #3. These arms have been machined so that it is possible to position the metal sources within about a centimeter of one another. The sources should be positioned close to one another to prevent shadow effects like those illustrated in Fig. 2.4c. Assuming a PMMA bilayer thickness of 1500 Å and a stage height of 30 cm, the evaporated metal from the two sources will be offset by 500d nm, where d is the separation between the sources (in meters). For d = 1 cm, this offset is only 5 nm, but these shadow effects become appreciable if care is not taken to limit the source separation. The Cr shadows are particularly insidious since the similar atomic numbers of Ga and Cr makes the metal virtually invisible under the SEM. With the AFM, however, these effects can be clearly imaged.

5) Pump down for 2 hours. The base pressure should reach 2×10^{-7} Torr.

6) Begin air-cooling the stage.

7) Pre-heat the Cr rod. This should be done slowly since there will be a lot of outgasing. After 50 Å have been evaporated, open the shutter and deposit 100 Å Cr onto the sample at a rate of 1-2 Å/sec.

8) Evaporate 50 Å from the Au boat, open the shutter, and deposit 400 Å Au at a rate of 2-4 Å/sec.

9) After the evaporation is complete and the sample is removed, pump the chamber back below 500 mTorr.

10) Place the sample in acetone and liftoff overnight, in a parafilm covered beaker. As shown in Fig. 2.4b, the PMMA bilayer should produce an undercut that facilitates easy liftoff by separating the metal to be removed, from the metal intended for the gates. If these metals are attached (e.g. a layer thicker than the PMMA is evaporated), the metal on the GaAs surface could be torn away with the PMMA. Several seconds of ultrasound are usually required to complete the liftoff. This time should be minimized as long periods of ultrasound can damage the gates.

2.7 Wirebonding

After liftoff, the final step in sample fabrication is to electrically connect the sample to some type of mounting system. Earlier group members used a crude but effective indium system to electrically wire their samples [e.g. Berry, (1994)]. When indium is properly cleaned, it sticks very well to the gold pads on the GaAs chip. Thin gold wire (1 mil diameter) can then be pressed into the indium pads to make electrical contact with the surface gates. Though elegant in its simplicity, there are a few drawbacks to this system. First, the spacing of the indium pads is limited by the dexterity of the hand that positions them. Realistically, no more than eight wires can be attached to one of our samples if it is wired by hand. This hand-wiring is a tedious, time-consuming step that must be performed while examining the sample under a microscope. Most importantly, gates are occasionally destroyed by static electric discharges during hand-wiring. Considering all of the effort that has been invested in a sample by the time it reaches this stage, any procedure that routinely destroys the sample at this late juncture should be avoided if possible.

The frustration of indium led us to experiment with wirebonding to our samples. The head of a wirebonder presses a thin gold wire into a gold bonding pad patterned onto the sample surface. Ultrasonic power is supplied at the point of contact in order to fuse together the metal of the pad and wire. Fig. 2.5a shows an example of a successful wirebond. Unfortunately, early attempts at wirebonding our samples were unsuccessful. As shown in Fig. 2.5b, the gold pads on the GaAs surface would often be torn from the

Wirebonding

a)

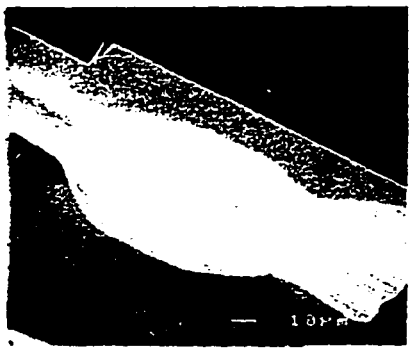

Good Bond

b)

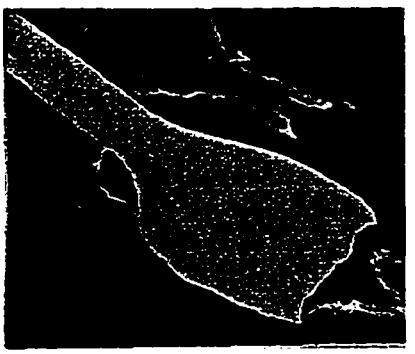

Bad Bond

c)

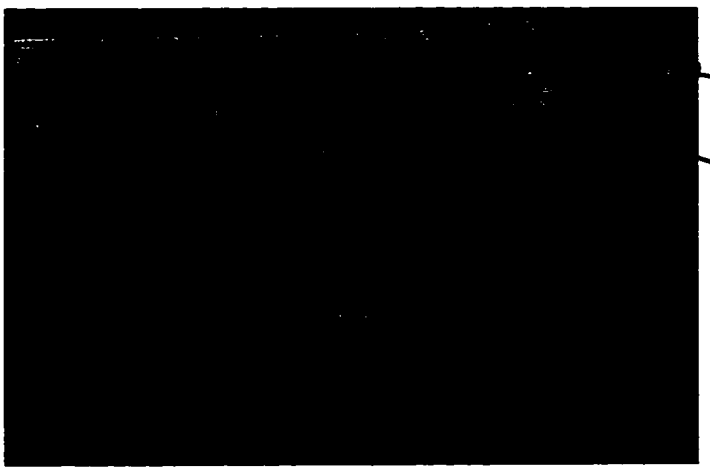

Sample Layout

Fig. 2.5 a) SEM photo showing a successful wirebond. b) SEM photo showing a marginally successful wirebond. Note the ripped gold from where previous attempts failed. c) Top view photograph of a sample with multiple Fabry-Perot interferometer devices (Chapter 7). Wirebonds are used to connect the gates and ohmic contacts to the chip carrier (out of field of view).

surface during the bonding procedure. The key to successful wirebonding is to improve the adhesion between the metal and the GaAs. At the suggestion of Steve Shepard, we began cleaning our samples in a dilute ammonium hydroxide solution just prior to the metal deposition. This solution etches away the top monolayer of the GaAs, leaving a clean surface onto which the Cr/Au bilayer sticks extremely well. This wirebonding technology allows for the creation of devices far more intricate than indium wiring would permit. It is possible to loop wires over one another, and wirebonds can be placed within 100 μm of each other. Since both the bonding head and the sample stage are grounded, it is not possible to "blow up" a gate while wirebonding to it. Wirebonding is also much faster than wiring a sample by hand. What previously required three hours can easily be finished in fifteen minutes with the wirebonder.

Below we sketch the current procedure used in wirebonding a sample. The manual for the wirebonder may be consulted for further details on the operation of the instrument. More so than most pieces of equipment in our laboratory, good wirebonding requires practice. Though it may seem difficult at first, wirebonding becomes easy once one develops a "feel" for the machine.

1) The chip needs to be mounted onto the chip carrier (described in Chapter 3). The "glue" used in mounting must hold the sample securely over repeated thermal cycles to 4.2 K. In addition, it must immobilize the sample during the bonding procedure. Rubber cement satisfies the first criterion, but when the bonder head applies force to one spot on the chip, the chip is pressed into the spongy cement causing it to tilt so much that previous wirebonds are sometimes ripped off. Double-side conducting tape presents a level bonding surface without much give, but samples occasionally fall off in the cryostat. A very *thin* layer of GE varnish satisfies both criteria. A single drop of varnish spread uniformly on the chip carrier is sufficient to hold the sample, and chips mounted in GE varnish do not wobble during bonding the way those in rubber cement do. Our measurements do not detect any signs that the sample is being noticeably stressed by the GE varnish.

2) If another group has been using the wirebonder (Kulicke-Soffa Model 4123), the settings should be readjusted to their gold optimum. These are: Time = 6, Force = 6, and Power = 230. The stage temperature should be set for 150° C. The wirebonder has two modes: fast bonding and slow bonding. All the groups that currently use the machine operate in the slow mode.

3) The stage height should be adjusted so that between the first and second bond, the bonder tip hovers just above the sample surface when both loop and search heights are set to zero. Although the loop height may be varied, we typically set the loop height = 1.

4) A test piece should be used to make a few bonds to insure that the bonder is threaded correctly and functioning properly.

5) Once the machine is bonding properly, the real sample may be wired. Since the annealed ohmic contacts are easiest to bond, these are generally done first. Occasionally a bond to a Cr/Au pad will fail, tearing part of the gold pad up with it (see Fig. 2.5b). The foot of a successful bond is a square only about 50 μm on a side; if the bonding pad is made larger than this, several attempts may be made. A number of tricks can be used if a particular bond proves troublesome. Sometimes reversing the order of the first and second bonds solves the problem. Increasing the power also helps occasionally. My guess is that problems are caused by poor metal adhesion that results from surface contamination prior to evaporation. Fortunately, such problems occur rather infrequently if care is taken during the sample cleaning steps.

With the wirebonder and the new chip carrier/socket system, it is possible to electrically connect samples with up to 24 leads. This allows several multiple-gate devices to be fabricated on a single chip and cooled down simultaneously. Placing several devices on a chip obviously increases the chances that a functional device can be measured on a given thermal cycle. This often eliminates the need to warm up the sample if the 2DEG has equilibrated in an unlucky configuration in a particular cooldown. In addition, having several identical working devices on a single sample provides an opportunity to examine

the reproducibility of a given effect. As described in later experimental chapters, the wirebonder even allows arrays of gated devices to be easily connected.

In searching for an optimal sample design, it is also nice to be able to vary a parameter in the sample geometry, and to place all of the variations on a single chip. An example of such a sample is shown in Fig. 2.5c. This sample has four Fabry-Perot electron interferometers (Chapter 7) in which the spacing between the quantum point contact and the reflector gate(s) is varied. This sample illustrates the planning involved in laying out a multi-device sample. Bonding pads should be well-spaced, allowing wirebonds to be made from all sides of the chip carrier. In addition, situations in which wires are looped over other wires or surface gates should be avoided, as such configurations may lead to shorts between gates. As shown in Fig. 2.5c, opposite sides of split-gate point contacts are typically bridged by a single wire. This allows point contacts to be tuned with a single gate voltage and prevents large voltage differences from existing on two closely-spaced metal gates.[14]

2.8 Some Common Sample Problems

Despite our best efforts, many of the gated 2DEG samples fabricated in our laboratory have problems. In this section, some of the more commonly encountered failure modes will be described. In addition, tips for avoiding these difficulties and resuscitating dead samples will be discussed.

The first class of problems are shorts. As might be expected when over twenty leads are attached to a sample, occasionally two wires accidentally contact one another. These shorts are usually easily corrected by reattaching the problematic leads, taking care to keep the gates grounded while working on them. Shorts between the electron gas and surface gates are somewhat more difficult to deal with. As described earlier, these shorts

[14]Such situations can lead to large electrical fields that destroy said gates.

are created when a surface gate overlaps a rogue microcontact. The best advice here is to be careful to avoid the formation of such ohmic contacts in the first place. If the gate/gas short is near the edge of the sample, however, it can sometimes be removed by scraping away the edge of the chip with a diamond-tip scribe. Shorts can be easily detected by performing a quick test measurement in a liquid helium storage dewar — a procedure that is recommended for all samples.

Another group of sample problems appears to be intrinsic to the GaAs/AlGaAs heterostructure itself. The worst of these is low frequency switching noise in the resistance of a quantum point contact. As shown in Fig. 2.6a, when the voltage applied to the point contact is fixed, the resistance may nevertheless fluctuate in discrete jumps. This phenomenon, which is very reminiscent of random telegraph switching, has been studied in detail by several groups [Dekker, *et al.*, (1991); Timp, *et al.*, (1990)]. These groups attribute the discrete switching to the presence of a single electron trap located in close proximity to the quantum point contact. As the trap charges and decharges, the electrostatic confining potential in the quantum point contact is altered, leading to fluctuations in the conductance of the point contact.

The behavior of our point contacts seems to confirm this hypothesis. Since electron traps are not distributed uniformly throughout the sample, the switching is worse in some point contacts that others, and in a fortunate few, is absent altogether. For point contacts with switching behavior, the amplitude and frequency of the resistance jumps increases as the number of transverse modes in the point contact decreases. Since the charging and decharging events most strongly affect the 1-D subband closet to depletion, it seems plausible that the switching noise should worsen as fewer subbands contribute to transport. In addition, as the number of propagating modes in a quantum point contact decreases, the conductance becomes more sensitive to the applied electrostatic gate potential. It is probable then, that as the number of modes decreases, the conductance would also become more sensitive to the potential fluctuations resulting from the traps. The switching behavior

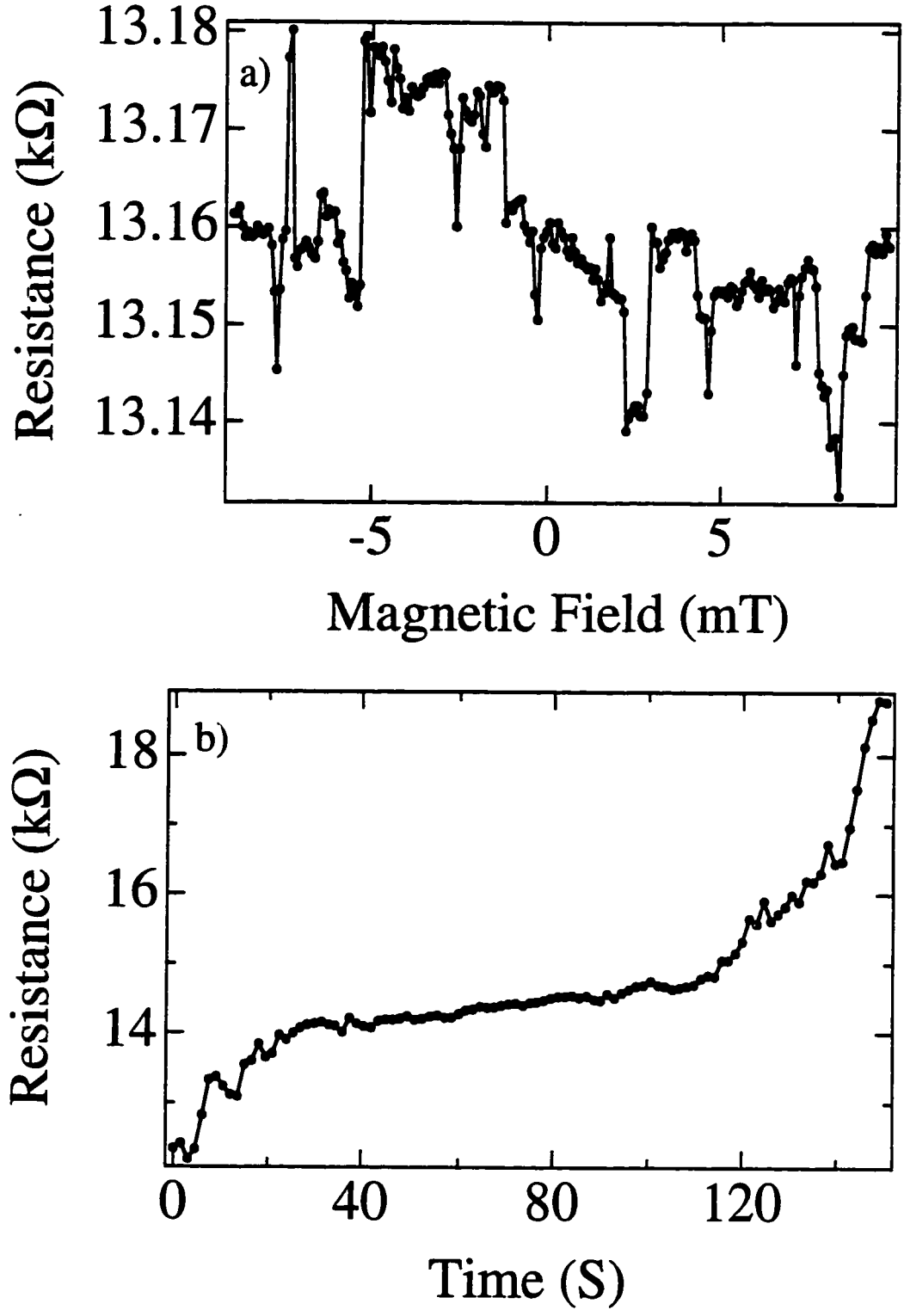

Fig. 2.6 a) Illustration of switching noise in a quantum point contact tuned to approximately one mode. The presence of the switching ruins the magnetoresistance measurement. b) An example of the upward monotonic resistance drift in a point contact initially tuned to one mode. Both traces are taken at 4.2 K.

seems to diminish on some occasions if the point contact voltage is tuned to a quantized conductance plateau. This is not surprising as the conductance is least sensitive to the external potential in such regions.

If a point contact's switching is especially bad, it becomes virtually impossible to perform any experiments with that contact. Thermally cycling the sample sometimes helps, but thermal cycling often causes switching problems to appear in a previously good point contact. A useful trick is to slowly increase the negative bias on a bad point contact to -5 Volts. This large voltage shock occasionally stops the switching behavior. For the most part, however, the switching problem seems intrinsic to the 2DEG, and there is very little that we can do about it. Certain wafers like KC2 are especially prone to switching and should be avoided. In addition, placing multiple devices on a chip increases the odds that a quiet point contact can be found.

Fig. 2.6b illustrates another difficulty that sometimes occurs when we attempt to maintain a fixed point contact resistance. Even though the applied bias voltage is fixed, the resistance of the quantum point contact increases monotonically. The origin of this behavior is unclear. The problem, however, can often be remedied by slowly increasing the negative bias voltage past pinch off. When the bias voltage returns to its initial value, the point contact resistance is larger than before, but it is usually stable. This suggests that an abnormally high sheet density may have existed near the quantum point contact. In this case, the upward drift in resistance could be due to electrons slowly migrating from this area.

Many of the experiments that are described in thesis involve measuring transport as a function of a some applied gate voltage. As a rule, the behavior of electrostatic gates is quite reproducible. Consecutive traces involving gate voltage sweeps should be indistinguishable from one another. There are, however, a few exceptions to this behavior that should be noted. The first time any particular gate is negatively biased, there is generally a small permanent drop in the electron sheet density underneath it. As a result,

the first and second data sweeps taken with a given gate often differ slightly. In a good sample, though, the behavior of that gate should be consistent thereafter. This is not the case with the wafer KC8. The electron sheet density is lower in KC8 than in most other wafers. More importantly, gate voltage sweeps are not reproducible. Successive depletions of a gate appear to incrementally lower the local electron density. This leads to hysteresis effects similar to those that make wafers KC5 and KC6 (the wafers which require illumination) unusable.

Chapter 3

Experimental Cryogenics and Electronics

3.1 Introduction

In this chapter, we will describe the experimental details important to the work presented in this thesis. Fig. 3.1 shows a schematic diagram of the apparatus used in many of the electronic transports reported in this thesis. Note the dashed cylinder labeled "cryostat" that surrounds the sample. All of our measurements are made at or below liquid helium temperature. The cryostat in Fig. 3.1 could refer to one of a number of cryogenic systems available in our laboratory. Depending on the temperature requirements of a particular experiment, the cryostat could be a ^{4}He storage dewar, a ^{3}He system, or even a ^{3}He/^{4}He dilution refrigerator. Since cryogenics play a vital role in our experiments, in the first portion of this chapter we will describe all of these systems.

Our experiments require cryogenic measurement because the small energy scales of the phenomena examined would be thermally smeared at higher temperatures. These energy scales also limit the excitation voltages that may be applied to samples. Typical signals are on the order of a few microvolts, and require sophisticated techniques for accurate measurement. The final sections of this chapter will discuss the electronics and noise considerations relevant to our work.

3.2 Kelvinox 100 Dilution Refrigerator

Although temperatures as low as 380 mK can be reached with our ^{3}He cryostat, it is sometimes necessary to perform experiments at lower temperatures. There are several

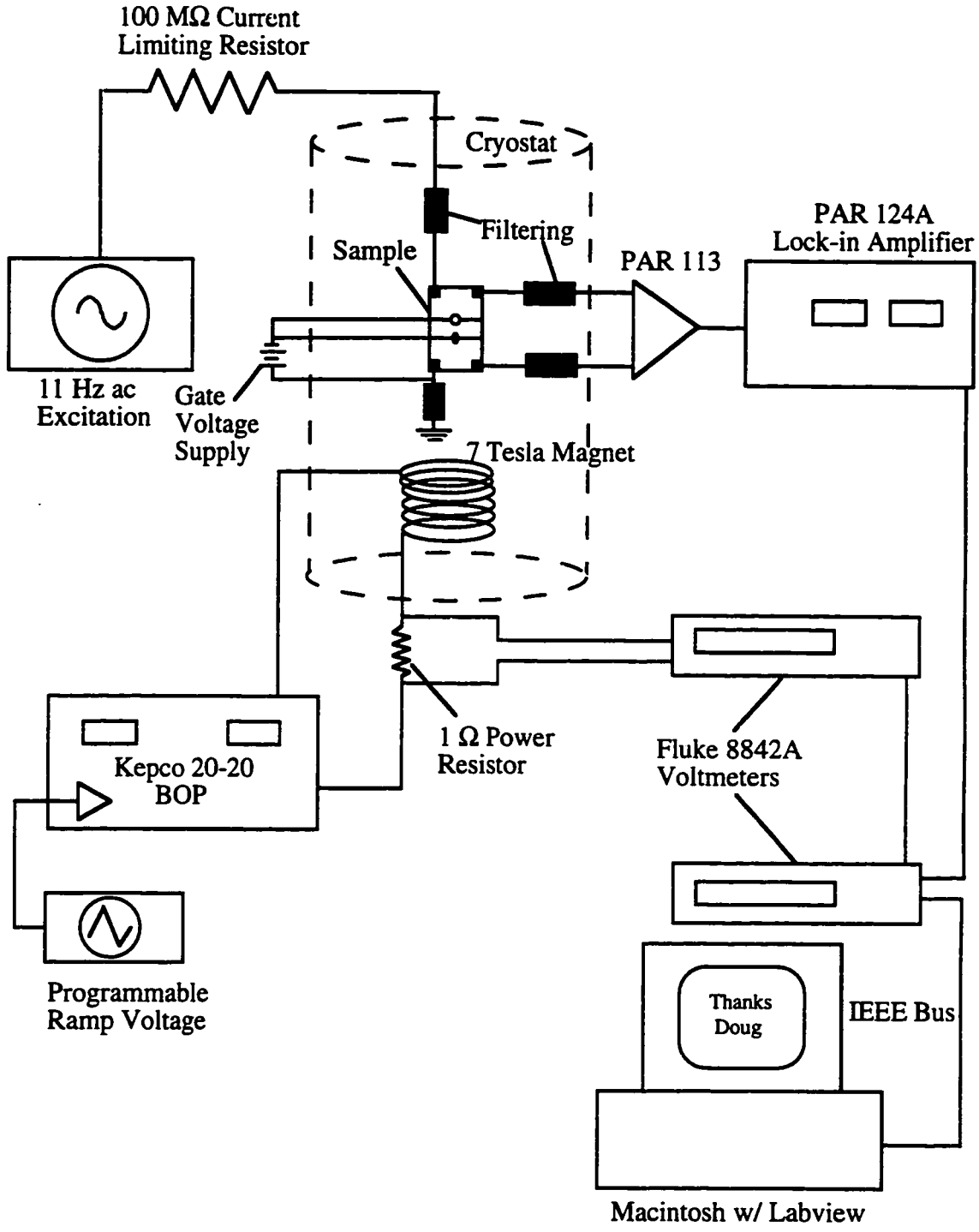

Fig. 3.1 Schematic view of the apparatus used in current-biased measurements of the sample resistance. The cryostat is either the ^{3}He system or the dilution refrigerator, depending on the temperature requirements of the experiment. 4-probe electrical contact to the sample is made at the ohmic contacts. The sample may be oriented parallel or perpendicular to the applied magnetic field.

reasons why lower temperatures may be necessary. By reducing the thermal energy, kT, it becomes possible to resolve energy levels which are smeared at higher temperatures. In addition, observation of Coulomb blockade oscillations requires the thermal energy to be smaller than the charging energy of the quantum dot. A final reason for reducing the sample temperature is that doing so increases the electron phase coherence length, allowing observation of quantum interference phenomena that may not have been detectable at higher temperatures. Helium dilution refrigeration allows us to achieve these lower temperatures.

The basic operating principle of helium dilution refrigeration is straightforward. When a mixture of ^{3}He and ^{4}He is cooled below a critical temperature (0.86 K), the mixture separates into a ^{3}He-rich concentrated phase and a dilute phase. Because of the enthalpy difference that exists between the two phases, it possible to obtain cooling by evaporating the ^{3}He from the concentrated phase into the dilute phase. There are many interesting subtleties in the operation and design of these dilution systems, and the interested reader may consult several excellent references [e.g. Lounasmaa, (1974)] for further details.

All of the dilution refrigerator data presented in this thesis was taken with a Kelvinox 100 Dilution Refrigerator manufactured by Oxford Instruments Ltd. This refrigerator became operational in our laboratory in January 1994, and has alleviated much of the congestion on the older Model 200 Oxford top-loading refrigerator which was installed in 1981 and has been described in numerous dissertations since then [e.g. Smith, (1989)]. The Kelvinox system is far more versatile and economical than the older refrigerator. For example, the top-loading refrigerator is limited by the sample slug design to 8 signal leads, while the Kelvinox system has 48 leads. There is direct access to the mixing chamber each time the samples are changed in the Kelvinox, allowing the filtering, thermometry, etc. to be customized for each sample. Opening up the dilution unit of the top-loading fridge is a far more arduous task, and is done about once every three years.

The Kelvinox system requires only 30 hours[1] and 45 liters of liquid helium to cool down from room temperature, and once cold, approximately 15 liters of liquid helium are consumed per day. The top-loader, on the other hand, takes a week and 65 liters to cool down, and, once cold, uses about 22 liters of liquid helium per day. Fortunately, the top-loading ability of this refrigerator allows samples to be cycled while the unit remains cold, but the time-consuming initial cooldown makes the top-loader ill-suited for a quick run. One limitation of the Kelvinox is its higher base temperature. As indicated by the their respective model numbers, the Kelvinox is a smaller system offering 100 microwatts of cooling power at 100 mK — half the cooling power available in the top-loading refrigerator. This lower cooling power combined with the increased heat load due to the larger number of leads yields a base temperature of about 30 mK for the Kelvinox compared to about 15 mK for the top-loader. Very few (if any) of the group's experiments, however, require the additional cooling power.

As a reference to future users, the following sections will detail the design and construction of our Kelvinox system. For completeness, I have included in this thesis Appendix A, which contains a description of the standard operating procedures that have been compiled by the first users of our Kelvinox system. Also included in this appendix are useful details on the diagnostic wiring and thermometry of the system.

Dewar and Magnet

The manuals supplied by Oxford Instruments provide an excellent description of the Kelvinox Dilution Refrigerator which will not be repeated here [Oxford, (1993)]. In the interests of cost and performance, our system has been modified from the standard Oxford design and these changes will be described below. As Oxford's dewars are notorious for

[1]If the sorption pump in the IVC functioned properly, we could go from room temperature to base in about 12 hours.

their helium consumption[2], we designed the Kelvinox unit to fit inside a dewar/magnet system very similar to the efficient ^{3}He cryostat dewar system designed by Bob Westervelt and Alex Rimberg. As shown in Fig. 3.2, the basis of this system is a superinsulated dewar with a narrow (6") neck (Precision Cryogenics, Inc., Indianapolis, IN). Due to space constraints, a transfer line for liquid helium cannot be inserted directly into the belly of the dewar, so an auxiliary transfer port is required. The magnet is supported from a stainless steel dewar insert. It is a 7 Tesla[3] superconducting solenoid with a 1.5" bore and a persistent current switch (American Magnetics Inc., Oak Ridge, TN). A cold finger extending from the mixing chamber allows the sample to be situated in the field center while cancellation coils on top of the magnet null this field at the mixing chamber. Three threaded brass rods support the magnet assembly such that the top plate of the cancellation coils is 38.7" below the top of the stainless steel insert.[4] Near the top of the stainless steel insert there are two KF-25 ports where military connectors soldered into KF-25 blank-offs provide vacuum-tight feedthroughs for the leads that go to the level meter, diagnostic resistor, power resistor, and persistent current switch. A wiring diagram for these diagnostic leads is included in Appendix A. The insert has three stainless steel support rods which extend to the baseplate from which the magnet is hung. Also attached to these rods are seven evenly spaced copper baffles. The actual dilution unit is raised and lowered into the dewar by a pulley and winch system, and fits rather snugly inside of these baffles. A thin mylar inner sheath was inserted inside of these baffles and prevents the dilution unit from banging into the baffles if it is lowered in a somewhat less than perpendicular fashion;

---

[2]You can find a large black Oxford dewar in the closet between rooms 201 and 203. It simply cost too much to run.

[3]Although rated to 7 Tesla, the magnet can be ramped up to 8.4 T before it quenches. Calibrating the magnetic field with a Hall probe, we found that the magnet to produced a field of 0.2609 T/Amp.

[4]This guarantees the sample will be centered in the magnetic field. Unfortunately, the engineers at Oxford were confused by our custom-built system and delivered us a unit where the fill tube for the 1K pot was too long and was mangled by crashing into the top magnet plate during the first cooldown. Fortunately, Louis DeFeo was able to shorten the tube. The repair is soft soldered on top, and has sprung a leak into the IVC on one occasion.

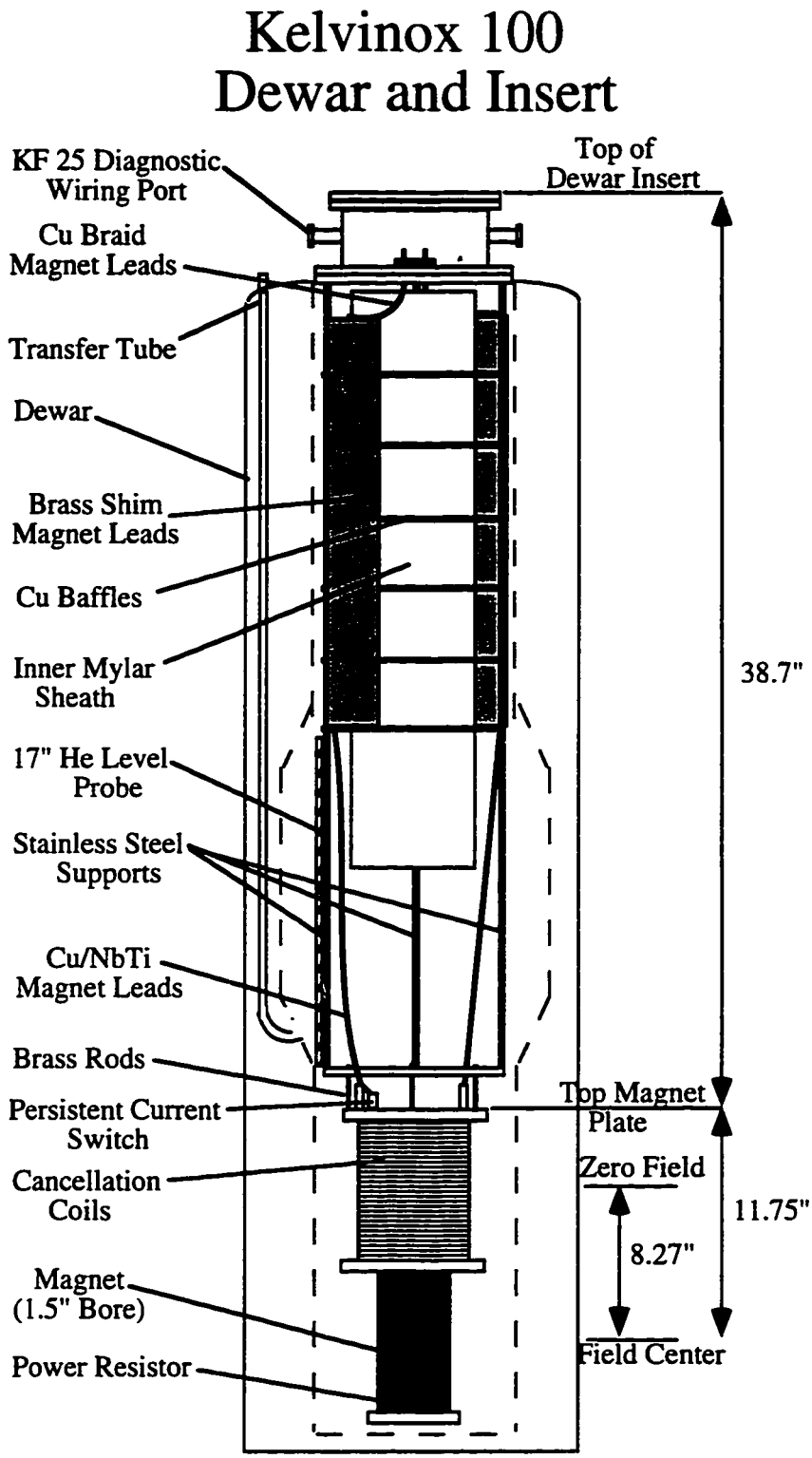

Fig. 3.2 Schematic view of of the dewar and magnet insert for the Kelvinox 100 system. The dilution unit itself slides inside the inner mylar sheath and mates to the top of the cryostat where it is bolted in place. Not shown are the concentric mylar sheaths that insulate the magnet leads from the baffles and dewar walls.

the sheath also keeps the diagnostic wires out of the dilution unit's path, reducing the chance that they will be broken during the insertion procedure. These diagnostic wires are snaked up through the offset holes in the copper baffles.

The trickiest part of the insert construction involved the magnet leads. As discussed in Alex Rimberg's thesis [Rimberg, (1992)], the top of the magnet leads is made from brass shim (20" x 6" x 3 mil) that extends down to the lowest baffle. The brass shim provides a large surface area for vapor cooling of the leads, which helps to mitigate the Joule heating associated with sending high currents ($\geq$ 32 Amps) down leads designed to minimize the heat leak into the dewar. Once in the helium bath, the magnet leads are no longer a heat leak so copper wires connect the brass shim leads to the magnet. In parallel with these copper leads, there is a filament of superconducting wire that, when immersed in helium, is capable of carrying the magnet current. Copper braid soldered to the top end of the brass shim connects the magnet leads to the copper feedthroughs on top of the dewar. It is essential that the brass shim be insulated from both the copper baffles and from the metallized neck of the dewar. Since there is only 1/16" clearance between the baffles and the dewar neck, thin insulating layers are required. The same mylar material that forms the inner sheath is used to make two concentric insulating layers: an inner layer separating the leads from the baffles, and an outer layer insulating the leads from the dewar neck.

The Oxford design circulates the mixture through a liquid nitrogen cold trap before it enters the condenser line. In order to avoid blockages that would likely have occurred on long runs without it, a helium trap was inserted before the nitrogen trap in the circulation path. The trap is simply a very narrow (1/16" O.D.) loop of stainless steel tubing that can be inserted into a 60 or 100 liter liquid helium storage dewar. The boil-off from the storage dewar is typically less than a liter per day, so a single storage dewar is adequate for the longest of runs. Thus far, the system has run for as long as four weeks without a major circulation problem. Typically, a quick clean (see Appendix A) needs to be performed almost daily on the helium traps in order to remove nascent clogs. Although they are only a

minor inconvenience, such clogs would occur less frequently if slightly wider tubing were used. In addition, this modification would allow the mixture to condense more quickly at the beginning of a run.

Kelvinox 100 Thermometry

There are several good overviews of low-temperature thermometry available [Balshaw, *et al.*, (1990); Richardson and Smith, (1988)]. The present discussion will be limited to the thermometry in our Kelvinox system. The system was purchased with an AVS-46 resistance bridge and TS-530 temperature controller (RV-Elektronikka Oy, Vantaa, Finland). The resistance bridge is capable of making accurate resistance readings with small excitation voltages that avoid heating the mixing chamber during measurement. The bridge has a multiplexer that allows seven different resistors to be measured. The temperature controller is a sophisticated feedback system that compares the resistance measured by the bridge to a set point, and adjusts the power supplied to the heater on the mixing chamber accordingly. The accuracy to which the temperature is known in our system is limited by the reliability of the secondary thermometer in the system. Oxford installed Matsushita carbon glass resistors on the sorption pump, 1K pot, still, cold plate, and mixing chamber. Appendix A gives mulitplexer settings and typical temperature readings for these resistors. The Matsushita resistors are fine for diagnostic purposes, but drift appreciably (~ 5%) with each thermal cycle. In addition, below 1 K this drift can be as much as 50%, making the carbon resistor on the mixing chamber essentially useless as a thermometer for our samples.

Therefore, we replaced that resistor with a pair of RuO_2 resistors given to us by Professor John Doyle. The uncalibrated resistors themselves are inexpensive, but a calibrated RuO_2 resistor from Oxford Instruments would cost well over $1,000. Our resistors were calibrated in the top-loading refrigerator versus the five superconducting

transition temperature standards mounted on the mixing chamber of that refrigerator. These calibrations are included in Appendix A. Unfortunately, although Dr. Robert Soulen informed me that the material used to make these standards is still in its possession, NIST no longer sells these standards, so there are none in the Kelvinox. It is standard operating procedure for the old top-loader to calibrate the RuO_2 resistor mounted on its mixing chamber against these standards every time the unit is cooled. Looking over these calibrations for some twenty thermal cycles over a period of ten years shows that below 210 mK, the drift from cycle to cycle is minimal and our single calibration should be accurate to within 2 mK for any given run. Above 300 mK, the RuO_2 resistor is less accurate and a calibrated Germanium resistance thermometer (Lakeshore Cryotronics, Westerville, OH), is used in the old refrigerator. The GRT supplied by Lakeshore is expensive and poorly heat sunk, so we are reluctant to purchase another. Dr. Eugene Haller at Lawrence Berkeley Laboratory has supplied us with isotopically pure germanium resistors which should be excellent thermometers above 200 mK. Unfortunately, their resistance is extremely strain sensitive and we have thus far been unable to mount them with either silver epoxy or mechanical clips so that the strain (and therefore the resistance) is reproducible from cycle to cycle. More of these resistors can be obtained, and I believe wirebonding the leads could possibly solve the strain problem if future users wished to use these resistors.

Our calibrated RuO_2 resistors have a pair of copper wires soldered to each end so that 4-probe resistance measurements can be made. Cigarette paper electrically insulates the resistors from the copper spool on which they are mounted. For additional heat sinking to the mixing chamber, the four leads are wound around the copper spool and are held in place by GE varnish (General Electric Co., Schenectady, NY[5]). The copper spools are

[5]The vapors from this varnish are extremely noxious, and it should only be used in well-ventilated areas. These fumes may also be responsible for the large number of physicists produced in this city.

bolted onto the mixing chamber.[6] The copper leads are soldered to miniature 4-pin male connectors (Microtech Inc., Philadelphia, PA) which allow them to be conveniently attached or removed from the wiring that connects them to Fischer connector #1 on top of the dilution unit. If a germanium resistor were to be added in the future, one of the RuO_2 resistors could be disconnected to clear a multiplexer slot for it. For the time being, though, the pair of well-matched RuO_2 resistors function as checks on one another in the absence of calibration standards.

Electrical Wiring

There are three 24-pin female Fischer connectors at the top of the dilution unit. Connector #1 has the leads to connect to the heaters and thermometry. Twisted pairs of high resistance (constantin) wires heat sunk to the 1K pot connect the Fischer connector to a 26-pin blue connector (Oxford Inst. Ltd., England) mounted near the still. From the blue connector, wires lead to the various heaters and resistors. All of the diagnostic wiring was done by Oxford Instruments, with the exception of the manganin leads connecting the RuO_2 resistors to the blue connector. A complete table of all of the diagnostic and signal wiring can be found in Appendix A.

The electrical leads to the sample are found in Fischer connectors #2 and #3. Extending down into the refrigerator from Fischer connectors #2 and #3 respectively are 24 constantin and 24 superconducting signal leads . Oxford wired these leads as ribbons of twisted pairs[7] heat sunk to the 1K pot, still, and mixing chamber. After being heat-sunk at the mixing chamber, the leads are soldered to 26-pin blue connectors mounted on the mixing chamber. We have labeled these #2 and #3 to indicate the Fischer connector each

---

[6]Another nice property of RuO_2 resistors is their small magnetoresistance. This is not essential to us, however, as they are mounted inside the cancellation coils.

[7]Consecutively numbered leads form the twisted pairs; e.g. 1 & 2, 3 & 4, etc.

one is connected to. For leads connecting the mixing chamber to the warmer parts of the refrigerator, low thermal conductivity wires are the obvious choice; but high thermal conductivity wires should be used to connect the sample to the mixing chamber. From the blue connectors mounted on the mixing chamber, copper wires lead to a modular filter box, also mounted on the mixing chamber. Twenty-four 1 kΩ metal film resistors are epoxied to the outside of each box, and each signal line is passed through these resistors in order to reflect some of the r.f. radiation in the signal lines. After each lead passes through a resistor, a length of wire (~ 2') is coiled inside the filter box. In addition to 24 coiled wires, the filter box contains a mixture of fine-grained copper powder in an epoxy (Stycast #1266, Emerson and Cumming Inc., Woburn, MA) matrix.[8] The copper particles in the matrix are insulated from one another by the native oxide layer.[9] As described by Martinis who first employed these filters [Martinis, *et al.*, (1987)], the copper grains present a large effective surface area which allows much of the microwave radiation to be absorbed through a skin-effect damping process. In order to maximize this absorption, inside the filters the 12 twisted pairs are grouped loosely to allow the copper/epoxy mixture to be in contact with as much of the wire surface as possible. Unlike the RC filtering we employ, these copper powder filters are effective at frequencies above 1 GHz.

The filters are a modular design with 26-pin blue connectors at both ends so they can be easily removed and inserted from the signal lines. In the current design, the mounted resistors are imbedded in Stycast #1266. Unfortunately, this epoxy has a thermal expansion coefficient which is different from that of the resistors imbedded within it, and over repeated thermal cycles several resistors have developed problems as a result of the strain induced by differential contraction. In addition, there is no stress relief on the leads

---

[8]By weight, the mixture was 5 parts copper to one part epoxy. At room temperature, the color and viscosity of the mixture was like that of molasses.

[9]At room temperature a few wires inside the filters appear to have high impedance shorts between them. This is likely due to nicks in the wire insulation combined with some sort of hopping conduction through the grains. At low temperatures (such as when the filters are dunked in liquid nitrogen) these shorts vanish.

as they come out of the filters, and it is easy to imagine that the wires could be accidentally broken someday when the filters are removed. Should future users of the Kelvinox need to replace these filter boxes, I would recommend using rubber cement or GE varnish instead of epoxy to mount the resistors, and placing teflon tubing around the wires as they enter and exit the filter box in order to protect them there. Photocopies of the mechanical drawings for both the filter boxes and the tailpiece (described below) have been placed in the Kelvinox operating manuals.

The final stage of filtering for the signal leads occurs in the tailpiece shown in Fig. 3.3. The tailpiece screws onto the bottom of the cold finger. The annular volume between the inner and outer walls of the tailpiece contains the same copper/epoxy mixture found in the filter boxes. Thirty-two twisted pairs of 36 gauge formvar insulated copper wire pass through this space. Currently, only 48 of the 64 wires are used, but the extras are there so that the entire tailpiece would not need to be replaced if a few of the wires were to be broken. Groups of four twisted pairs are loosely wound together and exit the annular region through one of eight holes in the bottom. Inside the annular region, there are three feet of wire per lead. This wire is coiled lengthwise to limit inductive pick-up when the magnetic field is swept. The inner wall extends an inch higher than the outer wall which allows the leads entering the copper/epoxy mixture to be stress-relieved by being taped against the inner wall.[10] In addition, teflon tubing protects the wires as they enter the epoxy. After the wires were in place, it was necessary to seal the bottom holes completely before the Cu/epoxy mixture could be poured in; if even a little epoxy were to leak out of the bottom holes, it would solidify on those wires, leaving them extremely brittle. Surprisingly, Elmer's glue was found to work extremely well.

The bottom of the tailpiece is an assembly designed to hold two ceramic sockets: one parallel to the magnetic field and one perpendicular to it. The sockets (AMP Corp.,

[10]A modification made after the leads to the first tailpiece were broken by a student who shall remain nameless here.

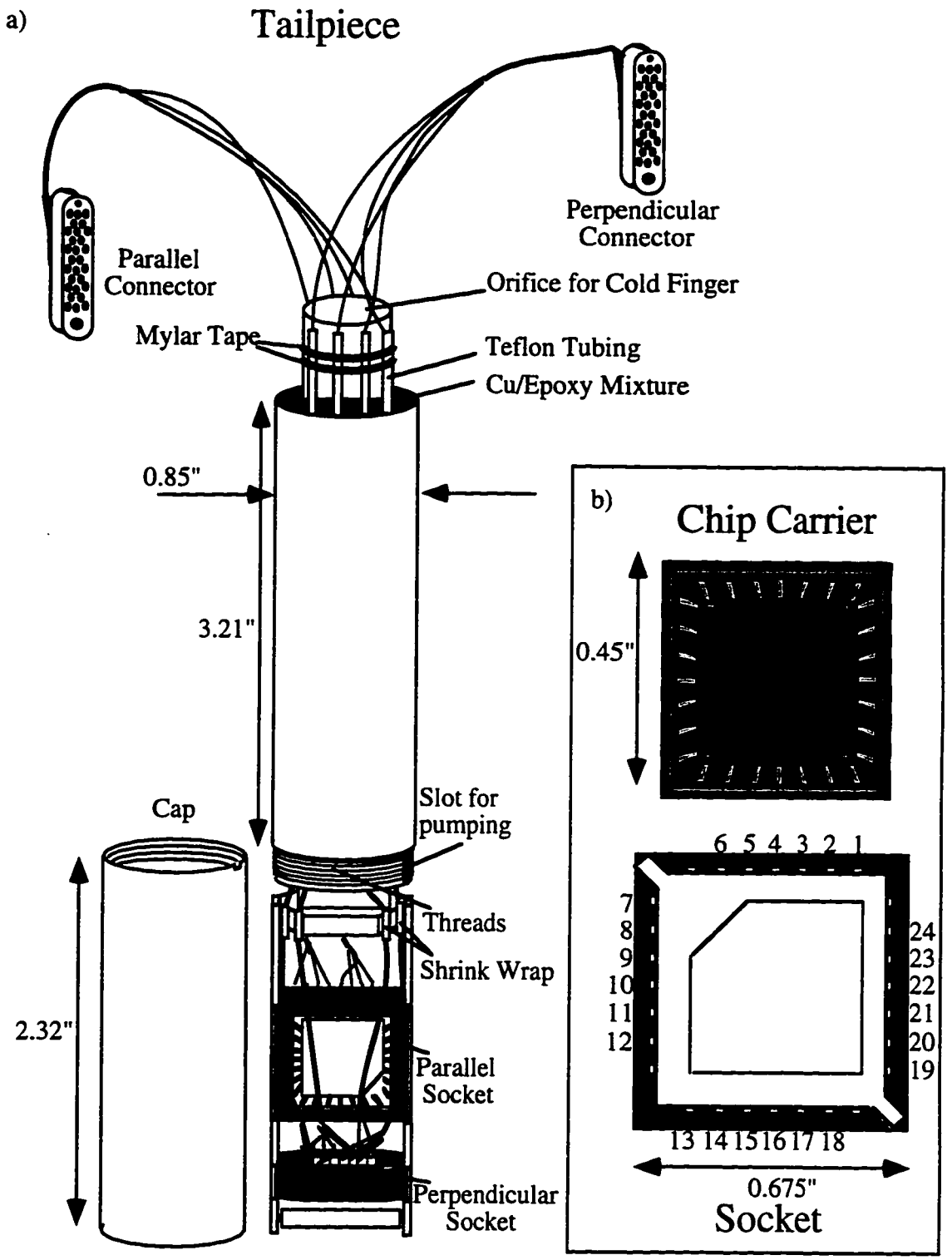

Fig. 3.3 a) View of tailpiece assembly shown with radiation cap unscrewed. Mechanical drawings for the assembly have been placed in the Kelvinox manual. b) Schematic representation of chip carrier and socket. Leads are labeled corresponding to their pinouts on the Fischer connectors.

Part #641444-2) and their associated chip carriers (Jade Corp., #28M270-J-060-U-06-4) allow our samples to be easily interchanged between the Kelvinox and our ^{3}He cryostat. Fig 3.3b shows the socket and chip carriers, along with their corresponding leads on the Fischer connectors. There is enough slack so that the 26-pin blue connectors for the perpendicular and parallel sockets can be interchanged between Fischer connectors #2 and #3. It is important, however, to insure that this extra slack does not cause a thermal short to the 600 mK radiation shield. A radiation-shielding cap screws over the bottom assembly; there is a slot in the threads onto which this cap screws, so the space may be evacuated when the IVC is pumped out.

In order to test the radiation shielding of samples in our Kelvinox system, Jack Hergenrother measured a single electron transistor that he found could function as a very sensitive radiation detector. The radiation shielding was found to be excellent as no secondary peaks near zero gate bias were detectable in the I-V traces taken with his transistor [Hergenrother, (1995)]. In fact, the radiation shielding of our tailpiece assembly is good enough that the 600 mK radiation shield appears to be superfluous. For example, Aram Adourian has performed Coulomb blockade experiments with and without it and observed no difference in his data.

Sample Base Temperature

The base temperature in a dilution refrigerator is achieved when the cooling power generated at the mixing chamber is equal to the heat load on the chamber. As mentioned earlier, the base temperature of the Kelvinox system in its current configuration is about 30 mK. When the Kelvinox system was first installed, the 48 signal leads were poorly heat sunk to the mixing chamber,[11] and the filters and tailpiece were not yet attached.

[11]The insulated leads were loosely wrapped around a post attached to the mixing chamber. John Betts did not solder the leads to the connector heat sunk on mixing chamber until after the first cooldown. Perhaps Oxford suspected that the 48 leads would prevent the refrigerator from reaching its 25 mK spec.

Following installation, John Betts measured the mixing chamber temperature with nuclear orientation thermometry and found it to be 12 mK. Once these 48 leads were electrically connected, the increase in base temperature indicated that the heat load they delivered to the mixing chamber had increased dramatically. Although the addition of the sizable mass of the tailpiece and filters drastically lengthens the thermal time constants involved in temperature control processes, their only contribution to the heat load is a negligible increase the radiative heat leak on the mixing chamber.

It is important to realize that when we measure the temperature of the mixing chamber, we are not actually measuring the temperature of the two-dimensional electron gas in our samples. In fact, even when the refrigerator is at base temperature (30 mK), our transport measurements indicate that the temperature of the electron gas appears to be no colder than 100 mK. This is a difficulty experienced by every group that we know of performing experiments in 2DEG systems. The following discussion will describe how the electron gas is cooled in our refrigerator and attempt to explain the difficulty we have in reaching very low temperatures.

In the present mounting configuration, essentially all of the 2DEG cooling occurs via electron-phonon coupling with the lattice, and all of the heat conduction between the lattice and the mixing chamber is through the electrical leads. We can neglect heat conduction through the chip carrier because the thermal conductivity of the carrier's ceramic body is about seven orders of magnitude lower than that of the gold wires and contact pads on the sample. It is probably possible to achieve better cooling of our samples by mounting them directly on the mixing chamber, but our measurements have never required us to attempt this. Since the sample cooling occurs through the leads, it is essential that the leads to the sample be well heat sunk to the mixing chamber. In addition to spooling the leads on the mixing chamber, the leads to the sample are cooled as they pass through two stages of copper/expoy filtering before reaching the sample. Ideally, a thicker gauge of copper wire would connect the sample to the mixing chamber, but the large number of

leads and tight space constraints would have made wiring the tailpiece a considerably harder task.

Several of this group's earlier dissertations [Hopkins, (1990); Rimberg, (1992)] have analyzed heat conduction through the leads to the sample, and their analyses will be applied to the Kelvinox system. There are three thermal resistances that may limit this process. First, the transfer of heat from the lattice to the leads can be limited by thermal boundary resistance at the interface between the AuNiGe contacts and the Ga(Al)As crystal. This thermal boundary resistance, R_B is given by

$$R_B = \frac{\alpha}{AT^3}, \tag{3.1}$$

where A is the contact area of the boundary (typically 5×10^{-4} cm^2) and $\alpha \sim 30$ K^{4}cm^2/W. As a result of the thermal boundary resistance, the rate of heat transfer from the leads to the lattice is limited to

$$\dot{Q}_B = \frac{AT^3\Delta T}{\alpha}, \tag{3.2}$$

where ΔT is the temperature difference between the ohmic contacts and the lattice.

This thermal boundary resistance is not the reason for the high electron gas base temperature. If the entire sample (2DEG and crystal lattice) were subjected to some heat leak (for example, from blackbody radiation) the thermal boundary resistance between the leads and the sample could allow a temperature gradient to exist at the interface between the AuNiGe contacts and the lattice. The sample base temperature would be reached when the heat transfer through this boundary resistance (Eq. 3.2) was equal to the external heat load on the sample. If $T_{sample} = 100$ mK and $T_{leads} = 30$ mK, this scenario would require a highly improbable heat load of 400 pW.

The second thermal resistance that could, in principle, limit the heat conduction is the thermal resistance of the lattice itself. We can safely neglect this resistance in our analysis as it is smaller than both the aforementioned boundary resistance and the electron-phonon coupling resistance described next [Lounasmaa, (1974)].

Electron-phonon coupling resistance is the third, and most important, thermal resistance that limits heat conduction from the 2DEG. Because of poor electron-phonon coupling, it is possible for the lattice to be at a temperature very close to that of the mixing chamber, and yet to have the electron gas be at a substantially warmer temperature. At low temperatures, electrons lose energy to the thermal lattice at a rate equal to

$$\dot{Q}_{e-ph} = \Sigma A\left(T_e^{\beta} - T_{ph}^{\beta}\right), \tag{3.3}$$

where T_e and T_{ph} are the respective temperatures of the 2DEG and the lattice, A is the area of the sample, and Σ is a coefficient that measures the strength of the coupling between the electrons and the lattice phonons. At sub-Kelvin temperatures in $GaAs/Al_xGa_{1-x}As$ heterostructures, the value of the exponent β has been experimentally measured to be about 5 [Ma, *et al.*, (1991); Wennberg, *et al.*, (1986)]. The value of the coefficient Σ is known with less certainty. In a $GaAs/Al_xGa_{1-x}As$ multiple-quantum-well structure, the coefficient Σ was measured to be $5x10^{-8}$ $WK^{-5}cm^{-2}$ [Wennberg, *et al.*, (1986)];[12] a value two orders of magnitude lower than predicted in calculations [Price, (1984)] and 36 times lower than the value measured in metallic systems [Roukes, *et al.*, (1985)]. The base temperature of the electron gas is achieved at a temperature T_e such that,

$$\dot{Q}_{2D} = \Sigma A\left(T_e^{\beta} - T_{ph}^{\beta}\right), \tag{3.4}$$

[12]The value of this coefficient was a matter of some confusion in earlier dissertations [Hopkins, 1990; Rimberg, (1992); Baskey, (1994)]. In the paper by Wennberg, *et al.*, the value of the coefficient is much larger, but previous dissertation authors did not realize that the area of the interface is implicit in the value of Σ quoted in that paper.

where $\dot{Q}_{2D}$ is the power coupled to the electron gas. Using the previously quoted value for Σ, a sample of our typical dimensions (3 x 5 mm) would require $\dot{Q}_{2D}$ to be only 0.1 pW in order to raise the electron gas temperature to 100 mK when the surrounding crystal lattice is at 30 mK. The question raised by this calculation is the source of $\dot{Q}_{2D}$. As will be discussed later in this chapter, we take precautions to insure that the source is not Joule heating associated with our sample measurements. The likely culprit (despite our best filtering efforts) is some radiation being transmitted through the sample leads. In metal systems, for example, it has been shown that poor electron-phonon coupling allows small electric fields (~ 1 μV/cm) to warm electrons well above the temperature of the phonon bath [Roukes, *et al.*, (1985)].

3.3 ^{3}He Cryostat

The Westervelt group has two ^{3}He cryostats.[13] The original system designed by Pete Hopkins and described in detail in his thesis [Hopkins, (1990)] was based on a cryostat at the Francis Bitter Magnet Lab . Alex Rimberg and Bob Westervelt designed a more economical dewar/magnet system around the existing sample probe, vacuum insert, and ^{3}He gas handling system. The current dewar, gas handling system, and vacuum insert remain essentially unchanged from those described in Alex Rimberg's thesis [Rimberg, (1992)]. We have, however, made several modifications to the sample probe and these changes will be described later in this section.

[13]Commonly referred to as the Shubi-dewar and Shubi-Deux as they were first used to perform Shubnikov-de Haas measurements.

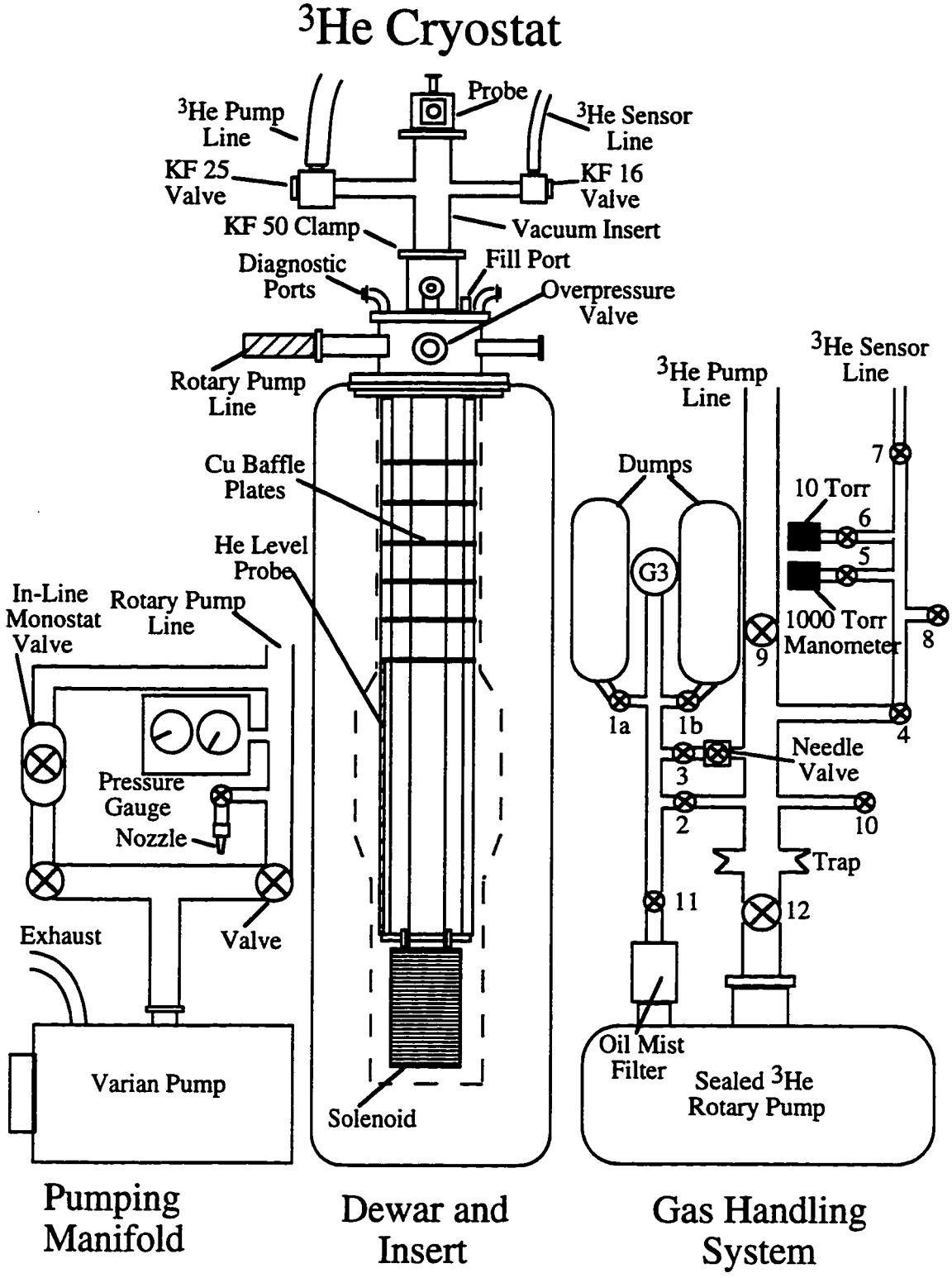

Fig. 3.4 Schematic representation showing the pumping manifold, gas handling system, and dewar for the ^{3}He cryostat. All valves are represented by the circles with the "x" in their center.

Cryostat Operation and Temperature Control

As shown in Fig 3.4, the ^{3}He system consists of a superinsulated dewar (Precision Cryogenics Inc., Indianapolis, IN) containing a 7-Tesla superconducting solenoid (AMI, Oak Ridge, TN), a ^{3}He gas-handling system, a stainless steel vacuum-tight insert that may be attached to the gas handling system, and a sample probe that may either be placed directly in the dewar (to operate at pumped ^{4}He temperatures) or in the ^{3}He insert.

To begin cooling the cryostat, the dewar is filled to the lowest baffle with liquid nitrogen. If the vacuum insert is being used, a small amount of ^{3}He (5 Torr is sufficient) should be introduced into the insert to act as an exchange gas. Once pre-cooled with liquid nitrogen, 5 litres of liquid helium are required to cool the system to where the liquid helium begins to collect in the dewar, and another 13 liters are needed to fill the dewar. A large rotary pump (Varian SD-700) is used to evaporatively cool the entire helium bath. When operating at full-throttle, the pump can cool the bath to 1.4 K and the helium will last approximately 48 hours (though the magnet will only be covered for about 36 hours). For comparison, when a smaller pump (Edwards 18) is used, the bath only reaches 1.8 K, which lowers the hold-time and base temperature of the condensed ^{3}He.

To achieve temperatures below 1.4 K, all of the ^{3}He from the gas handling system is introduced into the insert and allowed to condense. The gas condenses at the bottom of the insert which is surrounded by a 9" long heavy-wall vacuum can with a 1/8" space between the inner and outer cans. The vacuum space also contains a small amount of activated charcoal which is an effective cryopump at low temperatures. The vacuum space was evacuated through a soft copper pumpout tube and then crimped shut. On the insert John Baskey and I evacuated, we were never able to make a leak-tight crimp seal, so following crimping, we soldered the end of the tube. At room temperature, the vacuum can pressure may actually be close to atmosphere, but any gas in this space is cryopumped at

low temperatures. The vacuum can and low thermal conductivity of stainless steel allow the ^{3}He column to be at a lower temperature than the surrounding ^{4}He bath, and we reach those temperatures by evaporatively cooling the ^{3}He bath with a sealed rotary pump (Alcatel #AVUM2012AH). Only about 30 minutes of pumping are required before the ^{3}He column reaches its base temperature of 380 mK. Before opening any valves to the insert, the pair of three gallon dumps vessels are at a pressure of 600 mbar (gauge G3) indicating a total charge of 0.85 moles of ^{3}He.[14] The molar volume of liquid ^{3}He below 1K is approximately 37 cm^3, which means that when the sample is oriented perpendicular to the magnetic field,[15] it remains immersed in liquid until G3 reads approximately 475 mbar. We have confirmed this with some highly temperature-dependent transport measurements. Assuming the ^{3}He is given sufficient time to fully condense before we begin pumping on it, it is easy to reach base temperature with G3 remaining below 300 mbar; the dumps pressure increases at about 4 mbar/hour during operation, which means that is not necessary to recondense the ^{3}He between liquid helium transfers.

Although it does not have the sophisticated temperature control system of the dilution refrigerator, it is possible to regulate the temperature of the ^{3}He cryostat. For temperatures above 1.4 K, we use an in-line monostat valve (Lakeshore Cryotronics, Westerville, OH) to regulate the pressure (and corresponding temperature) of the helium bath. In order to insure that the sample equilibrates quickly with the bath temperature, all of the ^{3}He should be introduced into the insert as an exchange gas. Evaporatively cooling the bath is a straightforward but slow process, since much of the liquid helium is wasted unless the throttle on the pump is opened gradually. Because almost half of the helium has been evaporated by the time base temperature is attained, we can only perform one temperature series in this manner per helium transfer. Once the ^{3}He has condensed, the

---

[14] In Pete Hopkins' and subsequent theses, the total volume of the dumps is incorrectly given as 12 L; this error led them to inaccurately calculate how long the sample remained immersed.

[15] Approximately one inch above the bottom of the can.

temperature may be varied rather quickly between 1.4 K and 380 mK. We determine the temperature from the vapor pressure of the ^{3}He as read by a pair of capacitance manometers (Edwards High Vacuum Inc., 0 to 1000 Torr #72W60041811 and 0 to 10 Torr #72W60021811). When V4 is open, a significant pressure gradient exists between the manometers and the sample, so that valve must be closed for an accurate reading of the pressure. The temperature measured in this fashion should be accurate to within a millikelvin [Hopkins, (1990)]. There is no monostat valve in the gas handling system, but the pump may be manually throttled using V12 to regulate the pressure. With practice and almost constant attention, it is possible to hold the temperature steady to less than a millikelvin. If we are able to live with a ~2 mK variation over the course of a 30 minute data sweep, it is possible to leave the system unattended by slightly throttling V12 from its "stable" pressure setting, and letting the bath temperature creep upward. At any time, the sample can be quickly warmed for another temperature series either by reintroducing ^{3}He from the dumps or by using the metal-film heater.

As a final note in the area of temperature control, it is possible to perform measurements at temperatures above 4.2 K. A thermometer of some sort must be mounted near the sample. Once the exchange gas cools the sample to the desired temperature, pump the ^{3}He out of the insert and monitor the temperature. It will continue to drop very slowly due to radiative cooling, but this technique does allow us to reach an otherwise inaccessible temperature range.

Sample Probe

Fig. 3.5 shows a diagram of the ^{3}He vacuum insert and the sample probe. Both were manufactured by Dick Koch (American Cryogenic, Pelham, NH). The Westervelt group has two nearly identical inserts and three sample probes. All of the sample probes have seven copper baffles with offset notches to provide a pathway for pumping and

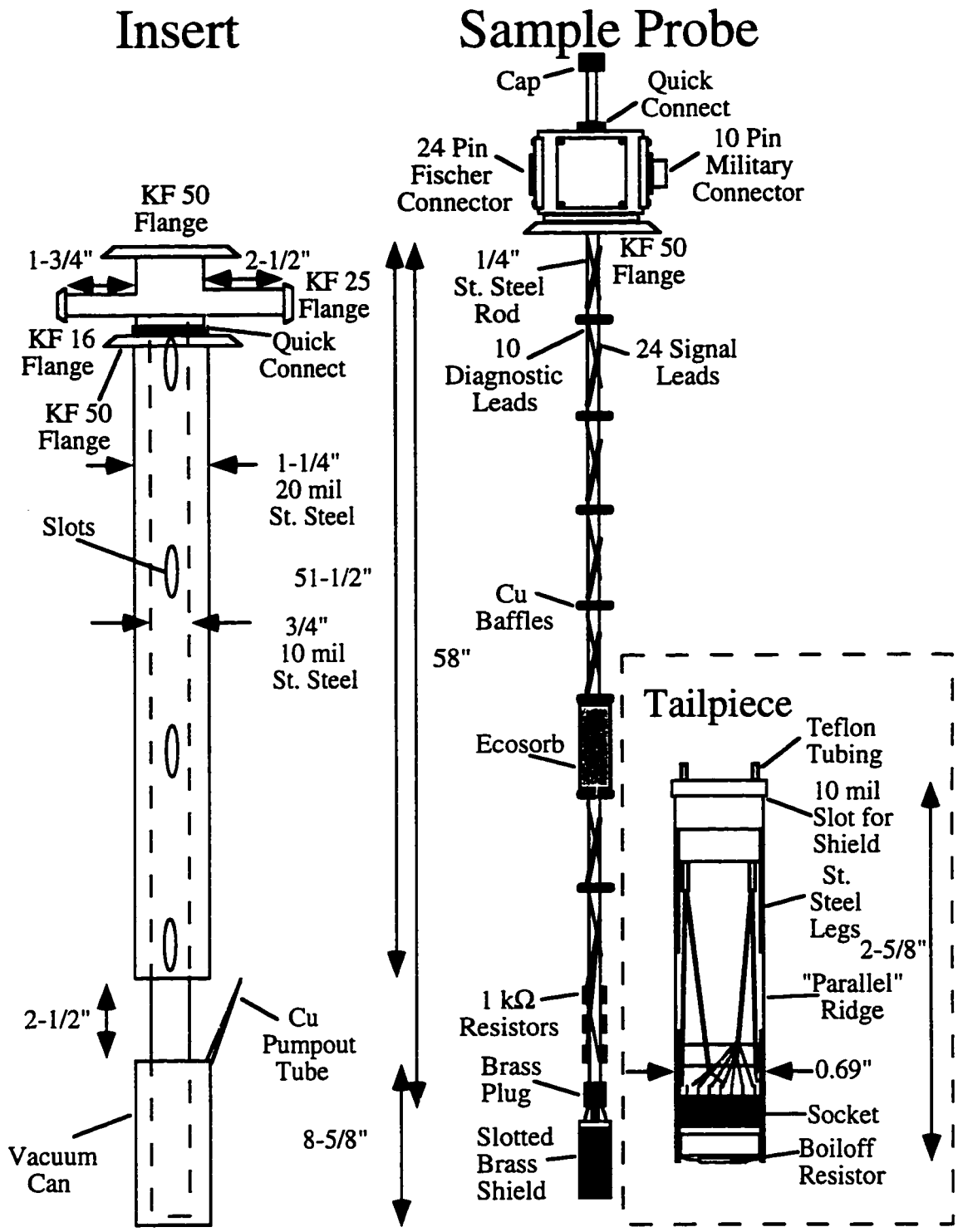

Fig. 3.5 The stainless steel vacuum insert and the sample probe used in the ^{3}He cryostat. The dashed inset shows an enlarged picture of the tailpiece found under the slotted brass shield at the bottom of the sample probe.

wiring. A quick-connect just above the probe head allows for adjustment of the probe length. Since these tended to be unreliable (e.g. the entire stick could rotate around the head stressing all electrical leads), and since I could think of no reason why we wouldn't want the probe length such that the sample would be centered in magnetic field, I epoxied that joint on the two sticks I modified once their lengths were set correctly.

One of the sample probes was left with the old indium mounting system that is described in earlier group dissertations [e.g. Mar, (1994)]. I redesigned the wiring and mounting system on the other two probes to improve the cryostat's performance and to allow compatibility with the Kelvinox mounting system. On the old probes, there were only eight signal leads consisting of two strands of Lakeshore 36 gauge (5 mil dia.) Cu 4-wire ribbon, and 2 copper wires connected to the boil-off resistor. On the redesigned probe there are 24 signal leads attached at the head of the probe to a 24-pin female Fischer connector (identical to the connectors on the top of the Kelvinox). These leads are 5 mil diameter manganin wire (California Fine Wire Co., Grover Beach, CA) which have a resistance of 12 Ω/foot. The wires attached to adjacent pins on the socket are tightly wound into twisted pairs and adjacent pairs are loosely wound to form groups of four wires. The 24 signal leads are securely wrapped around the probe with teflon tubing used to protect the wires where they pass through the notched baffles. Plenty of slack is left near the probe head so that the Fischer connector can be unmounted with ease. The wires are secured around the probe with a combination of mylar tape and dental floss.[16] Every signal line passes through a 1.5 kΩ metal film resistor mounted near the end of the probe. Each resistor is individually covered by a heat-shrunk wrap to avoid possible shorts. The main purpose of these resistors is to reflect r.f. radiation transmitted down the leads.

As shown in Fig. 3.5, a stainless steel tailpiece modeled after that of the Kelvinox is attached to the end of the probe. The manganin wires from the resistors enter through four holes at the top of the tailpiece, and teflon tubing is used to protect the wires from

[16]Though lacking in aesthetic value, the tape and dental floss never failed in over 100 thermal cycles.

possible damage there. The manganin wires are soldered to the socket, and there is enough slack in the lines so that the sample may be mounted perpendicular or parallel to the magnetic field produced by the superconducting solenoid. In order for it to fit inside the vacuum insert whose inner diameter (710 mil) is substantially narrower than the Kelvinox tailpiece, the ceramic body of the socket had to be almost completely shaved away. Manganin wires are used to minimize the heat leak into the ^{3}He column. Unfortunately, the manganin wire is rather difficult to strip and solder. Thermal wire strippers were found to remove the formvar insulation best, but would leave the wire somewhat brittle. In addition, we found #30 Flux (Superior Flux & Mfg. Co., Cleveland, OH) worked well in soldering the wires to both the resistors and the socket pins. We experimented with using copper wiring after the blocking resistors, but this was found to radically damage both base temperature and hold time. A 10 mil slotted brass shield slides over the tailpiece assembly to provide additional radiation shielding.

In addition to the 24 signal leads, there are 10 manganin diagnostic leads soldered to a military connector at the probe head. These leads are wrapped around the probe in a fashion similar to the signal leads, but do not pass through metal film resistors. Currently two leads (A and B) are attached to a 2.2 kΩ metal film resistor mounted at the base of the tailpiece; this resistor can be used as a heater which allows the ^{3}He to be quickly removed. In addition, four leads are attached to a miniature 4-pin female connector (Microtech Inc.) which allows LEDs, diagnostic thermometers, etc., to be easily attached to the probe. The four unused leads are taped to the brass plug just above the tailpiece and are available for future use.

As mentioned earlier, the base temperature and hold times for the current ^{3}He probes are 380 mK and >36 hours respectively, while the corresponding numbers for the old probes are 420 mK and 10 hours. Although the base temperature and hold time are influenced by factors such as the temperature of the helium bath and the length of the vacuum jacket, it is clear that the heat leak to the ^{3}He column is dominated by the electrical

leads on the probe. Otherwise, rewiring the probe would not have significantly affected the cryostat's performance. At 380 mK, the latent heat of vaporization for ^{3}He is about 21 J/mole. Based on our measured hold times, our current heat leak into the ^{3}He bath is about 33 μW, while it was about 130 μW when there were 10 copper leads. For a wire without heat sinking, the rate of heat transfer from an end at temperature T_1 to one at T_2 is given by:

$$\dot{Q}_{th} = \frac{A}{\ell} \int_{T_1}^{T_2} \kappa dT \qquad (3.5)$$

where A is the cross-sectional area of the wire, ℓ is the length of wire, and κ is the thermal conductivity. Although there were fewer copper leads on the old stick, the thermal conductivity per lead is 10-40 times (depending on the type of copper) greater for copper than manganin, which explains the improvement. Assuming $T_2 = 273$ K and $T_1 = 0$ K, $\dot{Q}_{th}$ calculated from Eq. (3.5) is roughly 800 μW as a result of 34 manganin wires. The heat sinking achieved by wrapping the leads around the stick clearly reduces this value, as evidenced our measured heat leak which is some 20 times smaller than this result.

Several modifications have been made to the probe to decrease the amount of radiation reaching the sample. Ecosorb microwave absorbing material (Schaal Assoc., Burlington, MA) has been wrapped in the space between the fifth and sixth baffles. In addition, we usually place some additional Ecosorb above the sample in the tailpiece. The metal film resistors near the bottom of the probe are intended to reflect r.f. radiation coming down the leads. When combined with the capacitance of the leads, they should also form a low-pass RC filter. We made modular Cu-powder/epoxy filters similar to those in the Kelvinox, but their wiring proved to handle thermal cycling rather poorly and they were removed from the probe. In addition, copper tape and silver paint may be used to seal the

tailpiece from blackbody radiation in a manner similar to that used for the old fridge slug [Waugh, (1994)].[17]

Choice of Cryostat

The main advantages of the ^{3}He cryostat over the Kelvinox are its faster cooldown time, lower initial cooldown cost, and lower daily cost of operation.[18] The ^{3}He cryostat can be cooled from room temperature to base in about 6 hours, while 30 hours is a realistic timescale for the Kelvinox. About 18 liters of liquid helium are required for the initial ^{3}He cooldown, compared to 45 liters for the Kelvinox. Once cold, the ^{3}He cryostat consumes about 8 liters of helium a day — about half of what the Kelvinox requires.

The above comparisons should make it clear that any experiments that can be performed in either cryostat should be performed in the ^{3}He system. The requirements of a particular experiment dictate whether the Kelvinox is required, or if the ^{3}He cryostat may be used instead. The main advantages of the dilution refrigerator are its lower base temperature and superior radiation shielding. As mentioned in Chapter 4, the electron dephasing rate is the same for samples measured in either the Kelvinox or current ^{3}He system over the temperature range available to both cryostats. Therefore, there is no reason to perform our quantum interference experiments in the Kelvinox unless extremely long phase coherence lengths are desired. Coulomb blockade experiments, however, seem to be far more sensitive to the cryostat's radiation environment than are quantum interference experiments. Aram Adourian has measured samples in both cryostats and found the peak-to-trough ratio of the Coulomb blockade in his devices to be better in the Kelvinox system,

[17]If that is done, I strongly urge that caution be taken to secure the brass shield in place. Otherwise, the tight fit will almost certainly leave the shield wedged at the bottom of the insert after the probe is removed.

[18]Another important advantage is its availability. With the heavy demand that exists for the Kelvinox, every experiment that can be performed in the ^{3}He cryostat should be. The limited time one has on the Kelvinox is also an excellent incentive to pretest samples in order to insure that limited time is put to good use.

presumably because there is less blackbody radiation-induced co-tunneling there [Waugh, (1994); Hergenrother, (1995)]. Although the ^{3}He cryostat can be useful in determining whether or not Coulomb blockade can be observed in a sample, it is not the cryostat of choice for detailed measurements.

Even if the dilution refrigerator is required for an experiment, the helium and effort required for a Kelvinox cooldown may very well make it cost- and time-effective to pretest a sample with a fast ^{3}He run before loading it into the dilution refrigerator. In the past, this was a risky proposition because gated samples would be destroyed a substantial fraction of the time they were mounted or unmounted with the old indium pad system. In addition, mounting procedures that typically involved tedious hours of meticulous tweezers manipulation were a strong disincentive to pretesting. With the compatible mounting system that now exists between the ^{3}He cryostat and the Kelvinox, a sample can be moved from one cryostat to the other in a couple of minutes without danger, making pretesting a more viable proposition.

Of course many of the problems that plague samples (e.g. gates shorted to one another, gates shorted to the electron gas, bad ohmic contacts, bad switching behavior in a point contact, etc.) can easily be detected at 4 K. This was our motivation for building a system that would allow us to quickly measure a sample in a helium storage dewar; such a system could screen a sample for the aforementioned problems in minutes while evaporating less than a liter of helium. The system we designed utilizes the probe from the ^{3}He cryostat. As shown in Fig. 3.6, the sample probe slides into a stainless steel adapter sheath with a brass KF-50 flange soldered to its top. Around the sheath there is a sliding stainless steel quick-connect (Varian CP-087S-5) soldered to a 2-1/2" diameter Ladish flange (Cryofab, Kenilworth, NJ) that mates to the helium storage dewars[19] and allows the probe to be dipped in storage dewars of different heights. The probe fits rather snugly

[19]When our helium supplier, B.O.C., recently merged with another company, they acquired dewars with a different diameter top. When ordering liquid helium, be sure to specify the 2-1/2" top if you may want to perform measurements in that dewar.

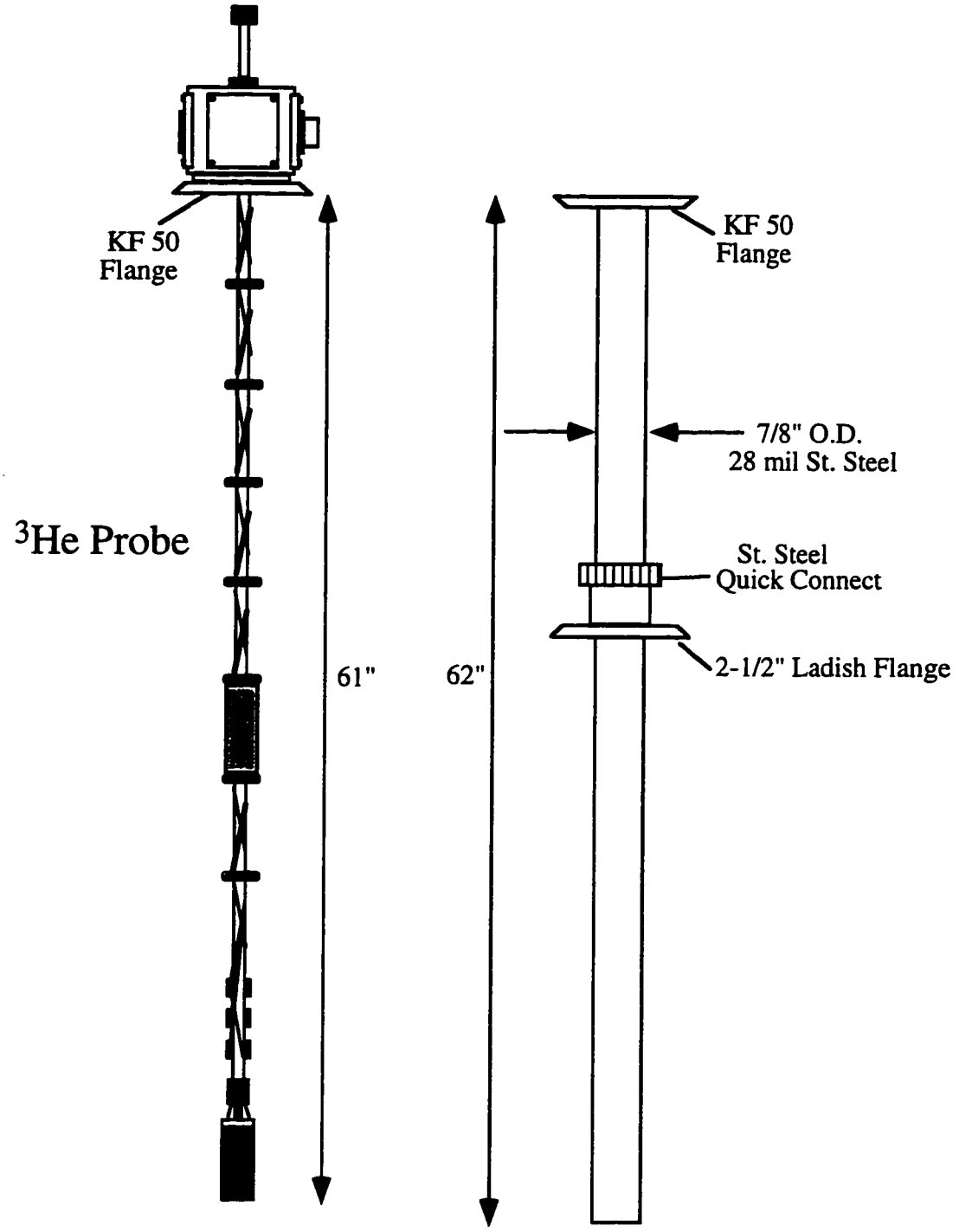

Fig. 3.6 Diagram of the stainless steel ^{4}He-adapter that allows the ^{3}He probe to test samples in liquid helium storage dewars. Samples are mounted on the probe built for the ^{3}He cryostat. The probe mates to the top of the adapter at the KF-50 flange.

inside the sheath to prevent it from rattling around too violently during these procedures. Thin-walled stainless steel (7/8" O.D., .028 wall, Tube Sales, Inc.) was found to resist denting while still boiling off less than a liter of liquid helium per dunk. Two identical ^{4}He adapters sticks have been made, and they have been valuable additions to the lab, especially when trouble-shooting sample fabrication difficulties.

3.4 Electronics

In this section of the chapter, we discuss the electronics used in the different experiments presented in this thesis. Both current- and voltage-biased transport measurements will be described. Special attention will be given to the battery-powered voltage supplies used to bias the electrostatic gates on our samples. Finally, the magnetic field control will be discussed.

Current-Biased Measurements

The majority of the data presented in this thesis come from resistance measurements of current-biased samples. I_{bias}, the RMS amplitude of the bias current applied to the sample, must be considered carefully. A larger amplitude increases the signal-to-noise ratio and allows the measurements to be made more easily. The amplitude, though, must be kept small enough so that heating effects do not influence the measurement. One such effect is Joule heating of the entire electron gas. Consider a large sample, such as a Hall bar, having a total resistance, R. In order to avoid Joule heating, we must limit the bias current so that the power input to the 2DEG as a result of the measurement ($= I^2R$), can be completely dissipated. In theory, this could severely constrain the bias currents used at low temperatures where heat transfer from the electron gas is quite limited. As we mentioned in

Section 3.2, there are, however, other sources of input power that overshadow Joule heating until the bias currents become rather large. Empirically, we find that at base temperature in the Kelvinox, large Hall bar samples with R = 5000 Ω show no signs of heating until $I_{bias} > 2.5$ nA.

The limitations on heating in ballistic electron experiments are more stringent. If we have a non-thermal distribution of carriers, the transport properties of the electrons can change. For carriers well above the Fermi energy, E_f, the elastic scattering time, τ, begins to decrease, shortening the range of ballistic motion. At energies much closer to E_f, the inelastic scattering time, τ_ϕ, begins to decrease, shortening electron phase coherence length. Experiments have studied the phase coherence time for hot electrons in ballistic systems [Yacoby, *et al.*, (1991)] and found τ_ϕ to agree well with the theoretical prediction [Giuliani and Quinn, (1982)]

$$\frac{1}{\tau_\phi} = \frac{E_f}{4\pi\hbar}\left(\frac{\Delta}{E_f}\right)^2\left[\ln\left(\frac{E_f}{\Delta}\right) + \ln\left(\frac{2Q_{TF}}{k_f}\right) + \frac{1}{2}\right] \quad \text{(cgs units)}, \tag{3.6}$$

where Δ is the energy above the Fermi energy, $Q_{TF} = 2me^2/\varepsilon\hbar^2$ is the 2D Thomas-Fermi screening wave vector, and m is the effective electron mass in GaAs. In order to avoid these effects, a bias current should be chosen small enough so that $eV < kT$, where V is the voltage generated by applying the bias current across the quantum point contact. Experimentally, we have found that $eV \sim 5kT$ before any heating effects can be observed, but we conservatively choose I_{bias} such that $eV \sim kT$. To give some idea of the numbers involved, for a quantum point contact transmitting one transverse mode (R = 12.9 kΩ) at a temperature of 100 mK, eV = kT when I_{bias} = 1 nA.

In general, we attempt to avoid heating our samples with the bias current, but there are instances where this is not the case. If we wish to study a quantum interference effects as a function of τ_ϕ, one means of accomplishing this is to take a temperature series. Since

such series are time-consuming, we can instead shorten τ_ϕ by applying an additional dc bias voltage on top of our small ac excitation. As shown in Eq. (3.6), these hot carriers dephase more quickly than those at the Fermi energy. Experimentally, all that we require to do this are a summing amplifier and an adjustable voltage source. Unfortunately, these measurements tend to be noisier than those without the dc bias, so the temperature series is still the preferred method for varying τ_ϕ. Sometimes, however, all we wish to do is suppress the quantum interference effects; for example, in order to distinguish a classical effect from a quantum interference effect. In this case, a large-amplitude ac bias current can be used. If the current is chosen such that the average carriers are injected about 1 mV above the Fermi energy, quantum interference effects can be almost completely quenched without measurably altering the elastic scattering time. Noise is not a problem in these measurements, because the signals involved are very large.

Fig. 3.1 contains a schematic of the circuit used to measure the small signals involved in these experiments. A dc measurement would not able to distinguish the signal from the background; by performing a low-frequency ac measurement, we can take advantage of the excellent background noise rejection provided by the lock-in amplifier. The frequency chosen (11 Hz) is many orders of magnitude slower than any of the timescales involved in the electron transport, so much of the physics is unchanged from a dc measurement. The 11 Hz frequency also allows a bandpass filter to block the known noise frequencies present in the laboratory, including the 60 Hz running in all power lines. Typically, our samples have a pair of ohmic contacts on each side, which allow us to perform 4-probe measurements of the sample resistance. The 4-probe technique eliminates the resistance of the 1 kΩ blocking resistors and the resistance of the ohmic contacts themselves.[20] We obtain the sample resistance through dividing the voltage difference measured across on pair of ohmic contacts, by the bias current applied across the other pair

[20]If the background were constant, it could be easily subtracted from a 2-probe measurement. The 4-probe technique is useful in removing any background magnetoresistance associated with the leads or ohmic contacts.

of contacts. The bias current is generated by placing a large[21] (100 MΩ) current-limiting resistor in series with an ac signal generator. This sine-wave generator could be external (e.g. Krohn-Hite model 4400A, Avon, MA) or the internal signal generator of the lock-in. This current is driven across the sample, with one side (I-) grounded. The voltage difference across the sample is first amplified by a PAR 113 pre-amp[22], and then transmitted single-ended to a PAR 124A lock-in amplifier (E.E.&G., Princeton, NJ). The 113 and 124A work well for low-noise cryogenic measurements, because they do not emit nearly as much high-frequency noise as newer digital models do.[23] The output from the lock-in is recorded by a digital voltmeter (Fluke model 8842A, Everett, WA), and shipped to a Macintosh computer through an IEEE interface bus. A Labview program called "Read n DMMs" is used to automate the data acquisition.[24]

Since we are dealing with such small signals, precautions against noise need to be taken. In order to shield the signal, the entire body of the cryostat is grounded, as are the cases of all electronics and Pomona boxes used in the circuit. In addition, all signals are carried in coaxial cables with grounded shields. To avoid ground loops, we are careful to make sure that all of these share a single common ground. Inductive pick-up is minimized by using twisted pairs of coax and attempting to minimize the length and motion of these cables.[25] All of the coaxial cables connected to the sample are mated at the top of the

---

[21]The current limiting resistor must be orders of magnitude larger than the sample resistance for the signal generator to behave like a current source.

[22]The lowest noise performance for the PAR 113 is obtained while it is running on its battery power supply.

[23]Unfortunately, both models have been discontinued and replaced by these evil successors.

[24]First written by Alex Rimberg, this program has been subsequently modified by Doug Mar and then Carol Livermore. It is described in Doug's thesis [Mar, 1994]. Recently, Carol has built a system that allows much faster automated data acquisition.

[25]The Kelvinox is kept in a shielded room with a fan. During one of Chuck Black's measurements, he noticed a low-frequency source of noise in his data that only appeared when the fan was on. It was due to a coax line being oscillated by the wind from the fan. The moral of this anecdote is that signal lines should be kept short and tied down.

cryostat using homemade "switcher boxes." These are medium-sized (6"x3"x1.5") Pomona boxes (ITT Pomona Electronics, Pomona, CA) containing 24 bnc receptacles. Signals pass from the bnc's to a master 24-pole/2-position make-before-break ceramic switch (CRL) that may be used to ground or float all of the leads connected to the sample.[26] As metal gates tend to blow up when sudden voltage changes occur, the sample should be grounded with this switch only after all applied gate voltages are turned off. From the master switch, each line passes to a single-pole/3-position anti-static switch (C&K) that may ground the lead, float the lead, or place it on a bus line. From these individual switches, each line is attached to the male Fischer connector that mates the switcher box to the internal cryostat wiring. By placing all of these connections in a shielded box that connects rigidly to the cryostat, we hope to minimize pick-up noise in our signals.

Voltage-Biased Measurements

During Coulomb blockade and large fluctuation quantum interference experiments, it is more natural to voltage-bias than to current-bias the sample during measurements. As the term implies, when we voltage-bias, the voltage drop across the sample is fixed, despite the fact that the conductance of the device can change by several orders of magnitude. In current-biasing such a sample, if we were to select a bias current small enough to avoid heating the sample when its resistance is high, the voltage across the sample would become immeasurably small when the sample resistance is low. This is especially inconvenient, because these conductance maxima are typically the region in which we are most interested.

The circuit we use in our Coulomb blockade measurements is very similar to that shown in Fig. 3.1, except that the current-limiting resistor is replaced by a voltage

[26]The standard configuration is 18-pole/2-position. We had three 24-pole versions custom built by ECCO electronics (Brooklyn, NY).

attenuator ($x10^{-5}$) and the voltage pre-amp is replaced by a current pre-amp (Ithaco 1211, Ithaca, NY). Using a two-probe, low-frequency lock-in technique, we determine the sample conductance through dividing the measured current by the voltage applied across the sample. Since this is a two-probe measurement, we are actually measuring the series conductance of the sample, the leads, and the r.f. blocking resistors, so it is important to know the values for the latter two, in order to correct for their presence. We apply a 10 μV excitation across the sample by attenuating the 1 volt signal from the function generator. Since the attenuated voltage is quite small, the signal should be shielded as well as possible following attenuation. This is best done by attaching the Pomona box housing the attenuator directly to the switcher box on the cryostat. In addition, to shield the small current exiting the cryostat, it is best to attach the input of the Ithaco 1211 directly to the switcher box. If this is not possible, a cable no longer than a foot should be used.

Electrostatic Gate Voltage Control

All of the devices presented in this thesis are defined by applying a negative bias voltage to metal gates on the sample surface. In some experiments, we want this applied voltage to remain constant so that the shape of the device remains stable while some external parameter (e.g. magnetic field) is varied. In other cases, we wish to study the effect of changing the potential applied to the gate. In order to perform both of these functions, I designed and built two adjustable voltage supply boxes. Each box has an output capable of producing a voltage that can be ramped either up or down at an adjustable rate, while the other 3 (or 7 in the later model) outputs provide adjustable fixed voltages. Obviously, we need these supplies to be low-noise and very stable. As a reference for future box builders, I will briefly explain the design of these supplies.

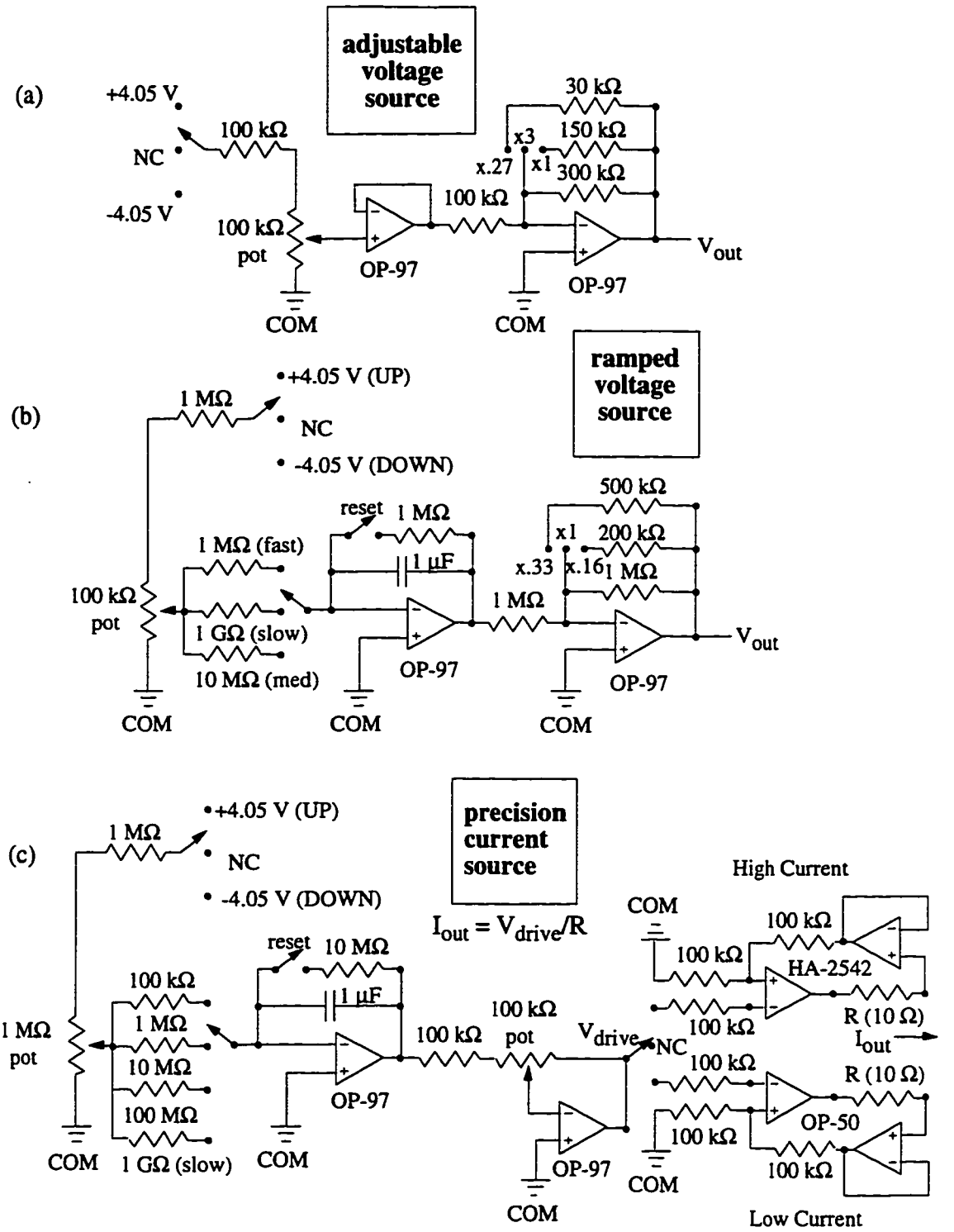

Fig. 3.7 a) Circuit schematic for the adjustable voltage sources. b) Circuit schematic for the ramped voltage source. The voltage boxes contain 1 ramped source and 3 (or 7) adjustable voltages. c) Circuit schematic for the low-noise current source. A high output, low output, or no current stage may be chosen. All op amps are powered by rechargeable 6V batteries (not shown).

Fig. 3.7 shows a circuit schematic for both the ramped and the adjustable output voltages.[27] These supplies are battery-powered to eliminate the noise inherent to any line-powered circuit. In order to improve the stability of the supplies, two pairs of batteries are used. Large ± 6V gel cells (Yuasa) supply the op amps with their power. Powering the op-amps is by far the biggest battery drain in the supplies; the smaller ± 4.05V batteries located inside the box are only drained by the small currents drawn through the initial voltage divider in the circuit (which explains the large resistances chosen for the divider). Over the course of a day, the gel cells may run down a little, but this will not be reflected in the output voltage unless it is near a rail. Rather, the output is determined by the internal batteries that set the programming voltage sent to the first op amps in the circuits. To improve the stability of this programming voltage, mercury batteries[28] (Duracell TR113R) whose voltage remains very flat over the entire discharge cycle were used. In addition to being battery-powered, the output voltage noise can be reduced by using low-noise op amps. I chose model OP-97 (Analog Devices) for their combination of low noise and low power consumption. With these op amps, the gel cells can power the box for a week without recharging. The OP-97 also has excellent bias and offset current characteristics which allow very slow ramp rates to be achieved without the need to compensate for these potential sources of drift. Although they are small, the offset and bias currents will cause the output voltage to drift slowly when the ramper circuit is in the "hold" position. The adjustable voltages should be used when a fixed voltage is needed. In the ramping circuit, a polycarbonate capacitor was chosen for its low noise. Finally, high-quality 10-turn

---

[27]The output voltage supplies are referred to as the "magic ramper boxes" by Fred Waugh. Arthur C. Clarke wrote that any sufficiently advanced technology would be indistinguishable from magic were a more primitive civilization to be confronted with it. Considering that the group was using a 50-year-old stepper motor attached with masking tape to a potentiometer knob to ramp voltages prior to their construction, theses simple boxes would seem rather sophisticated.

[28]Mercury batteries have been outlawed since these supplies were built. The lithium batteries #PC113 that have replaced them have a less-flat discharge curve. I believe the PC stands for politically correct.

potentiometers (Clarostat, #73JA), were chosen as cheaper models tend to be noisy and unstable.

The adjustable fixed voltage outputs drift less than 100 μV per hour, and have an output voltage noise of under 10 μV (measured over a 300 kHz bandwidth). In order to minimize the high-frequency noise applied to the gates with these supplies, low-pass RC filters ($\tau_c = 0.1$ sec) are recommended. These filters also suppress the digital noise from the DVMs which are often attached to monitor the output voltages sent to the gates.

Magnetic Field Control

Many of our transport measurements study the sample resistance as a function of the applied perpendicular magnetic field. As described earlier, samples may be mounted in the center of superconducting solenoids in both the ^{3}He and Kelvinox dewars. This section will briefly describe magnetic field measurement and control in our experiments.

As shown schematically in Fig. 3.1, our magnet is connected in series with a power resistor (Dale) and a bipolar power supply (Kepco BOP 20-20, Flushing, NY) capable of delivering 20 Amperes across the circuit. The output of the Kepco supplies can be programmed by an external voltage. The calibrations between current and magnetic field in the magnets are known, allowing a calculation of the field strength from the voltage drop measured across the power resistor. Due to trapped flux, zero current through the resistor does not equate to zero applied field. There is a random offset (roughly equal to ± 1 mT) between the two for any given cooldown. For many of the weak localization measurements described in later chapters, it is important to know the zero field location exactly. By using a bipolar power supply, we may sweep the magnetic field through zero, and use the location of the weak localization peak to precisely determine the value of this

offset. If larger bipolar currents are required, two Kepco supplies can be used in a master-slave configuration[29] to produce 40 A.

As you might expect from a current source plugged into the wall, the Kepco supplies output a fairly large amount of 60 Hz voltage noise. We feared that this noise could add an ac component to the applied field, which might smear very narrow magnetoresistance features. The magnet has an inductance, L, equal to 20 Henries. If the voltage noise on the output is described by

$$V_n = V_0 \sin(\omega t), \text{ then} \tag{3.8a}$$

$$I_n = \frac{V_0 \cos(\omega t)}{\omega L} \tag{3.8b}$$

would be the resulting current noise in the magnet. For a Kepco output whose 60 Hz noise has an amplitude of 100 mV, noise currents with 0.01 mA amplitude (~ 3 μT field variation) are expected.

Almost none of our experiments are sensitive to such small magnetic fields, but for those experiments that might be (like the bulk weak localization described in Chapter 4), we built a battery-powered current source. The schematic for this circuit is shown in Fig. 3.7.c. The first stage is almost identical to the ramper circuit described earlier, except that the maximum value of the output voltage (V_{drive}) can be continuously attenuated. Following the attenuator, a 3-position switch connects to drive voltage to either a low-output (±14 mA maximum) current source, a high-output (±100 mA) current source, or to no connection. The two current sources [Horowitz and Hill, (1989)] are identical except for the op amps used. The low-output source contains OP-50 (Analog Devices) low-noise op amps, while the high-output source uses slightly noisier HA-2542 (Harris

[29]This should not be confused with the situation in which a younger graduate student is working with a senior student on a project.

Semiconductor) op amps capable sourcing higher output currents. Experimentally, we find no observable difference between weak localization traces taken with the Kepco and with our low-noise current source. Typically, we use the Kepco in our measurements, and program it with the drive voltage output stage of our current source.

A final consideration in magnetoresistance measurements is selecting a sweep rate for the magnetic field. For most of the experiments presented in this thesis, the field is swept so slowly that eddy current heating is not a concern. We are more concerned that sweeping too quickly will round narrow magnetoconductance features. The sweep rate is usually limited by the time constant of the lock-in. In order to avoid attenuation, the rate should be set so that at least five time constants are required to sweep through the feature. Experimentally, we always vary the sweep rate to check that we are not smearing important features by sweeping too quickly.

Chapter 4

Measurement of the Phase Coherence Length

4.1 Introduction

The phase coherence length, ℓ_ϕ, is important in determining the length scale over which quantum interference effects may be observed. For the diffusive electron transport described in this chapter, the phase coherence length is related to the phase coherence time, τ_ϕ, by the diffusion coefficient, $\ell_\phi = (D\tau_\phi)^{1/2}$. A determination of ℓ_ϕ is an important precursor to the quantum interference experiments presented in this thesis. To a great extent, the phase coherence length establishes the size and temperature requirements of these experiments. In addition, knowledge of this length is crucial to understanding the results of our interference measurements.

In this chapter, we use the weak localization effect in narrow wires to measure the electron phase coherence time for our two-dimensional electron gas system. Previous experiments in low-mobility 2DEGs measured the phase coherence time in wide two-dimensional channels [Zheng, *et al.*, (1986), Choi, *et al.*, (1987a)]. As will be explained later in this chapter, such experiments are very difficult in much higher mobility electron gas systems. If the wire is made narrow enough so that diffusion is effectively one-dimensional, the weak localization effect is enhanced, allowing for a determination of τ_ϕ in these clean systems. Several groups have used one-dimensional wires to study τ_ϕ in high-mobility 2DEGs [van Houten, *et al.*, (1988a); Kurdak, *et al.*, (1992)], but their experiments were not optimized for a quantitative determination of the phase coherence time. The measurements reported in this chapter greatly improve on these earlier results in this respect.

The next section of this chapter will outline the theory of weak localization in quantum wires. Both one- and two-dimensional cases will be treated. The majority of the chapter will focus on a series of experiments that measure the phase coherence time in one-dimensional quantum wires. The dephasing rates are measured as a function of channel width and temperature. In these experiments, excellent agreement is found between the measured dephasing rates and the predictions of theories based on electron-electron interactions. The final section of the chapter will briefly discuss our attempts to measure weak localization in high-mobility, two-dimensional wires.

4.2 Theory of Weak Localization in Quantum Wires

The weak localization effect is a quantum mechanical correction to the classical (Drude) resistance. The theory of weak localization has been formulated in several ways. The most intuitive of these is the Feynman path integral formulation [e.g. Chakravarty and Schmid, (1986)]. In this description, weak localization arises from quantum interference between time-reversed pairs of backscattered trajectories. As a result of time-reversal symmetry, these backscattered trajectory pairs must interfere constructively, increasing the probability of backscattering; this results in a decrease in the conductance from its classical value.

The magnitude of the weak localization correction is proportional to the number of phase-coherent backscattered trajectory pairs. The phase coherence length exponentially suppresses the contribution of long trajectories. As a result, if the channel width W is much larger than $(2D\tau_\phi)^{1/2}$, the rms displacement of a electron traveling for a time τ_ϕ with diffusion coefficient D, the channel walls will not affect the probability for return to the origin.[1] Conversely, if $W << (2D\tau_\phi)^{1/2}$, the channel walls will limit lateral diffusion,

[1]In the channels, we assume that the electron travels diffusively along a channel whose length, L, is much greater than both ℓ (the mean free path) and ℓ_ϕ. In such channels, backscattering results from elastic collisions with impurities. In later chapters, we will discuss coherent backscattering due to ballistic trajectories reflected from device walls.

effectively creating a one-dimensional channel. In this one-dimensional limit, the expression for the weak localization correction to the channel conductance is [Beenakker and van Houten, (1991)]:

$$\delta G_{WL} = -\frac{2\hbar}{m} G \int_0^\infty e^{-t/\tau_\phi}\left(1-e^{-t/\tau}\right)\left[W^{-1}(4\pi Dt)^{-1/2}\right]dt$$
$$= -\frac{2e^2}{h}\frac{D^{1/2}}{L}\left[\tau_\phi^{1/2} - \left(\frac{1}{\tau_\phi}+\frac{1}{\tau}\right)^{-1/2}\right] \qquad (4.1)$$

In the integral, the factor e^{-t/τ_ϕ} is the long-time cutoff imposed by the finite phase coherence length. The second factor is an *ad hoc* correction that takes into account the fact that an electron cannot contribute to weak localization before it is backscattered.[2] The final bracketed expression is the fraction of electrons moving diffusively in a one-dimensional channel that return to their origin in a time t. In the two-dimensional limit, this fraction is independent of the channel width, and the bracketed expression in Eq. (4.1) is replaced with $(4\pi Dt)^{-1}$. By constraining the lateral diffusion, the channel walls enhance the weak localization effect. From Eq. (4.1) we see that in one-dimension, $\delta G_{WL}/G \sim (\ell_\phi/W)(1/k_f\ell)$ — a factor ℓ_ϕ/W times larger than the 2-D limit.

Experimentally, the easiest way to observe weak localization is by applying a magnetic field perpendicular to the sample. In the absence of the field, time-reversed pairs of backscattered trajectories always interfere constructively. When the field is applied, a phase difference ϕ is created between the time-reversed pairs:

$$\phi = 2\frac{2\pi\Phi}{\Phi_0} \equiv \frac{2S}{\ell_m^2}, \qquad (4.2)$$

---

[2]There is no firm basis for this *ad hoc* assumption. Fortunately, this assumption has almost no effect on δG_{WL} (and, hence, on our measurement of τ_ϕ) when $\tau_\phi >> \tau$.

where Φ is the magnetic flux enclosed by the loop, $\Phi_0 = h/e$ is the flux quantum, S is the area enclosed by a backscattered loop, and $\ell_m \equiv (\hbar/eB)^{1/2}$ is the magnetic length.[3] At sufficiently large magnetic fields, all phase-coherent backscattering is suppressed, and the magnetoconductance saturates at its classical value. This allows the magnitude of the weak localization correction to be determined:

$$\delta G_{WL} = G(0) - G(B_{saturated}). \tag{4.3}$$

After δG_{WL} is found, τ_ϕ can be computed using Eq. (4.1). However, as will be discussed later in this chapter, other magnetoresistance phenomena can sometimes make it difficult to accurately establish a value for $G(B_{saturated})$. In this case, the shape of the magnetoconductance dip centered at zero field can be fit to Eq. (4.4) (described below) to determine τ_ϕ.

The weak localization correction is the result of many trajectories enclosing a large distribution of loop areas. As the magnetic field is increased from zero, the trajectories enclosing the largest areas will be the first to dephase. Since the area enclosed by a trajectory scales with the time required to traverse the loop, the applied field introduces an additional long-time cutoff, τ_B, to the integral in Eq. (4.1). B_c, the characteristic field at which $\tau_B = \tau_\phi$, is reached when ϕ, the average phase shift for the trajectories contributing to localization, is unity. The total dephasing rate in the presence of a magnetic field equals $1/\tau_B + 1/\tau_\phi$. In Eq. (4.1), replacing $1/\tau_\phi$ with this sum gives the field-dependent expression for the weak localization correction to conductivity [van Houten, *et al.*, (1988a)]:

[3]The initial factor of two in Eq. 4.2 is there because the flux, Φ, is encircled in opposite directions by the time-reversed trajectories, and ϕ is the phase difference between the *pair*.

$$\delta G(B) = -\frac{2e^2 D^{1/2}}{hL}\left[\left(\frac{1}{\tau_\phi}+\frac{1}{\tau_B}\right)^{-1/2} - \left(\frac{1}{\tau_\phi}+\frac{1}{\tau_B}+\frac{1}{\tau}\right)^{-1/2}\right]. \qquad (4.4)$$

In the two-dimensional limit, the average area enclosed by loop traversed in a time τ_B equals $2D\tau_B$. Equating the resulting phase shift to unity, we have

$$\tau_B = \ell_m^2/2D. \qquad (4.5a)$$

Since, by definition, $\tau_B = \tau_\phi$ at B_c, the characteristic field in 2-D is given by

$$B_c = \frac{\hbar}{e}\frac{1}{2\ell_\phi^2}. \qquad (4.5b)$$

The characteristic field for the weak localization effect is broadened in the one-dimensional limit where $W << \ell_\phi$. There are actually two one-dimensional regimes that must be considered. In the first regime (fully diffusive), motion between the walls and along the channel is diffusive ($W >> \ell$). In this case [Altshuler and Aronov, (1981)],

$$\tau_B = \frac{3\ell_m^4}{W^2 D} \text{ and } B_c = \frac{\hbar}{e}\frac{\sqrt{3}}{W\ell_\phi}; \qquad (4.6)$$

note that the characteristic field in Eq. (4.6) is roughly a factor of ℓ_ϕ/W larger than in the two-dimensional limit.

The other one-dimensional regime is quasi-ballistic. Here motion along the channel is diffusive, but electrons travel ballistically between the channel walls ($W << \ell$), allowing the characteristic field for weak localization to be further enhanced by the flux cancellation effect. In this quasi-ballistic limit, backscattered trajectories self-intersect, creating smaller

loops which enclose flux in both a positive and negative sense. Because it is the net flux which appears in Eq. (4.2), a larger applied field is required before time-reversal symmetry is broken. In fact, in the absence of impurity collisions,[4] backscattered trajectories would enclose zero net flux.

No exact expression for τ_B exists for this ballistic case, but its value in the limits of weak and strong magnetic fields can be found [Beenakker and van Houten, (1988a)]. In the weak field regime ($W\ell << \ell_m^2$), trajectories must experience many impurity collisions before they enclose sufficient flux to dephase. In this limit,

$$\tau_B^w = \frac{C_1 \ell_m^4}{W^3 v_f} \text{ and } B_c = \frac{\hbar}{e}\frac{1}{W}\left(\frac{C_1}{W v_f \tau_\phi}\right)^{1/2}. \tag{4.7}$$

The coefficient C_1 in these expressions depends on the nature of the boundary scattering; $C_1 = 4\pi$ for diffuse boundary scattering, and $C_1 = 9.5$ for specular scattering. In the strong field limit ($W\ell >> \ell_m^2$), only a single impurity collision is required to dephase the trajectories. Here,

$$\tau_B^s = \frac{C_2 \ell_m^2 \ell}{W^2 v_f} \text{ and } B_c = \frac{\hbar}{e}\frac{C_2 \ell}{W^2 v_f \tau_\phi}, \tag{4.8}$$

with $C_2 = 3$ for diffuse boundary scattering and 24/5 for specular scattering. Experimentally, most of the weak localization peak is located between these two regimes. Numerical simulations by Beenakker and van Houten find a good interpolation to be the sum:

$$\tau_B = \tau_B^w + \tau_B^s. \tag{4.9}$$

[4]In this case, non-specular boundary scattering could lead to backscattering.

4.3 Experiments in a Single One-Dimensional Channel

As the work in single channels has been published previously [Katine, *et al.*, (1994); Berry, (1994)], this section will only briefly summarize the results of those experiments. Special attention will be given in this section to the effect of universal conductance fluctuations on magnetoconductance in narrow channels. We will also emphasize the differences between these early measurements, and the later experiments described in Section 4.4 of this chapter.

All of the channel experiments were performed using the wafer BW1, which has an electron gas 420 Å beneath the surface. Shubniknov-de Haas oscillations show the bulk sheet density to be ~3.9×10^{15} m^{-2}, and the bulk resistivity of the electron gas is roughly 40 Ω/sq.[5] From these measurements, the calculated electron mobility $\mu = 400{,}000$ cm^2/Vs, elastic scattering time $\tau = 15$ ps, and the mean free path $\ell = 4.1$ μm.

The one-dimensional channel in these measurements is defined by a split-gate technique. The channel is 100 μm long, and has a lithographic width of 770 nm.[6] As will be discussed in the next section, the actual width of the channel in the electron gas is likely narrower than this. The sample was mounted perpendicular to the magnetic field in the ^{3}He cryostat, and weak localization measurements were made between 4.2 K and the base temperature of the cryostat. It is important to note that these data were taken before the rewiring of the ^{3}He probe described in Chapter 3. As a result, the base temperature was only 420 mK, and there was no filtering in the sample leads.

Fig. 4.1 shows a base temperature trace of the differential conductance of the 770 nm wide channel plotted versus magnetic field. Note that in addition to the weak localization dip centered around zero field, there are other smaller amplitude

[5]There can be slight variations in the sheet density and resistivity in different thermal cycles.

[6]A 1230 nm channel was also studied, and found to have very similar behavior.

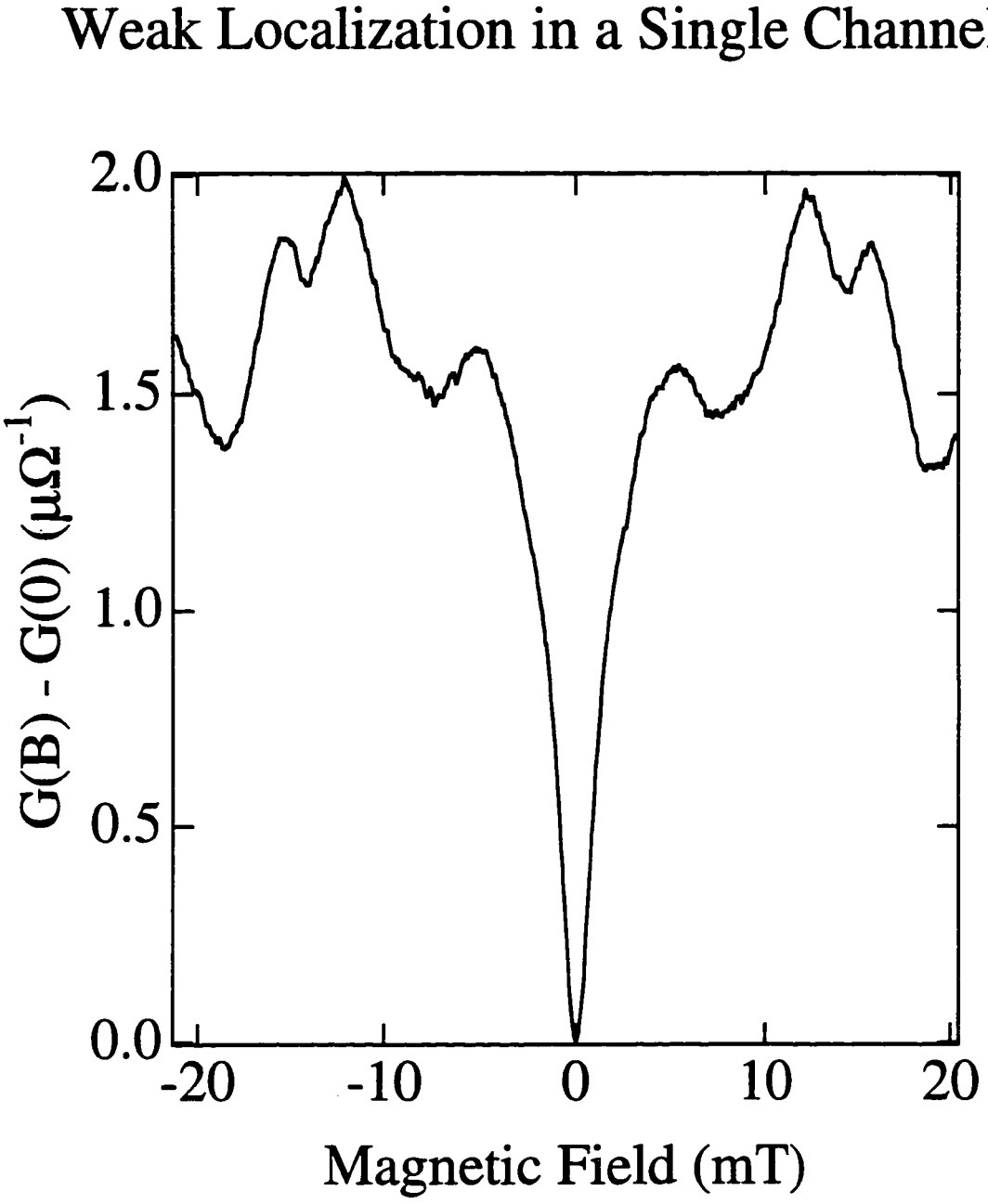

Fig. 4.1 Differential magnetoconductance in a single 100 μm long channel at 420 mK. Note the UCF whose amplitude is ~20% that of the localization feature.

magnetoconductance fluctuations present. These features are reproducible within a given thermal cycle, and are a manifestation of universal conductance fluctuations (UCF) [Lee and Stone, (1985)]. As expected for UCF, the fluctuations are sensitive to the particular impurity potential in the channel, and they are reshuffled following thermal cycling of the sample. Other measurements of UCF in narrow GaAs/AlGaAs channels produce results very similar to our own [Thornton, *et al.*, (1987)].

It is clear from the data in Fig. 4.1 that the amplitude of these fluctuations is smaller than the ~$0.7e^2/h$ value predicted for a long channel at zero temperature. This is a result of both the thermal averaging and the finite phase coherence length which exist at this temperature. For a channel in which $L > \ell_\phi$, the channel can be thought of as L/ℓ_ϕ independently fluctuating channels connected in series,[7] causing the amplitude of the conductance fluctuations to decay as $(\ell_\phi/L)^{3/2}$ [Beenakker and van Houten, (1991)]. The picture is somewhat more complicated than this because of thermal averaging. The universal conductance fluctuations are the result of interference from distinct electron trajectories. If these different trajectories are traversed in a time t with an energy difference $\approx kT$ resulting from thermal broadening of the Fermi surface, then a phase shift $\delta\phi \approx tkT/\hbar$ will develop between the trajectories.[8] The characteristic time scale for this dephasing τ_T occurs when $\delta\phi = 1$. The thermal length ℓ_T is defined as the distance the electron travels in this time; i.e. $\ell_T = (\hbar D/kT)^{1/2}$. In a regime such as ours where ℓ_T is less than or comparable to ℓ_ϕ, the ratio of the amplitude of the UCF to that of the weak localization correction is approximately [Beenakker and van Houten, (1988b)]:

---

[7]The weak localization correction is centered at zero field for all these sub-channels, and as such is not subject to averaging.

[8]This thermal dephasing does not apply to weak localization, since localization results from the interference of pairs of time-reversed trajectories which experience identical thermal fluctuations.

$$\frac{\delta G_{UCF}}{\delta G_{WL}} \approx \frac{\sqrt{6}}{2}\left(\frac{\ell_\phi}{L}\right)^{1/2} \frac{\left[1+\frac{9}{2\pi}\left(\frac{\ell_\phi}{\ell_T}\right)^2\right]^{-1/2}}{\left[1-\left(1+\frac{\tau_\phi}{\tau}\right)^{-1/2}\right]}. \qquad (4.10)$$

The phase coherence time calculated from the width of the weak localization feature in Fig. 4.1 is approximately 70 ps. Inserting this value into Eq. (4.10) yields a ratio of ≈ 0.21, which agrees well with our experimental observations. Measurements were also made on single narrow channels only 15 μm long. It was not possible to determine τ_ϕ with great accuracy in these channels, because the UCF and weak localization were of comparable amplitude.

The UCF are the main source of uncertainty in the phase coherence time deduced from the single channel measurements. In order to use Eq. (4.3) to compute τ_ϕ from the amplitude of δG_{WL}, both zero-field and baseline values for the conductance are required, but the UCF limit the accuracy to which these conductances are known. Alternatively if τ_ϕ is extracted from a fit to the low-field shape of the magnetoconductance dip (Eq. 4.4), the presence of UCF (whose field scale is comparable to that of weak localization) may compromise the value of τ_ϕ measured in this way. The solution to this problem is to eliminate the UCF through additional averaging. Results from such experiments will be discussed in the following section.

4.4 Experiments in an Array of One-Dimensional Channels

According to Eq. (4.10), a 1-D channel would have to be 2 mm long in order for the UCF amplitude to be less than 5% that of the weak localization correction. Due to limitations of the SEM, it is not possible to fabricate a single channel of that length without compromising the lithographic quality of the channel boundary. In several other

experiments described in this thesis, a gate voltage averaging technique is employed. When the bias voltage applied to the split-gate defining a channel is changed by an amount larger than the correlation voltage, V_c, the pattern of the UCF is reshuffled. If we were to average the data from a single channel taken at 20 uncorrelated voltages, the UCF could be suppressed below the 5% level. This technique has the obvious drawback that the data would take 20 times as long to acquire. In addition, the correlation voltage is large enough so that the channel width and the electron sheet density in the channel would change dramatically over a $20V_c$ range.

In the experiments described in this section, simultaneous measurements were performed in an array of 20 identical channels. As expected, a significant reduction in the amplitude of the UCF was observed, allowing a more accurate determination of the phase coherence length to be made. The additional filtering present in these measurements appears to have increased the value of τ_ϕ compared to that determined from experiments in single channels. Because the UCF grow dramatically at low temperature, dilution refrigerator measurements on a single channel would have been pointless. With the array, we were able to extend our measurements down to sample temperatures of 100 mK, where an apparent low-temperature saturation of the phase coherence length was observed. Finally, we will describe a series of measurements in which the effect of varying the gate voltage applied to the channels was studied.

Sample Design

The data in this section come from an array patterned on sample BW1.UU. The properties of this wafer were described in the previous section. Fig. 4.2a shows a photo of the entire sample. On the far right, there is a single 1 mm long x 27 μm wide channel used for the 2-D localization experiments described in Section 4.5. Though they are too narrow to be visible in this photograph, there are 25 105 μm long x 800 nm wide channels

Array of One-Dimensional Channels

a)

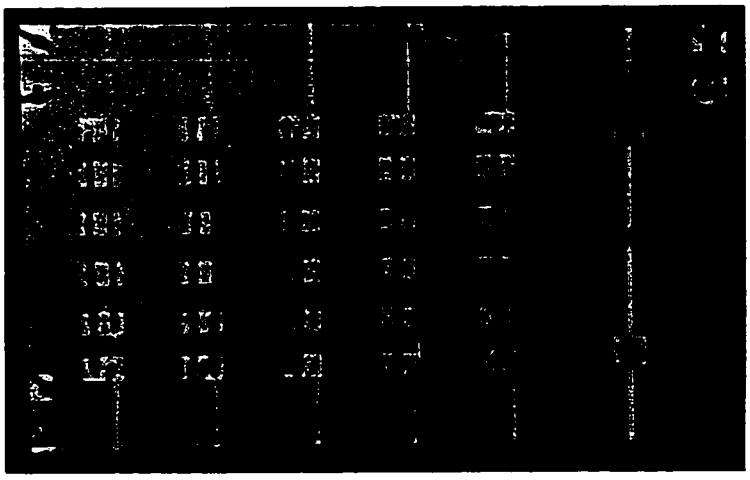

b)

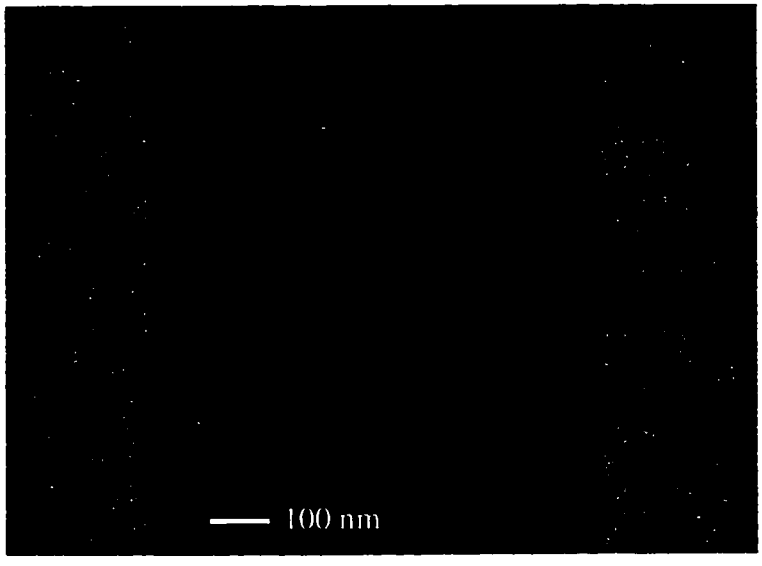

Fig. 4.2 a) Photo of sample BW1.UU. On the far right is the single 1 mm x 27 μm 2-D channel. To the left is the 5 x 5 array of 1-D channels. The channels (which are too narrow to be seen at this magnification) are located between the bonding pads, and are aligned parallel to the 2-D channel. Note that the second column from the right is not wirebonded to the chip carrier. b) SEM photo taken at x60,000 mag. of a channel segment (rotated 90 deg. from its orientation in (a)). The channels are 800 nm wide with very smooth boundaries.

patterned on the remainder of the chip. There are 5 columns in series. Each column contains 5 parallel channels, separated from one another by 500 μm. Four-probe current-biased resistance measurements were made using the ohmic contacts on the edges of the sample. When a negative bias voltage is supplied, the electron gas underneath the metal gates connecting the parallel channels is depleted, forcing electrons to travel through one of the five channels. Bonding pads are located between the parallel channels, allowing electrical contact to the entire array to be made without the need for a complicated trilayer structure [e.g. Yang, (1995)]. The five columns are laterally spaced 500 μm from one another, so there should be no correlation effects between the columns.[9]

Fig. 4.2b is an SEM photo of a channel from the array.[10] Using the SEM, the lithographic width of this channel was measured to be 800 ± 30 nm. An AFM was also used to insure that the Cr layer (which would be invisible under the SEM) did not extend further than the Au. To achieve uniform channel width over the entire array, the filament was allowed to stabilize for over an hour before the pattern was written. Spot checks of several channels found no detectable width variation. The geometry of our device allows each column of channels to be measured separately, but the channels may not be measured individually. The behavior of the four individual columns (resistance, depletion voltage, magnetoconductance, etc.) was virtually identical, which is an excellent indication that there were no anomalies in any of the 20 channels measured.

Although the surface gates that define the channels have a lithographic width of 800 nm, the channel defined in the 2DEG is likely narrower than this. As discussed later in this chapter (see Fig. 4.6), the depleted region of the electron gas extends an additional distance δ from the edge of the gate, meaning the actual channel width is given by

---

[9]Due to a short between the surface gates and the electron gas, one column of channels was not used; in the photo, this is the column not wirebonded to the chip carrier.

[10]This and all other imaging of the array was performed after the measurements were taken. Such examination may locally damage the electron gas.

$$W = W_{lith} - 2\delta. \tag{4.11}$$

Through increasing the negative bias voltage applied to a channel gate, it is possible to increase δ, thereby narrowing the channel.

Boundary Roughness and Channel Width

In channels such as ours where lateral motion is ballistic, the nature of the boundary scattering strongly influences the amplitude of the weak localization correction. This is due to the impact of boundary scattering on the diffusion coefficient. Recall from Eq. (4.4) that the size of the weak localization correction to conductivity is proportional to $D^{1/2}$. For purely specular boundary scattering, the diffusion coefficient is unchanged from its bulk value ($D = v_f\ell/2$), because momentum along the channel is conserved during boundary collisions. Conversely, for purely diffuse boundary scattering, D is reduced. In the limit that $\ell >> W$ [van Houten, *et al.*, (1988b)],

$$D = (v_f W/\pi)\ln(\ell/W). \tag{4.12}$$

For the parameters of our narrow channels, purely diffuse boundary scattering would reduce D by over a factor of 5 from its bulk value.[11]

In order to correctly calculate τ_ϕ from the weak localization effect, it is essential that we know the nature of the boundary scattering in our channels. There is good reason to expect the boundary scattering to be specular. In general, reflections from potential boundaries will be specular if the lengthscale of surface roughness is smaller than the wavelength of the reflected particle. Great pains were taken to achieve the lithographically

[11] In the quasi-ballistic regime, the nature of the boundary scattering also affects the value of τ_B. The effect, however, is quite small as the diffuse and specular coefficients appearing in Eqs. (4.7) and (4.8) are very close to one another.

smooth surface gates pictured in Fig. 4.2b for this reason. In addition, previous experiments have demonstrated reflections from electrostatically-defined boundaries similar to our channel walls to be $\geq 95\%$ specular [Thornton, *et al.*, (1989)].

The classical resistance of the channel can be used to place a lower bound on the specularity of the channel. Since the resistivity of the channel is inversely proportional to the diffusion coefficient, Eq. (4.12) may be rewritten as,

$$\rho_d = \frac{\pi}{2}\rho_0 \frac{\ell}{W}\frac{1}{\ln(\ell/W)}, \tag{4.13}$$

where ρ_d is the channel resistivity assuming diffuse boundary scattering, and $\rho_0 = m/(e^2 n_s \tau)$, is the resistivity in the fully specular limit. The sheet density in the channels can be directly measured from Shubnikov-de Haas oscillations, leaving τ as the only unknown in the formula for ρ_0. Although the slightly reduced sheet density in the channels may lower τ, an lower bound may be placed on ρ_0 by assuming the bulk value for the scattering time still holds in the channel. To estimate the specularity, we use a simple model in which boundary collisions are fully specular with probability, p, and fully diffuse with probability, 1-p [Fuchs, (1938)]. In this model, the resistance of a single channel is

$$R = \frac{L}{W}[\rho_0 p + \rho_d(1-p)]. \tag{4.14}$$

In BW1, full depletion of the electron gas beneath a gate is measured to occur at ~ -0.33 V. With the array biased at -0.400 V, the resistance per channel is 7,250 Ω, and $n_s = 3.74\text{x}10^{15}$ m^{-2}. Although there is almost certainly a non-zero depletion width, the most conservative estimate of p is made by assuming W is equal to the lithographic width of 800 nm. This establishes a lower bound of p = 92%. If we assume a depletion width equal to the depth of the 2DEG, the measured resistance implies p = 96% in our model. Based on

these results, we feel confident in analyzing our data in terms of a fully specular model. The lower bound established for p will be used later to estimate the effect uncertainty in boundary scattering has on our measurement of τ_ϕ.

The measured resistance places a lower bound of 610 nm for the width of the channel.[12] Therefore at a bias voltage of -0.400 volts, we estimate W ≈ 700 nm, with a maximum possible deviation of 100 nm in either direction. Previous 1-D channel experiments have used either ion[13] [van Houten, *et al.*, (1988a)] or wet chemical [Kurdak, *et al.*, (1992)] etches to define their channels. Like gated channels, reflection from these boundaries is highly specular. However, due to the large sidewall depletion inherent to etch techniques [Choi, *et al.*, (1987b)], the actual channel width in these experiments was known with far less certainty than is the case for our measurements.

The Determination of τ_ϕ

Fig. 4.3a shows the differential magnetoconductance of the array of channels biased at -0.400 V at 4.2 K (dotted) and at 385 mK (solid).[14] As shown, the weak localization correction grows dramatically at lower temperatures. The background magnetoconductance, however, is independent of temperature, which is an indication that it is a classical rather than quantum mechanical effect. Between 0 and 100 mT, there is a gradual negative magnetoconductance, which evolves into a much sharper positive magnetoconductance at higher fields. This behavior is likely due to a small amount of diffuse boundary scattering present in our channels [Thornton, *et al.*, (1989); Ditlefsen and Lothe, (1966)]. Similar phenomena have been observed in narrow channels with

[12]The lower bound is obtained by setting p = 100%.

[13]Ion poisoning can create rough boundaries.

[14]This and all other array conductances described in this chapter have been normalized to the value for a single channel.

Weak Localization in an Array of Channels

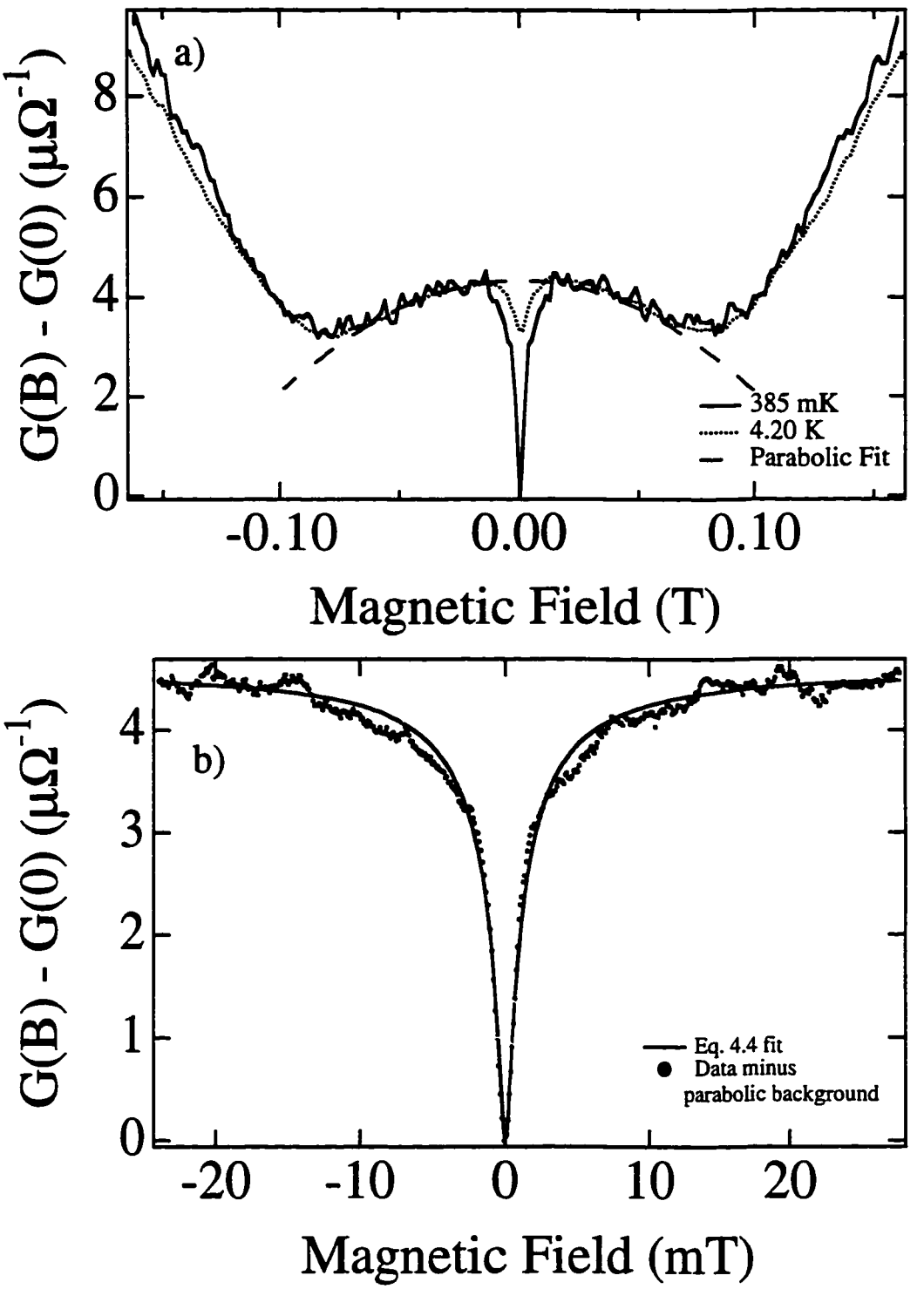

Fig 4.3 a) Graph of magnetoconductance at 385 mk (solid) and 4.2 K (dotted). There is a temperature independent classical background whose low-field behavior may be fit to a parabola (dashed). b) Plot of the low-field magnetoconductance from the array of channels following subtraction of the parabolic background. Included is a fit to Eq. (4.4) with the channel width left as an adjustable parameter.

predominantly specular boundaries [Choi, *et al.*, (1987a); van Houten, *et al.*, (1988a)].

In order to use Eq. (4.3) to determine the phase coherence time, it is necessary to subtract this classical background from the data. Unfortunately even at 4.2 K, the presence of the weak localization peak makes it difficult to experimentally establish the behavior of this background around zero field.[15] Using the expected parabolic form, the classical background was extrapolated to zero field. The parabolic fit to the low-field background is included in Fig. 4.3a (dashed). At low temperatures, the amplitude of the localization correction is much greater than this classical background, so any errors made in subtracting this background will have negligible effect (~ 1 ps) on the determination of τ_ϕ.

Fig. 4.3b is an enlargement of the low-field differential magnetoconductance of the channel array at 385 mK following subtraction of the parabolic background. The amplitude of the UCF is significantly suppressed from that of the single channel measurements. With the classical background subtracted, it is easy to establish a value for $G(B_{saturated})$. Subtracting this value from the zero-field conductance yields δG_{WL}, and Eq. (4.3) can be used to calculate $\tau_\phi = 150 \pm 5$ ps. UCF are the source of the uncertainty quoted in this value. By averaging over a large enough field range, it is possible to establish a very accurate value for $G(B_{saturated})$. However, because UCF may be influencing G(B=0), there is an uncertainty in δG_{WL} equal to the rms amplitude of the conductance fluctuations. This source of uncertainty will grow as the conductance fluctuations become more pronounced at dilution refrigerator temperatures. Note that by extracting τ_ϕ from the amplitude rather than from the lineshape of the weak localization correction, the uncertainty in the channel width does not affect the determination of τ_ϕ.

In using the bulk value for the diffusion coefficient (D_0) in the calculation above, it is possible that we are systematically underestimating the value of τ_ϕ. The diffusion coefficient will decrease in the channel if the elastic scattering time there is shorter than in

[15]Ideally, magnetoconductance traces would simply be taken at a higher temperature (e.g. 10 K) where all quantum interference effects would be suppressed. Unfortunately none of our cryostats is well-suited for such a measurement.

the bulk, or if any non-specular boundary scattering occurs. As discussed in Section 4.3, we may use the classical resistance of the channels to place a lower bound ($= 0.75D_0$) on the diffusion coefficient in our channels. A smaller diffusion coefficient would require a proportionally larger value of τ_ϕ in order to match the measured amplitude of δG_{WL}. In all likelihood, however, the diffusion coefficient in the channels is very near its bulk value, making any resulting systematic error small.

Included in Fig. 4.3b is a fit to Eq. (4.4) with the channel width as the only adjustable parameter. The range of the fit was limited to $\pm$ 1mT, as the theories used to compute τ_B in one-dimensional channels are only valid at values of magnetic field small enough so that $\ell_m >> W$.[16] In Section 4.3, W was estimated to be 700 $\pm$ 50 nm, which implies that $\ell_m = W$ when B = 1.4 mT. The fit shown in Fig. 4.3b yielded a width of 725 nm, in excellent agreement with our earlier estimate. Previous experiments were not able to quantitatively check Beenakker and van Houten's quasi-ballistic theory for weak localization, because the width of their etched channels was not known [van Houten, *et al.*, (1988b); Kurdak, *et al.*, (1992)]. It is interesting that the fit to Eq. (4.4) matches the experimental lineshape fairly well over its entire range even though the theory on which it is based is only strictly valid for $\ell_m >> W$. At fields higher than this in our channels, however, the one-dimensional theory should still apply because the specular boundaries and long mean free path insure that, on average, several boundary collisions will occur before an electron may be backscattered and contribute to the localization effect. It is only in the limit of $W \geq \ell$ that high fields should be able to induce a crossover to two-dimensional behavior when $\ell_m \sim W$.

[16]This is because the lateral confinement becomes irrelevant at fields large enough for the electron to dephase before it can reach the walls — effectively making the channel a two-dimensional system.

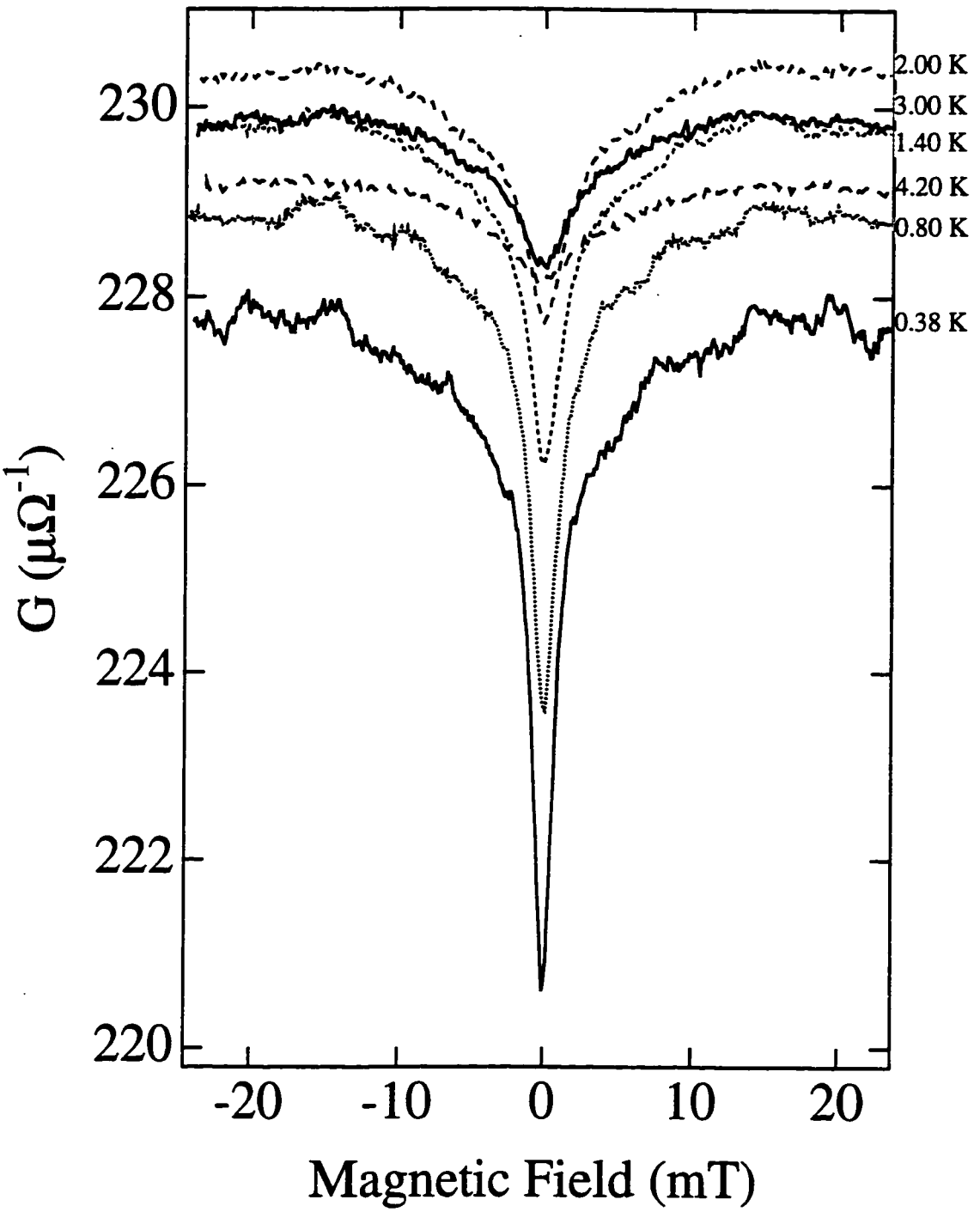

Fig. 4.4 Array magnetoconductance at six temperatures illustrating the non-monotonic behavior in the value of $G(B_{saturated})$ that results from competition between the temperature dependences of elastic scattering and electron-electron interactions.

Temperature Dependence of τ_ϕ

Fig. 4.4 is a plot of the array conductance vs. the perpendicular field taken at six temperatures between 4.2 and 0.38 K. The curves are not offset from one another. Rather the non-monotonic behavior in the value of the baseline conductance for the different temperatures is the result of two competing effects. Even below 4.2 K, the value of the mean free path continues to increase slightly as the temperature is decreased. This explains the rise in the baseline conductance that occurs until down to around 2.0 K. Below this temperature, the slow increase in ℓ is overshadowed by the decrease in conductance resulting from quantum mechanical correlations in the electron motion introduced by Coulomb interactions. The B-field independent conductivity correction resulting from these electron-electron interactions has previously been observed in narrow GaAs/AlGaAs 2DEG channels [Choi, *et al.*, (1986); Thornton, *et al.*, (1986)]. The predicted magnitude for the effect in the 1-D regime ($L >> \ell_T >> W$) is [Lee and Ramakrishnan, (1985)]:

$$\delta G_{ee} = -C\sqrt{2}\frac{e^2}{h}\frac{\ell_T}{L}, \qquad (4.15)$$

where the interaction parameter $C \approx 1.3$. Although these electron-electron interaction effects become comparable to the weak localization correction at low temperatures, they do not interfere significantly with the measurement of τ_ϕ because they are nearly independent of magnetic field.[17]

---

[17]The e-e interactions are dominated by diffusons which are field-independent. The magnetoconductance of the small cooperon component of the e-e interactions, however, is virtually indistinguishable from that of weak localization. The ratio of the two effects is approximately $\left(\ell_T/\ell_\phi\right)\left[1+\lambda\ln\left(E_f/kT\right)\right]^{-1}$, where the coefficient $\lambda \sim 1.13$ [Choi, *et al.*, (1986)]. At 385 mK, the amplitude of this cooperon component is only 5% that of the weak localization correction. Ignoring e-e interactions may lead to a small systematic overestimate of τ_ϕ in our measurements. Fortunately, our other potential source of systematic uncertainty, the assumption that $D = D_0$, has the opposite effect on τ_ϕ.

In Fig. 4.5a, the zero-field conductance has been subtracted at in order to emphasize the temperature-dependent behavior of δG_{WL}. As the temperature decreases, the phase coherence time increases leading to a larger weak localization correction. At the lowest temperature shown, the phase coherence length has increased to the point where UCF are once again visible despite all of the averaging present in the measurement. Using the procedure described earlier in this chapter, the phase coherence time at each temperature may be calculated from the amplitude of weak localization correction. At high temperatures where τ_ϕ is comparable to τ, the values of τ_ϕ so calculated are somewhat suspect, because the *ad hoc* incorporation of τ into Eq. (4.1) becomes significant in this range.

The experimentally measured phase coherence times at temperatures between 100 mK and 4.2 K are plotted in Fig. 4.5b. The data above 385 mK were measured in the ^{3}He cryostat, while the lowest temperature data were acquired when the same sample was later cooled in the Kelvinox dilution refrigerator.[18] Where the data from the two cryostats could be reliably compared (400 - 600 mK), nearly identical values for the phase coherence time were measured in the two thermal cycles. The fact that we measure the same phase coherence time in the ^{3}He cryostat and the Kelvinox (with its multiple layers of filtering), is an excellent indication that the current ^{3}He probe is well-suited for performing quantum interference measurements.

The same can probably not be said about the ^{3}He probe prior to the wiring modifications described in Chapter 3. The 150 ps phase coherence time measured for the array of channels at base temperature in the rewired ^{3}He cryostat is over a factor of two larger than the 70 ps time measured for a single channel at base temperature in the cryostat before rewiring. This discrepancy is much too large to be explained by the 35 mK difference in base temperature, or by any experimental uncertainties in the phase coherence times. Furthermore, the channels in the two measurements are almost lithographically

[18]We were forced to do this by the lack of adequate high temperature thermometry on the Kelvinox. In addition, the Kelvinox system is difficult to operate between 0.6 and 1.5 K.

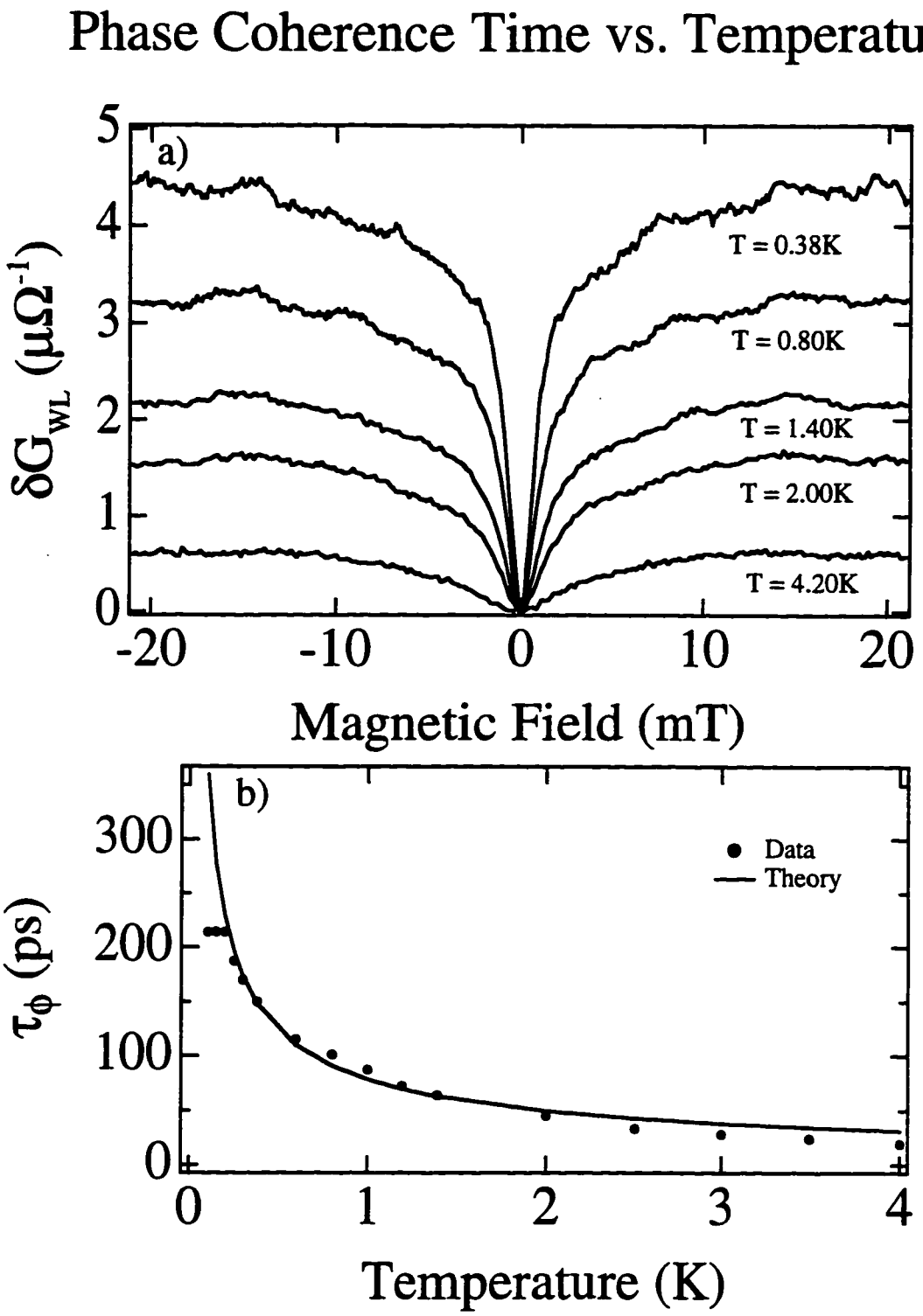

Fig. 4.5 a) Differential magnetoconductance of the array of channels shown for 5 different temperatures. b) Phase coherence times determined from the amplitude of the weak localization feature. For comparison to theory, the dephasing rate from Eq. (4.17) is included. Note that the measured rate saturates below 200 mK.

identical, and were fabricated from the same wafer using identical techniques. The main difference between the two measurements is that filtering not present when the single channel data were acquired was added to the ^{3}He probe prior to the array experiments. It is likely that without this filtering, the effective phase coherence time was being shortened by high frequency radiation reaching the sample.

At low temperatures, the loss of phase coherence is the result of e-e scattering events between the injected electrons and those in the Fermi sea. In the limit of a one-dimensional channel[19], theoretical models predict that [Altshuler, *et al.*, (1982)]:

$$\frac{1}{\tau_\phi} = \frac{\pi}{2}\frac{(kT)^2}{\hbar E_f}\ln\left(\frac{E_f}{kT}\right) + \left(\frac{\pi kT}{D^{1/2}Wm}\right)^{2/3} \quad . \tag{4.16}$$

The first term comes from momentum conserving processes involving large energy transfers. The second term describes what is known as Nyquist dephasing. During diffusive electron motion in the presence of disorder, electrons are scattered quasi-elastically by the fluctuating electric fields generated by the motion of other electrons; through many scattering events involving energy transfers much smaller than kT, electrons lose phase coherence. Inserting D_0 and W = 700 nm into Eq. (4.16),

$$\tau_\phi^{-1} = 1.2\text{x}10^9 T^2 \ln(160T^{-1}) + 1.1\text{x}10^{10} T^{2/3}. \tag{4.17}$$

At 1.7 K, the two terms are equal, with the Nyquist term dominating the phase-breaking at lower temperatures. The solid line in Fig. 4.5b represents the phase coherence times calculated using Eq. (4.17). Considering that there are *no adjustable parameters* in the calculated dephasing rate, there is remarkably good agreement between the calculated and

[19]For electron-electron interactions, it is the ratio of the channel width to ℓ_T (rather than ℓ_ϕ) that establishes the dimensionality of the system. This crossover to 1-D is expected to occur when $W < \pi\ell_T$, which is the situation for our array of channels.

measured values of τ_ϕ. Over the temperature range studied, the excellent agreement between our data and the dephasing rate predicted by Eq. (4.16) demonstrates that the e-e interactions are the dominant source of electron dephasing.

Previous measurements of τ_ϕ in narrow GaAs/AlGaAs 2DEG channels were not optimized for a quantitative comparison to the predictions of Eq. (4.16). As mentioned earlier, there was considerable uncertainty in the channel width in the earlier experiments, which prevented an accurate calculation of the Nyquist dephasing rate. In addition, the fabrication techniques used to make these channels degraded the electron mobility, creating uncertainty in the value of τ. Finally, previous experiments were performed in channels so narrow that τ_ϕ and τ were comparable even at 400 mK. As mentioned earlier, the theory of diffusive weak localization used to determine τ_ϕ is not strictly valid unless $\tau_\phi >> \tau$.

In channels whose mobility was more than a order of magnitude lower than that of our 2DEG, τ_ϕ at 400 mK was measured to be 21 ps [Choi, *et al.*, (1987a)] and 20 ps [van Houten, *et al.*, (1988a)]. The coefficient of the Nyquist dephasing rate in Eq. (4.16) ($\propto W^{-2/3}D^{-1/3}$) explains why previous measurements of τ_ϕ yield times significantly shorter than our own. The diffusion coefficients in these low-mobility channels are over an order of magnitude lower than in our samples, which helps to explain the discrepancy in τ_ϕ. In the same vein, for both the Choi and van Houten experiments, W (though not accurately known) is substantially less than the 700 nm in our measurement. In material whose mobility was almost identical to that of BW1, τ_ϕ at 410 mK was measured to be 51 ps [Kurdak, *et al.*, (1992)] — almost a factor of three shorter than in our measurement . This discrepancy might be explained by a difference in channel width, but a quantitative comparison is not possible due to the large uncertainties in W created by sidewall depletion in the etched channels used for their measurements.

As shown in Fig. 4.5b, for mixing chamber temperatures 200 mK and lower, in our measurements the amplitude of the weak localization correction saturates at a value corresponding to $\tau_\phi = 215$ ps. In Chapter 3 we discussed how, as the result of poor

coupling between the 2DEG and the lattice, the electron gas temperature could be significantly higher than that of the sample. Therefore, we must consider the possibility that the apparent saturation in δG_{WL} is not a real effect, but rather an indication that the 2DEG has reached its base temperature. We know, though, that the electron gas temperature does extend below 200 mK, because the electron-electron interactions discussed earlier continue to decrease the baseline conductance until the mixing chamber reaches ~100 mK. Evidence that the electron gas temperature reaches 100 mK in the Kelvinox is also seen in other experiments reported in this thesis (see Fig. 7.7 for example).

The amplitude of the weak localization correction would be expected to saturate once the temperature was low enough so that $\ell_\phi \geq L$. Even though the phase coherence length would continue to grow as the temperature further decreased, doing so would not augment the localization correction once all of the possible backscattered trajectories were fully phase coherent. At saturation in our experiments, though, ℓ_ϕ is still only 11 μm. This is an order of magnitude shorter than the channel length, which rules out this explanation.

Saturation of the weak localization correction to conductivity would also be expected once ℓ_ϕ exceeds the Anderson localization length, α^{-1}. Electronic states in long, 1-D wires are strongly localized for arbitrary disorder at zero temperature, decaying exponentially with a characteristic length α^{-1} [Thouless, (1977)]. This Anderson localization is unimportant when $\ell_\phi < \alpha^{-1}$. In the event that $\ell_\phi \geq \alpha^{-1}$, further increase in the phase coherence length would not be reflected in δG_{WL}, because strong localization would prevent the formation of backscattered trajectories longer than α^{-1}. In 1-D channels, the Anderson localization length is approximately given by, $\alpha^{-1} \sim N\ell$, where N is the number of occupied subbands [Suhrke and Wilke, (1992)]. Estimating N as W/λ_f, $\alpha^{-1} \sim$ 100 μm, which is much larger than ℓ_ϕ, and makes Anderson localization an unlikely explanation for the saturation. Saturation of δG_{WL} at temperatures between 0.1 and 0.5 K

has been observed in narrow channels ($W < 200$ nm) with far more disorder than is present in our samples ($\alpha^{-1} \sim 9$ μm) [Mani, *et al.*, (1993)].[20] Although the authors attribute this saturation to strong localization effects, this is unlikely since ℓ_ϕ in their samples is only ~ 1 μm.

Although there are r.f. blocking resistors and Cu-powder filters in the Kelvinox system, radiation above a GHz is notoriously difficult to block. Such radiation can induce additional Nyquist dephasing which could explain the observed saturation of δG_{WL}. The decrease of the experimentally measured dephasing rates in the ^{3}He system following the addition of filtering seems to indicate that radiation-induced dephasing can play an important role in quantum coherence measurements. The effect of high frequency electric fields on weak localization in 2DEG systems has been calculated [Altshuler, *et al.*, (1981)]. The electric fields introduce an additional dephasing rate, τ_{ext}, to the system, which is given by

$$\tau_{ext} = \int_{\omega_1}^{\omega_2} d\omega \left(\frac{2e^2 D}{\hbar^2} \right)^{-1/5} (\omega E(\omega))^{-2/5}, \qquad (4.18)$$

where ω is the frequency and E is the amplitude of the oscillating electric field. Assuming that the external and intrinsic dephasing rates are simply additive, the effective dephasing rate would equal $\tau_\phi^{-1} + \tau_{ext}^{-1}$. Under this assumption, we would expect the measured phase coherence time (which would be the inverse of this effective dephasing rate) to asymptotically approach τ_{ext} as τ_ϕ^{-1} becomes much smaller than τ_{ext}^{-1}. Experimentally, however, we observe a sharp plateau in the measured dephasing rate beginning at 200 mK. This could indicate that the Nyquist term which dominates the intrinsic dephasing rate at low temperature does not simply add with the external Nyquist dephasing rate. Of course,

[20]Although no data from below 0.5 K is shown in the paper, a saturation of τ_ϕ below 200 mK in channel experiments was also reported by [van Houten, *et al.*, (1988a)]. They offer no explanation except to warn that the weak localization correction is no longer a small perturbation at low temperatures.

if this is not the case, then the sharp plateau may be an indication that external radiation is not the cause of the saturation found in our measurements of τ_ϕ.

Width Dependent Effects

Since the channels in our array are defined by electrostatic gates rather than by etching, we are able to study weak localization as a function of the channel width by adjusting the bias voltage applied to the gate. In order to interpret our results, it is necessary to understand the effect the applied bias voltage has on the depletion width.

As illustrated in Fig. 4.6, the surface gates are capacitively coupled to the electron gas beneath them. Approximating this system as a parallel plate capacitor, the gate-gas capacitance is equal to

$$C = \frac{\varepsilon_0 \varepsilon A}{z_0}. \qquad (4.19)$$

The depletion voltage, V_{dep}, is the gate voltage at which all of the electrons have been removed from underneath the gate; using the definition, $Q = CV_g$, a parallel plate model predicts complete depletion when $CV_{dep} = en_s A_{gate}$. For the depth of the electron gas in BW1 ($z_0 = 420$ Å), this condition occurs when $V_g = -0.22$ V, which is somewhat lower than the experimentally measured value of -0.33 V. This discrepancy is not surprising since the crude model used ignores fringing fields which extend the region of depletion an additional length δ past the edge of the surface gate.

An involved quantum mechanical treatment would be required to exactly model the effect of V_g on δ at gate voltages more negative than V_{dep}. The problem may be simplified

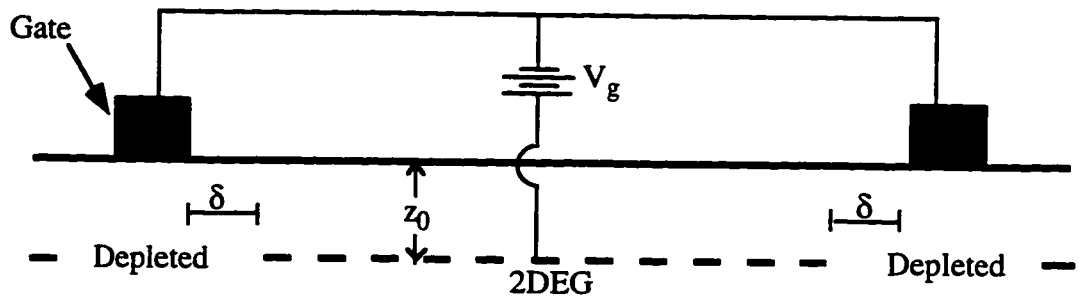

Fig. 4.6 Schematic illustrating the electrostatic depletion used to define the 1-D channels. Note that the depleted region extends a distance δ beyond the edge of the surface gates. This distance can be lengthened by increasing the negative bias on the gates relative to the 2DEG.

V_g (Volts)	n_s x10^{15} (m^{-2})	R/channel (Ω)	W (nm)	δ (nm)
-0.400	3.74	7,250	700	50
-0.600	3.69	8,650	595	100
-0.800	3.51	10,459	515	142
-1.000	3.38	12,820	440	180

Table 4.1 In this table, the channel width is calculated from the measured sheet density and resistance assuming τ is unchanged from its bulk value of 15.2 ps. These calculations assume 96% specular boundary scattering.

by assuming the depletion width to be much greater than both the depth of the electron gas[21] and the effective Bohr radius in the semiconductor (~ 10 nm in GaAs).[22] Under these assumptions, there exists a constant gate-gas capacitance leading to linear relation between V_g and δ [Chklovskii, *et al.*, (1992)],

$$\delta = \frac{2\varepsilon_0\varepsilon|V_g - V_{dep}|}{\pi n_s e} \approx 120|V_g - V_{dep}| \text{ nm for BW1.} \qquad (4.20)$$

Near V_{dep} in our channels, δ is comparable to z_0, so this result is not expected to strictly apply. We may, however, use the experimentally measured channel resistances to estimate the effect of V_g on δ in our channels. Table 4.1 lists the resistance per channel measured at V_g = -0.400, -0.600, -0.800, and -1.000 V. Even at -0.400 V, the sheet density determined via Shubnikov-de Haas oscillations in the channels has decreased slightly from its bulk value of 3.90×10^{15} m^{-2}. At higher voltages, n_s is found to decline further. The widths shown in Table 4.1 are calculated from the measured resistances assuming τ in the channels remains unchanged from its bulk value and that the depletion width at -0.400 V is 50 nm.[23]

The constant τ assumption may not be very accurate. The majority of the elastic scattering is due to ionized impurities in the donor layer. As the sheet density decreases, the screening of these impurities in the 2DEG probably diminishes, leading to increased elastic scattering.[24] All of the temperature series was taken at -0.400 V, where any

---

[21]Which allows the gate and the electron gas to be approximated as lying in the same plane.

[22]This assumption has to do with the screening length which is typically on the order of a_B. The change in electron sheet density from its bulk value to zero at the edge of depletion region occurs over a distance comparable to a_B.

[23]Which implies that the boundary scattering was a constant 96% specular. Assuming fully specular boundary scattering, δ would be 95 nm at -0.400 V.

[24]In channels whose mobility was an order of magnitude lower than that of our material, τ was found to scale as $n_s^{3/2}$ [Zheng, *et al.*, (1986)].

difference between τ in the channels and in the bulk is likely to be small, since n_s at this voltage is still over 95% of its bulk value. As the sheet density decreases at more negative bias voltages, however, the effect on τ may no longer be negligible. As a result, the actual channel widths may be larger than those calculated in Table 4.1 under the assumption of a constant elastic scattering rate.

Because of uncertainty in the boundary scattering and the elastic scattering time, it is difficult to make a quantitative evaluation of the depletion width. In the range of voltages studied, $d\delta/dV_g \sim 200 \pm 50$ nm/V, where the quoted uncertainty is the result of uncertainty in the value of δ at -0.400 V. Not considered is the possible decrease in τ at more negative bias voltages, which may explain why the depletion widths in Table 4.1 are slightly larger than those predicted by Eq. (4.20). Although we cannot rule out a linear relationship between δ and V_g, it does appear that the magnitude of $d\delta/dV_g$ is decreasing as δ increases. This would not be surprising since the gate-gas capacitance would not be expected to reach the constant value predicted by Eq. (4.20) until $\delta >> z_0$.

Fig. 4.7 shows the low-field differential magnetoconductance of the array of narrow channels at -0.400 V and at -1.000 V. Since the -1.000 V channel is narrower, backscattered trajectories enclose smaller average areas, and a larger perpendicular field is required to suppress the weak localization effect. At the 385 mK temperature at which these data were taken, the dephasing is dominated by the Nyquist term in Eq. (4.16), in which the phase coherence time is proportional to $W^{2/3}$. Although the amplitude of the weak localization correction has clearly decreased in the narrower channels, much of this correction is not associated with a width-induced change in τ_ϕ. Recall from Eq. (4.1) that $\delta G_{WL} \propto D^{1/2} \propto \tau^{1/4} n_s^{1/2}$. Using the measured value of n_s at -1.000 V and assuming $\tau =$ 15.2 ps (its bulk value), a phase coherence time of 125 ps is extracted from δG_{WL}. This 125 ps is actually a lower bound on τ_ϕ, because the decrease in sheet density is likely accompanied by a drop in τ which would further reduce the diffusion coefficient. We establish an upper bound of $\tau_\phi = 134$ ps by assuming $\tau \propto n_s^{3/2}$. Although much of this

Width Dependence of Weak Localization

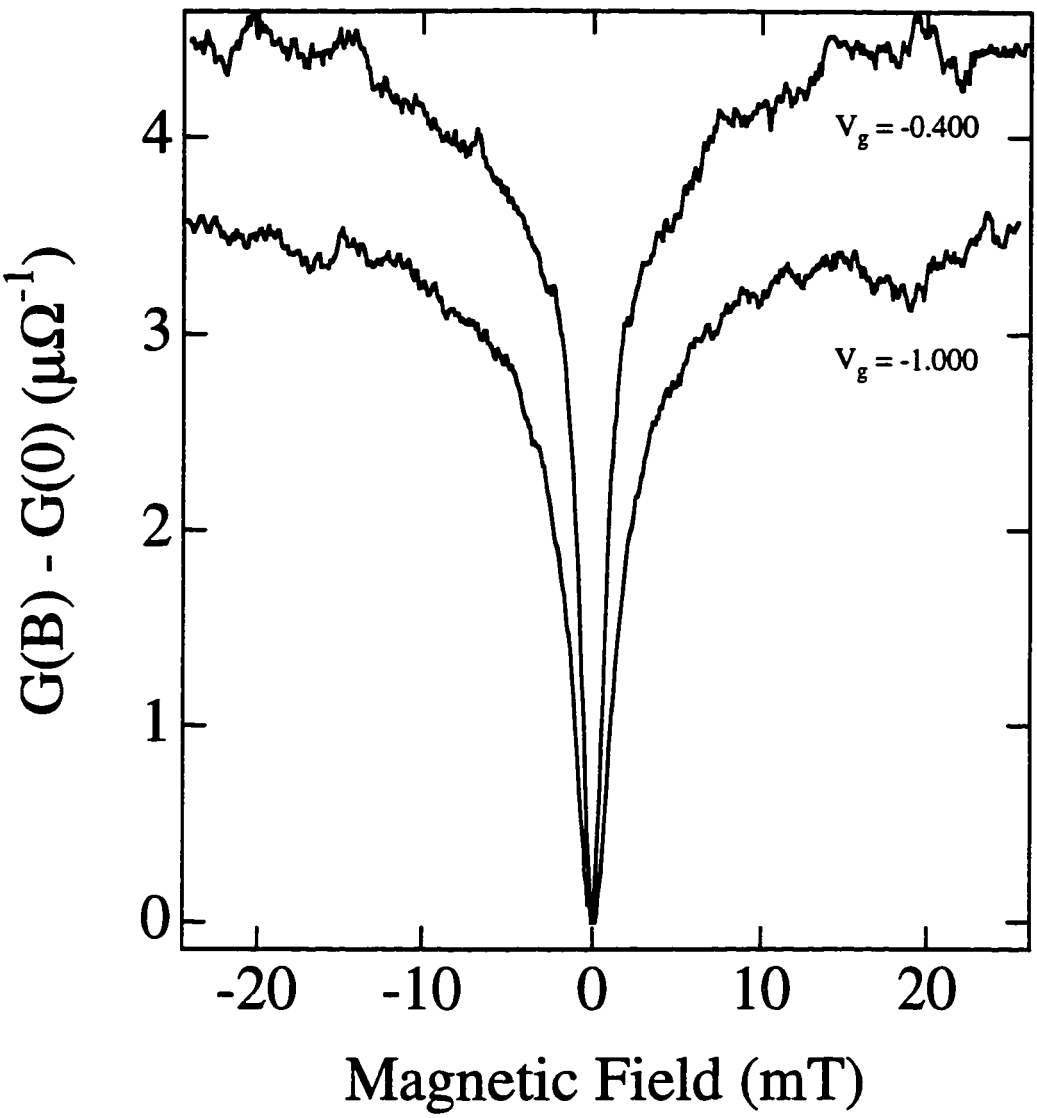

Fig. 4.7 Differential magnetoconductance of the narrow channel array biased at -0.400 V and -1.000 V. The -1.000 V channels are narrower, and require a larger field to suppress weak localization. The reduced amplitude at -1.000 V is in part the result of a reduction in the phase coherence time.

decrease from the 150 ps value of τ_ϕ at -0.400 V is likely the result of the decrease in the channel width, it is again difficult to quantify this, because in the Nyquist term τ_ϕ is also proportional to $D^{1/3}$. The decrease in sheet density that accompanies the decrease in channel width makes it impossible to quantitatively study the relationship between the channel width and phase coherence time. Qualitatively, though, it does appear that a decrease in the channel width does result in a reduction of τ_ϕ.

4.5 Experiments in a Two-Dimensional Channel

Previous experiments studying weak localization in two-dimensional GaAs/AlGaAs 2DEG channels have all been done in material with mobilities less than 27,000 cm^2/Vs [Paalanen, *et al.*, (1983); Choi, *et al.*, (1987a)]. Low mobility makes the weak localization correction easy to observe, because it facilitates the creation of backscattered trajectories that are short enough to remain phase coherent. In this section, we will discuss our attempts to measure 2-D weak localization effects in material whose mobility is over an order of magnitude greater than that in any previously reported work.

The initial motivation for attempting these 2-D measurements was provided by the difficulties in our early efforts involving 1-D channels (see Section 4.3). In 2-D channels there are no universal conductance fluctuations, so the fabrication difficulties associated with the 1-D arrays may be avoided.

A 2-D measurement would complement the 1-D results in several ways. Unlike the 1-D case, the phase coherence times obtained from 2-D measurements would be unaffected by uncertainties in either the nature of the boundary scattering or in the value of τ. This is because 2-D diffusion is independent of boundary scattering, and the elastic scattering time in the wide channel would almost certainly be equal to that of the bulk 2DEG. In addition, placing one- and two-dimensional channels on the same chip would provide an opportunity to observe the change in the temperature dependence of the Nyquist dephasing rate (Eq.

4.16) that is predicted to occur when the channel width is equal to the thermal length, $\ell_T = (\hbar D/kT)^{1/2}$. This dimensional crossover was examined by Choi, *et al.*, but the results were inconclusive.

As shown in Fig. 4.2a, the 2-D channel is located on the same chip as the 1-D array (BW1.UU). A negative bias voltage applied to Cr/Au surface gates defines the two dimensional channel. The channel length, L = 1,000 μm and the width, W = 27 μm. Four-probe current-biased resistance measurements at 400 mK (see Fig. 3.1) give $R_{channel}$ = 1,500 Ω, which corresponds to ρ = 40.3 Ω/sq. This value agrees with the bulk resistivity determined with a van der Pauw technique. Shubnikov-de Haas oscillations show that both the bulk sample and the two-dimensional channel have $n_s = 3.90 \times 10^{15}$ m^{-2}.

Despite considerable effort, we were not able to observe two-dimensional weak localization in the wide channel. Because of the high mobility of the 2DEG being used, the predicted amplitude of the weak localization correction is quite small. Nevertheless, the signal should have been detectable above the under 0.1 Ω noise in the resistance measurements. In terms of the channel resistance, R:

$$\delta R_{WL} = \rho^2 \left(\frac{L}{W}\right) \frac{e^2}{\pi h} \ln\left(1 + \frac{\tau_\phi}{\tau}\right). \tag{4.21}$$

As mentioned earlier, a dimensional crossover in the Nyquist term of Eq. (4.16) occurs when $W > \pi L_T$. In the 2-D regime [Altshuler, *et al.*, (1982)]:

$$\frac{1}{\tau_\phi} = \frac{\pi (kT)^2}{2 \hbar E_f} \ln\left(\frac{E_f}{kT}\right) + \frac{kT}{2mD} \ln\left(\frac{mD}{\hbar}\right). \tag{4.22}$$

At 400 mK, the above equation yields $\tau_\phi \sim 600$ ps. Inserting this value into Eq. (4.21), we obtain $\delta R_{WL} \sim 2.7$ Ω, a small but detectable correction to the channel's 1,500 Ω resistance.

The characteristic field of the localization correction, however, is extremely small. From Eq. (4.5b), $B_c \sim 0.9\ \mu T$. In the presence of a fluctuating magnetic field comparable to B_c, the expected zero-field resistance peak would be washed out. Several precautions were taken to prevent this. As discussed in Section 3.7, one potential source of magnetic field fluctuations is current noise in the supply connected to the solenoid. In order to minimize this, a battery-powered, low-noise current source was used in our 2-D measurements. Considering the size of B_c, the fluctuating fields produced by pumps, power supplies, and other laboratory equipment could easily be capable of obscuring the localization feature. Although the experiments were conducted in a screen room which is excellent for shielding r.f. radiation, the room provides very little protection against fluctuating magnetic fields. The superconducting solenoid itself is actually quite a good shield when it is operated in persistent current mode. Unfortunately, the magnetic field must be swept to observe the weak localization effect; this requirement precludes operation in persistent current mode.

I believe that the absence of a detectable 2-D weak localization peak is an indication that the current Kelvinox system is inadequate for such sensitive magnetic field experiments. A cryostat in which the sample is well shielded from fluctuating fields by a μ-metal cage would probably be required to resolve the ~ 1μT wide localization peak.

4.6 Summary

The enhancement of the weak localization effect that occurs in quasi-ballistic one-dimensional channels allows the phenomenon to be studied in high-mobility 2DEGs where 2-D localization effects are very difficult to measure. From the classical resistance of the channels, we were able to verify that boundary scattering in structures defined by electrostatic gates is highly specular. Magnetoconductance measurements were used to determine the amplitude of the weak localization correction. In order to perform a

quantitative analysis, an array of channels was used to suppress the UCF. From the amplitude of the weak localization correction, we were able to compute the phase coherence time. The lineshape of the weak localization feature very closely matched that predicted by theories including flux cancellation effects. The temperature dependence of the dephasing rate confirmed that the loss of phase coherence in clean 2DEG systems at low temperatures is dominated by electron-electron interactions. Below 200 mK we observed a saturation in the phase coherence time which may by due to high frequency radiation in the system. Finally, conductance measurements performed at a series of gate bias voltages allowed us to study the relationship between gate voltage and depletion width.

To conclude this chapter, we will briefly discuss how applicable the results from our channel measurements are to other systems. In these narrow channel experiments, the phase coherence time was measured in long channels in which electron transport is diffusive. Most of the experiments in this thesis, though, involve ballistic electron motion. An obvious difference in the ballistic regime is that the phase coherence length in that limit is $\ell_\phi = v_f \tau_\phi$.

Although the dephasing rate predicted by Eq. (4.16) agrees very well with the data from our channel measurements, this would not necessarily be the case in much higher mobility material. At low temperatures in all but the highest mobility material, the electron-electron scattering time ($\tau_{e\text{-}e}$) is larger than the elastic scattering time, τ, which means that the electons' momentum is not conserved throughout collisions. In this case, dephasing is dominated by e-e scattering events involving energy transfers much smaller than kT (the Nyquist dephasing of Eq. (4.16)). In contrast, if $\tau_{e\text{-}e}$ were less than τ, dephasing would be dominated by momentum-conserving processes involving energy transfer on the order of kT. $\tau_{e\text{-}e}$ has been calculated to be roughly [Giuliani and Quinn, (1982); Fasol, (1991)]

$$\frac{1}{\tau_{e-e}} \approx \frac{E_f}{\pi\hbar}\left(\frac{kT}{E_f}\right)^2\left[1+\ln(2)+\ln\left(\frac{Q_{TF}}{k_f}\right)-\ln\left(\frac{kT}{E_f}\right)\right], \qquad (4.23)$$

where $Q_{TF} = 2me^2/\varepsilon\hbar^2$ (ε = 12.9 for GaAs) is the 2D Thomas-Fermi screening wavevector (in cgs units). For the parameters of BW1, Eq. (4.23) yields $\tau_{e\text{-}e} \approx$ 500 ps at 1 K, significantly larger than τ = 15 ps. In very clean 2DEG systems, though, τ can be much larger than 15 ps. In a high-mobility ($\tau \sim$ 40 ps) 2DEG at temperatures above 4.2 K (where $\tau_{e\text{-}e} < \tau$), recent experiments have found dephasing rates which agree well with the values of $\tau_{e\text{-}e}$ from Eq. (4.23) [Yacoby, *et al.*, (1994a)].

Although our measurements of τ_ϕ were made in a one-dimensional system, some of the quantum interference experiments described in this thesis involve quantum dots. As discussed earlier in this chapter, there is a dimensional crossover in the dephasing rate when the width of the channel equals the thermal length, ℓ_T. A further crossover to a zero-dimensional limit occurs when the length of the system is also smaller than ℓ_T, as is typically the case for quantum dots. Measurement of τ_ϕ in quantum dots has proven to be quite difficult. From magnetoconductance fluctuations in these dots, it is, however, possible to indirectly infer a value of the phase coherence time [Clarke, *et al.*, (1995); Bird, *et al.*, (1995a)]. The phase coherence times so inferred in 0-D systems appear comparable to those found in our 1-D measurements; however, it is possible that the phase coherence length could be much longer in dots. This question is still unresolved, because the phase coherence time in quantum dots has yet to be determined conclusively.

Chapter 5

Coherent Backscattering in Open Ballistic Microstructures[1]

5.1 Introduction

In microstructures whose dimensions are smaller than the mean free path, electron transport is ballistic. Electrons travel in approximately straight line trajectories, with large angle scattering limited to specular reflection from the device boundaries. Because the device geometry rather than random impurities determines the behavior of trajectories, ballistic microstructures provide an opportunity to study the influence that the distribution of trajectories has on transport. For example, a device whose shape is classically chaotic is expected to have a distribution of trajectories which is very different from one with a classically integrable shape, and this difference should be manifested in certain conductance properties of the device.

By applying a perpendicular magnetic field, it is possible to observe two quantum interference effects that are sensitive to the characteristic areas enclosed by trajectories in the device. One is the coherent backscattering effect, which is the analog of weak localization in ballistic microstructures.[2] As described in the previous chapter, weak localization is a decrease in conductance that results from the constructive interference of time-reversed

---

[1]An abbreviated version of this chapter has already been published [Katine, *et al.*, (1996)].

[2]Due to the symmetry of the cavity, "off-diagonal" diagrams may partially cancel the effect of coherent backscattering [Hastings, *et al.*, (1994); Baranger, *et al.*, (1993)]. As a result, the authors of those papers feel that the conductivity correction observed in ballistic devices is most properly referred to as weak localization rather than coherent backscattering. It is unclear how important these "off-diagonal" are in real experimental systems where disorder likely destroys such symmetries.

pairs of backscattered trajectories in disordered systems. A similar decrease in conductance has been observed in ballistic microstructures, with the device walls rather than impurities serving as the origin of the backscattering [Berry, *et al.*, (1994a)]. Of course, trajectories other than time-reversed pairs may also interfere with one another. Quantum interference between paths that do not return to their originating contact mode is the origin of magnetoconductance fluctuations very similar to the UCF discussed in the previous chapter. As a perpendicular magnetic field is applied, these interfering trajectories will contribute to the magnetoconductance with a magnetic frequency $(\Delta B)^{-1} = S/\Phi_0$, where S is the enclosed area. Both the width of the coherent backscattering peak and the power spectrum of these magnetoconductance fluctuations are determined by the distribution of areas enclosed by the interfering trajectories in the device.

In recent years, there have been a number of magnetotransport experiments involving ballistic microstructures. The first experiments performed compared the power spectrum of fluctuations in circular and stadium-shaped billiards [Marcus, *et al.*, (1992)]. The distinctions between these two shapes were rather subtle. In order to demonstrate an unambiguous relationship between the device shape and the distribution of enclosed trajectories, Michael Berry and I compared transport in circular billiards and circular billiards with a central bar (a.k.a. the pacman billiard). These results have been previously published [Berry, *et al.*, (1994b)], and the article is included as an appendix to this thesis. We found that both the width of the coherent backscattering peak and the power spectrum of the conductance fluctuations are influenced by the shape and size of the device. The lineshape of the coherent backscattering peak in our circular devices is Lorentzian, which disagrees with the triangular[3] shape predicted for integrable devices [Baranger, *et al.*, (1993)]. The Lorentzian lineshape is predicted for systems exhibiting chaotic scattering [Baranger, *et al.*, (1992)], and our experimental observation of such a lineshape in a

[3]In the literature, this lineshape is often referred to as linear, since the amplitude of the localization correction decreases linearly with increasing magnetic field.

nominally integrable billiard may be an indication that disorder effects from small-angle scattering or boundary roughness are influencing trajectories in the devices. A coherent backscattering peak with a triangular lineshape has been experimentally observed in arrays of circular billiards below 400 mK [Chang, *et al.*, (1994)]. A similar lineshape has also recently been measured for coherent backscattering in a square billiard [Bird, *et al.*, (1995b)]. The square is also integrable, but this triangular lineshape only emerged when the contacts to the billiard were closed to approximately one mode. For wider contact openings, the observed lineshape was Lorentzian, which Bird, *et al.* believe is an indication that the contact openings were distorting the shape of the device and destroying the integrability. The dependence of the lineshape on the contact width may also be related to the effect the contact width has on the average dwell time for electrons in the billiard. Wide contacts facilitate the escape of electrons from the device and eliminate the long, circulating trajectories that distinguish integrable from chaotic billiards. The triangular lineshape is not observed in the devices of Chang, *et al.* at high temperatures, where the short phase coherence length prevents such long trajectories from contributing to coherent backscattering.

Although they provide useful information about the ensemble of trajectories present in ballistic microstructures, the power spectrum of conductance fluctuations and the coherent backscattering peak do not provide information about specific orbits in the device. In atomic [Holle, *et al.*, (1986); Holle, *et al.*, (1988)] and microwave [Sridhar, (1991)] chaos experiments, as well as in resonant tunneling diodes [Fromhold, *et al.*, (1995)], the wavefunction has been shown to be strongly "scarred" by the remnants of periodic orbits [Heller, (1984)]. Such scarring in ballistic microstructures could produce preferred orbits, the presence of which should be detectable as a periodic component in the magnetoconductance fluctuations of the device. Several groups have detected signs of such periodic orbits in the Fourier analyses of their magnetoconductance fluctuations [Marcus,

et al., (1993); Chang, *et al.*, (1994)[4]; Bird, *et al.* (1996)]. However, in ballistic microstructures with leads containing at most a few modes, electrons execute long interwoven trajectories typically involving many bounces from the device walls before exiting the dot; the complexity of the trajectories in these devices makes it very difficult to associate the magnetoconductance fluctuations with a specific orbit.

In this chapter, we will discuss a series of experiments in which coherent backscattering is studied in very open ballistic microstructures. Long, circulating trajectories cannot exist in these devices, greatly simplifying the interpretation of magnetoconductance measurements. The results from this simplified system offer some insight into the behavior of more complex quantum billiards.

5.2 Device Design

Fig. 5.1a shows a schematic view of a device from sample KC7.T. All of the coherent backscattering samples described in this thesis were made with the wafer KC7 in which the 2DEG is located 570 Å beneath the surface of the GaAs/$Al_{0.3}Ga_{0.7}As$ heterostructure and has a mean free path of 5.4 μm. The experiments were performed in the ^{3}He cryostat, with the sample aligned perpendicular to the magnetic field. Unless indicated otherwise, the measurements were made at base temperature (385 mK). From our measurements of τ_ϕ in the narrow channels (Chapter 4), we believe that the phase coherence length for ballistic electron motion ($\ell_\phi = v_f\tau_\phi$) should greatly exceed the device dimensions at this temperature. Electrical contact is made to the 2DEG through AuNiGe contacts located in the corners of the sample. We use electrostatic gates to define our

[4]The quasi-periodic fluctuations observed by Chang, *et al.* were in an array of rectangular devices. There is no reason why conductance fluctuations (other than those associated with time-reversed orbits) would be in phase for all 48 different devices. This would seem to suggest that the observed oscillations may be a periodic modulation of the coherent backscattering effect similar to that discussed later in this chapter. The frequency of the oscillations observed by Chang, *et al.*, however, seems to correspond to an enclosed area much smaller than that which would be expected for coherent backscattering in their devices.

Open Coherent Backscattering Devices

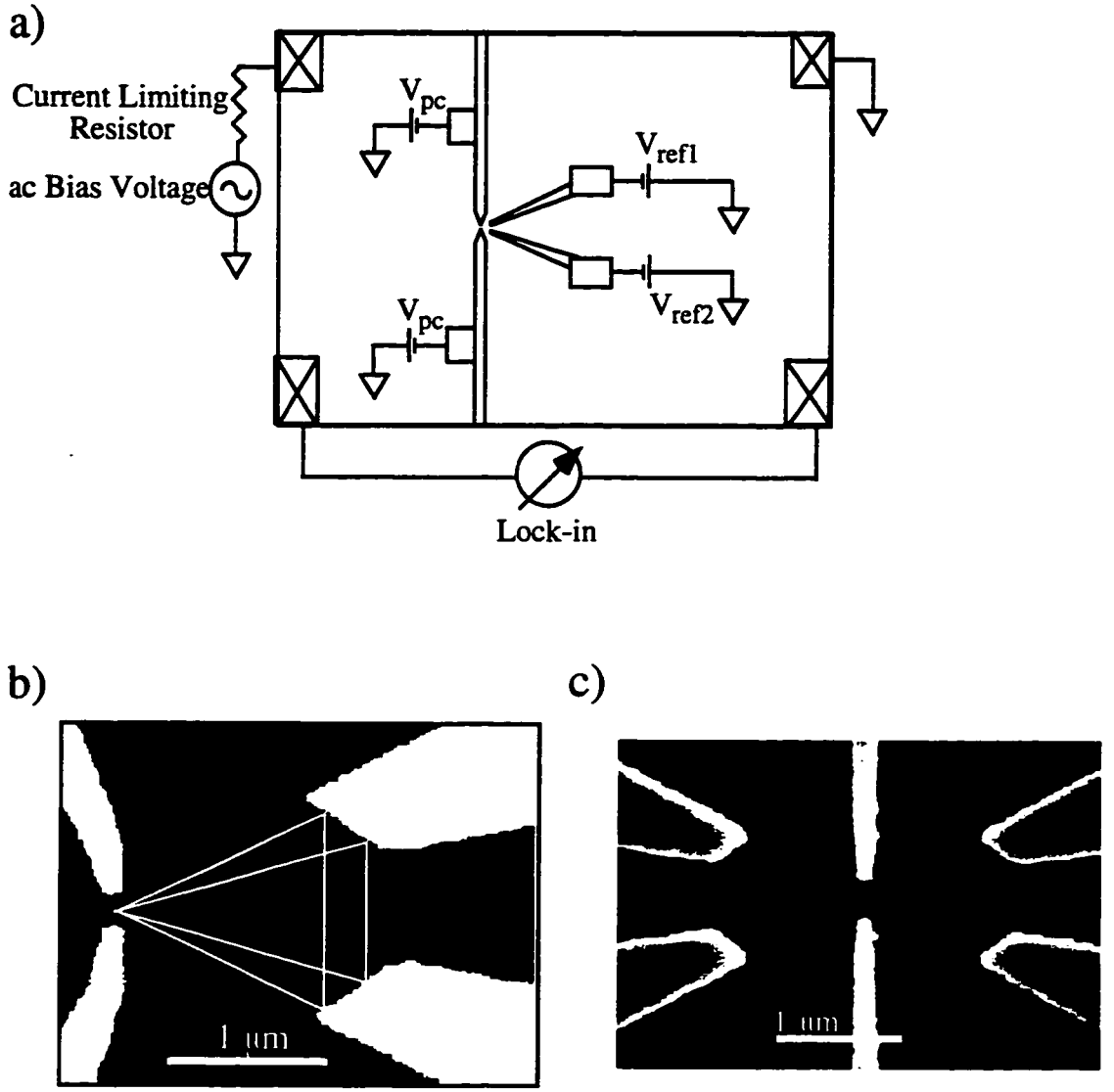

Fig. 5.1 a) Schematic top-view of a sample with a single device. The gates are electrostatically depleted by applying a negative bias voltages. The resistance of the device is measured with a current-biased, low frequency lock-in technique. b) SEM photo of the central region of a large device. Triangular orbits created by specular boundary scattering have been added. c) SEM photo of the central region of a small device. Unlike the large devices, the small devices have reflector gates on both sides of the point contact.

devices, which consist of a single quantum point contact and an independently tunable pair of "reflectors." Using a low-frequency ac lock-in technique, the resistance across the entire sample could be measured. Unlike those of the point contact, the gates defining the reflectors do not extend to the edge of the sample. With the reflectors defined and the point contact gates grounded, the resistance across the sample is only a few ohms. Even though the intrinsic resistance of the reflector gates is low, once the point contact is electrostatically defined, the reflectors substantially increase the sample resistance by scattering electrons back through the point contact.

Fig. 5.1b shows an SEM image of the central region of the device. As discussed in Chapter 4, it is well-established that electron reflection from electrostatically-defined gates is almost perfectly specular. Assuming specular reflection, the reflector gates are designed to produce coherent backscattering by focusing electrons back to the quantum point contact in two-bounce triangular orbits such as those depicted in Fig. 5.1b. With the point contact located at the origin, the edges of the reflector gates are defined by the equations

$$x = f(\theta)\cos(\theta),\ y = \pm f(\theta)\sin(\theta),\ f(\theta) = \frac{2R_0}{1+\sin(\theta)},\ 12^\circ < \theta < 30^\circ, \quad (5.1)$$

where the angle θ is measured from the x-axis, and $R_0 = 0.975$ μm for the device shown. This makes the separation between the point contact and the reflectors ~ 1.5 μm, and the entire triangular orbit ~ 4 μm. The reflectors are positioned at small values of θ, because our measurements of similar point contacts indicate that the ballistic electron flux from such contacts is collimated about $\theta = 0^\circ$ (see Section 6.2).

In order to examine how the coherent backscattering effect in open microstructures scales with device size, smaller versions of the structures described above were also fabricated (Fig. 5.1c).[5] The point contacts are essentially identical to those of the larger

[5]Ideally, the size dependence would be studied by placing samples of different sizes on the same chip. As will be discussed in Section 5.3, because of conductance fluctuations, multiple identical devices are required

devices, but the other dimensions are all scaled down by a factor of $2^{1/2}$ (i.e., $R_0 = 0.69$), which should result in backscattered trajectories which enclose areas a factor of two smaller than those in the large devices. Another significant design change in the smaller devices is the presence of reflectors on both sides of the point contact. Resistance measurements are made by applying a low-frequency ac bias current across the sample, which implies that the direction of electron current injection through the point contact changes over the course of each cycle. The resistance so measured is the time-average of the device resistance over the course of a cycle. For devices with reflectors on only one side of the point contact, half of the time no coherent backscattering is taking place because electrons are being injected towards the region without reflectors. Our magnetoresistance measurements indicate that the reflectors on opposite sides do not have a detectable effect on one another; i.e. the magnetoresistance of the small devices when the reflectors on both sides of the point contact are defined is equal to the sum of the magnetoresistance with only either the left or right side defined.[6]

5.3 Observation of Coherent Backscattering

Although coherent backscattering is a robust effect in ballistic dots, it was not clear that the backscattered electron flux in our open devices would be sufficient to produce an observable peak in the device resistance. Coherent backscattering in a very open microstructure has only been reported on one previous occasion, and the geometry of that device differed substantially from our own [Taylor, *et al.*, (1995)].[7] The goal of our

---

for accurate study of the coherent backscattering effect. This requirement places stringent space restrictions on our samples. The smaller devices are located on a separate sample (KC7.X).

[6]This dual-sided design increases the size of the coherent backscattering effect. In addition, it provides some averaging for the conductance fluctuations described in section 5.3.

[7]This experiment measured the resistance of two point contacts in series. A peak in magnetoresistance at zero field is attributed to coherent backscattering from very narrow triangular orbits. Taylor, *et al.* believe the reflectors in their structure are the two closely-spaced gates defining opposite sides of a split-gate quantum point contact, which can support triangular orbits if sufficient rounding of the potentials in the

preliminary measurements was to verify the existence of a coherent backscattering effect in our devices. Fig. 5.2 shows three magnetoresistance traces from a single device. The bias voltage defining the quantum point contact is the same for all traces, but in one case (dashed) no bias voltage is applied to the reflectors, while in the other traces, bias voltages sufficient to fully deplete the electrons underneath those gates are applied. A prominent zero-field resistance peak is only present when the reflector gates are depleted, indicating that the peak is related to the electron trajectories reflected from these gates. This evidence, along with the temperature and magnetic field dependences discussed later, allow us to confidently attribute this magnetoresistance peak to coherent backscattering.

In addition to the coherent backscattering peak, other magnetoconductance features appear when the reflector gates are depleted. As seen in the top trace in Fig. 5.2, these features occasionally appear to be periodic. In order to perform a quantitative analysis of the coherent backscattering effect, it is necessary to distinguish interference effects related to time-reversed orbits, from magnetoconductance fluctuations caused by interference between other trajectories. We accomplish this through several averaging techniques.

Averaging can be achieved through simultaneous measurement of multiple devices. For each individual device, coherent backscattering effects are centered around zero field; conversely, the positions of magnetoconductance fluctuations in different devices are uncorrelated in magnetic field, and are therefore averaged in an array. Arrays of identical devices have been employed by other groups studying coherent backscattering in ballistic dots [Chang, *et al.*, (1994)], and were quite effective in suppressing the UCF in the narrow channel measurements described in Chapter 4. Several multiple-device samples were fabricated for our coherent backscattering experiments. The sample with the smaller devices (KC7.X) had four individually tunable point contacts with reflectors on both sides. Because conductance fluctuations associated with reflectors on opposite sides of the same

---

2DEG is assumed. In the collimation experiments described in Chapter 6, we essentially performed an identical experiment to Taylor, *et al.*, but observed no such localization effect, perhaps because our near-surface 2DEG did not allow sufficient rounding of the potentials.

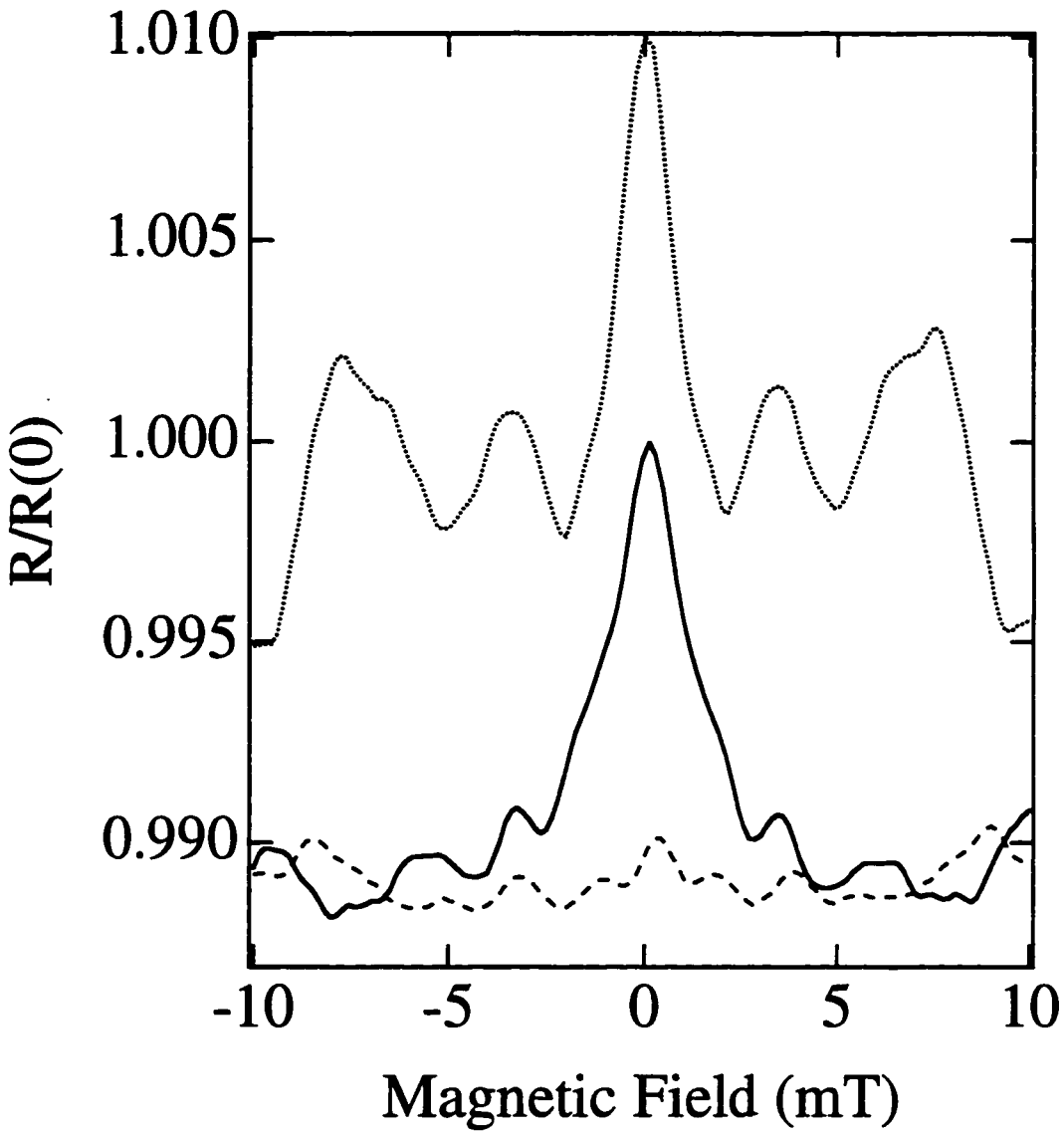

Fig 5.2 Normalized magnetoresistance data from a single device taken with a constant bias applied to the point contact. The bottom trace (dashed) was taken with the reflectors grounded. The solid (dotted) traces were taken with reflector bias voltages of -400 (-500) mV. The curves have been offset for clarity.

point contact are uncorrelated, from an averaging standpoint this sample is equivalent to eight devices with reflectors on only one side of the point contact. For the larger structures, a 5 x 5 array of devices nominally identical to the one pictured in Fig. 5.1b was fabricated (KC7.U). As shown schematically in Fig. 5.3a, there are 5 point contacts in each column, with their associated reflector gates in an adjacent column. Each column of point contacts is controlled by a separate bias voltage, but within a column, it is not possible to independently bias the individual point contacts. The most effective way to check for anomalous point contacts is to compare the behavior of the individual columns. Just past depletion, there was ~20% variation in the resistances of the columns biased at the same voltage, which is consistent with the variation in resistances typically observed in lithographically identical point contacts. In addition, conduction through all of the columns was "pinched off" at nearly the same bias voltage.

Gate voltage averaging techniques were used in conjunction with the multiple-device samples to suppress conductance fluctuations. Both the narrow channel measurements (Chapter 4) and the electron interferometer experiments (Chapter 7) demonstrate that a small (50 mV) change in the bias voltage on a gate changes the position of depletion boundary by less than 10 nm. Therefore varying the bias voltage applied to the reflector gates by this amount produces a negligible change in the areas enclosed by trajectories scattered from these gates. Nevertheless, as illustrated in Fig. 5.2, such small voltage changes are sufficient to completely reshuffle the conductance fluctuations, allowing us to further suppress these fluctuations by averaging magnetoresistance traces taken at several closely-spaced reflector bias values.

Fig. 5.3b is a magnetoresistance trace from the 5 x 5 array of larger devices. The curve shown is the average of 5 traces taken at reflector voltages separated by 50 mV; the individual traces were all quite similar to one another. Note that although the conduction fluctuations have been suppressed, there is still some structure in the magnetoresistance

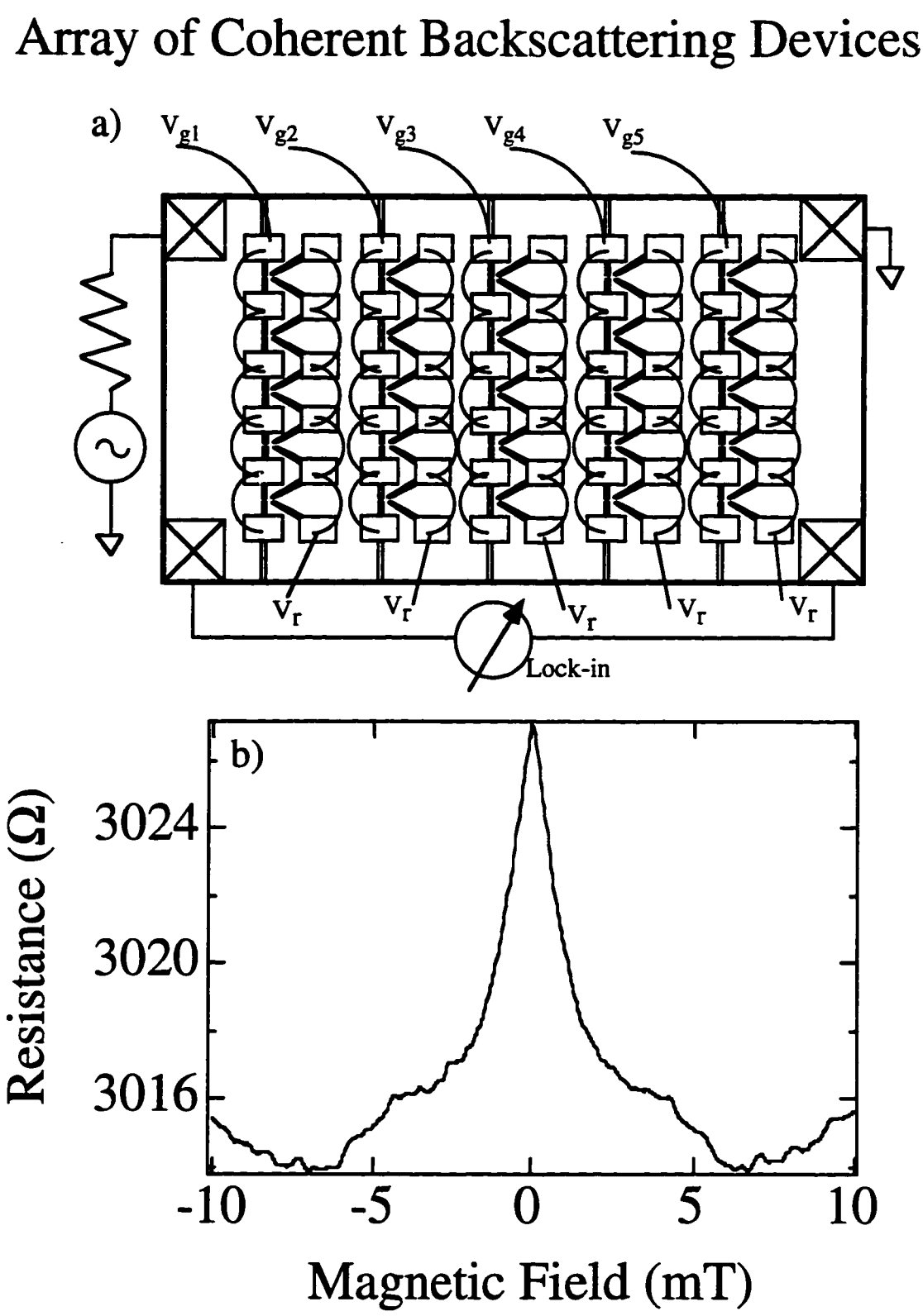

Fig. 5.3 a) Schematic of the 5 x 5 array of open backscattering devices. The sizes of the point contacts and reflector gates have been exaggerated. The wirebonds connecting the 5 devices in each column are also shown. b) Magnetoresistance of the array sample (averaged over 5 reflector voltages). Note that the conductance fluctuations present in Fig. 5.2 have been suppressed.

away from B = 0. Similar structure is also seen in the averaged data for the smaller devices, and may be due to classical collimation effects in the point contacts.

5.4 Analysis of Coherent Backscattering

With the effect of conductance fluctuations averaged away, it is possible to perform a detailed analysis of the coherent backscattering effect in these open structures. This section will discuss how device size, temperature, and the number of transverse modes in the point contact affect the coherent backscattering peak.

Device Size Dependence

In Fig. 5.4 we plot the magnetoresistance of (a) large and (b) small open backscattering devices. The data for the large devices are from the 5 x 5 array, while the data in Fig. 5.4b come from the four small dual-side reflector devices. For both large and small devices, the point contacts were tuned to N = 4 transverse modes.[8] The magnetoresistance curves in Fig. 5.4 are averages of traces taken at five evenly spaced reflector voltages between -0.400 and -0.600 V. The measured resistance of the small devices (which are located in series) is roughly four times larger than that of the 5 x 5 array. For ease of comparison, normalized magnetoresistance values are shown in Fig. 5.4.

Lithographically, the areas in the open structures pictured in Figs. 5.1b and 5.1c differ by a factor of two.[9] The measured half-widths at half-maximum (HWHM) of the coherent backscattering peak for the large and small devices respectively are 0.85 ± .05 mT

[8]Due to the two-fold spin degeneracy, the point contact conductance equals $2Ne^2/h$. Throughout this thesis, the term "number of modes" refers to N.

[9]If the effect of the depletion width is included, this ratio increases slightly (e.g. the ratio is 2.1 for δ = 100 nm). A given depletion width will yield a greater percentage change in area for the small devices.

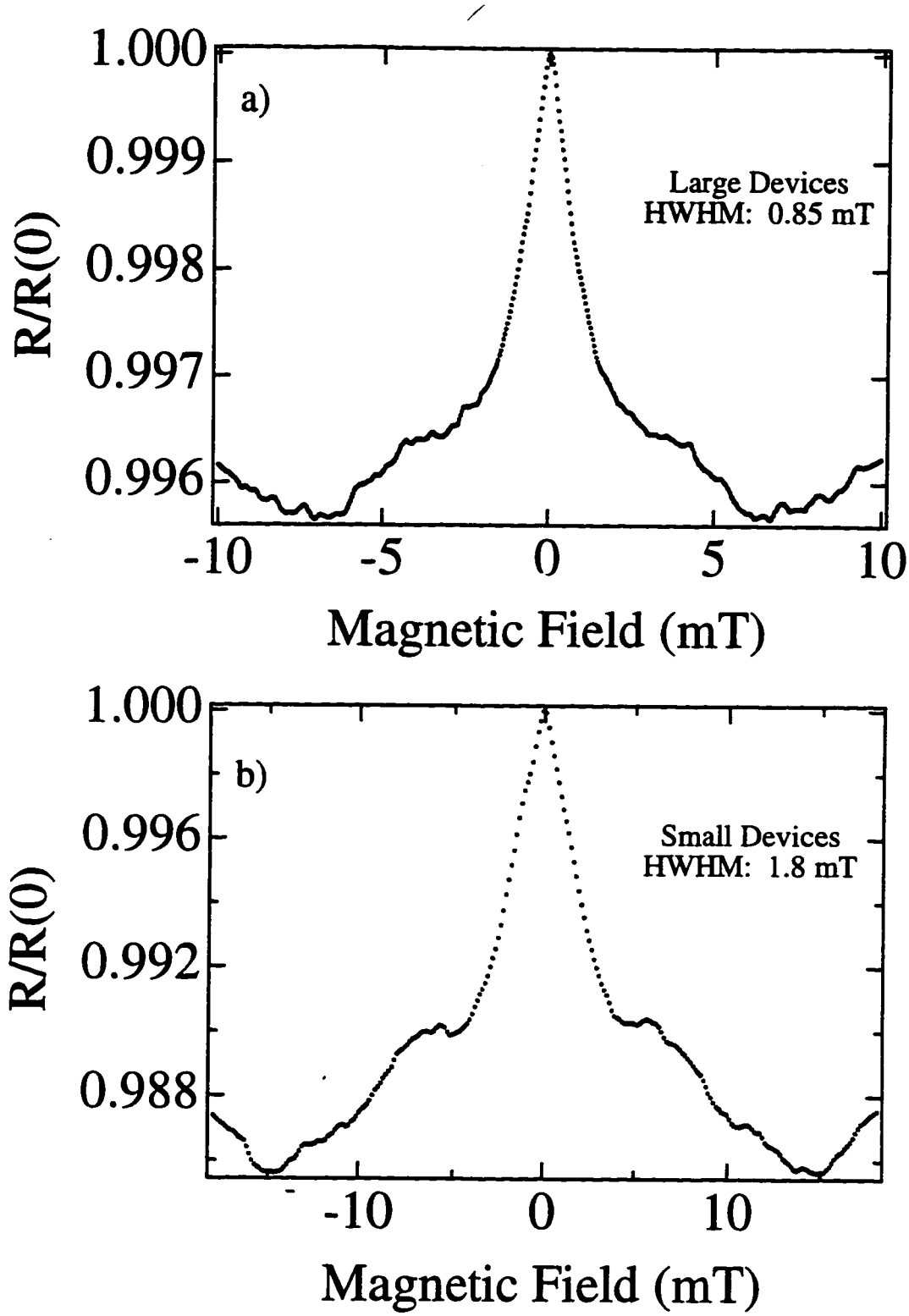

Fig 5.4 Comparison of the averaged coherent backscattering peak in (a) the large and (b) the small devices. The width of the peak scales inversely with the device area. The peak amplitude is larger in the small devices, primarily due to having reflectors on both sides of the point contact.

and $1.8 \pm .2$ mT, where the uncertainties are due to the slow background magneto-resistance variation which makes it difficult to establish a baseline. To within our experimental uncertainty, these widths are inversely proportional to the device area. This scaling of the peakwidth with the device dimensions is another indication that reflections from the electrostatic boundaries (rather than random impurity scattering) produce the backscattered trajectories in our structures.

Fig 5.4 also shows that the amplitude of the coherent backscattering peak for the small devices is more than a factor of two greater than the amplitude of the large devices. As mentioned earlier, the coherent backscattering effect should be enhanced by a factor of two in the small devices, because those devices have reflectors on both sides of the point contact. It is not surprising that the amplitude difference is somewhat larger than this factor of two. As discussed in the next paragraph, the ballistic phase coherence length should easily exceed 50 μm at 385 mK, essentially making all backscattered trajectories in both the large and small devices fully phase coherent. The mean free path, however, is only 5.4 μm, so elastic scattering doubtless prevents some of the trajectories which strike the reflector gates from returning to the point contact. The larger devices would lose a greater number of backscattered trajectories to such effects, resulting in a smaller coherent backscattering peak.

Temperature Dependence

In Fig. 5.5a, we show magnetoresistance data from a single large device taken at 0.385 K and 1.41 K. At the higher temperature, the phase coherence length is shorter, leading to an attenuation of quantum interference effects like coherent backscattering.

The effect of phase breaking on the amplitude of the coherent backscattering effect in quantum dots has recently been analyzed using random matrix theory [Baranger and Mello, (1995)] and semiclassically [Aleiner and Larkin, (1996)]. In ballistic dots in which

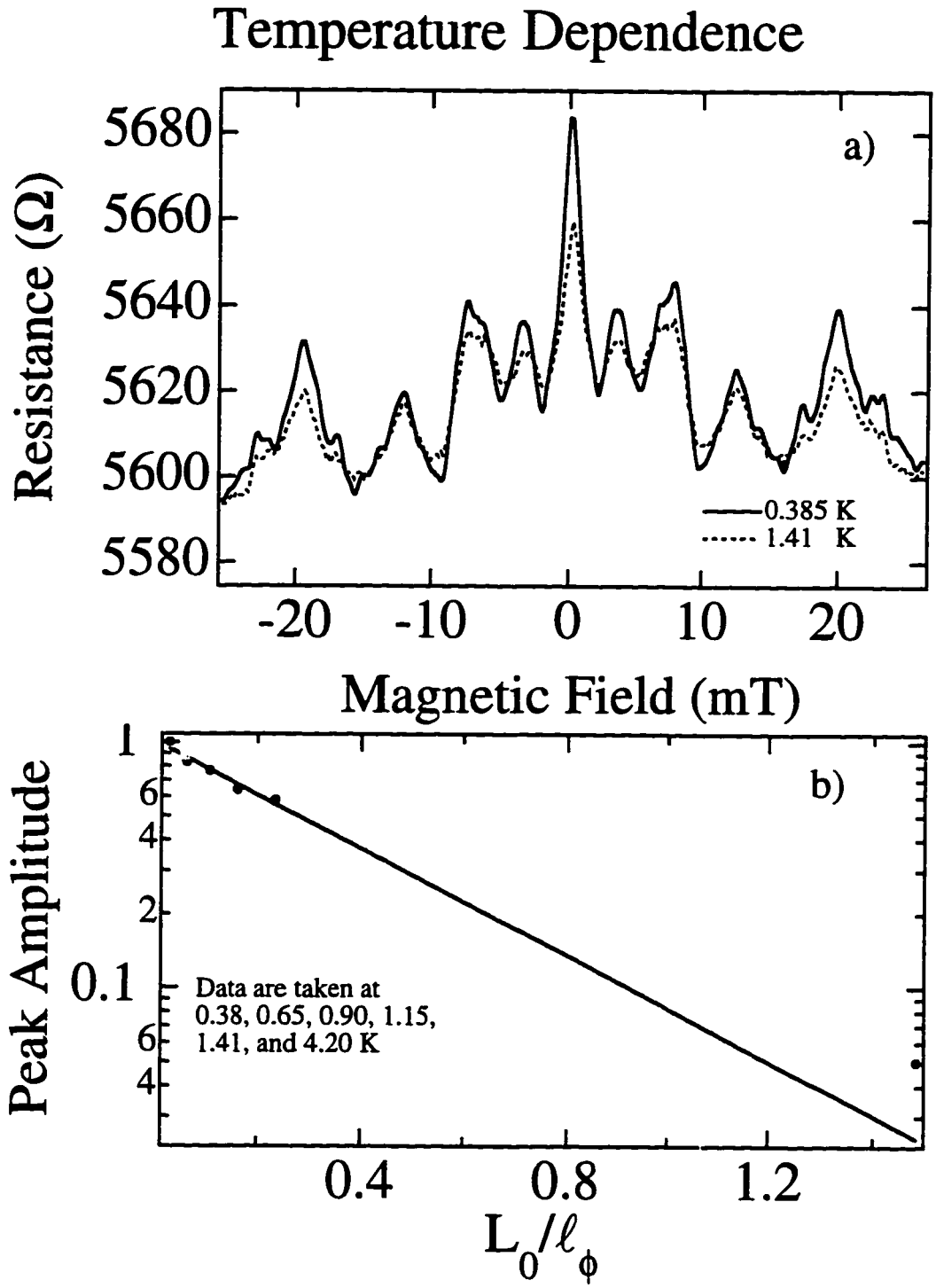

Fig. 5.5 a) Data from a single device shows the decrease in amplitude of both the central peak and the secondary oscillations with increasing temperature. b) For each of the six temperatures listed, we plot the average amplitude of the coherent backscattering peak vs. L_0/ℓ_ϕ, where ℓ_ϕ is calculated from Eq. (4.22). The solid line is a fit illustrating the exponential decay of the amplitude with decreasing phase coherence length.

electrons typically experience many collisions with the device walls before exiting, there exists a broad distribution of pathlengths, F(L), for backscattered trajectories. If the point contacts are sufficiently narrow,[10] the distribution of backscattered trajectory lengths is roughly constant. The amplitude of the coherent backscattering effect, δG, is proportional to the number of phase-coherent backscattered trajectories:

$$\delta G \propto \int_0^\infty e^{-L/\ell_\phi} F(L) dL \propto \ell_\phi. \qquad (5.2)$$

At low temperature, the ballistic phase coherence length, ℓ_ϕ, is proportional to T^{-2}, creating a power law dependence between δG and temperature.

No similarly broad distribution of trajectory lengths contributes to coherent backscattering in our open structures. Assuming coherent backscattering is dominated by triangular orbits such as those depicted in Fig. 5.1b, nearly all of the backscattered trajectories will have the same pathlength, $L = L_0$, the perimeter of the triangle. In this case, the amplitude of the coherent backscattering peak depends exponentially on the phase coherence length, $\delta G \sim \exp(-L_0/\ell_\phi)$. In Fig. 5.5b, we plot the measured amplitude of the coherent backscattering peak versus L_0/ℓ_ϕ. At each temperature, the data are the average amplitude for a single device (KC7.T) measured at five different reflector voltages, normalized such that the amplitude of our lowest temperature is unity. Identical magnetoresistance measurements were performed at .385, .65, .90, 1.15, 1.41, and 4.2 K. From the geometry of the device, L_0 is known to be approximately 4 μm. For each temperature, we estimate ℓ_ϕ as $v_f\tau_\phi$, where τ_ϕ is calculated from Eq. (4.22). The linear decay of the amplitude in the semi-log plot indicates an exponential, rather than power law, dependence on ℓ_ϕ. Fitting our data to $\exp(-\alpha L_0/\ell_\phi)$, we find $\alpha = 2.4$. That α is larger

[10]This insures that the phase coherence length rather than escape through the leads establishes the trajectory length cutoff for contribution to coherent backscattering.

than unity may be an indication that the actual phase coherence length is somewhat shorter than that estimated using Eq. (4.22).

Mode Dependence

We have obtained some data on how the coherent backscattering effect in our devices scales with N, the number of transverse modes in the quantum point contact. In Fig. 5.6a, magnetoresistance data from the 5 x 5 array of large devices is shown. As shown in Fig. 5.3a, the columns of point contacts may be biased separately, but there is no way to individually bias or measure the point contacts in each column. For the N = 5 data, each column was biased such that the resistance of that column equaled $(1/50)h/e^2$, which corresponds to the resistance of five parallel point contacts, each of which is transmitting 5 spin-degenerate modes. Likewise, for the N = 4 data, each column was biased such that its resistance equaled $(1/40)h/e^2$. For both values of N, the data shown in Fig. 5.6a are averaged over the same 5 reflector gate voltages. The peaks of these two normalized traces practically lie on top of one another, which indicates that ΔR_{cb}, the amplitude of the coherent backscattering peak, scales linearly with the point contact resistance: $\Delta R_{cb} \propto R$. The same scaling behavior was observed in our circle vs. pacman quantum dot experiments.

Unfortunately we were not able to study a wide range in the number of transverse modes. Larger numbers of transverse modes were inaccessible because N was less than 6 at depletion. As discussed in Chapter 2, our point contacts often exhibit switching noise — the behavior of which worsens as N is lowered. For the array, this switching noise made measurements with $N < 4$ virtually impossible.[11] It was possible to extend our measurements to N = 3 modes for the sample with the four small devices. This sample had

[11] In hindsight, it seems rather miraculous that the array worked as well as it did. Even if the yield for switch-free point contacts were 95% (it's closer to 50%) there would only be a 25% chance that all 25 devices would be free of this problem.

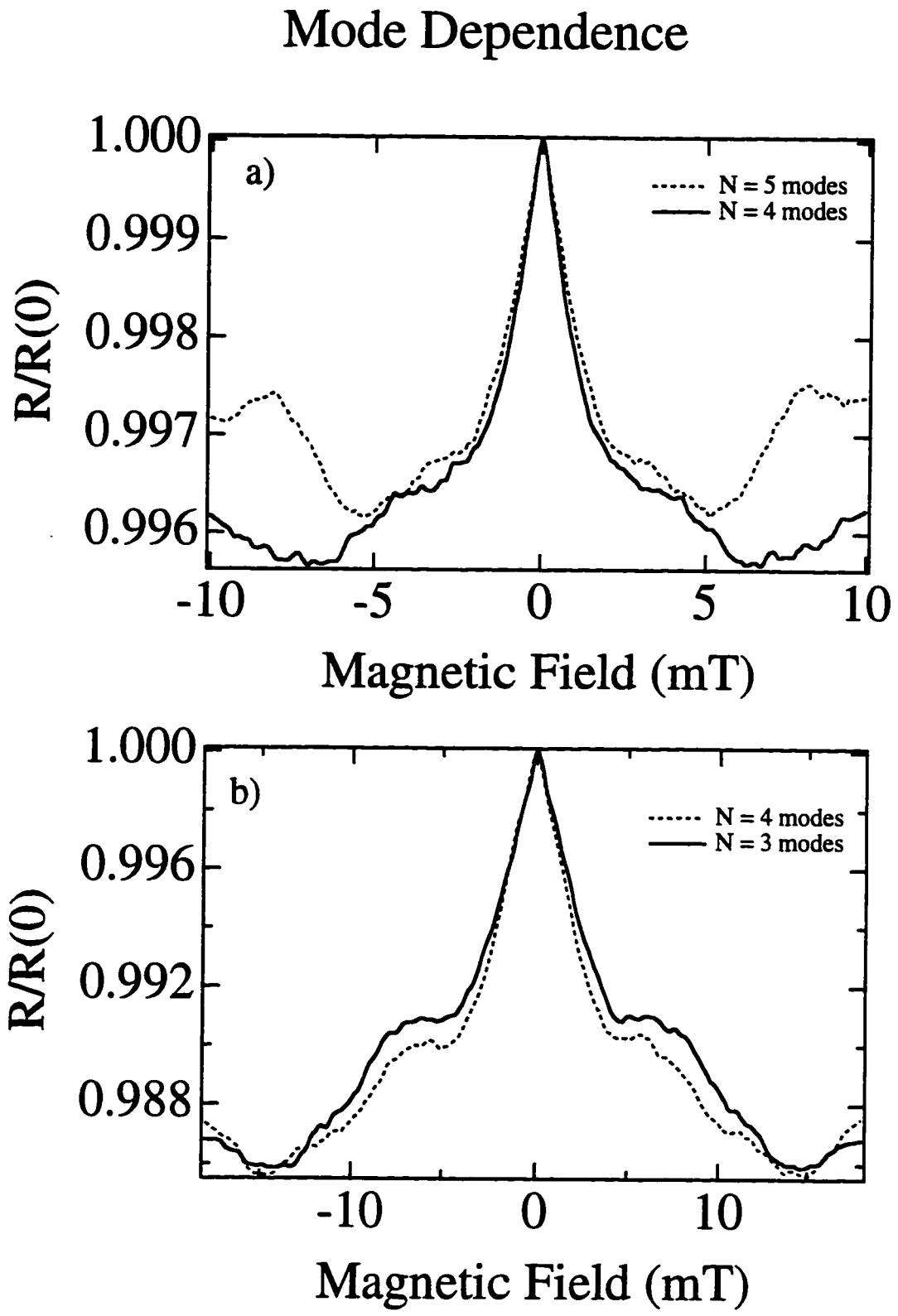

Fig. 5.6 Averaged magnetoresistance data for (a) the array of large devices and (b) the smaller devices. The similarity of normalized curves with different numbers of modes indicates that the amplitude of the coherent backscattering correction is proportional to the device conductance.

the added advantage that we could individually tune and measure each point contact. As shown in Fig. 5.6b, we still observe approximately linear scaling between the device resistance and the amplitude of the coherent backscattering effect. Unfortunately, switching events in this sample prevented measurements with fewer transverse modes.

5.5 Lineshape

In the quantum billiard experiments discussed in the introduction to this chapter, the backscattered trajectories enclose a wide distribution of areas. As the perpendicular magnetic field increases, the phase shift generated between pairs of time-reversed orbits grows in proportion to the area which they enclose, contributing to a single peak in the device magnetoresistance centered around zero field, the lineshape of which is determined by the nature of the trajectory distribution.

The situation is quite different for our devices. Due to the narrow angular range subtended by the reflectors, many of the electrons injected through the QPC do not strike a gate, and, therefore, cannot contribute to a coherent backscattering effect. In the absence of disorder, the only contributions to coherent backscattering would come from time-reversed pairs of trajectories like those illustrated in Fig. 5.1b. Furthermore, our device is so open that almost no multiple-loop trajectories should exist. In theory, our devices could approach a limit in which all of the backscattered trajectories enclose the same area, 2S, where S is the area of the inscribed triangular orbits.[12] In this limit, a perpendicular magnetic field induces a phase shift equal to $4\pi\frac{e}{h}SB$ between all paired trajectories. Therefore, rather than a single magnetoresistance peak, coherent backscattering in the same-area limit produces oscillations in the resistance with a period equal to:

[12]The factor of two is present since coherent backscattering is sensitive to the phase difference between the pairs of time-reversed orbits.

$$\Delta B = \frac{h}{2eS}. \tag{5.3}$$

Previously, periodic oscillations due to coherent backscattering have been observed using Aharonov-Bohm geometries in which the narrow arms of the rings constrain all backscattered trajectories to enclose very nearly the same area [for a review of these experiments see Aronov and Sharvin, (1987)].

As shown in Fig. 5.5a, some of the magnetoresistance traces from individual devices exhibit oscillations whose period closely matches that expected for coherent backscattering. Oscillations resulting from coherent backscattering, however, should be robust to averaging. The absence of a periodic resistance modulation in our averaged data suggests oscillations occasionally observed in individual devices are magnetoresistance fluctuations not related to time-reversed trajectory pairs. Since the expected periodic modulation of the coherent backscattering effect appears to be absent in our samples, it is necessary to consider why this might be so.

One reason is that in real devices, every backscattered trajectory cannot enclose the same area. This broadening of the distribution of enclosed areas suppresses the periodic modulation of coherent backscattering. To illustrate this, consider a simplified model of the trajectories in our devices in which all of the backscattered orbits return to the point contact in triangular orbits like those illustrated in Fig. 5.1b. In a semiclassical approximation, we can calculate ΔR, the resistance increase due to these trajectories, by squaring the sum of the probability amplitudes, A_i, of the individual backscattered orbits:

$$\Delta R \propto \left|\sum_i A_i\right|^2 = \sum_i |A_i|^2 + \sum_{i \neq j} A_i A_j^*. \tag{5.4}$$

The first term is the classical contribution of the backscattered trajectories to the device resistance, while the second term considers the quantum interference effects. The solid line

in Fig. 5.7a shows the periodic modulation of ΔR assuming all of the backscattered trajectories enclose identical areas equal to the 0.62 μm^2 lithographic area of the large devices. Suppose instead these triangles enclose a distribution of areas. Fig. 5.7a also shows calculations for ΔR assuming there exists a Gaussian distribution of enclosed areas centered around 0.62 μm^2. As the width of the this Gaussian distribution increases, the secondary oscillations are averaged away.

In real devices, there are several potential sources of area broadening. First, in order to have a substantial number of backscattered electron trajectories, it is necessary to give the reflectors finite spatial extent. Because of this, the triangular areas enclosed by trajectories that strike different spots on the reflectors can vary by as much as 25%. Although this broadening of the area distribution will dampen successive oscillations, it is not sufficient to suppress the oscillations in less than one period.

Size variation among the elements of the array is another potential source of area broadening. We have, however, inspected our devices and found no detectable lithographic variation in the array. Of course, by averaging data taken at different gate voltages, we are intentionally varying the enclosed trajectory areas. As mentioned earlier, though, we use gate voltages that are spaced closely enough so that the resulting variation is an insignificant fraction of the total enclosed area.

Elastic scattering likely also contributes to any area broadening effects. The elastic mean free path in our system is 5.4 μm, only about a micron longer than the pathlength of a typical triangular orbit in a large device. Considering these dimensions, elastic scattering should play a major role in our experiment. We expect that small-angle scattering events create a distribution of enclosed areas very similar to the Gaussian distribution of our model. Large angle scattering events could have a more dramatic impact on the trajectory distribution, especially if they permit backscattered trajectories that do not strike both reflectors to exist.

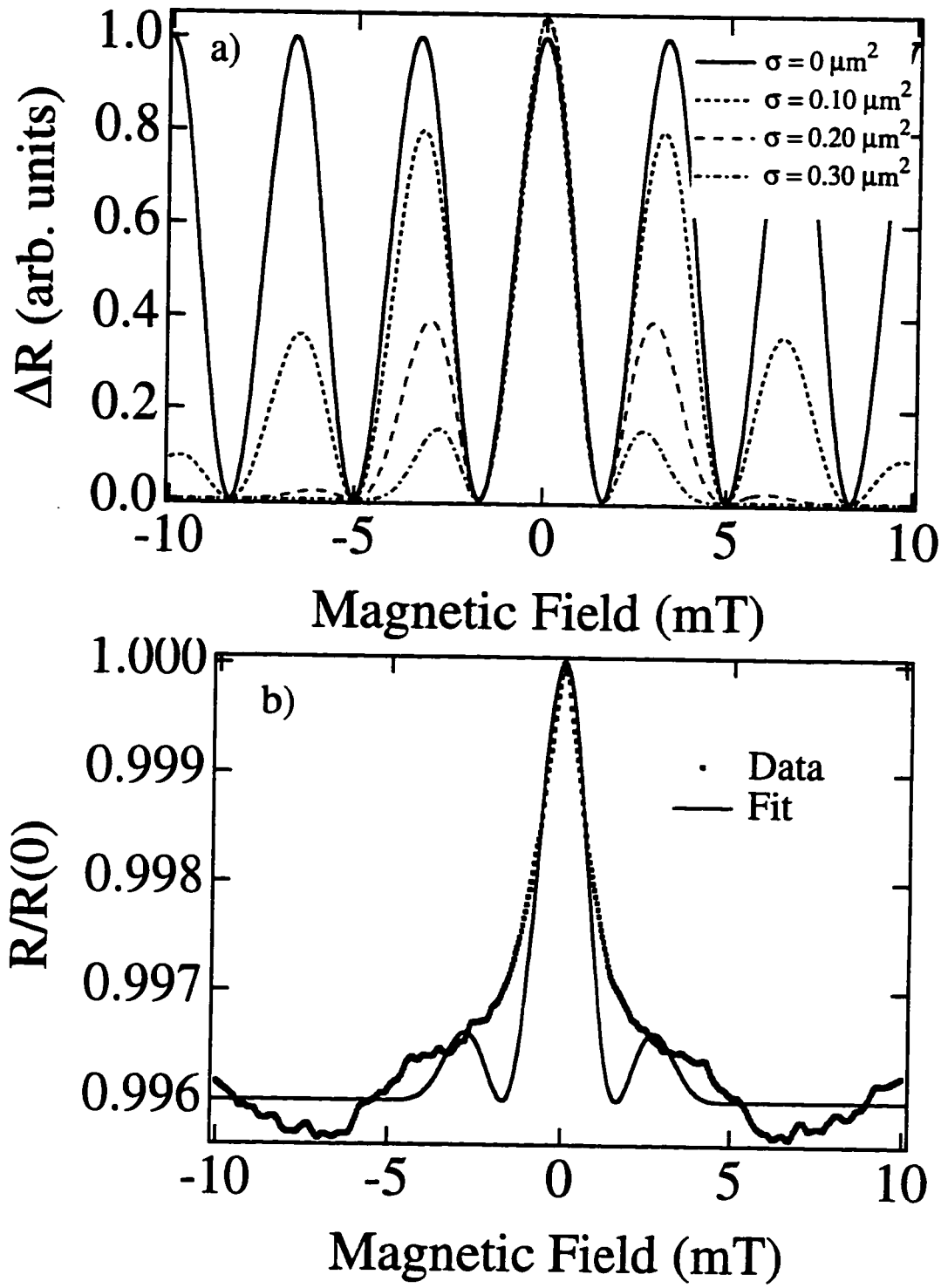

Fig. 5.7 a) The coherent backscattering correction to the device resistance, ΔR, calculated assuming a Gaussian distribution of enclosed areas. The solid trace assumes that there is no broadening about the central value of 0.62 μm^2. b) We fit the $\sigma = 0.30\ \mu m^2$ trace from (a) to data from the large array with the amplitude as the only free parameter.

Although our lithography allows us to precisely pattern the reflector gates on the surface, the shape of the actual electrostatic depletion boundary in the 2DEG beneath these gates is not fully known. It is, however, likely that some of the focusing from the precise lithographic shape of the reflectors (Eq. 5.1) is lost. In general, any sharp surface features become rounded in the electron gas. As a result, the corners of the reflectors are probably somewhat rounded in the 2DEG. Such rounding could have important consequences. Although trajectories that travel from the point contact, strike a gate, and return directly to the point contact are not supported by our lithographic device design, rounding of the reflector edges could make such single-reflection backscattered trajectories possible.

As shown in Fig. 5.7a, broadening of the distribution of enclosed trajectories suppresses the secondary coherent backscattering oscillations, but has very little effect on the shape of the central peak. In Fig. 5.7b, we fit the lineshape calculated from our model based on a Gaussian distribution of enclosed triangular areas about a central area, S_0, to the averaged data from the large array. Since we observe no secondary oscillations in our data, we have arbitrarily chosen a large enough value for the standard deviation of the Gaussian distribution so that these oscillations are strongly damped ($\sigma = 0.5S_0$). S_0 is fixed equal to the average lithographic area of the inscribed triangular orbits (0.62 μm^2); the only free parameter in the fit is the amplitude of the localization correction. Near zero-field, the fit matches the data from the array quite well. At higher fields, however, the tails of our experimental data lie well above the fit, indicating that there is a more significant contribution from small-area backscattered trajectories in real devices than uniform area broadening would predict. As described in the preceding paragraphs, both impurity scattering and rounding of the device walls could create backscattered trajectories that return directly to the point contact after striking the reflector. Such orbits could be responsible for the small-area tails in the data.

5.6 Summary

In this chapter, we examined coherent backscattering in very open ballistic microstructures. The zero field resistance peak associated with coherent backscattering is only present when the reflector gates are defined. In addition, the temperature dependence of the peak amplitude and the scaling of the peak width with device size both indicate that this coherent backscattering results from trajectories scattered from the reflector gates.

Although our devices should allow several periodic oscillations associated with coherent backscattering to be visible, no such structure is seen in the averaged data. This is likely due to experimental imperfections (e.g. small-angle scattering, boundary roughness, shape distortion) inherent to experiments in 2DEG systems. It is therefore not surprising that it has been difficult to observe the periodic magnetoconductance oscillations in quantum dots which are expected to exist as a result of scarred orbits. Quantum billiards fabricated in 2DEG systems will suffer from these same experimental imperfections, which could easily suppress periodic oscillations in such structures.

Chapter 6

Quantum Interference of Forward-Scattered Ballistic Electrons

6.1 Introduction

The previous chapter examined interference effects which arise when electrons injected by a quantum point contact are reflected back into that point contact. In this chapter we consider a complementary group of experiments, in which electrons are injected by a quantum point contact and travel towards a second point contact. If the separation between the point contacts is shorter than the phase coherence length, the forward-scattered electrons may interfere with one another at the second point contact.

Before discussing these quantum interference experiments, this chapter begins with a discussion of collimation effects which are present in quantum point contacts. These effects impose rather stringent limitations on the device geometries for which quantum interference effects may be observed when point contacts are used as coherent electron sources and detectors.

The remainder of the chapter is devoted to experiments involving quantum interference of forward-scattered ballistic electrons. The devices studied are designed such that there are two sets of electron trajectories that connect the point contacts: a group that moves directly between them, and a group that must strike a reflector gate in order to reach the second point contact. Throughout this chapter, these structures will be referred to as forward-scattering interference devices (FIDs). Section 6.3 deals with interference effects which are observed when the bias voltage on the reflector gate is varied. Such variation shifts the position of the electrostatic boundary in the 2DEG, which changes the pathlength of the reflected trajectories. When used in this manner, the forward-scattering interference

devices act like electron interferometers. Section 6.4 describes experiments in which a perpendicular magnetic field is used to induce a phase shift between the electron trajectories which traverse the device.

6.2 Point Contact Collimation

With the exception of the narrow channel devices in Chapter 4, all of the quantum interference experiments presented in this thesis use quantum point contacts as coherent electron injectors and detectors. As a result of collimation effects, the angular distribution of electrons transmitted by a quantum point contact can be quite narrow. It is important to consider these collimation effects when designing device geometries. For example, in the coherent backscattering experiments described in the previous chapter, the reflector gates needed to be located at angles less than 30°, because at larger angles there are virtually no injected electrons available for backscattering. In this section, we will briefly discuss the origin of collimation in quantum point contacts. In addition, an experimental determination of the collimation in our point contacts will be described.

Collimation in quantum point contacts is a classical effect that was first explained by Beenakker [Beenakker and van Houten, (1989)]. In the absence of collimation effects, one would expect an angular injection distribution proportional to $\cos(\alpha)$, which reflects the $\cos(\alpha)$ distribution of the flux incident on the point contact. Collimation effects abruptly truncate this distribution for angles greater than some critical angle, α_{max}. Assuming the point contact gradually opens from its narrowest point, W_{min}, to a maximal width, W_{max}, all electrons that approach the point contact from an angle larger than this critical angle will be reflected. This critical angle is equal to

$$\alpha_{max} = \arcsin\left(\frac{1}{f}\right); \qquad (6.1a)$$

with the collimation factor, f, given by the product:

$$f = \left(\frac{v_f}{v_f^{pc}} \right)^{1/2} \frac{W_{max}}{W_{min}}, \qquad (6.1b)$$

where v_f^{pc} is the Fermi velocity for electrons at the point at which they encounter the largest potential barrier in the quantum point contact, and v_f is the Fermi velocity in the wide 2DEG regions.

The first factor in Eq. (6.1b) results from any electrostatic potential barrier that may exist in the point contact, and is known as barrier collimation. A potential barrier lowers the velocity of electrons in the point contact region. Electrons striking this barrier at angles greater than arcsin(v_f^{pc}/v_f) from the normal are reflected; this is analogous to the total internal reflection which occurs in optics. For point contacts several times wider than the Fermi wavelength, such barrier collimation is relatively unimportant, but these effects can become significant as the number of transverse modes decreases.

The second factor in Eq. (6.1b) is a purely geometrical horn collimation effect. If the contact opens gradually from W_{min} to W_{max}, all electrons attempting to enter from an angle greater than arcsin(W_{min}/W_{max}) will be backscattered via a series of specular reflections from the potential boundaries. From the lithographic design of our point contacts (Fig. 6.1a), it might appear that such horn collimation effects would be negligible. In the 2DEG there is, however, considerable rounding of the electrostatic gate boundaries.[1] When the gates are negatively biased such that N transverse modes are being transmitted by the point contact, it is plausible to assume that $W_{min} \sim N\lambda_f$, while W_{max} is closer to the lithographic width of the point contact.

[1] A detailed simulation of the potential contours in the 2DEG for a quantum point contacts has been performed by M. Stopa [Bird, *et al.*, (1994)].

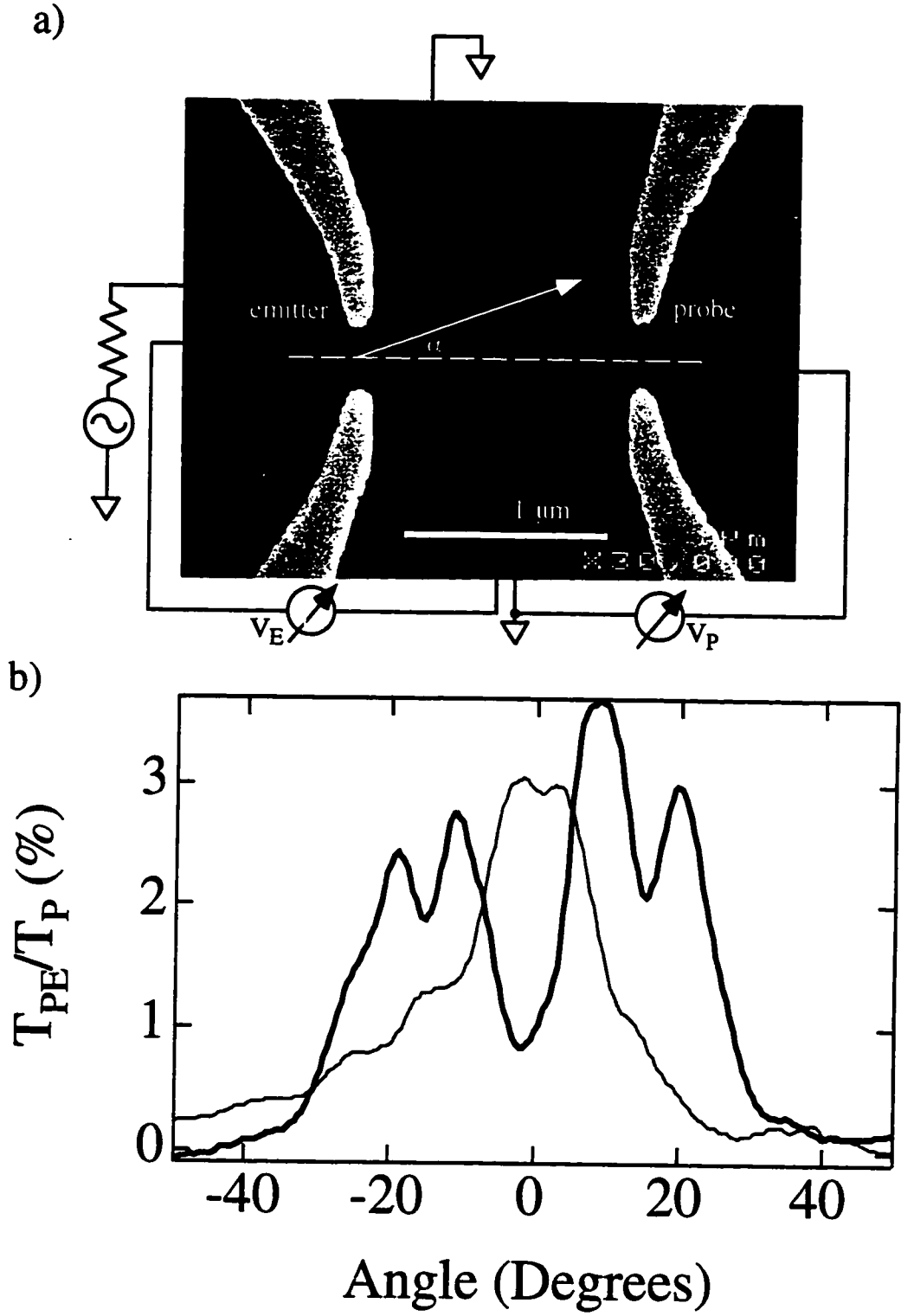

Fig. 6.1 a) SEM photo of a device used in the point contact collimation experiment. Included is a schematic illustrating the dual lock-in measurement technique described in the text. b) Plot of the percent of the injected flux that travels ballistically from the emitter to the probe as a function of the angle of injection for two different devices. In both devices there exists a strong collimation effect with α_{max} ~ 30 degrees, although additional structure is present in one device.

If two point contacts are placed near one another in series, because of collimation effects there will be a number of electrons that travel ballistically through both point contacts. Application of a perpendicular magnetic field produces a Lorentz force that deflects the collimated electron beam and inhibits direct transport through the series contacts. By measuring the direct transport as a function of the perpendicular field, a determination of the point contact collimation can be made in such a system [Molenkamp, *et al.*, (1990)].

In order to measure the collimation effect in our point contact design, we performed a measurement very similar to that of Molenkamp, *et al.* As shown in Fig. 6.1a, each device consists of a pair of aligned quantum point contacts separated by L = 1.2 μm. The lithographic width of the point contacts is 250 nm. Three identical devices were fabricated on sample KC7.C (570 Å gas depth, ℓ = 5.4 μm). The sample was aligned perpendicular to the magnetic field in the ^{3}He cryostat, and measurements were made at 4.2 K. As a result of direct transmission between the point contacts, the series resistance of the contacts is less than the sum of their individual resistances. However, even with collimation effects, only a small fraction of the injected electrons are transmitted directly between the pair of contacts. Hence, the percentage change in the series resistance that occurs when a magnetic field deflects the collimated direct flux is quite small. A much larger percentage change may be observed by directly measuring the fraction of the injected flux that is transmitted through the second point contact.

The technique used to accomplish this is shown schematically in Fig. 6.1a. There are ohmic contacts in the region between the point contacts, as well as on both sides. The left point contact in Fig. 6.1a is denoted as the emitter, and the right point contact as the probe. An ac bias current flows between an ohmic contact on the left-hand edge of the sample and one in the grounded central region; this results in the injection of electrons through the emitter. A lock-in is used to measure the size of the resulting voltage, V_E. Because some of the injected electrons will travel directly through the probe contact before

they may equilibrate with the ground reservoir, a voltage drop, V_P, will develop across this point contact. We simultaneously measure V_P with a second lock-in. Using the Landauer-Büttiker formalism described in Chapter 1, it is easy to show that the voltage developed across the second point contact is:

$$V_P = V_E \frac{T_{PE}}{T_P}, \tag{6.2}$$

where T_{PE} is the coefficient for direct transmission from emitter to probe, and T_P, the transmission coefficient of the probe, is equal to the number of modes in the point contact: $T_P = (h/2e^2)G_P = N_p$. Since there is no net current flow through the probe contact, Eq. (6.2) can also be obtained by simply balancing the current incident on the probe[2] ($I_E T_{PE}/N_E$) against the current that flows in response to it ($G_P V_P$). In our collimation measurements, we tune the conductance of both point contacts to the same number of modes; i.e. $T_P = T_E$. In this case, Eq. (6.2) may be expressed as: $V_P/V_E = T_{PE}/T_E$; in other words, the ratio V_P/V_E represents the fraction of the injected current that moves directly from emitter to probe.

Fig. 6.1b is a plot of this fraction as a function of the applied perpendicular field.[3] At any given value of the magnetic field, the Lorentz force will focus the electrons injected at the angle α into the probe contact,

$$\alpha = \frac{L}{2\ell_{cyc}}. \tag{6.3}$$

---

[2]Recall from Chapter 1 that T_{ji}/N_i is the fraction of the current in lead i transmitted to reservoir j.

[3]Experimentally, there is always some offset voltage present in V_P, and this offset has been subtracted from the data in Fig. 6.1b (and elsewhere in the chapter). We determine this offset by requiring that the plateau in the value of T_{PE}/T_P that occurs at high field should correspond to zero direct transmission between the point contacts.

For the horizontal axis in Fig. 6.1b, this relation has been used to convert the applied magnetic field into the corresponding injection angle. Data from two separate devices is displayed in the figure; in both cases, the point contacts were tuned to N = 2 modes. In one case (the light line) there is a single peak centered around zero degrees. This behavior was observed in two of our three devices and is similar to that reported by Molenkamp, *et al.* For one device (the darker line), there is a more complex structure in the angular injection of the ballistic current. These measurements were made at 4.2 K with bias currents large enough to suppress any quantum interference effects. The dip in the direct transmission at zero degrees is therefore a classical effect, which is probably the result of an impurity located between the two point contacts. In both devices, α_{max} is approximately 30°, which corresponds to a collimation factor of f = 2.

In the experiments of Molenkamp, *et al.*, the collimation factor was found to increase as the number of transverse modes in the point contacts was reduced. Barrier collimation effects are likely more important in narrow contacts, and horn collimation effects probably also increase as the contact is further constricted. There is, however, a limit to how large these collimation effects can become. As the width of the point contact approaches the Fermi wavelength, diffraction effects begin to destroy the collimation of the injected electrons. In the diffraction limit ($k_f W << 1$), collimation effects are no longer expected, and the angular distribution of injected electrons should be proportional to $\cos^2\alpha$. Since some of the measurements in Chapter 7 involve point contacts with resistances over 1 MΩ, an experimental determination of the distribution of injected electrons in this diffraction limit would have been useful. Unfortunately, such a determination was not possible, because in none of our three devices were both point contacts stable in the tunneling regime.

Forward-Scattering Interference Devices

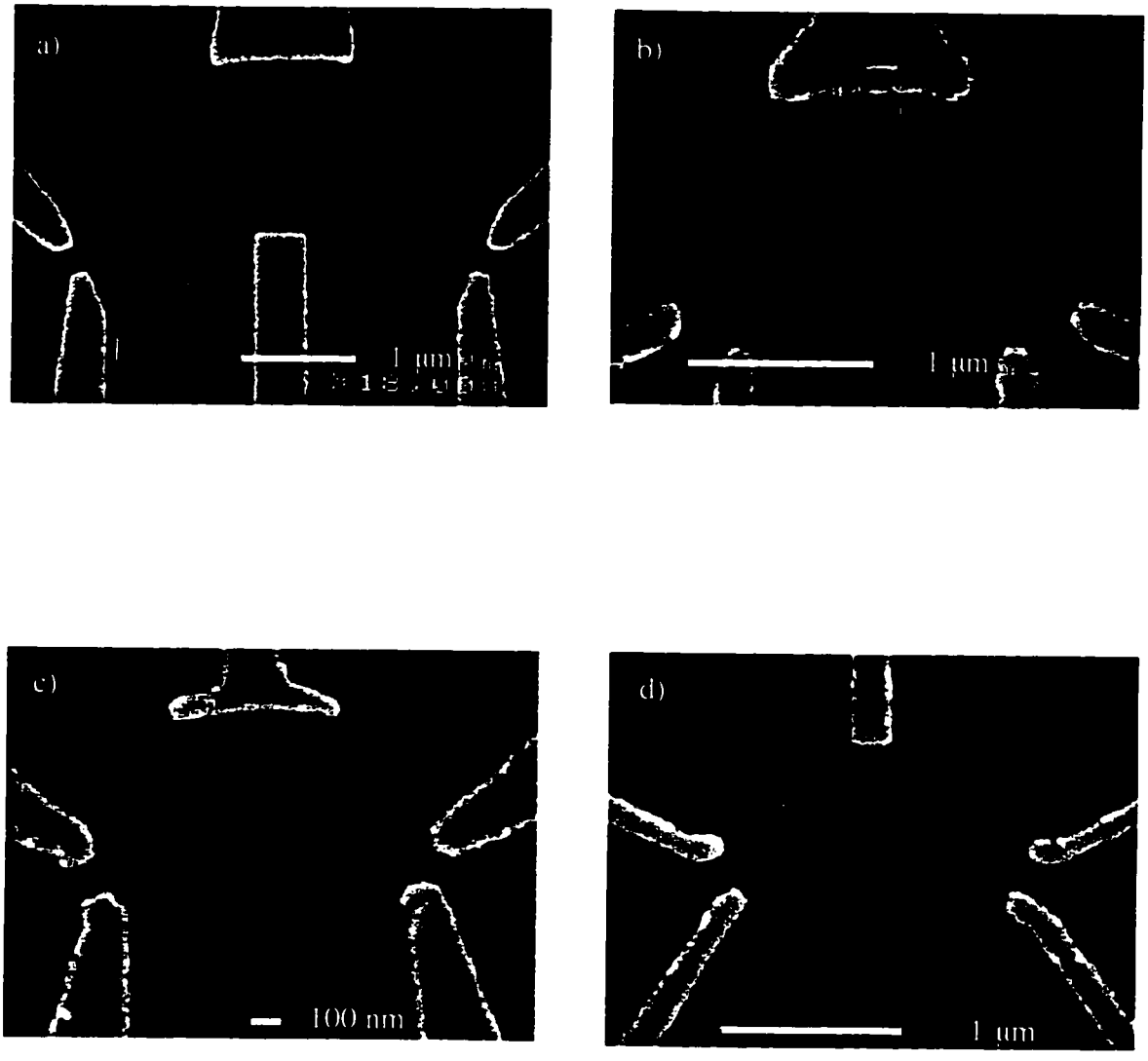

Fig. 6.2 SEM photos of four of the over one dozen forward-scattering interference devices measured in our experiments. All devices consist of a pair of quantum point contacts and an elliptical arc designed to reflect trajectories injected from one point contact into the other. The size, injection angle, and arc length are varied in the different devices. The additional gate shown in device (a) was usually grounded.

6.3 Electron Mirror Interferometers

Fig. 6.2 shows four of the over one dozen forward-scattering interference devices that were measured. Although the specific geometries of the devices differs, they are all designed to produce two *distinct* groups of electron trajectories that move ballistically between the point contacts. One of these groups consists of electrons that move directly between the point contacts. The other group of trajectories must strike the reflector gate in order to reach the second point contact. The reflector gate is an elliptical arc whose foci are located at the centers of the two point contacts. If reflections from this gate are specular, electrons injected towards the reflector from the emitter point contact should be focused onto the probe contact. This focusing should survive in the presence of trajectory bending produced by a perpendicular magnetic field. Using the same dual lock-in measurement technique described in Section 6.2, it is possible to measure the fraction of the injected current that is transmitted through the probe point contact.

In this section, we discuss periodic oscillations in T_{PE} that are observed by sweeping the negative bias voltage applied to the reflector gate. When the gate voltage is swept, the depletion boundary of the reflector in the 2DEG changes, changing with it the pathlength of all of the reflected trajectories. Because the pathlength of all reflected trajectories changes by nearly the same amount as the gate voltage is swept, varying the gate voltage does not create phase shifts among the different reflected orbits. Conversely, changing the reflector gate voltage does create a phase shift between all reflected and direct trajectories, since the direct trajectories are unaffected by the change in the reflector bias.

In Fig. 6.3a, we plot T_{PE}/T_P as a function of the bias voltage applied to the reflector gate. The data shown were taken at 1.4 K using the device pictured in Fig. 6.2a. The rectangular gate between the two point contacts can be ignored, as it was grounded during the measurements. As the negative bias voltage on the reflector gate is increased towards its depletion value (~ -0.3 V), a larger percentage of the electrons incident on the

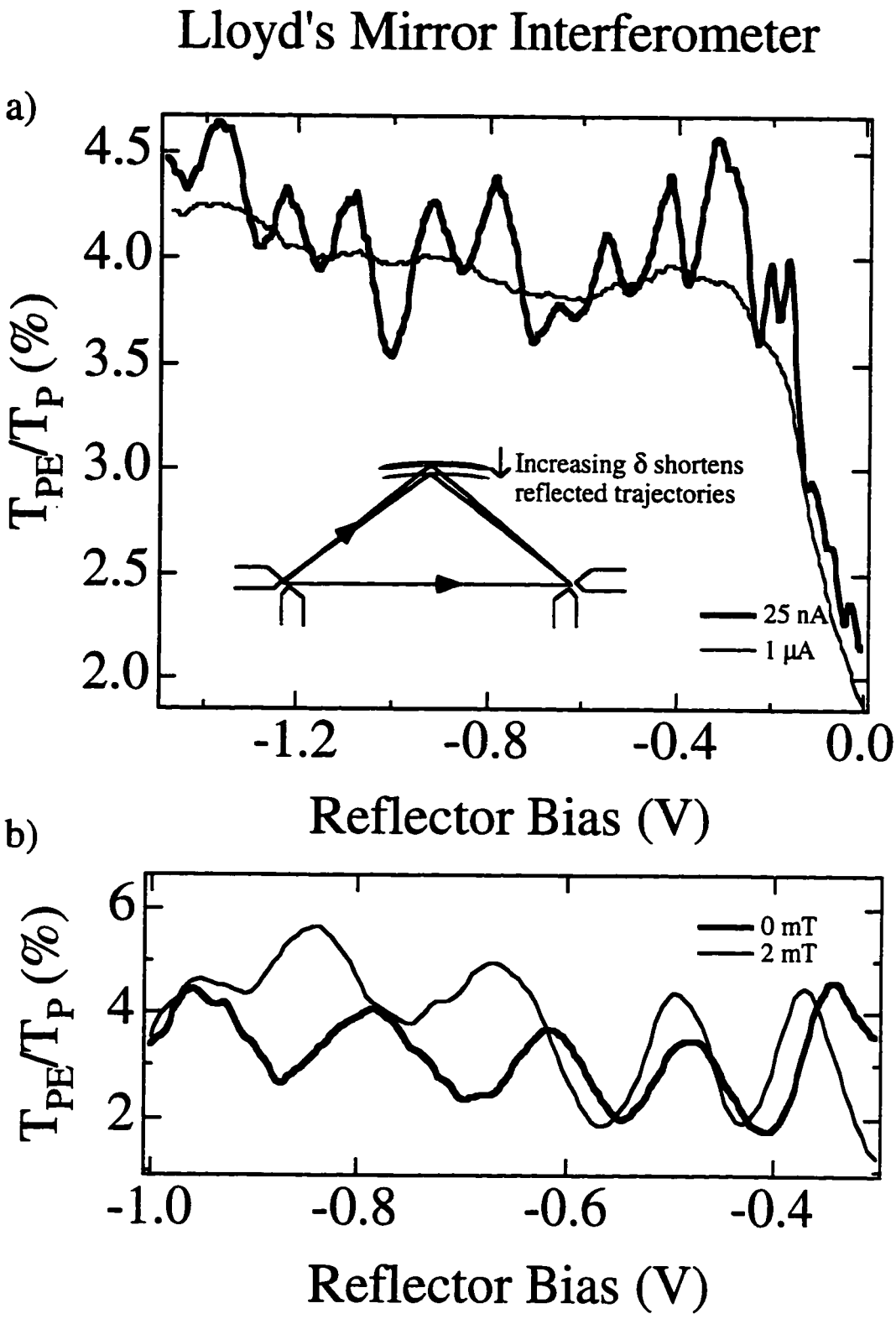

Fig 6.3 a) As illustrated in the inset, increasing the negative bias voltage on the reflector gate, shortens the pathlength of the reflected trajectories which leads to quantum interference oscillations. b) The pattern of the oscillations can be shifted by the application of a perpendicular magnetic field.

gate are reflected, which leads to the sharp rise in T_{PE} observed between 0 and -0.3 V. Once the gate is fully depleted, further increasing the negative bias voltage increases the depletion width, δ. The cartoon inset to Fig. 6.3a shows how the pathlengths of all reflected trajectories are shortened as δ increases. The changing pathlength produces a phase shift between the direct and reflected trajectories, which leads to the periodic oscillations in T_{PE}. Presumably, each oscillation period corresponds to a decrease, λ_f, in the pathlength of the reflected trajectories. When used in this way, electron interference in our FIDs is very similar to that of light in a Lloyd's Mirror Interferometer [Jenkins and White, (1950)].

In this device geometry, the depletion boundary must move in $\lambda_f/\sqrt{2}$ (= 28 nm) in order to shorten the pathlength of the reflected trajectories by an amount equal to the Fermi wavelength. The period of the T_{PE} oscillations increases slightly as the bias voltage on the gate becomes more negative, with an average period equal to about 130 mV.[4] Although the gate geometry in the FIDs is different from that of the narrow channel experiments in Chapter 4, the relationship between δ and V_g should be similar in the two systems, and the results of Chapter 4 can be used to check if the period of oscillation in the FIDs roughly corresponds to the change in depletion width required to shorten the reflected trajectories by λ_f. Multiplying the 130 mV period by the 200 ± 50 nm/V value for $d\delta/dV_g$ found in the narrow channel measurements, each oscillation corresponds to a change in the depletion width of 26 ± 6 nm, which is consistent with the expected value of 28 nm.

As shown in Fig. 6.3a, the oscillations are suppressed when the phase coherence length is shortened by using a larger bias current.[5] This confirms that the oscillations are the result of quantum interference. The oscillations are sensitive to the perpendicular

[4]A constant period would be expected for an infinitely long reflector in the limit of constant gate-gas capacitance (i.e. $\delta >>$ gas depth; see Eq. (4.20)). When the gas depth and δ are comparable, the gate-gas capacitance decreases with increasing δ, which leads to a corresponding increase in the period, ΔV. In addition, the finite length of the reflector creates edge effects which can also increase ΔV for successive oscillations.

[5]This technique is described in Chapter 3.

magnetic field. Although a thorough analysis was not performed, it is clear from Fig. 6.3b that application of a perpendicular B-field shifts the phase of the oscillations. This is not surprising since the direct and reflected trajectories undoubtedly enclose some non-zero average area. We emphasize this shift in the oscillations in response to a magnetic field, because very different behavior will be seen in the interferometers of Chapter 7. Finally, we note that the voltage measured across the emitter does not oscillate in response to sweeping the gate voltage. Such oscillations could result from interference between electrons backscattered into the emitter (as is the case in Chapter 7); in this geometry, however, there should be very few trajectories backscattered from the reflector gate.[6]

6.4 Aharonov-Bohm Oscillations

Using the dual lock-in technique, it is possible to selectively measure T_{PE}, the probability for transmission from the emitter to the probe. The interferometer results in the previous section clearly showed that two distinct sets of trajectories — one reflected and one direct — contribute to this transmission. Because the devices are so open, the majority of the injected electrons will neither strike the reflector nor travel directly between the point contacts; rather they will equilibrate in the wide grounded region of the 2DEG between the two point contacts and, therefore, not contribute to the measured current. If electron motion is fully ballistic (i.e. the electrons move in only straight line trajectories except when they collide with the boundaries), the two distinct groups of trajectories which contribute to the total transmitted current will enclose a triangular area, S. Therefore, we expect that T_{PE} would oscillate as function of the applied perpendicular magnetic field with a period, $\Delta B = h/eS$ due to the acquisition of an Aharonov-Bohm phase shift between the direct and reflected trajectories.

---

[6]In the device pictured in Fig. 6.2b, periodic oscillations in V_E are evident when the reflector gate voltage is ramped. In this device, the point contacts are aimed directly at the reflector gate, and rounding of the gate edges in the 2DEG likely creates backscattered trajectories which produce these oscillations.

Aharonov-Bohm oscillations in 2DEG systems were observed over a decade ago in ring geometries [for a review, see Washburn and Webb, (1986)]. In these doubly-connected geometries, a potential barrier (produced either by electrostatic gates or etching) explicitly prevents electron motion through the excluded region in the center of the device. Recently, Aharonov-Bohm oscillations have been observed in a two-slit geometry [Yacoby, *et al.*, (1994b)]. Unlike the situation in rings where electrons are constrained by the narrow arms of the devices, electrons in the double-slit geometry are free to move ballistically, with the important exception that they may not pass through the barrier between the two slits. When combined with the ballistic motion of the electrons, this narrow barrier effectively creates a diamond-shaped excluded region, and application of a perpendicular magnetic field produces an Aharonov-Bohm phase shift between electrons traversing the device on either side of this excluded region. In our FID design, there are no barriers to produce the excluded region that is required for observation of Aharonov-Bohm oscillations. Rather it is hoped that the ballistic motion of the electrons combined with the open geometry of the device will lead to the formation of such an excluded region. The observation of periodic magnetoconductance oscillations in our structures would provide the first conclusive demonstration that the Aharonov-Bohm effect can be observed at low-fields without using some form of barrier to create an excluded region.[7]

Indications of such Aharonov-Bohm oscillations have been seen in the magnetoconductance of ballistic quantum billiards. As described in the introduction to Chapter 5, the periodic magnetoconductance oscillations reported in low-field ballistic quantum billiard measurements have been associated with Aharonov-Bohm interference between certain especially important trajectories in these devices.[8] Unfortunately, the

---

[7]In high magnetic fields, the formation of edge states that travel along the device walls can produce A-B oscillations in quantum dots without using potential barriers to create a central excluded region. In the current discussion, however, we are limiting our attention to low-field measurements.

[8]For example, in describing their quasi-periodic oscillations in a square dot, Bird, *et al.* state, "In the absence of a nominally doubly connected geometry, the survival of a classical periodic orbit gives rise to a well defined Aharonov-Bohm effect." [Bird, *et al.*, (1996)].

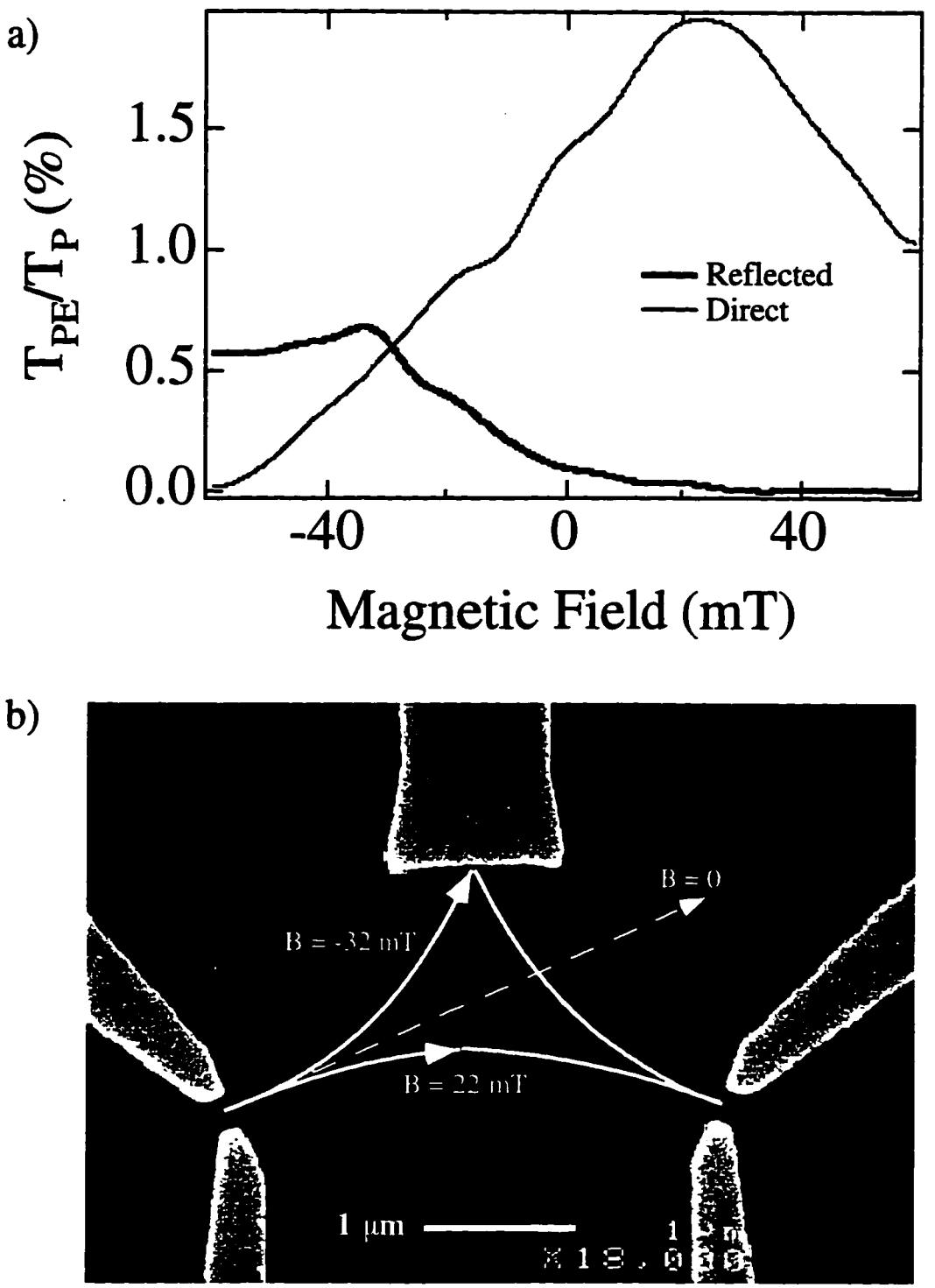

Fig 6.4 a) Plot showing how the contributions to the ballistic flux from direct and reflected trajectories change as a function of the perpendicular B-field. b) Diagram illustrating how the behavior in (a) can be explained by point contact collimation effects.

complex ensemble of trajectories which exist in billiards makes determining the origin of such oscillations very difficult. As was the case for the coherent backscattering devices studied in the previous chapter, the open device geometry used in our FIDs eliminates such ambiguity.

In addition to quantum interference, classical collimation effects are evident in our magnetoconductance measurements. The data shown in Fig. 6.4a are from the device pictured in Fig. 6.4b.[9] One trace (light line) is obtained with the reflector gate grounded and therefore represents the fraction of injected trajectories that travel directly to the probe contact (i.e. without reflection). There is a peak in T_{PE}/T_P around 20 mT, which, as illustrated in Fig. 6.4b, is the field at which the collimated electron flux injected from the emitter contact is magnetically focused into the probe contact. The trace with the reflector grounded is the background that must be subtracted from the trace with the reflector negatively biased in order to isolate the contribution of reflected trajectories to T_{PE}/T_P. The result from such a subtraction is also plotted in Fig. 6.4a (darker line). The contribution of the reflected trajectories to T_{PE} peaks at negative magnetic fields where the collimated electron beam is steered towards the reflector gate.

These classical effects add a rather large background that could somewhat obscure any quantum interference effects which may be present in the magnetoconductance measurements. However, it is easy to differentiate between classical and quantum mechanical effects by comparing magnetoconductance data taken with large and small bias currents. Fig. 6.5a shows two sweeps that differ only in the amplitude of the bias current. While quantum interference effects are clearly evident in the 25 nA trace, these oscillations have been completely suppressed by using a 1 μA bias current. In Fig. 6.5b, we have subtracted the classical background from magnetoconductance traces taken at 1.4 K with the reflector biased at -400 mV and the point contacts tuned to N = 2, 3, and 5 modes. The

[9]This is the same device which appears in Fig. 6.2a. To eliminate confusion, the barrier gate which is grounded in all of the experiments discussed in this chapter has been "air-brushed" from the photo.

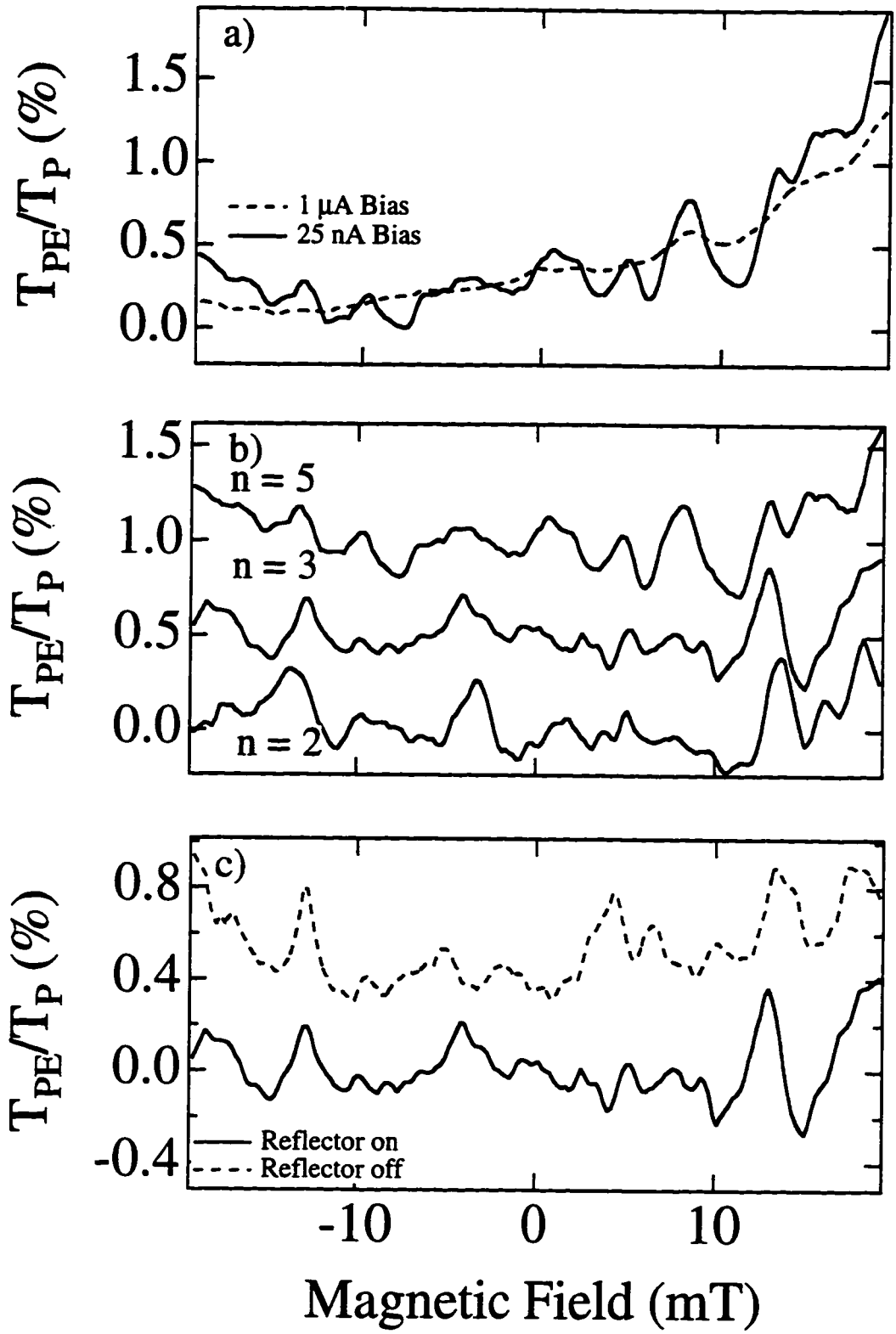

Fig 6.5 Low-field magnetoconductance traces from a FID. a) In addition to quantum interference effects, there is a classical background due to collimation that is still visible at bias currents high enough to destroy phase coherence. b) As the number of modes in the point contacts is varied, the pattern of the fluctuations changes. c) The pattern of the fluctuations also changes depending on whether the reflector is negatively biased or grounded.

quantum interference pattern is basically aperiodic, with no signs of the 1.5 mT oscillations that would correspond to Aharonov-Bohm type interference between the direct and reflected trajectories. As illustrated in Fig. 6.5c, these aperiodic fluctuations are present, though rearranged, when the reflector is grounded. In fact, these fluctuations appear to be very similar to the magnetoconductance fluctuations that are also observed in the coherent backscattering devices. In this instance, however, averaging techniques may not be used to distinguish the Aharonov-Bohm oscillations from the magnetoconductance fluctuations, because the A-B oscillations are not related to time-reversed trajectory pairs.

Despite the presence of these conductance fluctuations, several devices were studied in an attempt to find signs of periodic A-B oscillations; some of which are shown in Fig. 6.2. Periodic oscillations in the magnetoconductance were never observed, and possible reasons for this will be discussed in the following paragraphs.

Collimation effects make it very difficult to design FIDs in which experimental observation of Aharonov-Bohm oscillations is possible. In order to observe such oscillations, comparable fluxes of direct and reflected trajectories are required, and there must exist an excluded area that is enclosed by these two sets of trajectories. The collimation effects evident in Fig. 6.4 show that if the angular separation between the reflector and the probe contact is made too large, there will be no value of magnetic field at which there are significant fluxes of both direct and reflected trajectories. Unfortunately, as will be described below, the A-B oscillations can best be resolved experimentally if the angular separation between the direct and reflected trajectories is much larger than the angular width of the injection cones corresponding to the individual groups of trajectories. As a compromise, we used angular separations between 30° and 60° in our FIDs.

In several of our devices, the peak heights in collimation measurements seemed to indicate that the reflected flux was somewhat lower than the direct flux in our devices. One obvious solution to this problem would be to simply increase the arc length of the elliptical reflector, and indeed this was found to increase the reflected electron flux. Regrettably, as

the arc length of the reflector grows, the separation in the magnetic field scales of the A-B oscillations and the conductance fluctuations decreases. The conductance fluctuations are caused by interference among the reflected (or direct) trajectories. For a short elliptical arc, all of the reflected trajectories must follow very nearly the same path, so the average area enclosed by any two such interfering trajectories is small. As the arc length grows, the average area enclosed by any two reflected trajectories grows approximately in direct proportion to the arc length. As the average area enclosed by pairs of reflected trajectories approaches S, the average area enclosed by a direct and a reflected trajectory, the field scales of the aperiodic conductance fluctuations and the A-B oscillations become comparable. This is very similar to the situation in Aharonov-Bohm ring experiments where the periodic oscillations were obscured by aperiodic fluctuations once the arms of the ring became wide enough so that the average area enclosed by trajectories within an arm of the ring became comparable to the average area enclosed by trajectories in different arms [Webb, *et al.*, (1985)]. In addition, the distribution of areas enclosed by direct and reflected trajectories broadens with increasing arc length, which creates a smearing of the periodic oscillations much like that described in relation to the periodic coherent backscattering oscillations of Chapter 5. As illustrated in Fig. 6.2, a number of different arc lengths were tried. For relatively wide reflectors such as the one in Fig. 6.2a, there are ranges of magnetic field where the direct and reflected fluxes are both substantial, while the field scale of the conductance fluctuations is several times larger than the expected periodicity of the A-B oscillations. Therefore, it should be possible to distinguish A-B oscillations even in the presence of conductance fluctuations.

The mean free path for the wafer used in all of these measurements (KC2) is only 5 μm, so devices as large as those shown in Fig. 6.2a are affected by elastic scattering. Because of elastic scattering, the direct and reflected trajectories that contribute to T_{PE} no longer necessarily follow straight line paths. This scattering of trajectories could effectively destroy the excluded region that must exist between the two sets of trajectories for the

Aharonov-Bohm oscillations to be observed. In response to this concern, devices as small as that depicted in Fig. 6.2c were measured. Even in the smallest devices, A-B oscillations were not observed. Although this may not be the explanation for the absence of such oscillations, it should be pointed out that as the dimensions of the device are scaled down, quantum mechanical diffraction effects will begin to eliminate the excluded region. In the semiclassical approximation, only classically allowed paths are considered in calculating the conductance between two points. More precisely, there exists a bundle of closely spaced trajectories around each classically allowed trajectory that contributes to the probability amplitude for conduction between any two points [Yacoby, *et al.*, (1991)]. So long as the separation between the points is much greater than the Fermi wavelength, the "thickness" of this bundle can be safely neglected. As the dimensions of the device continue to be scaled down, however, these non-classical paths become significant and may blur the distinction between the two sets of trajectories. Instead of scaling down the device dimensions, scattering effects would be better combated by using higher mobility 2DEG material, but such material was not available for our experiments. It may very well be that the relatively short mean free path of our 2DEG material, combined with the constraints on the device design imposed by collimation effects, make it impossible to observe Aharonov-Bohm oscillations in the current FID geometry.

Note that these constraints do not hinder the observation of the gate-voltage-induced oscillations described in Section 6.3, because a different mechanism is responsible for creating the phase shift in that instance. All of the difficulties mentioned in relation to Aharonov-Bohm oscillations involve effects that limit the spatial separation between the direct and reflected trajectories. Because the interferometer oscillations do not require such a separation, it is easy to believe that periodic gate voltage oscillations could be present in our FIDs, when Aharonov-Bohm oscillations are not.

6.5 Summary

Using a dual lock-in technique, it is possible to sensitively measure T_{PE}, the probability for transmission from the emitter to the probe point contact in our forward-scattering interference devices. Two classes of trajectories contribute to T_{PE}: a group that travels between the contacts via reflection from a focusing gate, and a set that travels between the contacts without such a reflection. These two classes of trajectories may interfere with one another at the probe contact. Increasing the negative bias applied to the reflector gate selectively shortens only those trajectories that strike the reflector. As the pathlength of the reflected trajectories is shortened, periodic oscillations in T_{PE} are observed, just as they would be in an optical interferometer.

These periodic oscillations are clear evidence that two distinct classes of trajectories (reflected and direct) exist in our devices. By applying a perpendicular magnetic field, we had hoped to induce an Aharonov-Bohm phase shift between the two classes of trajectories that would produce periodic oscillations in T_{PE} as a function of the applied field. Despite numerous attempts, no such oscillations were observed in any of our devices. The absence of periodic oscillations may be due to the lack of a well-defined excluded area between the two sets of trajectories. It was hoped that the ballistic motion of the electrons combined with the open geometry of our devices would create the excluded region that is necessary for periodic Aharonov-Bohm oscillations to exist, but experimental deviations from straight line trajectories may be sufficient to eliminate this region. Such deviations would not have to be large to eliminate the excluded region, because the collimation of electrons in point contacts constrains us to device designs in which the angular separation between electrons injected towards the reflector and those injected directly towards the probe is quite narrow.

Chapter 7

Fabry-Perot Electron Interferometers

7.1 Introduction

In the previous chapter, it was shown that forward-scattering interference devices could behave very much like a Lloyd's Mirror Interferometer. This is just one example of electron optics. The term electron optics is used to describe a number of experiments in which ballistic electrons in a two-dimensional system are manipulated in ways analogous to geometrical optics. For example, electron focusing has been demonstrated in 2DEGs by patterning a gate in the shape of a concave lens between two point contacts [Sivan, *et al.*, (1990); Spector, *et al.*, (1990)]. The lensing effect is generated by applying a negative bias which lowers the velocity of electrons passing underneath the gate.[1] Both these electrostatic refraction experiments and magnetic focusing experiments [van Houten, *et al.*, (1989)] involve purely classical effects. In fact, the concave lens experiments had to be performed over distances longer than the phase coherence length so that fluctuations resulting from quantum interference would not camouflage the classical focusing effect [Spector, *et al.*, 1992].

In some instances, quantum interference effects have been studied in these ballistic electron systems. In a version of Young's double slit experiment, an electrostatic gate was used to partially deplete the electron gas in front of one slit. The wavelength for electrons passing under this gate could be varied by adjusting the gate potential, leading to observable quantum interference oscillations when electrons passing through the two slits were combined at a point contact [Yacoby, *et al.*, (1991)]. As we saw in the last chapter,

[1] In electron systems this lower velocity corresponds to a longer wavelength. Hence, the concave lens focuses electrons. Conversely, the wavelength of light is shortened in an optically denser medium, and convex lenses focus light.

electrostatic gates can also act like mirrors, the position of which may be adjusted by changing the bias voltage applied to the gates. Such electrostatic mirrors have been employed to fashion an electron Fabry-Perot interferometer [Smith, *et al.*, (1989)].

We begin this chapter with a description of experiments in a Fabry-Perot cavity very similar to that of Smith, *et al.* The remainder of the chapter is devoted to a novel Fabry-Perot geometry in which a quantum point contact in the tunneling regime serves simultaneously as an injector, reflector, and detector of ballistic electrons. Extremely large, periodic conductance oscillations are observed in this device as a function of the bias voltage applied to reflector gate patterned directly in front of the point contact.

7.2 Dual Reflector Fabry-Perot Cavity

Fig. 7.1a contains an SEM photo of the central region of the dual reflector Fabry-Perot interferometer device (sample KC8.B) very similar to one measured by Smith, *et al.* The device consists of a central quantum point contact, with narrow reflector gates spaced 500 nm from either side of the QPC. As shown schematically in Fig. 7.1a, a small ac bias voltage (10 μV) is placed across the entire sample, and the resulting current is used to calculate the device conductance.[2] The bias voltages on the QPC and the two reflectors can be individually tuned.

Fig. 7.3a is a trace taken at 1.45 K with the voltages on the point contact and the left reflector held fixed, and the bias voltage on the right reflector gate ramped. The point contact is fairly open, transmitting approximately N = 6 transverse modes when both reflectors are grounded.[3] A trace was taken with a large bias voltage (1 mV) to suppress

---

[2]Voltage biasing is preferable to current biasing in these measurements, as the device conductance can change by orders of magnitude in our most effective interferometer designs. As discussed in Chapter 3, in such instances, bias currents small enough to prevent Joule heating at resistance maxima, generate immeasurably small signals at conductance maxima.

[3]Due to the two-fold spin degeneracy, the conductance is $2Ne^2/h$.

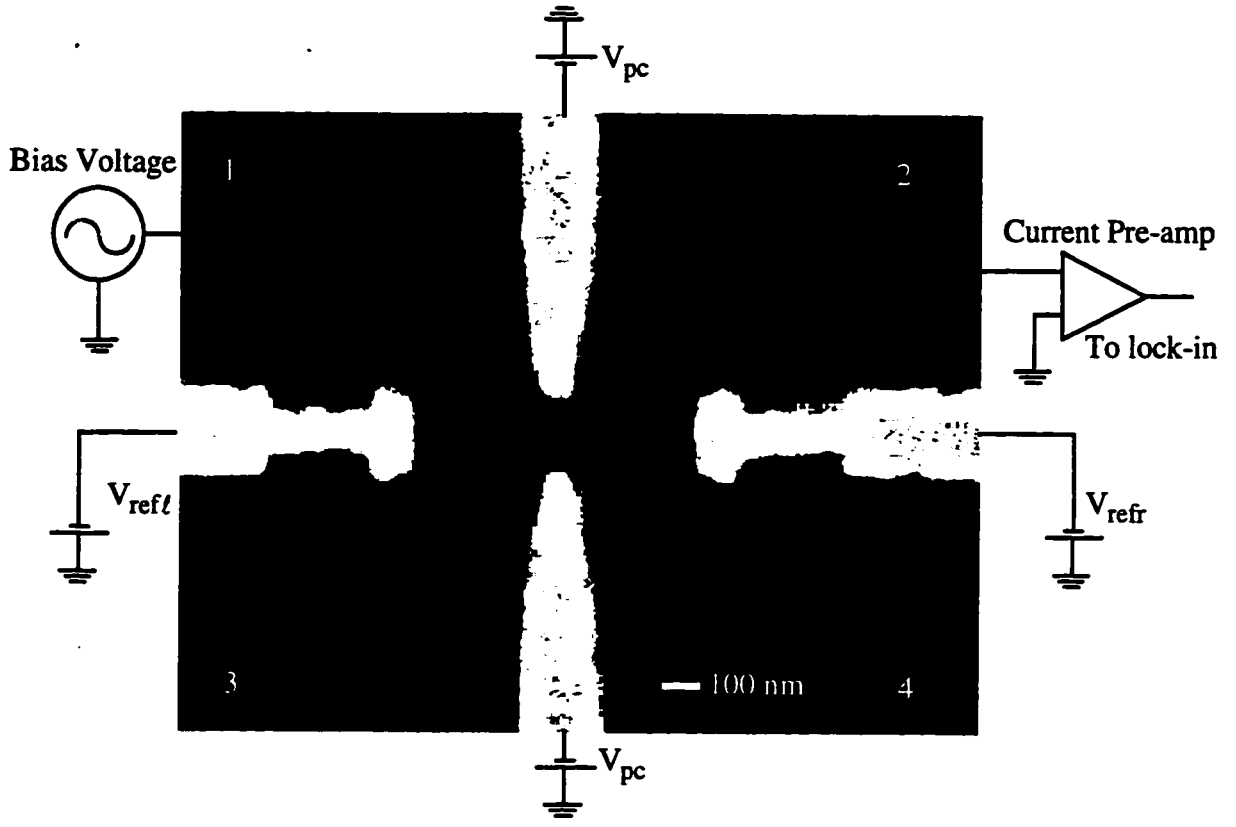

Fig. 7.1 SEM photo of the dual reflector interferometer device. The reflector gates are 500 nm from the center of the QPC. All three gates are independently tunable. A schematic representation of the typical voltage-biased measurement circuit is shown. The ohmic contacts are located far from the device in the four numbered regions.

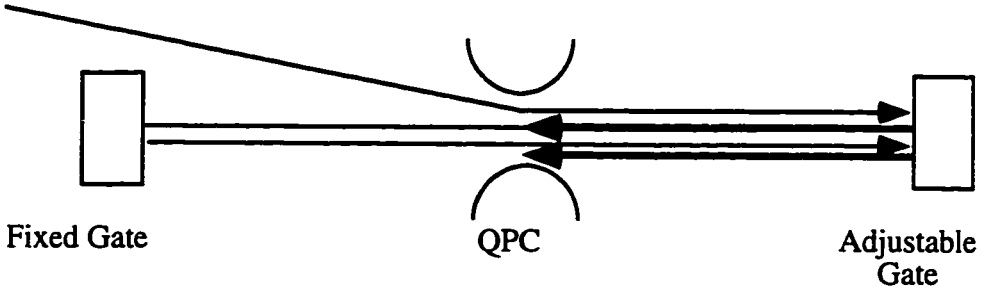

Fig 7.2 Schematic representation of the dual reflector Fabry-Perot cavity. The position of the adjustable "mirror" may be moved in by increasing the negative bias voltage applied to that gate. The backscattered trajectories are shown in the thicker lines.

quantum interference effects. The device conductance drops as a result of the backscattering that becomes possible as the electron gas under the right reflector is depleted. The conductance is also reduced by the creation of an additional narrow constriction between the reflector gate and QPC.

After depletion, there is a further gradual decrease in the device conductance as the bias applied to the reflector is increased. There are two causes for this gradual decrease. As the bias on the right reflector is made more negative, the depletion edge boundary of the 2DEG moves towards the QPC. This narrows the constriction between the reflector and the point contact gate. Since we are essentially measuring the series conductance of the QPC and this constriction, an increase in the resistance of this constriction results in a decrease in the overall device conductance. The second reason for the decrease in device conduction is more subtle. Because of the close proximity of the reflector gate to the QPC, increasing the negative bias on the reflector lowers the electron sheet density in the QPC. With a constant bias applied to the QPC, this reduction in sheet density decreases the conductance of the point contact. As will be shown later, this "cross talk" effect is especially important for point contacts in the tunneling regime, where the conductance is exponentially sensitive to the applied gate voltage.

Fig. 7.3a also includes a trace which is identical except that a smaller (10 μV) bias voltage is applied across the sample. In addition to the aforementioned classical background, there are also small quantum interference oscillations present. These oscillations can be easily seen following the subtraction of the classical background (Fig. 7.3b). As illustrated by the Fourier transform shown in Fig. 7.3c, these oscillations are periodic, with conductance maxima occurring approximately every 120 mV.

These oscillations are the result of interference between trajectories scattered from the reflector gates, with peaks in conductance occurring when the transmitted electron wavefunction is maximized at the QPC. As a concrete example, consider an electron injected through the QPC with transverse momentum small enough so that it strikes the

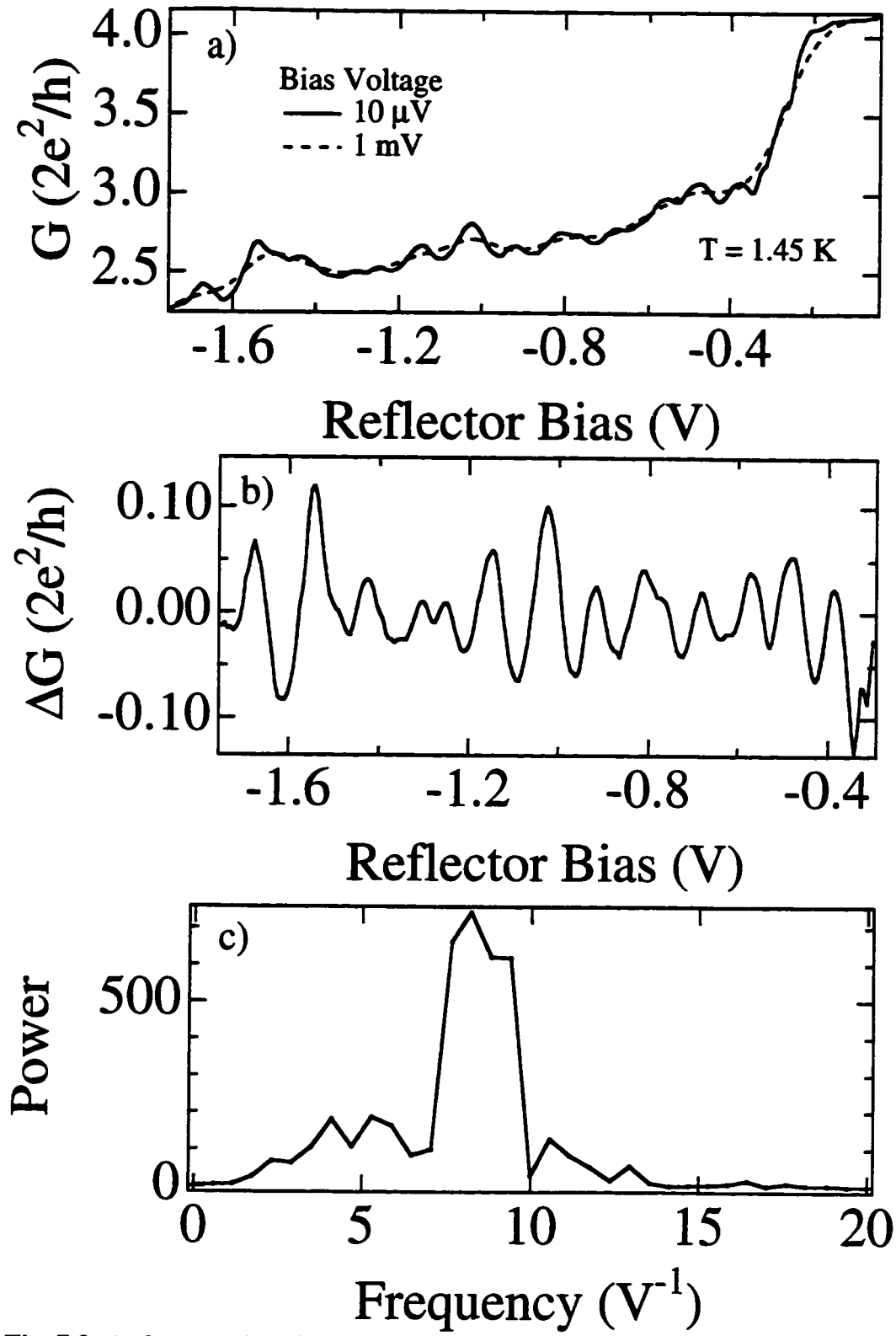

Fig. 7.3 a) Quantum interference oscillations in the dual reflector device may be distinguished from the classical background by taking traces with low and high bias voltages. b) To isolate the oscillations, the classical background has been subtracted. c) FFT of the oscillations in (b) illustrates their periodicity.

right reflector gate.[4] Upon reflection, it may be backscattered through the point contact. Some fraction of these backscattered electrons will strike the left reflector, return through the QPC, strike the right reflector a second time, and then travel back towards the QPC where they may interfere with the original backscattered electron wave; this motion is illustrated in Fig. 7.2. In many ways, this device is the ballistic electron analog of a Fabry-Perot interferometer. Although we may not simultaneously view interference fringes, the conductance of QPC can be used as a local probe of the interference pattern — a pattern which may be shifted by changing the separation between the right reflector and the point contact.

Suppose as the negative bias voltage is increased, the depletion boundary of the right reflector moves in by an amount δx. For a given δx, the resulting change in the pathlength difference between trajectories striking the right reflector n and n+1 times equals $2\delta x$. The interference pattern should be periodic in δx, with period equal to $\lambda_f/2$. A 120 mV period was measured for this device, whereas a 130 mV period was measured for the Lloyd's mirror interferometer of Chapter 6 where the period should equal $\lambda_f/\sqrt{2}$. In comparing these periods, it is important to keep in mind that the experiments were performed using different gate geometries on wafers with different electron gas depths and sheet densities. Although these differences make a quantitative comparison difficult, we believe the similar periods are a good indication that the electrostatic modulation of trajectory lengths is responsible for both interference effects.

7.3 Single Reflector Fabry-Perot Interferometers

If we repeat the trace shown in Fig. 7.3a, but in this case ground (rather than hold at a constant voltage past depletion) the reflector on the left side of the interferometer, the periodic oscillations disappear. As the QPC width is decreased, however, similar

[4]Because of QPC collimation effects, the number of such electron trajectories is expected to be fairly large.

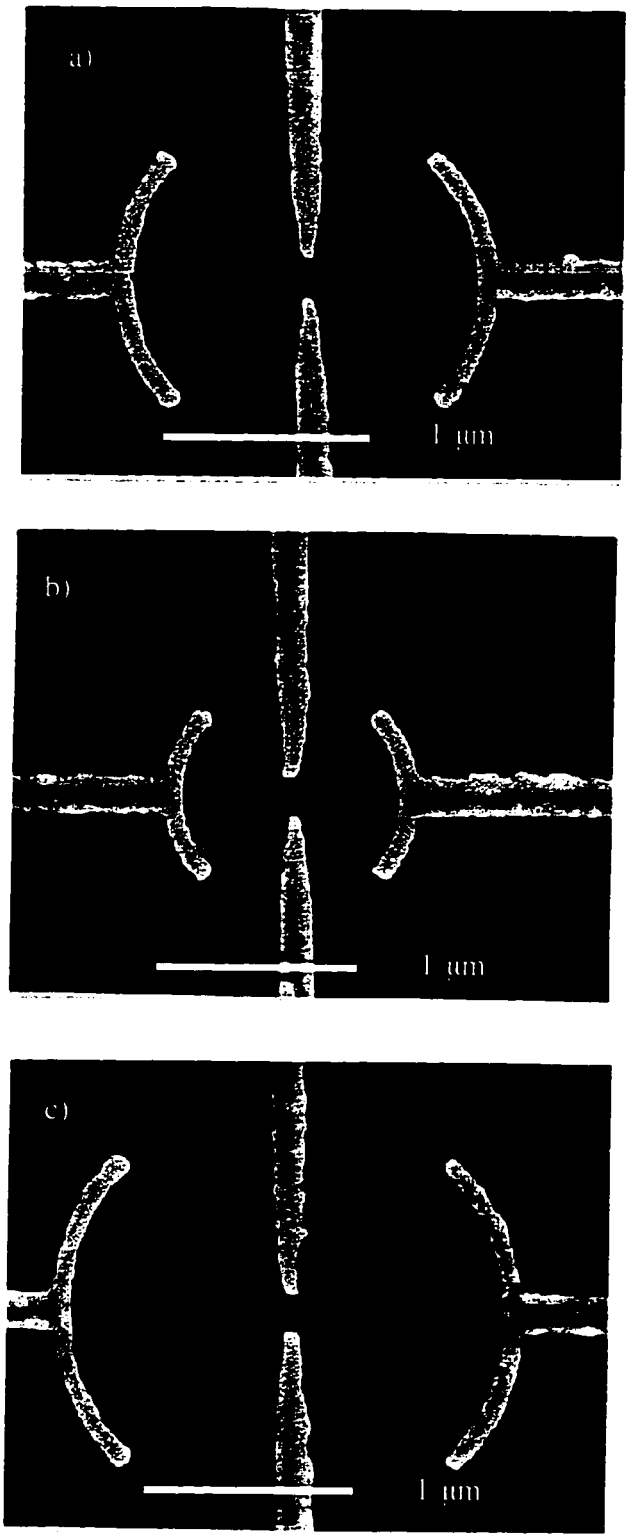

Fig. 7.4 Devices used in the single reflector interferometer experiments. Although two reflectors are present, one is grounded during these measurements. All reflectors are 90 degree arcs designed to foucs reflected electrons back to the QPC. The separations between the QPC and reflector gates are 800, 500, and 1000 nm for (a), (b), and (c) respectively.

conductance oscillations begin to reappear in what is now a single reflector device. Such oscillations are made possible by electron reflection at the point contact, which becomes more probable as the constriction is narrowed.[5] This point contact reflection should be especially pronounced when less than one mode is transmitted by the QPC (tunneling regime). As we will see in this section, these single reflector devices also behave very much like Fabry-Perot interferometers, with reflection at the QPC eliminating the need for a second mirror.

Fig. 7.4 shows SEM photos of the three sizes of devices used in the single reflector experiments. Note that all devices in fact have two reflectors. For any given sweep, however, one reflector is grounded. By placing reflectors on both sides of the point contacts, it is possible to check the reproducibility of any observed single reflector interference effects in a given point contact. The reflectors themselves are 90° circular arcs, the centers of which are located at the center of the QPC.[6] If specular reflection occurs when electrons strike these gates, the reflectors should focus the electrons back to the point contact. The data presented in this section come from two samples fabricated using wafer KC9 (2DEG depth 470 Å, $\ell = 5.0$ μm). Sample KC9.B contains the three devices pictured in Fig. 7.4. A second sample, KC9.E, contains two of the 800 nm separation devices. Sample KC9.E was measured in the Kelvinox dilution refrigerator, while the measurements on KC9.B were performed in the ^{3}He cryostat.

Fig. 7.5 shows data from an 800 nm device on KC9.E taken at 100 mK. In Figs. 7.5a-f, we plot the conductance as a function the reflector bias with the gate voltage on the point contact held constant at successively larger negative bias voltages. In Fig 7.5a, the point contact is fairly open, transmitting over two modes. There are multiple periodicities

---

[5]Similar non-unity transmission of modes was used to form a Fabry-Perot type resonance cavity involving edge state transport in a quantum dot [van Wees, *et al.*, (1989)].

[6]The choice of circular reflector gates is a deliberate one. In 2DEG devices, the rounding of surface equipotentials in the electron gas layer would distort the shape of any reflector geometry that relied on sharp features. Such distortions should be minimal in the circular arc, except perhaps at the endpoints of the reflector.

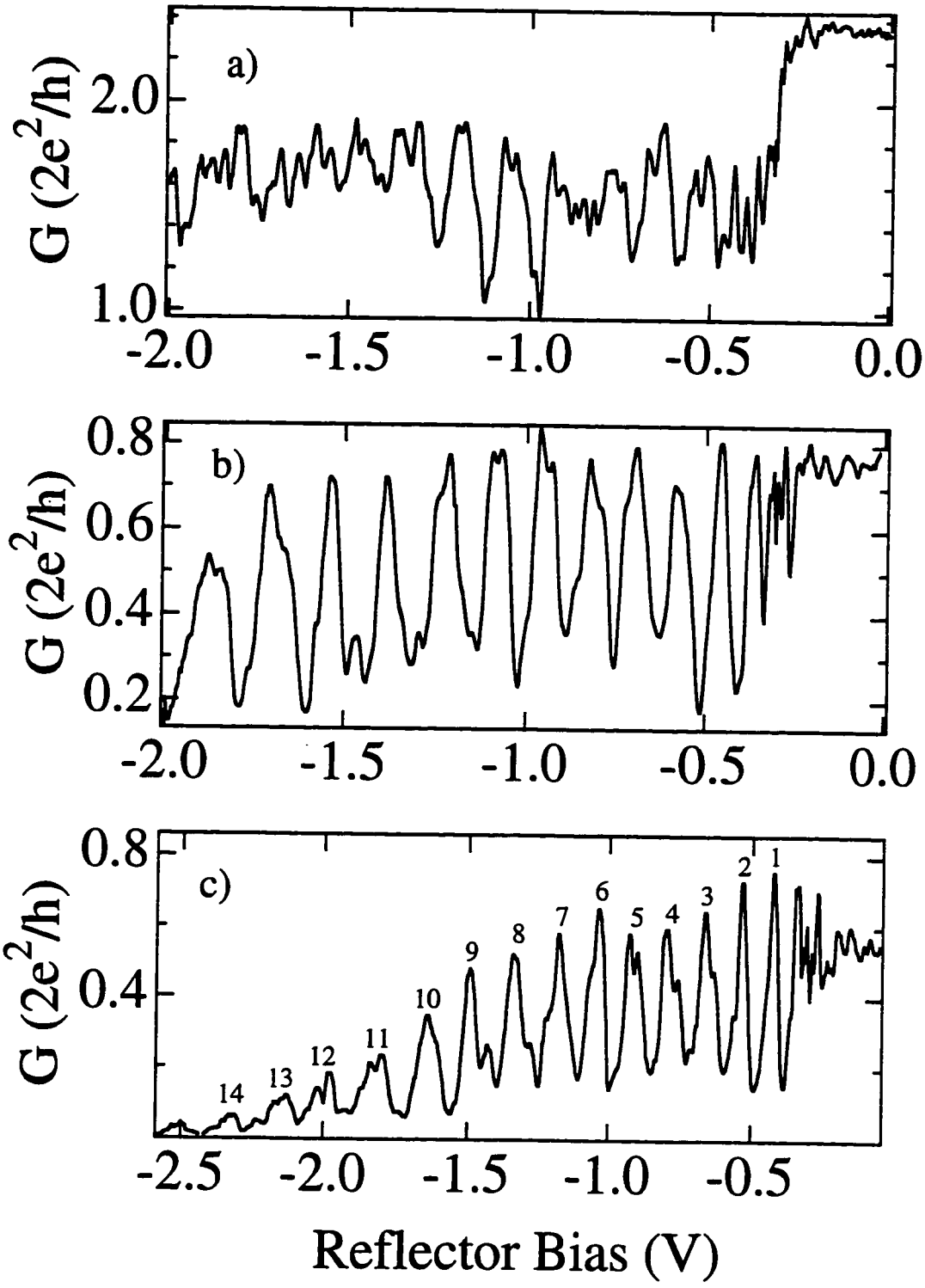

Fig. 7.5 a-f) Device conductance as a function of the bias voltage applied to the reflector gate at T = 100 mK. Traces a-f illustrate the change in the observed oscillations as the quantum point contact is further constricted. As we move from several modes to the tunneling regime, a single periodicity emerges. Once the point contact is sufficiently narrow, finesse is observed in the oscillations, and the resonant conductance may exceed G(V = 0).

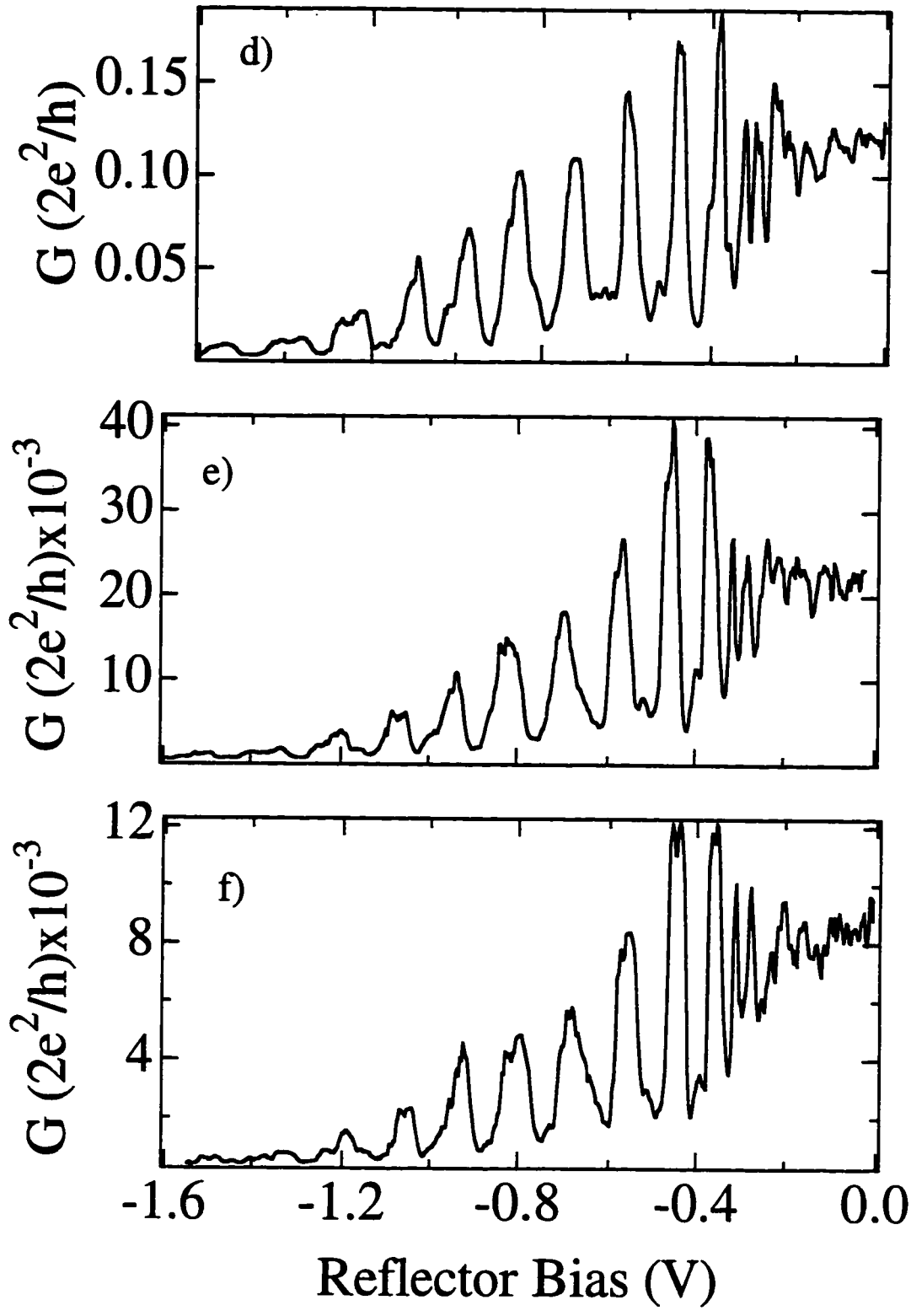

Fig. 7.5 (continued)

evident in the quantum interference oscillations. With the point contact this open, the single reflector device behaves very much like the dual reflector device discussed in Section 7.2, with reflections at the point contact taking the place of the second mirror.

The remainder of the traces in Fig. 7.5 examine the device conductance when the point contact is biased in the tunneling regime. Before the electron gas under the reflector is fully depleted in these traces (-0.33 V), there are many aperiodic oscillations in the conductance. The aperiodic fluctuations are the result of interference of electron waves which are only partially reflected at this barrier. Following depletion, a regular series of sharp, periodic conductance oscillations is clearly visible In the tunneling regime, transmittance of all but the lowest mode is strongly suppressed, and there is a single, clean periodicity. Conversely, Fig. 7.5a shows that multiple periodicities are evident when the point contact is wide enough to transmit several modes. It is likely that there are slight differences in the period and phase of Fabry-Perot oscillations associated with different modes, which explains why a single clean periodicity is only observed when one mode is contributing to conductance (i.e. in the tunneling regime). Another striking feature of the oscillations in the tunneling regime is that it is possible for the conductance at a maxima to exceed the conductance in the absence of the reflector. This and other characteristics of these oscillations will be explained in greater detail below.

Origin of the Oscillations in the Tunneling Regime

When a point contact is wide enough so that several modes are transmitted, only trajectories traveling through the point contact in the same direction can interfere with one another, because electron waves with anti-parallel $\bar{k}$-vectors are nearly orthogonal.[7] This is not the case as the constriction narrows to less than a Fermi wavelength. Thinking of

[7]So, for example, in the coherent backscattering experiments of Chapter 5, we are only concerned with how the backscattered trajectories interfere with one another, and ignore interference between the backscattered and injected electron waves in the QPC.

this in terms of the uncertainty principle, localizing the electron position to less than a Fermi wavelength leads to a momentum uncertainty greater than $\hbar k_f$. In the limit of a true "point" point contact, interference is no longer sensitive to the momentum direction.

If ψ denotes the electron wavefunction in the point contact, the current, and hence, the conductance in the tunneling regime should be proportional to $\psi^* \nabla \psi$. The electron wavefunction in the point contact is the sum of direct and scattered parts. Therefore, the conductance of the point contact is sensitive to the amplitude and phase of the scattered electron waves returning to the point contact. This is very similar to the situation in recent "Quantum Corral" experiments, with the tip of an STM playing the same role that the point contact in the tunneling regime performs in our measurement [Crommie, *et al.*, (1993); Heller, *et al.*, (1994)].

In many ways, the scattering of electron waves in our devices is analogous to the reflection of light waves in a Fabry-Perot resonance cavity, a description of which can be found in standard optics texts [e.g. Guenther, (1990)]. Suppose electrons from a single mode are injected through the QPC (transmission coefficient $T < 1$) towards the reflector. Let this transmitted wave be denoted by ψ_0:

$$\psi_0 = ATe^{i(\omega t + \vec{k}\cdot\vec{r})} \qquad (7.1)$$

A fraction R_r of the injected electrons are reflected back towards the QPC by the circular gate. Although the reflector only extends $\pm 45°$ from the normal, R_r can be quite large as the result of collimation effects.[8] Any disorder effects that may free electrons from the resonance cavity, such as impurity scattering and non-specular reflection, are implicitly included in the value of R_r. The electron wave backscattered towards the QPC after one reflection is given by:

---

[8]In the tunneling regime, a diffraction-limited $\cos^2\alpha$ distribution of injected electrons is expected. In this case, ~82% of the injected electrons will be at angles less than $\pm$ 45 deg.

$$\psi_1 = ATR_r e^{i(\omega t - \bar{k}\cdot\bar{r} + \phi_1)}, \tag{7.2}$$

where ϕ_1 is a phase factor. Let R_{pc} represent the fraction of this backscattered wave that is reflected from the point contact back towards the circular gate. In the absence of disorder effects, $R_{pc} = 1 - T$, but we use a distinct notation since the value of R_{pc} is likely lower than this in actual devices. In this resonance cavity, the electron wave backscattered towards the QPC following the n^{th} bounce off the reflector gate is given by:

$$\psi_n = ATR_r^n R_{pc}^{n-1} e^{i(\omega t - \bar{k}\cdot\bar{r} + \phi_n)}. \tag{7.3}$$

In this idealized model, each backscattered wave will have a constant phase difference relative to its nearest neighbor:

$$\delta = 2\pi \frac{2L}{\lambda_f}, \tag{7.4}$$

where L is the separation between the reflector and the point contact. With this phase difference known, Eq. (7.3) for the general form of the n^{th} backscattered wave may be written as

$$\psi_n = Ce^{in\delta} R_r^n R_{pc}^n, \quad C \equiv ATR_{pc}^{-1} e^{i(\omega t - \bar{k}\cdot\bar{r})}. \tag{7.5}$$

The effect of backscattering on the device conductance is determined by the interference among the transmitted wave and these multiply scattered trajectories. The conductance is proportional to $\psi^* \nabla \psi$, where the total electronic wave function is the sum of the initial and all backscattered waves. The conductance is at a maximum when the direct and backscattered trajectories interfere constructively at the QPC; i.e., when δ is an

integer multiple of 2π. From the expression for δ (Eq. 7.4), we see that successive maxima are expected every time the separation between the QPC and reflector is decreased by $\lambda_f/2$. This explains the periodicity of our oscillations.

In the above discussion, we have considered the example in which electrons are injected through the point contact towards the reflector. In all of our measurements, an ac bias voltage was used, which means that half of the time, electrons are injected through the point contact towards the side without a reflector. In the tunneling regime, the analysis above can also be applied to show how quantum interference oscillations may be created by electrons that are reflected at the point contact and return to the QPC after striking the reflector one or more times. The interference oscillations for electron injection in the two directions are in phase; i.e., maxima and minima in conductance occur at the same reflector bias voltages. Due to the asymmetric device design, however, the amplitude of the oscillations could be different in the two directions. One would expect larger oscillations when electrons are injected towards the reflector, because in that direction, specular reflection from the circular arc traps electrons in the cavity. Conversely, when electrons are injected in the opposite direction, there are no collimation or focusing effects to help trap electrons initially backscattered from the point contact. Although we have not performed such measurements, it would be interesting to add a dc offset to the ac bias in order to see if there any direction-sensitive injection effects observable in the conductance oscillations.

Interferometer Finesse

If the wavefunction at the point contact were only the sum of the injected electron wavefunction and the one-bounce reflected wavefunction, the resulting interference pattern would be sinusoidal. As the number of multiple-reflection trajectories contributing to this sum increases, the conductance peaks become sharper. The same is true for the sharpness of the interference fringes in a Fabry-Perot interferometer, where a quantity known as the

finesse, F, is used to measure the Q of the resonance cavity. In other words, the finesse is a measure of the "lifetime" of an electron in the cavity. If the effective reflectivity of the boundaries in the cavity, R_{pc} and R_r, is low, it will result in a low value for the finesse. As an operational definition, F is calculated from $\delta_{1/2}$, the half-width of the conductance peak (in radians);

$$F = \frac{\pi}{2\sin(\delta_{1/2}/2)}. \tag{7.6}$$

For a sine wave, $\delta_{1/2}$ is $\pi/2$, which corresponds to a finesse of roughly 2.2. By explicitly summing the multiply reflected electron waves (Eq. 7.5), it is possible to determine the relationship between the finesse and the effective reflectivities of the interferometer boundaries:

$$F = \frac{\pi\sqrt{R_r R_{pc}}}{1 - R_r R_{pc}}. \tag{7.7}$$

Comparing the oscillations in Figs. 7.5b and 7.5c, we see that the conductance peaks are distinctly sharper for the latter trace. In Fig. 7.5b, the finesse of the first several oscillations following depletion is close to that of a sine wave, while in Fig. 7.5c, the average finesse of the first four oscillations following depletion (numbered in the diagram) is about 3.0 — an indication that multiple reflections are contributing to the interference pattern. The point contact is transmitting close to a full mode in Fig. 7.5b. Hence, the reflectivity of the point contact is low, and a low value for the finesse is expected. In Fig. 7.5c, the negative bias on the point contact has been increased, which increases the reflectivity of the QPC and the finesse of the cavity. We see in Figs. 7.5d through f, however, that further narrowing of the constriction is not accompanied by a corresponding

increase in the device finesse. This saturation is an indication that once the point contact reflectivity is sufficiently high, R_{pc} is no longer the limiting factor on the value of F.

In addition to the width of the point contact, there are several other factors that determine the interferometer's finesse. Indeed, when one considers all of the effects that can adversely affect F in a 2DEG device, achieving even our relatively low level of finesse is fairly impressive. Although elastic scattering is doubtless playing a role in our devices, keeping the device dimensions much smaller than the mean free path allows some level of finesse to be achieved. Another factor that could damage the finesse in our devices is boundary roughness. In addition to increasing the chances of non-specular reflection, any roughness in the reflector boundary will lead to phase shifts between different reflected trajectories. In optical interferometers, mirror roughness is often the limiting factor for the instrument's finesse, but this is probably not so for our devices. Care is taken to fabricate gates which are lithographically smooth to within a fraction of the Fermi wavelength, and the roughness that does exist should be smoothed to some extent in the 2DEG.

As shown in Figs. 7.5c-f, the finesse of the oscillations decreases as the negative bias is increased. With each oscillation, the separation between the reflector arc and the center of the point contact is decreasing. As this separation becomes smaller than the radius of the arc, electrons striking near the endpoints of the reflector gate will no longer be focused back to the point contact, lowering R_r and the interferometer finesse. In addition, as the negative bias is increased, the separation between any given point on the reflector gate and the center of the QPC is no longer constant over the entire length of the arc. Variation in this separation results in phase shifts among the reflected trajectories and broadens the lineshape of the conductance oscillations.

Background Conductance Decrease

For the traces taken in the tunneling regime, the average conductance of the device decreases monotonically as a more negative bias is applied to the reflector. For example, in Fig. 7.5c the average device conductance is about 0.4 modes just following depletion of the reflector, but conduction is completely pinched off at a reflector bias of -2.7 V. A similar, albeit less dramatic, effect was described earlier in the dual reflector measurements. As mentioned then, in the tunneling regime, the conductance of a point contact is extremely sensitive to nearby potentials. We believe that the decrease in the average device conductance is due to the influence that the negative bias applied to the reflector has on the sheet density in the QPC.

Experimentally, we are able to rule out the other possible explanation for this effect: that the narrow constrictions between the reflector and QPC gates are increasing the device resistance. Although the spacing and shape of the reflectors is different, the same measurement circuit illustrated in Fig. 7.1 is also employed in the current experiment. For the traces shown in Fig. 7.5, the right reflector is grounded, and the gate defining the left reflector is swept. This left gate extends to the edge of sample, separating the ohmic contacts in the reservoirs labeled 1 and 3.[9] This separation allows us to directly measure the conductance through these side constrictions by moving the current pre-amp from ohmic contact #2 to #3. When the experiment is repeated in this configuration, we find that the series conductance of these narrow constrictions is over 6 modes, and decreases only slightly as the reflector bias is increased from depletion to -2.5 V.

[9]The reflector gate does not need to separate these two regions for the oscillations to be observed. The trace in Fig. 7.7a was obtained using the right reflector which does extend to the edge of the sample.

Amplitude of the Conductance Oscillations

As illustrated in Fig. 7.5, when the conductance of the QPC is decreased between successive traces, the size of conductance oscillations, $\Delta G = G_{max} - G_{min}$, also decreases. However, if ΔG is divided by G_0, the average conductance of the device at a given reflector voltage[10], we find that the ratio of ΔG to G_0 is roughly constant (on the order of unity) for all five traces in the tunneling regime; when more than one mode is transmitted through the point contact, as in Fig. 7.5a, the value of $\Delta G/G_0$ is lower. The scaling between ΔG and G_0 is also evident in the individual traces where the amplitude of the oscillations decays proportionally to the overall conductance of the device.

When more than one mode is transmitted through the point contact, the conductance following depletion of the reflector gate is always lower than the conductance with the reflector gate grounded. As discussed earlier, when the point contact is open, the backscattered waves do not interfere with the transmitted waves, and the reflector may only decrease the conductance. Conversely, when the point contact is in the tunneling regime, interference between the transmitted and backscattered electron waves does occur. Therefore, at a cavity resonance in the tunneling regime, it is possible for the device conductance to exceed the value of the conductance with the reflector grounded. This crossover is illustrated quite clearly in Fig. 7.5. As we first enter the tunneling regime (Fig. 7.5b), the conductance maxima are equal to the conductance with the reflector grounded, but when the conductance is around 0.02 modes (Fig. 7.5e), the conductance at a resonance can be nearly twice as large as it is when the reflector is grounded. In other words, due to quantum mechanical interference between the incident and backscattered electron waves, placing a wall in front of the point contact can lead to instances where the current through the QPC is higher than it is in the absence of such a barrier.

---

[10] G_0 may be obtained by suppressing the quantum interference oscillation with a large bias voltage.

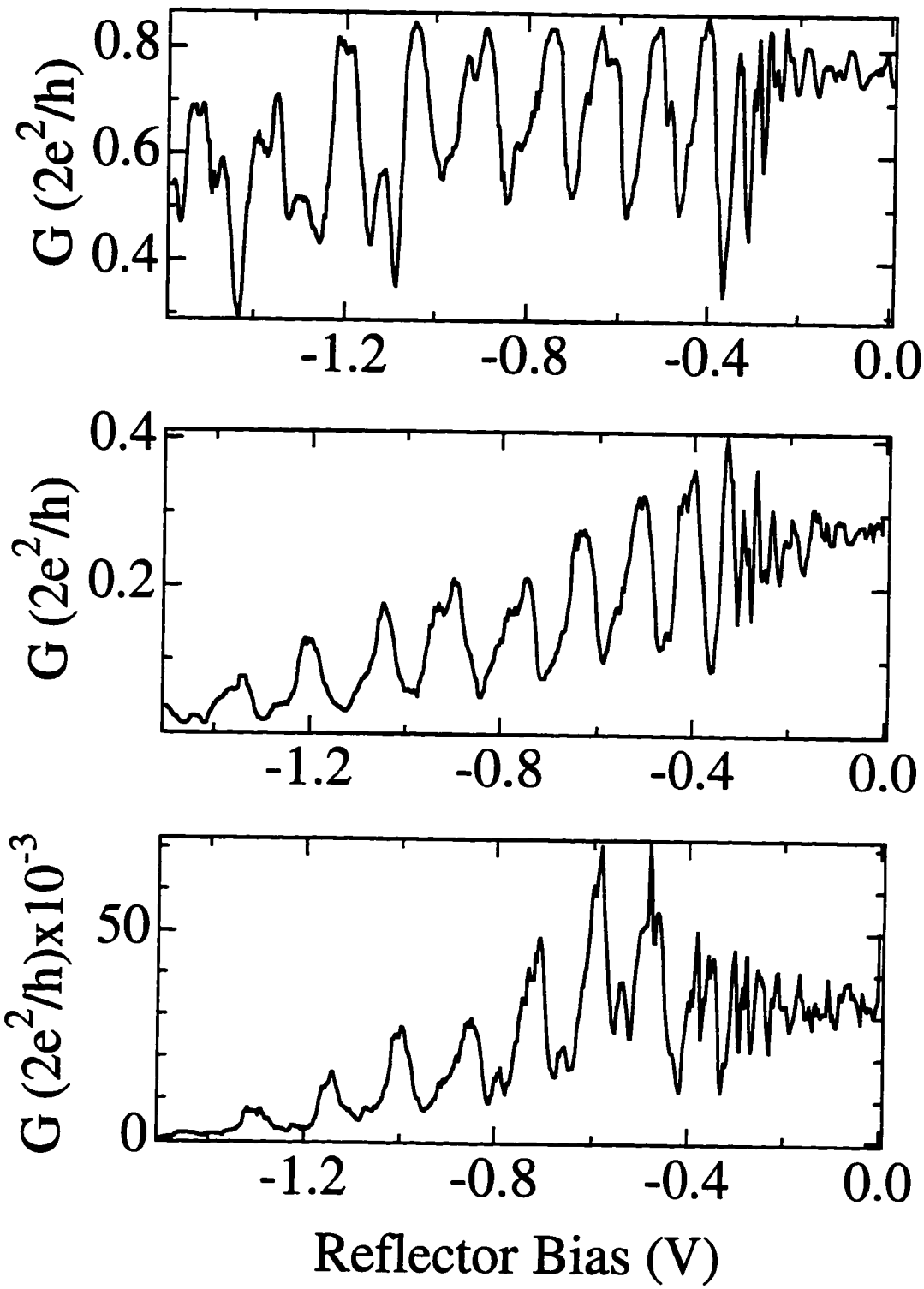

Fig. 7.6 The measurements shown in Fig. 7.5 are repeated here in a different 800 nm device to illustrate the robust nature of the effect.

Reproducibility

The oscillations described above are quite robust, and have been observed in a number of different devices. Fig. 7.7a shows oscillations measured in the same device as those depicted in Fig. 7.5. However, the data in Fig. 7.5 were obtained by ramping the left reflector gate and grounding the right gate, while Fig. 7.7a shows data taken with the roles of the two reflector gates reversed. A further example of the robust nature of the interference effects is provided by Fig 7.6. This figure depicts a series of traces similar to those of Fig. 7.5, but these data were obtained from a completely different device. Oscillations from yet another 800 nm are shown in Fig. 7.7b. In addition, similar oscillations have been observed in 500 and 1000 nm devices.

Comparing Figs. 7.5 and 7.6, the periodicity and amplitude of the oscillations is very similar in the different devices. The finesse of the oscillations is higher for the device of Fig. 7.5, but the finesse is quite sensitive to impurity scattering which will vary from device to device. At 100 mK in both devices, there is some additional structure on top of the oscillations. This structure is very fragile, and typically is not reproducible when identical consecutive sweeps are performed on the same device. The structure may be due to switching noise in the point contacts. In several other samples, much worse manifestations of switching noise in the tunneling regime made measurements such as these impossible.

Finite Temperature Effects

In the above discussion, the effects of a finite phase coherence time have been neglected. At finite temperature, two effects limit the phase coherence length of electrons. As described in Chapter 4, electron-electron scattering leads to a loss of phase memory

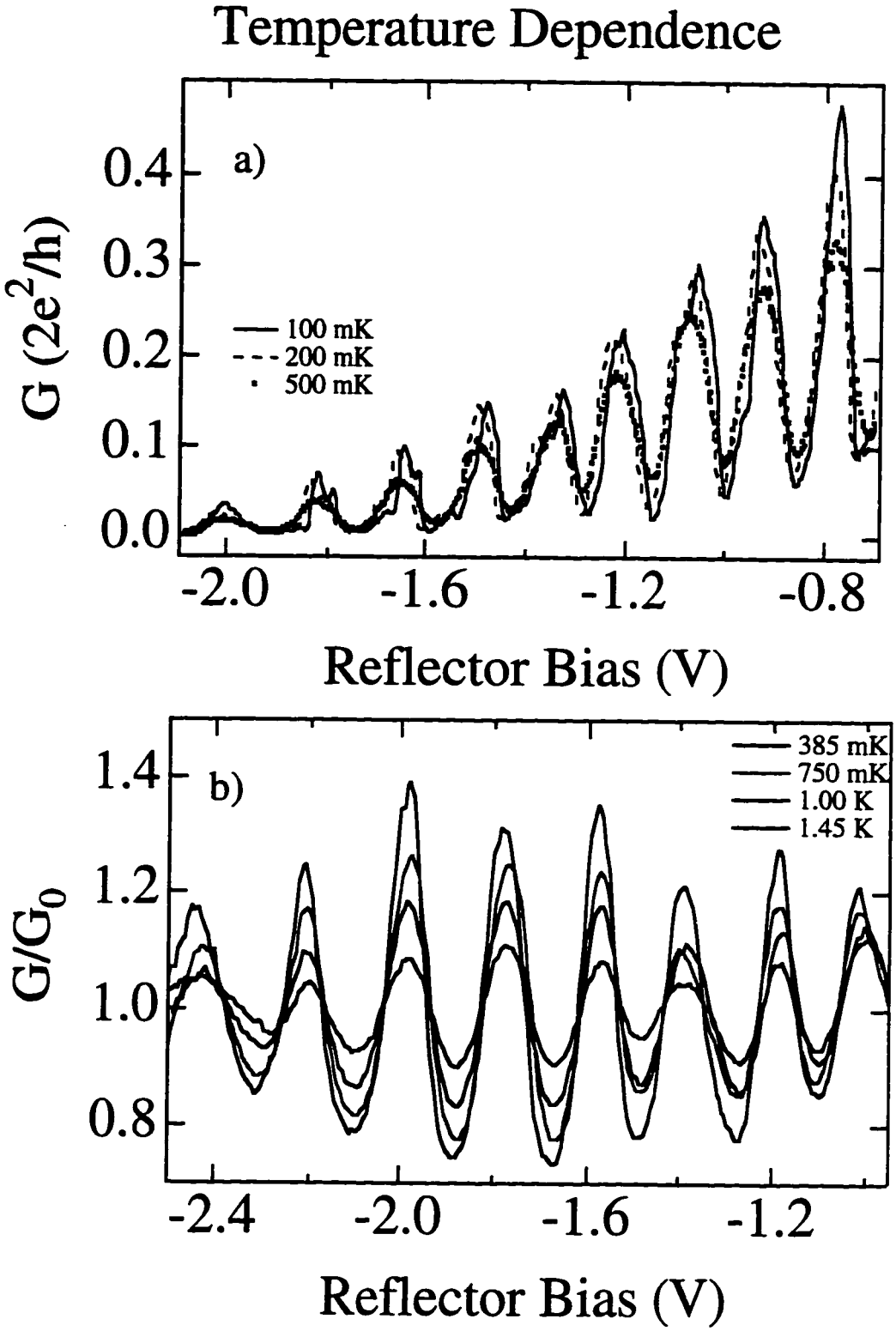

Fig. 7.7 a) Dilution refrigerator temperature series on an 800 nm device. Note that the amplitude and finesse of the oscillations continue to increase as the sample is cooled below 200 mK. b) Higher temperature range with a different 800 nm device. The data have been normalized to the smooth background conductance G_0.

over a characteristic time τ_ϕ. This phase coherence time is temperature dependent, and is well over 100 ps at 100 mK. In addition to e-e scattering, thermal smearing of the Fermi surface limits the range of phase coherent electron transport. As also discussed in Chapter 4, this thermal smearing results in a loss of phase coherence after a time $\tau_T = \hbar/kT$. At 100 mK, this time is roughly 75 ps, and the thermal length, $\ell_T = v_f\tau_T$, determines the range over which phase coherent electron motion is possible at this temperature. Since the thermal length is over 20 μm, it would seem likely that the amplitude of the quantum interference oscillations would saturate at low temperatures. This, however, is not found to be so.

Fig. 7.7a shows Fabry-Perot oscillations from the same device from which the data in Fig. 7.5 were obtained. Note that as the temperature is raised from 100 to 200 mK, there is a slight decrease in both the amplitude and finesse of the Fabry-Perot oscillations. Such a change over this low temperature range is an indication that some very long trajectories are contributing to the interference pattern. Although the short elastic mean free path of our 2DEG would seem to preclude the existence of such trajectories, electrons traversing particularly stable paths could remain trapped in the cavity for large number of oscillations. Fig. 7.7a also shows a trace taken at 500 mK, where the amplitude of the oscillations has been further attenuated. Fig. 7.7b shows data from a different, though lithographically identical, device taken in the ^{3}He cryostat .[11] In this case, background effects have been eliminated by dividing the conductance by G_0, a smooth background trace obtained by using a bias voltage large enough to suppress quantum interference effects. The amplitude of the oscillations continues to decay with increasing temperature, eventually dying out around 2.5 K. At 1.4 K, the Fabry-Perot oscillations are essentially sinusoidal — the contribution to the finesse made by longer trajectories having been suppressed by the shortened phase coherence length.

[11]Where thermometry above 500 mK is available.

Magnetic Field Dependence

Fig. 7.8a shows consecutive traces from an 800 nm device taken at 385 mK, in which the value of the applied perpendicular magnetic field is incremented with each trace. In Fig. 7.8b, the same data is replotted for 0, 25, and 50 mT, after the background effects have been removed by dividing by G_0 (as was done for Fig. 7.7b). The curves in Fig. 7.8a are not offset from one another. The device conductance increases with increasing field, because the increased Lorentz force is able to bend trajectories away from the reflector gate. Not surprisingly, this decrease in the number of backscattered trajectories is accompanied by decreases the amplitude and the finesse of the oscillations. For example, at 50 mT, the average finesse of the oscillations pictured in Fig. 7.8b is 2.35, compared to a value of 2.77 at zero field. By 75 mT, the Fabry-Perot oscillations are almost completely destroyed.

In the Lloyd's Mirror Interferometers of Chapter 6, application of a perpendicular magnetic field on the order of a 10 Gauss was found to induce a noticeable phase shift in the interference pattern. In Fig. 7.8b, it is clear that no discernible shift occurs when perpendicular fields as large as 50 mT are applied. This difference in behavior is the result of the very different trajectory geometries in the two devices. In the Lloyd's Mirror Interferometer, the interfering trajectories enclose some area and may acquire an Aharonov-Bohm phase shift when a perpendicular field is applied. Conversely, in the absence of trajectory bending the interfering electron paths enclose zero area in the Fabry-Perot Interferometer, and therefore no A-B shift is acquired in the presence of a perpendicular field.

Even though a perpendicular field may not induce an Aharonov-Bohm phase shift in the Fabry-Perot Interferometer, the change in the pathlength of the trajectories that results from trajectory bending should eventually create some phase shift in the interference

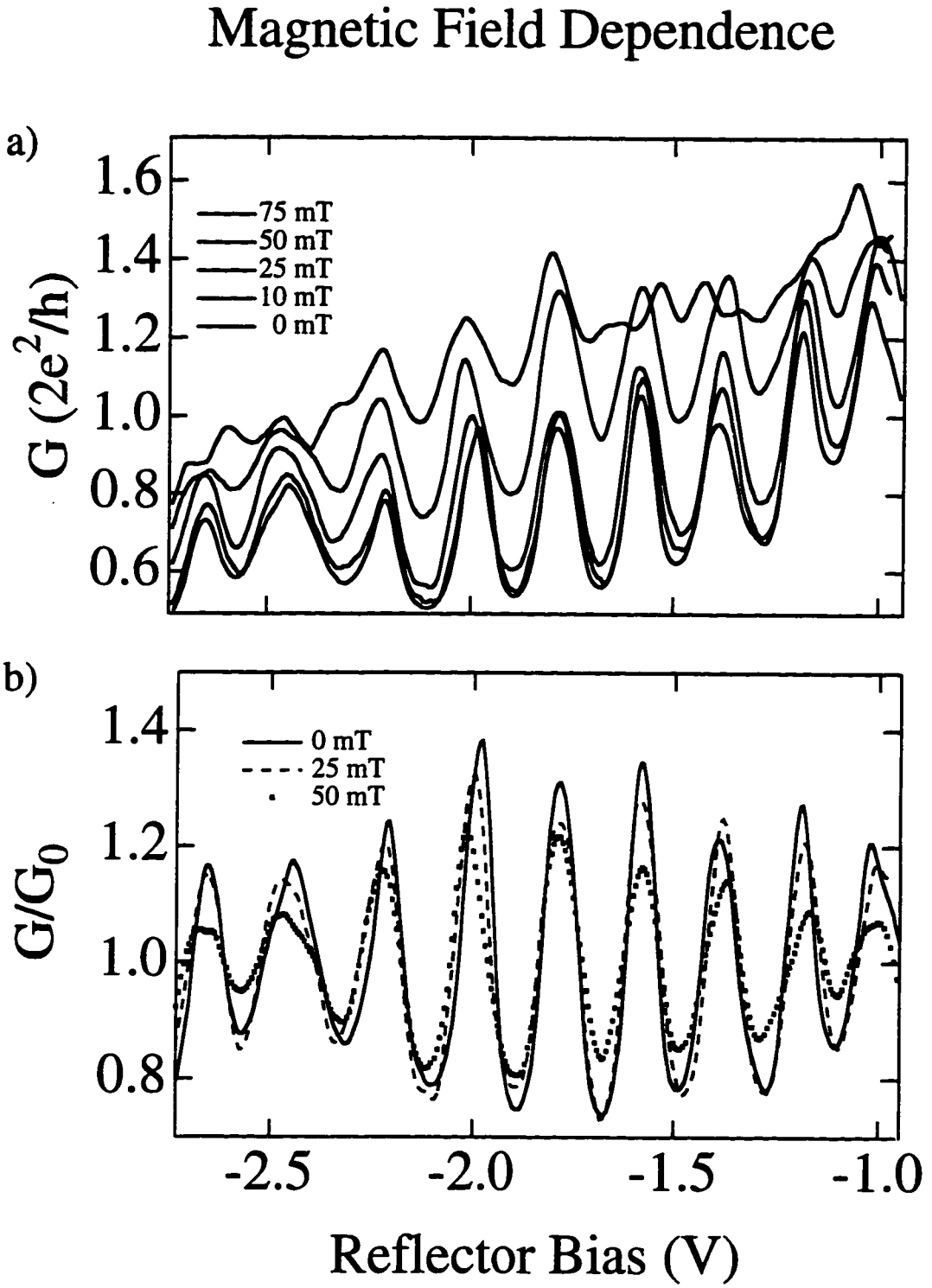

Fig. 7.8 a) Raw conductance data in an 800 nm device at 385 mK for 5 different values of the applied perpendicular field; the bottom trace is 0 mT. b) The same data is replotted after normalization to the smooth background conductance, G_0. The field does not shift the oscillations, but does attenuate their amplitude.

pattern. The ratio of the change in pathlength to the Fermi wavelength determines the phase shift, δ_{bend}. Simple trigonometry can be used to show that δ_{bend} is equal to:

$$\delta_{bend} = \frac{4\pi}{\lambda_f}\left[2\ell_{cyc}\arcsin\left(\frac{L}{2\ell_{cyc}}\right) - L\right], \tag{7.8}$$

where L is the separation between the QPC and the reflector, and ℓ_{cyc} is the cyclotron radius. Inserting numbers into the above formula, for an 800 nm separation at a field of 25 mT, δ_{bend} is only $(0.04)2\pi$, which is consistent with the absence of a detectable phase shift in the data.

Device Size Dependence

Fig. 7.4 shows three devices that were all fabricated next to one another on the same chip (sample KC9.B). In all three cases, the reflectors extend to ±45 deg, but L, the spacing between the reflector gates and the QPC center, is varied in the three devices. The three values of L are 800, 500, and 1000 nm for the devices pictured in Figs 7.4a, b, and c respectively. Devices of different sizes were measured in order to observe the effect this spacing has on the Fabry-Perot oscillations.

In Fig. 7.9, we show point contact depletion traces for the 500 nm and 1000 nm devices. For each device, traces were taken with both reflectors grounded (reflector off), and with one reflector energized past depletion (reflector on). As discussed in Chapter 1, isolated point contacts exhibit steps in their conductance at integer values of $2e^2/h$. These steps are rounded as the temperature is increased, which explains the rounding of the steps in our 1.45 K measurement. Note that with the reflectors grounded, the conductance plateaus occur slightly below the expected integer values, and these plateau conductances drop significantly when a reflector is negatively biased past depletion. The fact that

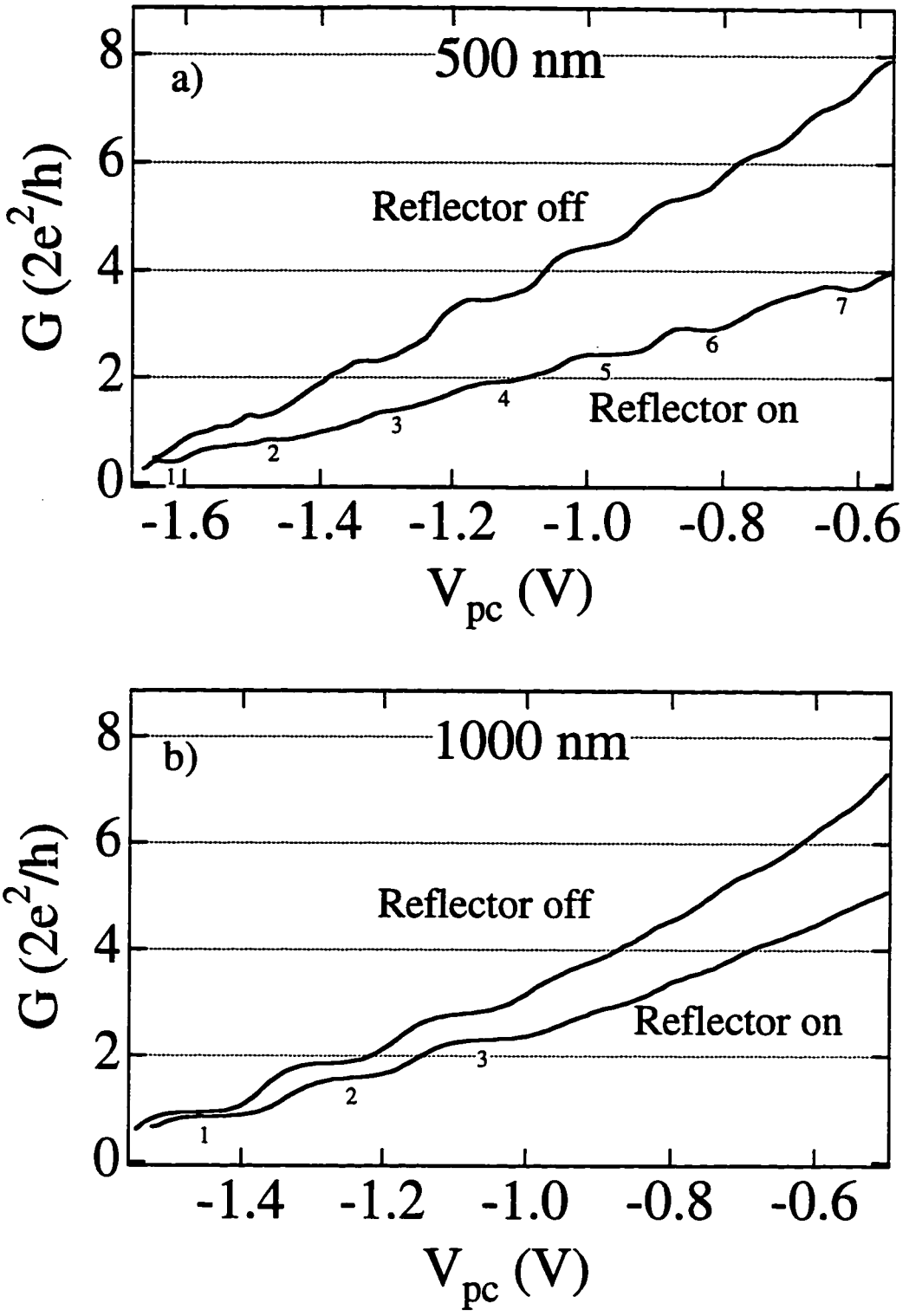

Fig. 7.9 Point contact traces taken at 1.45 K are shown for the 500 and 1000 nm devices in (a) and (b) respectively. In both cases depleting the reflector gate decreases the conductance values of the plateaus, with the effect being larger in the smaller device.

plateaus are observed at conductances lower than $2Ne^2/h$ is an indication that the transmission probabilities of the propagating modes is less than unity; i.e. they are being scattered back through the QPC. Even when the reflector gates are grounded, the electron sheet density beneath them is slightly lower than the sheet density in the ungated regions, resulting in the reflection of a small fraction of the electrons incident on the gate. This explains the non-unity transmission of propagating modes when the reflectors are off. The transmission coefficient is further lowered when the gate is fully depleted and all of the electrons are reflected back towards the QPC.

A reflected electron will only lower the point contact conductance if it passes back through the QPC. Elastic scattering from ionized donors and impurities lowers the odds of this occurring. Therefore, in the larger device where elastic scattering should be able to play a greater role, we expect that reflectors will have a smaller impact on the conductance. Fig. 7.9 shows that this does indeed appear to be the case. The decrease in the conductance plateaus from their integer values is over twice as great in the 500 nm device than it is in the 1000 nm device.

As the separation between the reflector and the point contact increases, the reflector is able to focus fewer electrons back to the QPC. Since the amplitude of the quantum interference oscillations is proportional to the number of electrons that return to the point contact, these oscillations should be attenuated in the larger devices. This effect is illustrated in Fig. 7.10. The figure shows Fabry-Perot oscillations from the 800 and 1000 nm devices taken at the same temperature (385 mK) and approximately the same conductance (~0.65 modes). For ease of comparison, we have once again divided the conductance by G_0 to eliminate background effects. We have also shifted the 1000 nm trace by 50 mV in order to align the oscillations. The amplitude of the oscillations is roughly five times larger in 800 nm devices. Since only one 1000 nm device was measured, it is not clear if such a drastic change is typical or anamolously large. Although the finite phase coherence length is responsible for some of this large difference in

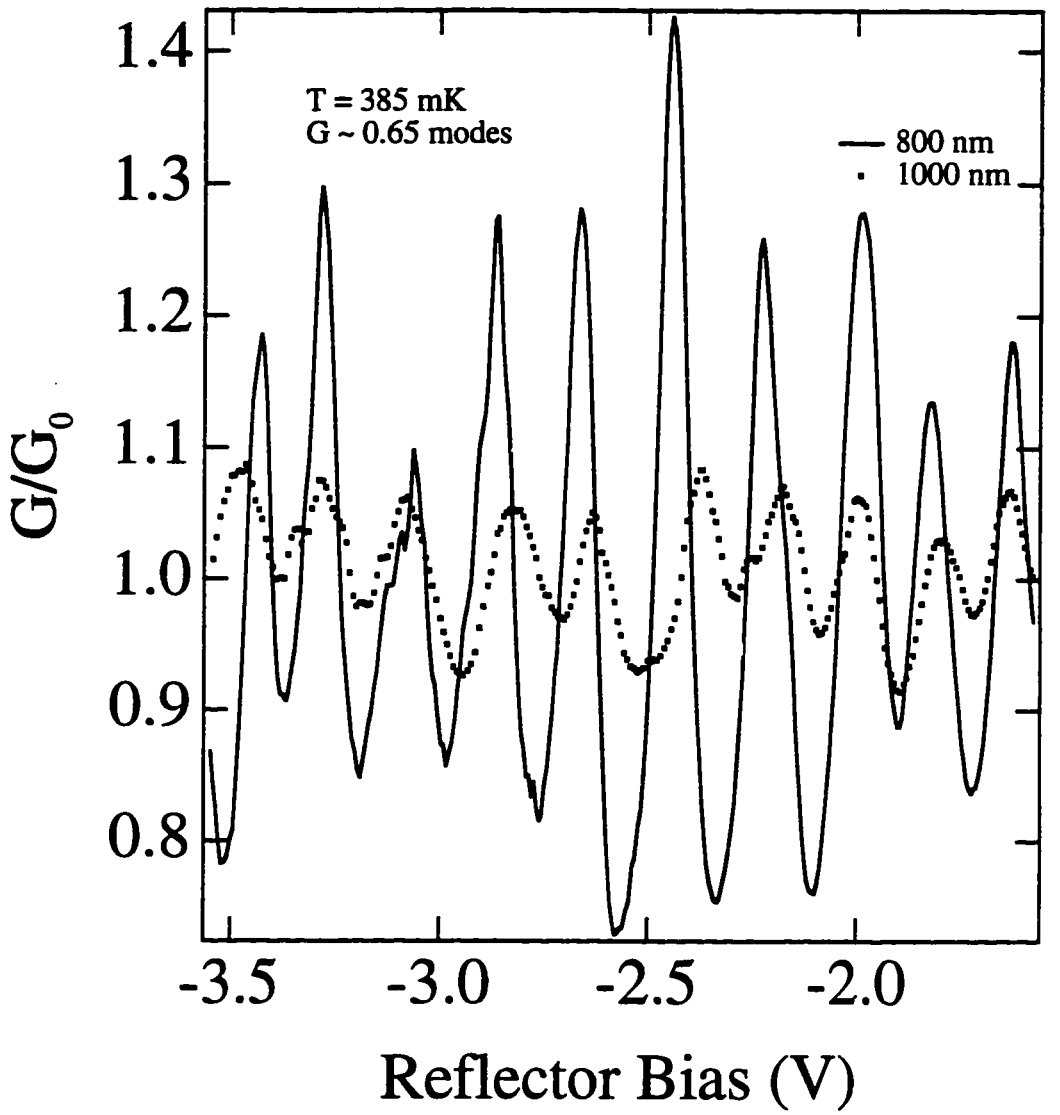

Fig. 7.10 Comparison of the Fabry-Perot oscillations in the 800 and 1000 nm devices. The amplitude of the oscillations is clearly larger in the smaller device. The reflector bias voltages for the two traces have been slightly offset to align the oscillations.

amplitude, elastic scattering is the dominant cause; the small amplitude of the oscillations in the 1000 nm device could be the result of one or more impurities located near the resonance cavity. Data from the 500 nm device is not included in the comparison shown in Fig. 7.10. As a result of the close proximity of the reflector gate to point contact in the 500 nm device, ramping the voltage on the reflector gate has a greater impact on the average QPC conductance in this device than in those with greater separations. Because of this "cross talk", a 500 nm device with point contacts in the tunneling regime will quickly be completely pinched off. Nevertheless, we were able to determine that the amplitude of the oscillations around $G = 0.6$ modes in the 500 nm device were roughly two times larger than those in the 800 nm device. Not surprisingly, the 500 nm device also had the highest finesse of any Fabry-Perot interferometer we measured ($F \sim 3.5$).

Charging Effects

In a quantum dot isolated from electron reservoirs by tunnel junctions, due to electron-electron repulsion there is a charging energy, E_C, that must be overcome in order for an additional electron to tunnel onto the dot. At sufficiently low temperature, this charging energy leads to the Coulomb blockade oscillations that may be observed by sweeping a gate capacitively coupled to such a quantum dot [for a review, see Grabert and Devoret, (1992)]. Even though our Fabry-Perot interferometers are not well-defined quantum dots, if the average lifetime of electrons in the cavity were long enough, charging effects might be visible in such a structure.

How long would the lifetime have to be in order to observe such charging effects? A crude estimate can be made from simple energy/time uncertainty arguments. To begin, we need a value for the charging energy. Although we are not dealing with a quantum dot, the charging energy of the resonance cavity should be comparable to that of isolated dots with similar dimensions; in such a dot, the charging energy has been measured to be ≈ 0.2

meV [Waugh, *et al.*, (1995)]. From the finesse of the oscillations, Eq. (7.7) can be used to determine the average boundary reflectivity, $R_{avg} = \sqrt{R_{pc}R_r}$. For a typical finesse value of 3.0, $R_{avg} = 0.6$. From this average boundary reflectivity, we can estimate M, the average number of oscillations for which an electron remains in the cavity:

$$M = \frac{1}{2}\left(\frac{1}{1-R_{avg}}\right). \tag{7.9}$$

M = 1.2 for $F = 3.0$. The average dwell time in the cavity is simply $2ML/v_f$, which is about 4 ps for a cavity with L = 500 nm and M = 1.2. Dwell times this short have an associated energy uncertainty $\Delta E \approx \hbar/4$ ps ≈ 0.2 meV, which is very close to the estimated charging energy. This crude argument suggests that longer dwell times are required before clear evidence of charging effects would be visible in our interferometers.

Fig. 7.11a shows 100 mK data from a 500 nm device located on yet another sample (KC8.F). Fabry-Perot oscillations somewhat poorer than what were obtained with the superior KC9 wafer are clearly evident, but there are no periodic, higher frequency oscillations indicative of charging effects.[12] This device is lithographically identical to the one pictured in Fig. 7.4b, except it has only one reflector gate. This gate extends to the edge of the sample, which allowed us to directly measure the series conductance of the constrictions between the reflector arc and the point contact. The conductance of an individual constriction should be twice the series value. At depletion (-0.33 V), the series conductance of the side constrictions is nearly 4 modes.

In Fig. 7.11c, data from the same device is shown with a larger negative bias voltage is applied to the reflector gate. In this case, the reflector gate has moved in far enough so that electrons must tunnel to pass through the constrictions between the QPC

[12]The spikes in the data may be related to charging effects, but, unlike the Fabry-Perot oscillations, they are not reproducible on consecutive sweeps.

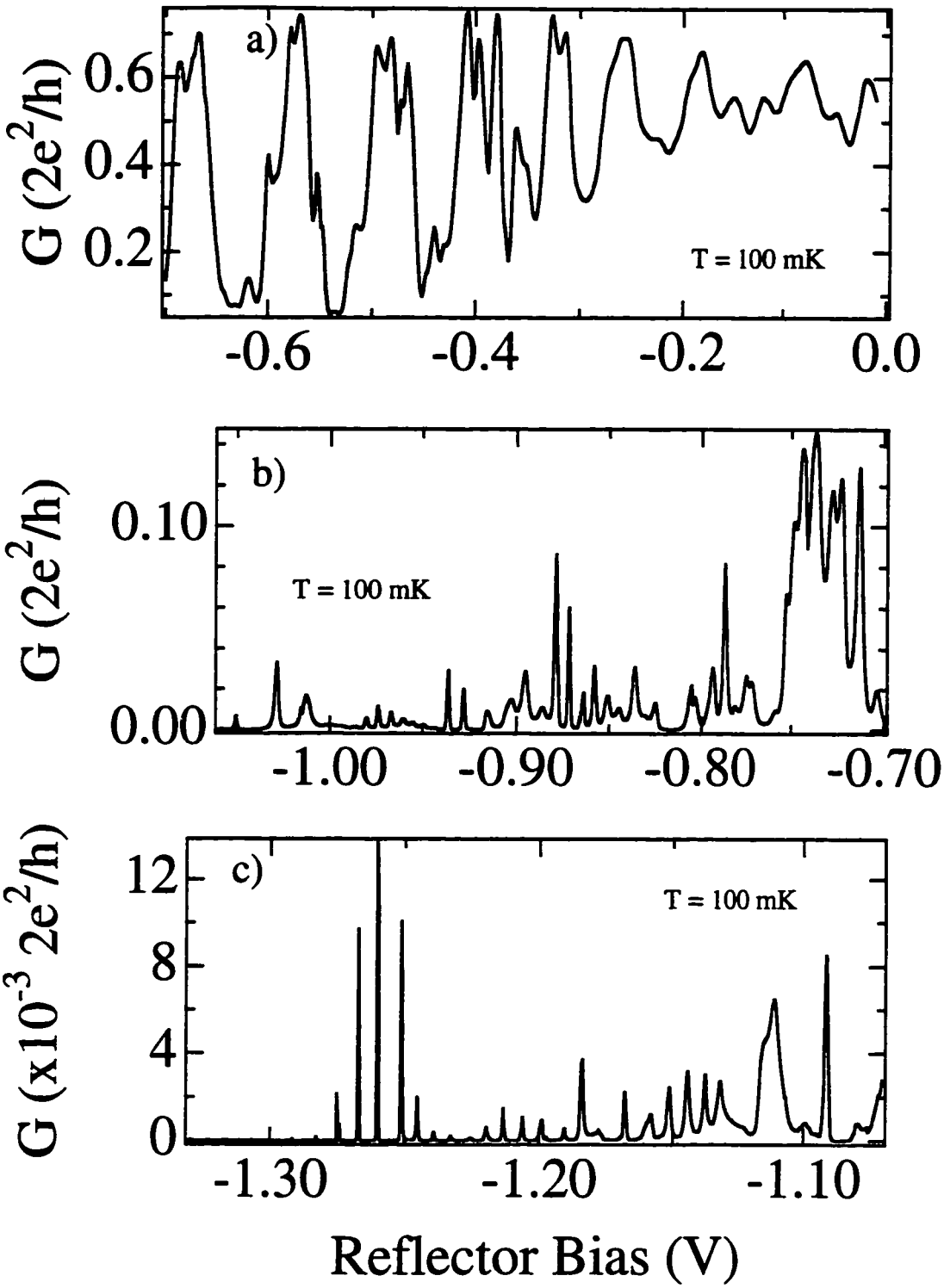

Fig. 7.11 a) In this 500 nm device, Fabry-Perot oscillations are seen in the conductance when the bias voltage on the reflector is ramped. b) As the constrictions between the reflector and point contact continue to narrow, higher frequency oscillations reminiscent of Coulomb blockade appear. c) In the limit of a well-defined dot, we obtain sharp Coulomb oscillations.

gate and the reflector. Instead of Fabry-Perot oscillations, we now observe Coulomb blockade oscillations, with each oscillation corresponding to the removal of another electron from the now well-defined quantum dot formed between the reflector and QPC gates. There is some interesting behavior in the amplitude of the Coulomb blockade oscillations, such as the envelope around -1.26 V. Although the origin of such structure is unclear, it may be related to quantum interference resonances.

Between these two extremes, we see weak Coulomb blockade oscillations superimposed on top of longer frequency quantum interference oscillations (Fig. 7.11b). The Coulomb blockade oscillations do not appear until the series conductance of the side constrictions is equal to about N = 2 modes (bias ≈ -0.7 V). At this reflector bias, the regular Fabry-Perot oscillations have been replaced by aperiodic conductance fluctuations. At low reflector bias voltages where a large opening exists between the reflector and the QPC gate, electrons that experience large-angle elastic scattering events typically exit the cavity. Such losses lower the finesse of the device, but do not otherwise affect the Fabry-Perot oscillations. As the gaps between the edges of the reflector ar.1 the point contact gate become smaller, trajectories that previously exited the Fabry-Perot cavity are instead trapped within the quasi-dot, where they now contribute to the interference pattern. The periodic Fabry-Perot oscillations are destroyed by such trapped electrons, leaving only aperiodic quantum interference fluctuations. If we could fabricate cavities with higher finesse, it might be possible to observe charging effects when the edge gaps are wide enough so that clean Fabry-Perot oscillations would still be attainable. In this case, we would expect to see high frequency Coulomb blockade oscillations superimposed on these Fabry-Perot resonances.

7.4 Summary

In this chapter, we have examined periodic conductance oscillations in two varieties of electrostatically tunable Fabry-Perot electron interferometers. The first class of devices uses two reflector gates to form a resonance cavity. The best oscillations are observed in this dual reflector design when the point contact between the two gates is open enough so that several transverse modes are transmitted. Even more striking periodic oscillations are present in a single reflector interferometer. In these devices, the point contact must be in the tunneling regime in order to obtain the sharpest periodic oscillations. When in the tunneling regime, significant finesse is apparent in the oscillations, which indicates that multiply-reflected electron trajectories are contributing to the interference effects. The amplitude of the oscillations can be quite large. In fact, where the resonance condition is satisfied in the tunneling regime, it is possible for the conductance of the device to exceed that of the naked point contact.

The oscillations are quite robust, and have been observed in a number of different samples. They work reproducibly enough so that it should be possible to use them as a building block in a larger quantum interference experiment. On their own, they could serve as quantum interference based transistors with switching powers orders of magnitude less than that of classical transistor devices, although the low temperatures required for their operation make such transistor applications rather impractical.

Chapter 8

Concluding Remarks and Future Directions

Our measurements of the weak localization effect in narrow channels indicate that at dilution refrigerator temperatures, it is possible for the electronic phase coherence time to be an order of magnitude larger than the elastic scattering time in our two-dimensional electron gas systems. An interesting open question in these measurements is the apparent saturation of the phase coherence time at temperatures below 200 mK. Although dephasing induced by external radiation is a likely source of this saturation, a systematic investigation of the effect would be required to confirm this suspicion.

The long phase coherence lengths in our 2DEG allow us to observe a variety of quantum interference phenomena in ballistic devices. The largest interference effects are seen in electron interferometers. The clean, periodic conductance oscillations present in our Fabry-Perot interferometers show that an electrostatically-defined gate may be used to shorten the pathlength of ballistic trajectories in a controlled fashion. A very similar effect was also observed in the electron analog of a Lloyd's mirror interferometer. The finesse of the oscillations in the Fabry-Perot device indicates that significant focusing of ballistic electron trajectories is possible as the result of specular reflection from the mirror gate. These Fabry-Perot oscillations are quite robust to the disorder present in 2DEG systems, and have been observed in a number of different devices. Because of their robust nature, these and similar electron interferometers show promise for use in future work with ballistic electrons.

The coherent backscattering effect in very open ballistic structures also proved to be quite reproducible. In Chapter 5, a strong zero field magnetoresistance peak was observed in devices specifically designed to support a limited number of backscattered orbits. A variety of measurements demonstrate that the magnetoresistance peak results from coherent backscattering involving electrons scattered from a pair of reflector gates. Due to the presence of magnetoconductance fluctuations, several averaging techniques, including fabrication of multiple identical devices, were required in order to perform a quantitative analysis of coherent backscattering in these structures. It seems likely that experimental imperfections in our 2DEG system, such as impurity scattering and the distortion of gate boundaries, affect the shape of the coherent backscattering peak. In particular, such imperfections are the probable reason why a periodic modulation of the coherent backscattering effect was not observed in our open devices. The same imperfections help explain the absence of Aharonov-Bohm oscillations in the forward-scattered interference devices discussed in Chapter 6.

One obvious way to improve all of our experiments in the future would be to perform the experiments in higher mobility 2DEGs. Mean free paths over four times as long as that in our current material should be attainable. Such an improvement might significantly increase the lifetime of electrons in our Fabry-Perot resonance cavities. In fact, it might even become possible to observe charging effects in devices with very wide exit leads. For our magnetic field experiments, higher mobility would increase the chances of observing periodic Aharonov-Bohm oscillations in ballistic microstructures.

Even with higher mobility material, it is not at all clear that Aharonov-Bohm oscillations would be visible in devices which do not use some potential barrier to create a doubly-connected geometry. It might be interesting to fabricate structures similar to the forward-scattering interference devices of Chapter 6, but to also include an isolated electrostatic gate over what is supposed to be the excluded region for trajectories in the device. An air bridge or tri-layer technique would have to be used to contact the central

gate. If Aharonov-Bohm oscillations were visible with the 2DEG beneath the central gate depleted, but absent with the 2DEG present, it would be strong evidence that ballistic trajectories somehow penetrating this region are responsible for suppressing the Aharonov-Bohm effect.

Currently, such an experiment would be difficult to perform due to the challenges involved in creating such three-dimensional structures. A promising technique for performing such experiments in the future involves the use of a cryogenic scanned probe microscope (SPM). The SPM allows a conducting tip to be scanned over a sample. Therefore, a negatively-biased tip could replace the central gate in the above experiment. A similar use of the SPM tip has already been demonstrated in experiments involving transport through a wide point contact [Eriksson, *et al.*, (1996)].

Used in this way, the cryogenic SPM should be a powerful new tool for studying ballistic electron transport. For example, our current understanding of electron trajectories inside quantum dots has been primarily obtained from quantum interference experiments like those in the Circle/Pacman experiment (Appendix B). Although average trajectory lengths and enclosed areas can be inferred from magnetoconductance fluctuations, the actual trajectories have never been directly observed. Suppose we were to scan a negatively biased tip over the dot, while simultaneously measuring the device resistance. If correlations between the device resistance and the tip position were detectable, it might be possible to determine the regions of high trajectory density inside the quantum dot. It would be especially interesting to couple these direct imaging techniques with quantum interference experiments. Doing so would require the cryogenic SPM to work at temperatures lower than the current 4.2 K base temperature for the instrument, and also require some way to apply a magnetic field to the samples.

Appendix A

Kelvinox 100

A.1 Abridged Operating Procedures
(compiled by A.S. Adourian)

Cooling to 77 K

- Remove old grease from cone seal and apply new grease.
- Fit IVC over insert and form cone seal.
- Test IVC cone seal for leaks at room temperature.
- Secure 1K pot fill tube to IVC with mylar tape.
- Perform throughput test/dilution unit leak check as described below. *(optional)*
- Introduce helium exchange gas into IVC.
- Lower insert into dewar, align, and secure using fastening bolts.
- Attach still, condenser, and 1K pot pumping lines to insert; make sure pipe from cabinet intended for IVC is blanked off.
- Attach leak detector to cabinet "IVC/OVC" port branch and evacuate still, condenser and 1K pot pumping lines through 2A, 7, 2, 3, 1 to P1 $< 5 \times 10^{-2}$ mbar.
- Leak check lines and joints.
- Open still and condenser valves at top of insert and pump dilution unit to P1 $< 5 \times 10^{-2}$ mbar.
- Close still and condenser valves at top of insert and all valves on cabinet; detach leak detector from cabinet.
- Perform optional room temperature throughput test and dilution unit leak test (see procedure below).
- Evacuate 1K pot through 4A; make sure needle valve and 1A are closed.

- Transfer liquid nitrogen into dewar. Watch value of resistor E-J on connector B change to be sure that level is above top of magnet.
- Wait until thermometry reads 77 K; typically takes 2-3 hours.
- Perform optional 77 K throughput test and dilution unit leak test (see procedure below).
- Attach 'Main Bath' pipe with valved hose attachment to dewar exhaust.
- Overpressure dewar with helium gas through 'Main Bath' pipe and blow out liquid nitrogen.
- Withdraw blow out tube, insert bung, and pump out bath using rotary pump through 4A and 1A, making sure 5A, 2A, 3A and 1K pot valve at insert are all closed.
- If G3 hesitates around 100 mbar, there is still some liquid in bath. Repressurize bath and repeat pump down.
- Repressurize bath to atmosphere with helium gas.

Cooling to 4.2 K

- Evacuate 1K pot through 4A; make sure needle valve and 1A are closed. Stop pumping once 1 K pot is empty.
- Open dewar exhaust and transfer liquid helium slowly (typically longer than 1-2 hours). It takes ~ 45 liters to cool and fill bath.
- When thermometry reads 4 K, pump helium exchange gas from IVC by attaching leak detector directly to IVC port at insert. Pump overnight until leak signal is less than $3x10^{-7}$ atm cc/s.

Condensing and Circulating Mixture

- Turn on helium rotary pump and check the oil level (this pump requires special oil-contact Oxford for details).
- Clean traps by pumping on them through 5A, 2A, 7 and 11A (with all other valves on panel closed) while warming nitrogen trap thoroughly with heat gun. It is essential that the pump is not removed during heating, as high pressures can develop in the traps. Close all valves once traps are clean and back at room temperature.
- Cool nitrogen trap by inserting it in its dewar. Cool helium trap by inserting it in a full 60 liter storage dewar.

- Fill and pump on 1 K pot by opening needle valve ~1/4 turn and opening 4A and 1K pot valve at insert. R6 should settle to 650-700 Ω , and P2 should read 6-10 mbar, after a few minutes.
- At insert, open only still valve; mixture will be condensed on still side.
- Open 3.
- Open 13a and let mixture from behind pumps cool in traps for ~1 minute.
- Open 12a and let precooled mixture into still line.
- Open 9 and dumps valve to allow dumps mixture into circuit. Check that still is cooling by noting increase in R2.
- After ~1 hour close 9 and open 10 slowly, keeping G2 < 400 mbar, to pump remaining mixture out of dumps.
- It will take 1-2 additional hours to condense mixture (impedance of helium trap is high); the longer you wait, the easier it will be to start circulation.
- To start circulation: open 1 and condenser valve at top of insert, close 3 and 10, and open 6 by cracking the valve very slowly, keeping G2 < 400 mbar (at this point, 2, 3, 4, 5, 7, 8, 9, 10, 11a should all be closed). Keep cracking 6 until it is all the way open. Be patient; this may take more than half an hour.
- Operate resistance bridge at 30 μV excitation, and watch R4 and R7 values rise. It will take a few hours to reach base temperature.
- The still heater can be adjusted to 0.5 - 1.0 mW to decrease base temperature.

Daily Maintenance

- Transfer liquid helium daily (or at least every 36 hours), keeping level above 30% to ensure 1K pot remains filled.
- Replenish liquid nitrogen trap twice daily.
- Perform a 'quick clean' of the helium trap daily: close 1, 6 and open 5; lift helium trap out of its storage dewar and hold at room temperature for a few seconds; reinsert helium trap into dewar and close 5, open 1 and 6 (don't forget to re-close vent on storage dewar). A slow rise in base temperature and an increase in G2 likely indicate that the helium trap is becoming clogged and requires a quick clean.

Warming Up

- Close needle valve evacuate 1K pot. Close 1K pot pumping valve at top of insert.
- Close 13a and open 5 and 9, and make sure dumps valves are open. This sets the fridge in single shot mode, with the ^{3}He being extracted from the insert but not returned.
- Increase the power supplied to the still and mixing chamber heaters to maximum.
- Check that all the mixture has been returned to the dumps by reading G2 and comparing it to the value at the beginning of the cooldown (~525 mbar as of this writing, although G2 is not independent of atmospheric pressure and may vary by a few percent).
- Once all the mixture is out of the insert and P1 < 0.1 mbar, close 1, 5, 6, 9, 12a and the dumps valves. Note that there is mixture left behind pump and up to valve 13a. Close all valves on fridge insert.
- Make sure all the valves on the cabinet and on the insert are closed, disconnect the piping and electrical leads to the insert, and remove the insert from the dewar. A small amount of helium or air can be used to soften the IVC.
- Reconnect and monitor the diagnostic thermometry and wait until the insert has reached room temperature.
- To remove the IVC, fit the slide hammer ring over the IVC and bolt the plate to the underside of the large diameter part of the IVC. Vent the IVC by opening the IVC valve at the top of the insert. Support the IVC to prevent it from falling when the seal is broken, and slide the slide hammer ring down sharply against the plate. It may take a few impacts to free the IVC tube.
- If warming traps, pump on them through 5A, 2A, 7, 11a.

Optional Throughput Test / Dilution Unit Leak Check Procedure
(using external ultrapure helium supply)

- All valves on cabinet panel should be closed, as well as still and condenser valves at top of insert.
- Attach leak detector directly to IVC pumping port at top of insert and monitor leak signal from IVC.
- If traps haven't been cleaned, clean them following procedure outlined in 'Condensing and Circulating Mixture' section above.

- Cool nitrogen trap by inserting it in its dewar. Cool helium trap by inserting it in a full 60 liter storage dewar.
- Attach a valved hose nipple to 'Vent 1' port at rear of cabinet and connect it to a UHP helium gas supply with a thick flexible hose (the old Airco regulator and hose in the screen room work well).
- Pump out flexible hose through 5A and 2A; the overriding concern throughout is to prevent any air from getting into the dilution unit. Close 5A and 2A.
- Open 11a, 12a and 3.
- Pressurize still pipe to ~ 950 mbar on G1 by introducing UHP helium through Vent 1, 7, 11a, traps, 12a, 3. To avoid damaging the traps, do not overpressure (set regulator ~ 3 psi) and close 7 periodically to allow helium in traps to flow into still line. Be patient: this will take ~15 minutes.
- Close off hose nipple valve at cabinet and helium supply.
- Close 12a.
- Evacuate traps through 11a, 7, 2A, 5A; after traps are empty, close 11a.
- Close 3 and pump out G1 gauge space through 2, 7, 2A, 5A until G1 = 0. G1 will be used to monitor throughput.
- Close 2 and 7.
- Open still valve at top of insert to let purified helium into dilution unit.
- Open condenser valve at top of insert.
- Open 1 and record throughput rate by monitoring G1.
- Check leak detector for leak signal, which would indicate a leak from dilution unit to IVC.
- Typical throughput rates are ~50 mbar/minute at 300 K, ~300 mbar/minute at 77 K.
- Evacuate helium from system by pumping through 1, 3, 2, 7, 2A, 5A. Pump until P1 reads less than ~ 3×10^{-2}.
- Close still and condenser valves at top of insert and close all valves on cabinet.
- Disconnect leak detector from IVC port and introduce helium exchange gas into IVC.

A.2 Diagnostic Tables

RuO_2 Calibration Table

T (mK)	R7 (kΩ)	R4 (kΩ)
12	94.940	88.603
14	75.553	71.370
16	62.444	59.549
18	53.068	50.997
20	46.073	44.553
22	40.676	39.542
24	36.401	35.543
26	32.938	32.285
28	30.081	29.583
30	27.688	27.308
32	25.657	25.369
34	23.912	23.697
36	22.398	22.241
38	21.074	20.963
40	19.905	19.832
42	18.867	18.825
44	17.939	17.922
46	17.105	17.109
48	16.351	16.372
50	15.666	15.701
52	15.041	15.089
54	14.470	14.527
56	13.944	14.010
58	13.460	13.533
60	13.012	13.090
62	12.597	12.680
64	12.210	12.297
66	11.850	11.940
68	11.513	11.606
70	11.197	11.292
72	10.901	10.998
74	10.623	10.720
76	10.360	10.459
78	10.113	10.212
80	9.878	9.978
82	9.657	9.757
84	9.446	9.546
86	9.247	9.347
88	9.057	9.156
90	8.876	8.975
92	8.704	8.802
94	8.539	8.637
96	8.382	8.480
98	8.232	8.329
100	8.088	8.184
105	7.754	7.848
110	7.452	7.543
115	7.178	7.267
120	6.927	7.014
125	6.698	6.781
130	6.486	6.568
135	6.291	6.370
140	6.111	6.187
145	5.943	6.017
150	5.787	5.858
155	5.641	5.709
160	5.504	5.570
165	5.375	5.440
170	5.255	5.317
175	5.141	5.201
180	5.034	5.091
185	4.932	4.988
190	4.836	4.890
195	4.744	4.796
200	4.658	4.708
205	4.575	4.623
210	4.497	4.543
220	4.350	4.393
230	4.216	4.256
240	4.093	4.130
250	3.979	4.014
260	3.874	3.906
270	3.777	3.806
280	3.686	3.713
290	3.601	3.626
300	3.522	3.545
400	2.938	2.944
500	2.576	2.572
600	2.327	2.314

Table A.1 Temperature calibrations for the RuO_2 resistors. The copper spools onto which R4 and R7 are mounted are marked in blue and red respectively.

Typical Diagnostic Resistor Values

Channel	Location	R at 300 K	R at 77 K	R at 4.2 K	R at ~1.5 K
1	sorb	450 Ω	525 Ω	4,300 Ω	---
2	still	400	420	550	---
3	cold plate	325	340	400	---
4	m/c	1,000	1,017	1,087	1,620
5	m/c	315	325	350	---
6	1K pot	380	400	525	675
7	m/c	1,000	1,015	1,087	1,620

Table A.2 Typical values of the Kelvinox diagnostic resistors during the cooldown from room temperature. These values are only guidelines, as there is considerable drift between thermal cycles.

Wiring Diagram for the Military Connectors

Connector #1 (for Level Probe)

Lead	Pin	Wire Color
I-	J	orange stripe
V+	H	blue stripe
I+	K	blue
V-	A	orange

Connector #2

Item	Pins	Wire Color
Persistent	D	black
Current Swt.	B	red
Power	A	white
Resistor	K	purple
Allen-Bradley	E	blue
Resistor	J	green

Table A.3 Diagnostic wiring diagram for the two 10-pin military connectors on the Kelvinox. The connectors are distinguished from one another by orange paint on the brass blank-off of connector #1. Including leads, the persistent current switch has a room temperature resistance of 58 Ω. At helium, it is driven normal by a current of 40 mA.

Wiring Diagram, Fischer Connector #1

a) RuO_2 resistors located on mixing chamber (4-probe)

Ch. #	Lead	Fischer	37-pin	Color
7	V_{lo}	18	17	blk/purp
	I_{hi}	17	16	blk/yellow
	I_{lo}	15	36	blk/green
	V_{hi}	16	35	blk/blue
4	V_{lo}	11	28	solid orange
	I_{hi}	13	27	orange stripe
	I_{lo}	14	10	blk/orange
	V_{hi}	12	9	blk/red

b) Carbon Resistors (2-probe); Common Ground = Fischer pin 7

Channel	Location	Fischer	37-pin (I_{hi}, V_{hi}, V_{lo}, I_{lo})
1	sorb	1	1, 20, 2, 21
2	still	2	22, 4, 23, 5
3	cold plate	3	6, 25, 7, 26
n/c	mixing ch.	4	n/c
5	mixing ch.	5	11, 30, 12, 31
6	1K pot	6	32, 14, 33, 15

c) Heaters

Location	Nominal Resistance	Fischer
still	500 Ω	19, 20
mixing ch.	500 Ω	21, 22
sorb	70 Ω	23, 24

Table A.4 Wiring diagram for Fischer connector #1. a) A true 4-probe measurement of the RuO_2 resistors is possible. For the two multiplexer channels, the table lists the Fischer connector pin number, the 37-lead connector pin number, and the color code of the wiring in the 37-pin connector. b) The resistance of the carbon diagnostics is found with a 2-probe measurement. A common Fischer connector pin, #7, is used for low on all carbon resistors. One of the carbon resistors on the mixing chamber has been disconnected to make room for R4. c) The Fischer pins and nominal resistance values for the three heaters.

Appendix B

Reprint of the paper:

"Influence of Shape on Electron Transport in Ballistic Quantum Dots"

This paper examines coherent backscattering and conductance fluctuations in ballistic quantum dots of different shapes and sizes. These experiments clearly demonstrate that the shape and size of the device affect the characteristic magnetic field scales for these effects. The coherent backscattering experiments discussed in Chapter 5 represent an extension of this work.

PHYSICAL REVIEW B VOLUME 50, NUMBER 23 15 DECEMBER 1994-

Influence of shape on electron transport in ballistic quantum dots

M. J. Berry, J. A. Katine, and R. M. Westervelt
Division of Applied Sciences and Department of Physics, Harvard University, Cambridge, Massachusetts 02138

A. C. Gossard
Materials Department, University of California, Santa Barbara, California 93110
(Received 29 August 1994)

We have investigated the low-temperature ($T=0.43$–4.25 K) magnetotransport of quantum dots fabricated in the shape of an open circle and a circle having a central bar. The characteristic magnetic fields for both coherent backscattering and conductance fluctuations are strongly shape dependent: both are larger by a factor ≥ 3 in the device with the central bar. Comparison of large and small devices of nominally identical shape shows that characteristic trajectory areas are proportional to the device area.

Mesoscopic transport in diffusively scattering metals and metallic semiconductors has been carefully studied:[1] interference of forward-scattered electron waves traveling by different paths causes time-independent conductance fluctuations; interference of time-reversed pairs of backscattered electron waves leads to weak localization. Analogs of both phenomena have recently been observed in ballistic microstructures for which the mean free path greatly exceeds the size of the device. At low temperatures, the magnetoconductance of circular and stadium-shaped quantum dots with quantum point contacts show conductance fluctuations due to the interference of electron waves traveling between the contacts by different paths,[2] and a coherent backscattering peak at zero magnetic field due to the interference of time-reversed pairs of backscattered trajectories.[2–6]

Quantum interference phenomena in ballistic microstructures are of great interest because they are produced by scattering from the walls of the structure rather than by randomly located impurities and are thus inherently shape dependent, and because they make contact with the fundamental theory of statistical mechanics and quantum chaos in billiards.[7] A circular billiard differs from a stadium in that an ideal circle has integrable trajectories that conserve angular momentum, while an ideal stadium produces chaos. The differences observed between circles and stadia in measurements of conductance fluctuations and coherent backscattering are, however, not large and require quantitative analysis to discern.[2–5] The lack of obvious differences between data from circles and stadia may in part be due to the redirection of electron trajectories by the small-angle scattering and boundary roughness present to some degree in all samples.[8]

In this paper we present magnetoresistance data on quantum dots fabricated in the shapes of an open circle and a circle with a barrier between the point contacts, which show large, unambiguous shape- and size-dependent changes in both the conductance fluctuation spectra and the coherent backscattering peak. Figures 1(a) and 1(b) show electron micrographs of quantum dots with quantum point contacts fabricated in two shapes: shape A, an open circle and shape B, a circle with a central barrier; the bright area is a patterned Au gate used to define the dot in a two-dimensional electron gas located underneath the gate in a $GaAs/Al_xGa_{1-x}As$ heterostructure. Conductance fluctuations originate from interference of forward-scattered electron waves as indicated for

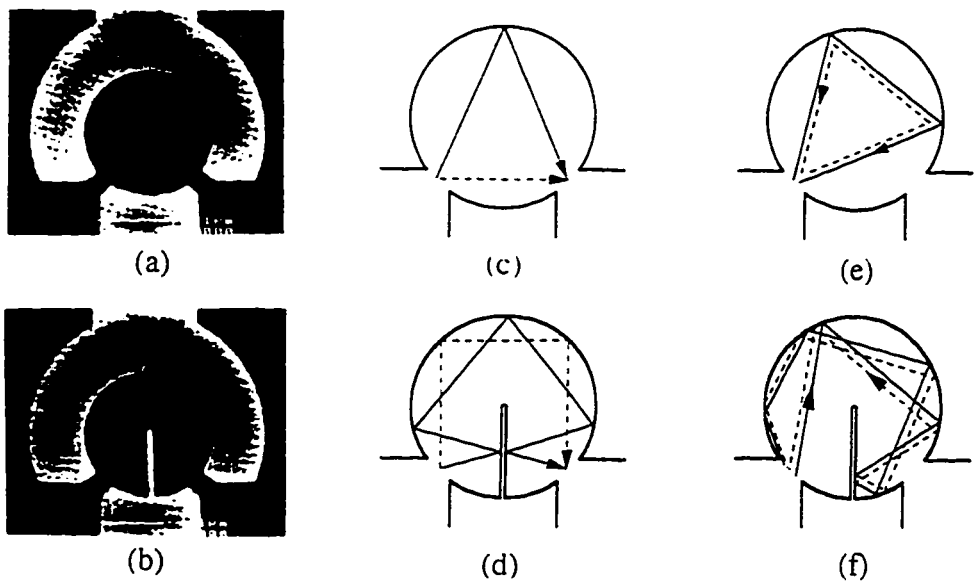

FIG. 1. Scanning electron microscopy micrographs of (a) large-shape A and (b) large-shape B; length bar is 1 μm. In shape A, forward-scattered (c) and backscattered (e) trajectories circulate in a single direction; in shape B [(d) and (f)], they reverse direction with each rebound off the central bar, partially canceling the accumulated area. Trajectories circulating clockwise (counterclockwise) are shown in solid (dashed) lines.

0163-1829/94/50(23)/17721(4)/$06.00 50 17 721

the open circle in Fig. 1(c), while coherent backscattering originates from the interference of pairs of time-reversed paths as shown in Fig. 1(e). For the same device, the enclosed area for coherent backscattering is larger than that for conductance fluctuations by roughly a factor of 2. Characteristic areas can be measured experimentally via the magnetic field necessary to insert a fraction of a flux quantum, $\Phi_0/2\pi=\hbar/e$, and thereby change the interference. For open circular dots, electrons circulate in the same direction, and the enclosed areas can be quite large.

As illustrated in Figs. 1(d) and 1(f), the barrier in shape B reflects electron trajectories and greatly reduces the enclosed area of both forward-scattered trajectories linking the two contacts, as well as the enclosed area of time-reversed pairs of backscattered trajectories. Thus we expect the characteristic areas associated with conductance fluctuations and coherent backscattering in shape B to be smaller than for the open circle, and the corresponding characteristic magnetic-field scales to be larger. This difference should be robust to small amounts of disorder: although small-angle scattering and boundary roughness destroy the perfect symmetry of the open circle, they are unlikely to completely reverse the direction of circulation.

Quantum-dot devices were fabricated using electron-beam lithography and Cr/Au metallization to define gate structures on the surface of $GaAs/Al_xGa_{1-x}As$ heterostructures containing a two-dimensional electron gas with density $n=4.4\times10^{11}$ cm^{-2} and mobility $\mu=350\,000$ cm^2/V sec, located 420 Å below the surface. Two pairs of devices were made with nominally identical shapes; one large pair (pictured in Fig. 1) with electron-gas area $\cong1.6$ μm^2 obtained by subtracting the depletion width from the lithographic size, and one small pair (not shown) with electron gas area $\cong0.43$ μm^2. The width of the bar in the devices with barriers is less than 50 nm. All four devices are much smaller than the measured mean free path 3.8 μm, so electron trajectories inside the dots approximate straight lines, and we say that transport is ballistic. In our devices, the measured small-angle scattering time $\tau_s\cong0.5$ psec.[9] At 0.43 K, the measured phase coherence length was 19 μm for ballistic motion.[10] The samples were cooled in a ^{3}He cryostat to temperatures between 0.43 and 4.25 K, inside a superconducting solenoid. The magnetic field was oriented perpendicular to the plane of the electron gas, and the precision of the field sweeps was ±0.01 mT. Magnetoresistance measurements were made using ac lock-in techniques at 11 Hz.

Figure 2 shows four magnetoresistance plots taken at $T=0.43$ K that illustrate the striking difference between shapes A and B. Data for the large devices are shown as the upper (B) and lower (A) traces in Fig. 2(a), data for the smaller versions of the devices are shown in Fig. 2(b). All four magnetoresistance traces have the same qualitative features: a resistance peak centered at zero magnetic field due to coherent backscattering,[2–6] superimposed on conductance fluctuations due to interference of forward-scattered paths.[2] The magnetic-field scales for shapes A and B, however, are quite different. As predicted by theory, the width of the zero-field peak and the characteristic field for conductance fluctuations are both much larger for the circles with a barrier than the open circles. Comparing large and small devices of

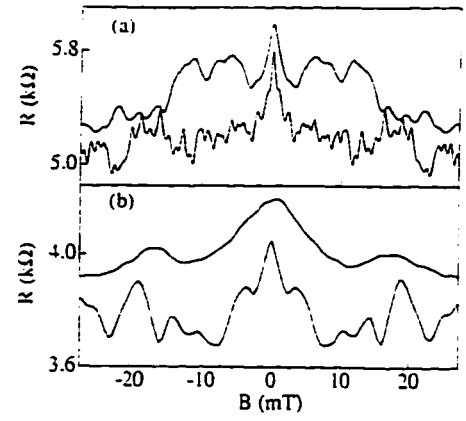

FIG. 2. Representative raw magnetoresistance data taken at $T=0.43$ K with (a) both large devices biased at -0.7 V and (b) both small devices biased at $V=-0.5$ V. Shape-A data (lower traces) offset for clarity from shape B (upper). Note more rapid oscillations and narrower zero-field peak in large vs small and in A vs B.

the same shape, we find that the magnetic-field scales are inversely proportional to the area of the electron gas, also in agreement with theory.

Figures 3(a)–3(d) show the resistance change $\Delta R/R$ due to coherent backscattering (solid lines), averaged over five gate voltages, for all four devices at $T=0.43$ K. The zero-field resistance peaks are fit by the Lorentzian line shape predicted by chaotic scattering theory (dashed lines). The coherent backscattering peak is robust: we observed the resistance peak at all bias voltages and temperatures in all devices on five separate thermal cycles. For a given sweep, conductance fluctuations distort the zero-field peak shape. In order to average away the effect of the conductance fluctuations, data were taken at five gate voltages in the conducting regime ($G_{dot}>e^2/h$) for all four devices at 0.1000-V intervals. Chaotic scattering theory predicts that the conductance minima near zero field is a Lorentzian:[11]

$$G(B)=G(0)-\Delta G_0/[1+(B/B_c)^2], \qquad (1)$$

where B_c is the half width at half maximum. As shown in Fig. 3, a Lorentzian fits our data well at $T=0.43$ K. The

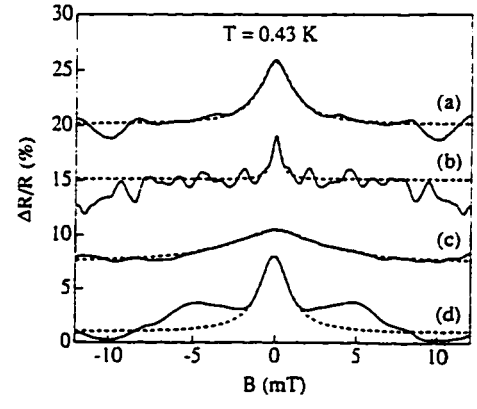

FIG. 3. Fractional change in magnetoresistance of (a) large-B-, (b) large-A-, (c) small-B-, and (d) small-A-shaped devices averaged over five gate voltages. Data (solid) are offset for clarity and fit to Lorentzian line shape (dashed).

TABLE I. Characteristic magnetic fields and corresponding enclosed trajectory areas for all devices at $T=0.43$ K; values from chaotic theory fits of coherent-backscattering peak widths (B_c) and power spectra of conductance fluctuations (B_α). Averaged over all four devices, $A_c \cong 2.4 \pm 0.8 A_\alpha$.

Size, shape	B_c (mT)	B_α (mT)
	A_c (μm^2)	A_α (μm^2)
Large, B	1.2±0.2	2.2±0.4
	0.55±0.09	0.30±0.06
Large, A	0.30±0.06	0.80±0.12
	2.2±0.4	0.82±0.12
Small, B	3.4±0.7	7.8±1.2
	0.19±0.04	0.084±0.013
Small, A	1.1±0.2	2.6±0.4
	0.6±0.1	0.25±0.04

predicted line shapes for devices A and B at zero temperature are more sharply peaked[11,12] due to the presence of large-area trajectories. Both small-angle scattering and the loss of phase coherence due to inelastic scattering at finite temperatures eliminate long trajectories that sharpen the peak shape in an integrable structure. Recently Chang *et al.*[6] found a Lorentzian line shape for the zero-field peak in an array of open circles at higher temperatures, and a more sharply peaked line shape for $T<0.4$ K.

Table I lists the half-width B_c of the coherent backscattering peak for all four devices, measured via the Lorentzian fits shown in Fig. 3, along with the corresponding trajectory areas $A_c=\Phi_0/2\pi B_c$. The error in B_c (~20%) is dominated by uncertainty in the base line, whose value was a free parameter in the fit. Comparing the characteristic areas of shapes A and B, we find that the area A_c of the open circle is larger for both the large and small devices by factors 3.9 and 3.1, respectively. Comparing the characteristic areas A_c of large and small devices of the same shape, we find that the ratio for the large A_c to small is 3.6 to 1 for shape A and 2.9 to 1 for shape B, in good agreement with the $\cong 3.7$ to 1 ratios for the electron-gas area in both shapes.

The characteristic area A_α enclosed by pairs of forward-scattered paths leading to conductance fluctuations can be measured via power spectra of the resistance vs magnetic-field data. For chaotic systems, semiclassical analysis[13] predicts that the power spectrum $S(f)$ of conductance fluctuations vs magnetic frequency f (cycles/T) is

$$S(f)=S_0(1+2\pi B_\alpha f)\exp(-2\pi B_\alpha f), \qquad (2)$$

where B_α is the magnetic-field change necessary to increase the flux through the characteristic area $A_\alpha=\Phi_0/2\pi B_\alpha$ by $\Phi_0/2\pi$. For the open circle, no analytic form for the power spectrum corresponding to Eq. (2) exists; numerical results[8,11] give spectra with more power at higher magnetic frequencies, which resemble power laws. For consistency with our coherent-backscattering analysis, we use Eq. (2) to fit data for all four devices, despite the fact that we expect deviations from this form.

Figure 4 shows measured average power spectra of the conductance fluctuations vs magnetic frequency f in the large [Fig. 4(a)] and small [Fig. 4(b)] shape-A (circles) and shape-B (triangles) devices; the power spectra for shape-B devices have been offset downward by a decade for clarity. The solid lines in Fig. 4 are fits to theory [Eq. (2)]. These power spectra were obtained from low-field ($|B|<0.3$ and $|B|<0.5$ T for the small and large devices, respectively) magnetoconductance data to minimize the effects of trajectory curvature. A fourth-order polynomial was subtracted from each magnetic-field sweep to remove background magnetoconductance associated with the point contacts. As for the coherent-backscattering analysis above, power spectra were averaged over five gate voltages. At each gate voltage, 31 half-overlapping power-spectra segments were logarithmically averaged to suppress sharp structure at low frequencies associated with periodic orbits.

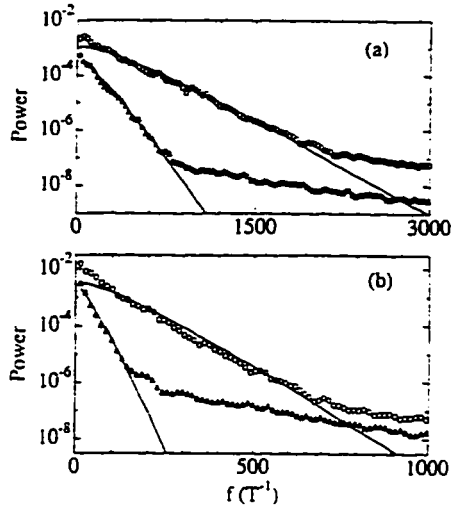

FIG. 4. Power spectra of conductance fluctuations for (a) large and (b) small devices vs magnetic frequency, averaged over five gate voltages. Data for shape A (circles) and shape B (triangles) are offset for clarity. Curve fits to Eq. (2) (solid) agree with data over four orders of magnitude in power. Note discrepancy between fit and data for both open circles at low f. The tail at high f is a noise effect.

As shown in Fig. 4, chaotic theory provides a good fit to the conductance-fluctuation power spectra for the circles with barriers, suggesting that orbits within the actual devices are chaotic.[14] The fit for data from the open circular devices is less good: the power spectra for both circular devices are concave up, in agreement with numerical simulations[8] for open circular devices, whereas the power spectra predicted by chaotic theory are concave down. Nonetheless, the fit provides a good operational definition of a characteristic area A_α, which quantifies the large differences in power spectra between the two device shapes in Figs. 4(a) and 4(b).

Table I summarizes the fitted characteristic fields B_α and characteristic areas A_α for the data of Fig. 4; the estimated error (~15%) is largely due to uncertainty in the high-magnetic-frequency cutoff chosen for the fits. Comparing conductance fluctuations in our devices we find ratios of characteristic area A_α for shapes A to B of 2.8:1 and 2.9:1 for large and small devices, respectively, and large-to-small A_α ratios of 3.4:1 and 3.3:1 for shapes A and B, respectively. These ratios agree well with those obtained from our

coherent-backscattering analysis, suggesting that the electron trajectories contributing to both phenomena are similar. An important difference is that the characteristic area for coherent backscattering is expected to be approximately twice that for conductance fluctuations, because a *pair* of closed time-reversed paths are required for coherent backscattering. Averaging over all four devices, we find $A_c \cong 2.4 \pm 0.8 A_\alpha$, in good agreement with theory.

The authors thank Scott Yang, John Baskey, Doug Mar, and Mark Eriksson for help in conducting this experiment, and Harold Baranger, Charlie Marcus, and Douglas Stone for useful discussions. Two of us (M.J.B. and J.A.K.) acknowledge support from the Office of Naval Research. This work was supported at Harvard by ONR Grant No. N00014-89-J-1592 and NSF Grant No. DMR-91-19386, and at UCSB by Grant No. AFOSR-91-0214.

[1] *Mesoscopic Phenomena in Solids*, edited by B. L. Altshuler, P. A. Lee, and R. A. Webb (North-Holland, New York, 1991).

[2] C. M. Marcus, A. J. Rimberg, R. M. Westervelt, P. F. Hopkins, and A. C. Gossard, Phys. Rev. Lett. **69**, 506 (1992).

[3] M. J. Berry, J. H. Baskey, R. M. Westervelt, and A. C. Gossard, Phys. Rev. B **50**, 8857 (1994).

[4] M. J. Berry *et al.*, Surf. Sci. **305**, 495 (1994).

[5] M. W. Keller *et al.*, Surf. Sci. **305**, 501 (1994).

[6] A. M. Chang, H. U. Baranger, L. N. Pfeiffer, and K. W. West, Phys. Rev. Lett. **73**, 2111 (1994).

[7] M. C. Gutzwiller, *Chaos in Classical and Quantum Mechanics* (Springer, New York, 1990).

[8] W. A. Lin, J. B. Delos, and R. V. Jensen, Chaos **3**, 655 (1993).

[9] Shubnikov–de Haas oscillations measured at 430 mK were used to determine τ_s [J. P. Harring *et al.*, Phys. Rev. B **32**, 8442 (1985); F. Fang *et al.*, Surf. Sci. **196**, 310 (1988)].

[10] J. A. Katine, M. J. Berry, R. M. Westervelt, and A. C. Gossard, Superlatt. Microstruct. (to be published).

[11] H. U. Baranger, R. A. Jalabert, and A. D. Stone, in *Transport Phenomena in Mesoscopic Systems*, edited by H. Fukuyama and T. Ando (Springer, New York, 1992).

[12] H. U. Baranger, R. A. Jalabert, and A. D. Stone, Phys. Rev. Lett. **70**, 3876 (1993).

[13] R. A. Jalabert, H. U. Baranger, and A. D. Stone, Phys. Rev. Lett. **65**, 2442 (1990).

[14] Trajectories inside an ideal-shaped *B* device are integrable since they differ from those in an open circle by only a mirror reflection for each collision with the bar. Realistic devices with rounding of the bar and disorder are expected to possess chaotic orbits.

References

Adachi, S., in *Gallium Arsenide*, J.S. Blakemore, ed., AIP, New York (1987).

Aleiner, I.L., and A.I. Larkin, to be published in *Phys Rev. B*, (1996).

Altshuler, B.L., and A.G. Aronov, *JETP Lett.* **33**, 499 (1981).

Altshuler, B.L., A.G. Aronov, and D.E. Khmelnitsky, *Solid State Comm.* **39**, 619 (1981).

Altshuler, B.L., A.G. Aronov, and D.E. Khmelnitsky, *J. Phys. C* **15**, 7367 (1982).

Aronov, A.G., and Y.V. Sharvin, *Rev. Mod. Phys.* **59**, 755 (1987).

Balshaw, N.H., G.J. Batey, R. Ling, J.P. White, and E.P. Whitehurst, *Introduction to Thermometry Below 1 K*, Oxford Instruments Ltd., Witney, England (1990).

Baranger, H.U., R.A. Jalabert, and A.D. Stone, in *Transport Phenomena in Mesoscopic Systems*, H. Fukuyama, and T. Ando, Eds. Springer, New York (1992).

Baranger, H.U., R.A. Jalabert, and A.D. Stone, *Phys. Rev. Lett.* **70**, 3876 (1993).

Baranger, H.U., and P.A. Mello, *Phys. Rev. B* **51**, 4703 (1995).

Baskey, J.H., Ph.D. Thesis, Harvard University (1994).

Beenakker, C.W.J., and H. van Houten, *Phys. Rev. B* **38**, 3232 (1988a).

Beenakker, C.W.J., and H. van Houten, *Phys. Rev. B* **37**, 6544 (1988b).

Beenakker, C.W.J., and H. van Houten, *Phys. Rev. B* **39**, 10445 (1989).

Beenakker, C.W.J., and H. van Houten, "Quantum Transport in Semiconductor Nanostructures," *Sol. State Phys.* **44**, H. Eherenreich and D. Turnbull, eds., Academic Press, San Diego, CA (1991).

Berry, M.J., J.H. Baskey, R.M. Westervelt, and A.C. Gossard, *Phys. Rev. B* **50**, 8857 (1994a).

Berry, M.J., J.A. Katine, R.M. Westervelt, and A.C. Gossard, *Phys. Rev. B* **50**, 17721 (1994b).

Berry, M.J., J.A. Katine, C.M. Marcus, R.M. Westervelt, and A.C. Gossard, *Surf. Sci.* **305**, 495 (1994c).

Berry, M.J., Ph.D. Thesis, Harvard University (1994).

Bird, J.P., K. Ishibashi, M. Stopa, Y. Aoyagi, and T. Sugano, *Phys. Rev. B* **50**, 14983 (1994).

Bird, J.P., K. Ishibashi, D.K. Ferry, Y. Ochiai, Y. Aoyagi, and T. Sugano, *Phys. Rev. B* **51**, 18037 (1995a).

Bird, J.P., D.M. Olatona, R. Newbury, R.P. Taylor, K. Ishibashi, M. Stopa,, Y. Aoyagi, T. Sugano, and Y. Ochiai, *Phys. Rev. B* **52**, 14336 (1995b).

Bird, J.P., K. Ishibashi, D.K. Ferry, Y. Ochiai, Y. Aoyagi, and T. Sugano, *Phys. Rev. B* **51**, 18037 (1995c).

Bird, J.P., D.K. Ferry, R. Akis, Y. Ochiai, K. Ishibashi, Y. Aoyagi, and T. Sugano, to appear in *Europhys. Lett.*, (1996).

Braslau, N., *J. Vac. Sci. Tech.* **19**, 803 (1981).

Büttiker, M., *Phys. Rev. Lett.* **57**, 1761 (1986).

Büttiker, M., *IBM J. Res. Develop.* **32**, 63 (1988a).

Büttiker, M., *IBM J. Res. Develop.* **32**, 317 (1988b).

Chakravarty, S., and A. Schmid, *Phys. Rep.* **140**, 193 (1986).

Chang, A.M., H.U. Baranger, L.N. Pfeiffer, and K.W. West, *Phys. Rev. Lett.* **73**, 2111 (1994).

Choi, K.K., D.C. Tsui, and S.C. Palmateer, *Phys. Rev. B* **33**, 8216 (1986).

Choi, K.K., D.C. Tsui, and K. Alavi, *Phys. Rev. B* **36**, 7751 (1987a).

Choi, K.K., D.C. Tsui, and K. Alavi,, *Appl. Phys. Lett.* **50**, 110 (1987b).

Chklovskii, D.B., B.I. Shklovskii, and L.I. Glazman, *Phys. Rev. B* **46**, 4026 (1992).

Clarke, R.M., I.H. Chan, C.M. Marcus, C.I. Duruoz, J.S. Harris, K.L. Campman, and A.C. Gossard, *Phys. Rev. B* **52**, 2656 (1995).

Crommie, M.F., C.P. Lutz, and D.M. Eigler, *Nature* **363**, 524 (1993).

Das Sarma, S., and F. Stern, *Phys. Rev. B* **32**, 8442 (1985).

Dekker, C., A.J. Scholten, F. Liefrink, R. Eppenga, H. van Houten, and C.T. Foxon, *Phys. Rev. Lett.* **66**, 2148 (1991).

Dingle, R., H.L. Stormer, A.C. Gossard, and W. Weigmann, *Appl. Phys. Lett.* **33**, 655 (1978).

Ditlefsen, E., and J. Lothe, *Phil. Mag.* **14**, 759 (1966).

Eriksson, M.A., R.G. Beck, M. Topinka, J.A. Katine, R.M. Westervelt, K.L. Campman, and A.C. Gossard, *Appl. Phys. Lett.* **69**, 671 (1996).

Fasol, G., *Appl. Phys. Lett.* **59**, 2430 (1991).

Fischer, M.E., *Phil. Mag.* **7**, 1731 (1962).

Fromhold, T.M., P.B. Wilkinson, F.W. Sheard, L. Eaves, J. Miao, and G. Edwards, *Phys. Rev. Lett.* **75**, 1142 (1995).

Fuchs, K., *Proc. Cambridge Phil. Soc.* **34**, 100 (1938).

Giuliani, G.F., and J.J. Quinn, *Phys. Rev. B* **26**, 4421 (1982).

Grabert, H. and M.H. Devoret, eds. *Single Charge Tunneling*, Plenum Press, New York (1992).

Guenther, R.D., *Modern Optics*, John Wiley, New York (1990).

Harris, J.J., J.A. Pals, and R. Woltjer, *Rep. Prog. Phys.* **52**, 1217 (1989).

Hastings, M.B., A.D. Stone, and H.U. Baranger, *Phys. Rev. B.* **50**, 8230 (1994).

Heller, E.J., *Phys. Rev. Lett.* **53**, 1515 (1984).

Heller, E.J., M.F. Crommie, C.P. Lutz, and D.M. Eigler, *Nature* **369**, 464 (1994).

Hergenrother, J.M., Ph.D. Thesis, Harvard University (1995).

Herman, M.A., and H. Sitter, *Molecular Beam Epitaxy: Fundamentals and Current Status*, Springer-Verlag, Berlin (1989).

Holle, A., G. Wiesbusch, J. Main, B. Hager, H. Rottke, and K.H. Welge, *Phys. Rev. Lett.* **56**, 2594 (1986).

Holle, A., J. Main, G. Wiebusch, H. Rottke, and K.H. Welge, *Phys. Rev. Lett.* **61**, 161 (1988).

Hopkins, P.F., Ph.D. Thesis, Harvard University (1990).

Horowitz, P., and W. Hill, *The Art of Electronics, 2nd Edition*, Cambridge Univ. Press, Cambridge, England (1989).

Jenkins, F.A., and H.E. White, *Fundamentals of Optics, 2nd Ed.*, McGraw Hill, New York (1950).

Katine, J.A., M.J. Berry, R.M. Westervelt, A.C. Gossard, *Superlatt. and Microstruct.* **16**, 211 (1994).

Katine, J.A., M.A. Eriksson, R.M. Westervelt, K.L. Campman, and A.C. Gossard, *Superlatt. and Microstruct.* **20**, Sept. Issue (1996).

Klem, J., W.T. Masselink, D. Arnold, R. Fischer, T.J. Drummond, K. Morkoc, K. Lee, and M.E. Shur, *J. Appl. Phys.* **54**, 5214 (1983).

Kurdak, C., A.M. Chang, A. Chin, and T.Y. Chang, *Phys. Rev. B* **46**, 6846 (1992).

Lakhani, A.A., *J. Appl. Phys.* **56**, 1888 (1984).

Landauer, R., *IBM J. Res. Dev.* **1**, 223 (1957).

Landauer, R., *Phil. Mag.* **21**, 863 (1970).

Lee, P.A., and T.V. Ramakrishnan, *Rev. Mod. Phys.* **57**, 287 (1985).

Lee, P.A., and A.D. Stone, *Phys. Rev. Lett.* **55**, 1622 (1985).

Look, D.C., *Electrical Characterization of GaAs Materials and Devices*, John Wiley, New York, (1989).

Lounasmaa, O.V., *Experimental Principles and Methods Below 1 K*, Academic Press, New York, (1974).

Ma, Y., R. Fletcher, E. Zaremba, M. D'Iorio, C.T. Foxon, and J.J. Harris, *Phys. Rev. B* **43**, 9033 (1991).

Mackie, S., and S.P. Beaumont, *Solid State Technol.* **28**, 117 (1985).

Mani, R.G., K. von Klitzing, and K. Ploog, *Phys. Rev. B* **48**, 4571 (1993).

Mar, D.J., Ph.D. Thesis, Harvard University (1994).

Marcus, C.M., A.J. Rimberg, R.M. Westervelt, and A.C. Gossard, *Phys. Rev. Lett.* **69**, 506 (1992).

Marcus, C.M., R.M. Westervelt, P.F. Hopkins, and A.C. Gossard, *Chaos* **3**, 643 (1993).

Martinis, J., M. Devoret, and J. Clarke, *Phys. Rev. B* **35**, 4682 (1987).

Molenkamp, L.W., A.A.M. Staring, C.W.J. Beenakker, R. Eppenga, C.E. Timmering, and J.G. Williamson, *Phys. Rev. B* **41**, 1274 (1990).

Nabity, J.C., *Rev. Sci. Instrum.* **60**, 27 (1989).

Nabity, J.C., *Nanometer Pattern Generation System Manual*, Bozeman, MT (1991).

Oxford Instruments, *Kelvinox 100 Dilution Refrigerator Operator's Handbook, Issue 3.6*, Scientific Research Division, Witney, England (1993).

Paalanen, M.A., D.C. Tsui, D.C., and J.C.M. Hwang, *Phys. Rev. Lett.* **51**, 2226 (1983).

Parikh, M., and D.F. Kyser, *J. Appl. Phys.* **50**, 1104 (1979).

Petroff, P.M., R.C. Miller, A.C. Gossard, and W. Wiegmann, *Appl. Phys. Lett.* **44**, 217 (1984).

Pfeiffer, L.N., K.W. West, H.L. Stormer, and K.W. Baldwin, *Appl. Phys. Lett.* **55**, 1888 (1989).

Price, P.J., *Phys. Rev. B* **30**, 2236 (1984).

Richardson, R.C., and E.N. Smith, *Experimental Techniques in Condensed Matter Physics at Low Temperatures*, Addison-Wesley, New York (1988).

Rimberg, A.J., Ph.D. Thesis, Harvard University (1992).

Rooks, M.J., S. Wind, P. McEuen, and D.E. Prober, *J. Vac. Sci. Technol. B* **5**, 318 (1987).

Roukes, M.L., M.R. Freeman, R.S. Germain, R.C. Richardson, and M.B. Ketchen, *Phys. Rev. Lett.* **55**, 422 (1985).

Shih, Y-C., M. Murakami, E.L. Wilkie, A.C. Callegari, *J. Appl. Phys.* **62**, 582 (1987).

Sivan, U., M. Heiblum, C.P. Umbach, and H. Shtrikman, *Phys. Rev. B* **41**, 7937 (1990).

Smith, C.G., M. Pepper, H. Ahmed, J.E.F. Frost, D.G. Hasko, R. Newbury, D.C. Peacock, D.A. Ritchie, and G.A.C. Jones, *J. Phys. Condens. Matter* **1**, 9035 (1989).

Smith, W.F., Ph.D. Thesis, Harvard University (1989).

Spector, J., H.L. Stormer, K.W. Baldwin, L.N. Pfeiffer, and K.W. West, *Appl. Phys. Lett.* **56**, 1290 (1990).

Spector, J., J.S. Weiner, H.L. Stormer, K.W. Baldwin, L.N. Pfeiffer, and K.W. West, *Surface Science* **263**, 240 (1992).

Sridhar, S., *Phys. Rev. Lett.* **67**, 785 (1991).

Suhrke, M., and S. Wilke, *Phys. Rev. B* **46**, 2400 (1992).

Taylor, R.P., P.T. Coleridge, Y. Feng, M. Davies, J. McCaffrey, and P.A. Marshall, *J. of Appl. Phys.* **76**, 7966 (1994).

Taylor, R.P., R. Newbury, R.B. Dunford, P.T. Coleridge, A.S. Sachradja, and J.A. Adams, *Phys. Rev. B* **51**, 9801 (1995).

Thronton, T.J., M. Pepper, H. Ahmed, D. Andrews, and G.J. Davies, *Phys. Rev. Lett.* **56**, 1198 (1986).

Thronton, T.J., M. Pepper, H. Ahmed, G.J. Davies, and D. Andrews, *Phys. Rev. B* **36**, 4514 (1987).

Thornton, T.J., M.L. Roukes, A. Scherer, B.P. van der Gaag, *Phys. Rev. Lett.* **63**, 2128 (1989).

Thouless, D.J., *Phys. Rev. Lett.* **39**, 1167 (1977).

Timp, G., R.E. Behringer, and J.E. Cunningham, *Phys. Rev. B* **42**, 9259 (1990).

Timp, G. in *Mesoscopic Phenomena in Solids*, P.A. Lee, R.A. Webb, and B.L. Altshuler, eds., Elsevier, Amsterdam (1992).

van Houten, H., C.W.J. Beenakker, M.E.I. Broekaart,, M.G.H.J. Heijman, B.J. van Wees, H.E. Mooij, and J.P. Andre, *Acta Electronica* **28**, 27 (1988a).

van Houten, H., C.W.J. Beenakker, B.J. van Wees, and J.E. Mooij, *Surf. Sci.* **196**, 144 (1988b).

van Houten, H., C.W.J. Beenakker, J.G. Williamson, M.E.I. Broekaart, P.H.M. van Loosdrecht, B.J. van Wees, J.E. Mooij, C.T. Foxon, and J.J. Harris, *Phys. Rev.B* **39**, 8556 (1989).

van Wees, B.J., H. van Houten, C.W.J. Beenakker, J.G. Williamson, L.P. Kouwenhoven, D. van der Marcel, and C.T. Foxon, *Phys. Rev. Lett.* **60**, 848 (1988).

van Wees, B.J., L.P. Kouwenhoven, C.J.P.M. Harmans, J.G. Williamson, C.E. Timmering, M.E.I. Broekaart, C.T. Foxon, and J.J. Harris, *Phys. Rev. Lett.* **62**, 2523 (1989).

Washburn, S., and R.A. Webb, *Adv. Phys.* **35**, 375 (1986).

Waugh, F.R., M.J. Berry, C.H. Crouch, C. Livermore, D.J. Mar, R.M. Westervelt, K.L. Campman, and A.C. Gossard, *Phys. Rev. Lett.* **75**, 705 (1995).

Waugh, F.R., Ph.D. Thesis, Harvard University (1994).

Webb, R.A., A. Hartstein, J.J. Wainer, A.B. Fowler, *Phys. Rev. Lett.* **54**, 1577 (1985).

Wennberg, A.K.M., S.N. Ytterboe, C.M. Gould, H.M. Bozler, J. Klem, and H. Morkoc, *Phys. Rev. B* **34**, 4409 (1986).

Wharham, D.A., T.J. Thornton, R. Newbury, M. Pepper, H. Ahmed, J.E.F. Frost, D.G.Hasko, D.C. Peacock, D.A. Ritchie, and G.A.C. Jones, *J. Phys. C* **21**, L209 (1988).

Wittels, N.D., in *Fine Line Lithography*, R. Newman, ed., North-Holland, Amsterdam (1980).

Woodall, J.M., J.L. Freeouf, G.D. Pettit, T. Jackson, and P. Kirchner, *J. Vac. Sci. Technol.* **19**, 626 and 794 (1981).

Yacoby, A., U. Sivan, C.P. Umbach, and J.M. Hong, *Phys. Rev. Lett.* **66**, 1938 (1991).

Yacoby, A., M. Heiblum, V. Umansky, H. Shtrikman, and D. Mahalu, *Semicon. Sci. and Tech.* **9**, 907 (1994a).

Yacoby, A., M. Heiblum, V. Umansky, H. Shtrikman, and D. Mahalu, *Phys. Rev. Lett.* **73**, 3149 (1994b).

Yang, Scott, Ph.D. Thesis, Harvard University (1995).

Zheng, H.Z., H.P. Wei, D.C. Tsui, and G. Weimann, *Phys. Rev. B* **34**, 5635 (1986).